

University of Nottingham
UK | CHINA | MALAYSIA

Novel surface generation and characterisation by electrochemical jet processing

Advanced Component Engineering Laboratory, Faculty of Engineering, University of Nottingham

Alistair Speidel MChem

November 2018

Abstract

Electrochemical jet processing (EJP) is an applied electrochemical technique capable of exercising highly localised control of material removal independent of mechanical properties. This makes the process suitable for both micromachining and surface texturing operations in high-value engineering materials, without altering the near-surface in a thermomechanical manner.

The research presented in this thesis primarily investigated the generation and characterisation of topographies arising from EJP, since topography can strongly affect functional and mechanical properties of the material. It was found that the resulting surface texture was directly influenced by the starting material microstructure, even in processing regimes beyond which the microstructure was thought to make a difference. This was proposed to be the result of the high flow velocities in EJP.

In addition, under appropriate processing regimes, the microscale topography is sensitive to underlying microstructural characteristics such as orientation, localised composition, defect density and thermal history. This was applied to develop a large-area microstructural characterisation technique, which when calibrated against a conventional approach, is capable of identifying localised crystallographic texture. This was applied to common engineering materials such as nickel, aluminium alloys and copper.

The second objective of the thesis was to innovate the geometry of processed features. Conventionally, material removal is shown to be a transformation of the Gaussian energy distribution within the electrolyte jet. Through small additions of doping agents, the low energy area, responsible for tapering of the machined feature, can be reduced. This leads to an increase in precision and dimensional

accuracy. In addition, it is shown that individual corrosion pits can be propagated, which represents the development of a novel form of electrochemical processing, capable of further reducing the scale of this micromachining process, as well as easily generating fractal surface patterning.

In addition, the thesis explores the viability of EJP as a coating technology. This was firstly observed through electroplating operations, where a high level of control over the deposit morphology was demonstrated through electrolyte design. Subsequently a methodology was presented regarding the co-deposition of particulate matter within a metallic deposit. Finally, EJP was presented as a route through which more robust surfaces with interesting functional properties could be generated as part of an in-jet plasma electrolytic oxidation process.

Publications

Included in this thesis

- **Speidel, A**., Su, R., Mitchell-Smith, J., Dryburgh, P., Bisterov, I., Pieris, D., Li, W., Patel, R., Clark, M., Clare, A.T., (2018) Crystallographic texture can be rapidly determined by electrochemical surface analytics. Acta Materialia, 159, 89-101.
- **Speidel, A.**, Mitchell-Smith, J., Bisterov, I., Clare, A.T., (2018) The importance of microstructure in electrochemical jet processing. Journal of Materials Processing Technology, 262, 459-470.
- Clare, A.T., **Speidel, A.**, Bisterov, I., Jackson-Crisp, A., Mitchell-Smith, J., (2018) Precision enhanced electrochemical jet processing. CIRP Annals – Manufacturing Technology, 67, 205-208.
- **Speidel, A.**, Mitchell-Smith, J., Bisterov, I., Clare, A.T., (2018) The dependence of surface finish on material precondition in electrochemical jet machining. Procedia CIRP 68, 477-482.
- Mitchell-Smith, J., **Speidel, A.**, Clare, A.T., (2018) Transitory electrochemical masking for precision jet processing techniques. Journal of Manufacturing Processes 31, 273-285.
- Clare, A.T., **Speidel, A.**, Mitchell-Smith, J., Patwardhan, S., (2017) Electrolyte design for suspended particulates in electrolyte jet processing. CIRP Annals – Manufacturing Technology 66, 201-204.
- **Speidel, A.**, Lutey, A.H.A., Mitchell-Smith, J., Rance, G.A., Liverani, E., Ascari, A., Fortunato, A., Clare A.T., (2016) Surface modification of mild steel using a combination of laser and electrochemical processes. Surface and Coatings Technology 307a, 849-860.
- **Speidel, A.**, Mitchell-Smith, J., Walsh, D., Hirsch, M., Clare, A.T., (2016) Electrolyte jet machining of titanium alloys using novel electrolyte solutions. Procedia CIRP 42, 367-372.

Not included in this thesis

- Mitchell-Smith, J., **Speidel, A.**, Bisterov, I., Clare, A.T., (2018) Electrolyte multiplexing in electrochemical jet processing. Procedia CIRP 68, 483-487.
- Bisterov, I., Mitchell-Smith, J., **Speidel, A.**, Clare, A.T., (2018) Specific and programmable surface structuring by electrochemical jet processing. Procedia CIRP 68, 460-465.
- Mitchell-Smith, J., **Speidel, A.**, Clare, A.T., (2018) Advancing electrochemical jet methods through manipulation of the angle of address. Journal of Materials Processing Technology 255, 364-372.
- Mitchell-Smith, J., **Speidel, A.**, Gaskell, J., Clare, A.T., (2017) Energy distribution modulation by mechanical design for electrochemical jet processing techniques. International Journal of Machine Tools and Manufacture 122, 32-46.

Conferences

- 19th International Symposium on Electrochemical and Electro-physical Machining (ISEM XIX), Bilbao, 2018.
  Paper written and presented.
  Best paper award, 500€ ONA Grant

- 18th International Symposium on Electrochemical and Electro-physical Machining (ISEM XVIII), Tokyo, 2016.
  Paper written.
  Special Focus Paper Award, ¥100,000

Acknowledgements

I would like to thank my principal supervisor, Professor Adam Clare, who has allowed me to develop within the research group, offering invaluable help, advice, as well as interesting contributions. No part of this project would have been possible without Adam's vision and guidance. In addition, special thanks go to Dr Jonathon Mitchell-Smith, who contributed significantly towards this work both intellectually and practically, and for his seemingly endless patience – despite my best efforts at apparatus destruction. Alongside the talented Alexander Jackson-Crisp, the tools to accomplish this body of work were supplied to me. The work in this thesis would not have been possible without either member of the research group. Thanks also go to Ivan Bisterov for intellectual discussion and laboratory assistance.

Dr Rong Su was instrumental, helping with data analysis and I am also grateful that he shared my vision. My gratitude is extended to the rest of the Manufacturing Metrology Team for the use of characterisation apparatus. I am grateful to Dr Graham Rance for training and assistance with Raman spectroscopic acquisitions and zeta potential analysis. I am also grateful to Dr Matthias Hirsch for his practical support from when I arrived at Nottingham, and my co-supervisor Dr Darren Walsh, who has always gladly offered support and input when required. I would also like to thank Professor Graham McCartney and the other CDT directors who enabled me to carry out this body of work.

Finally, but not least, I would like to thank my family and my partner Agathe, who has unconditionally supported me in this journey since the very beginning, while helping me develop, and generally making me into a better person.

Contents

Abstract i
Publications iii
Included in this thesis iii
Not included in this thesis iv
Conferences iv
Acknowledgements v
Contents vi
Abbreviations xi
Nomenclature xii
1. Introduction 1
1.1. Aims and objectives 2
1.2. Thesis outline 5
2. Literature review 7
2.1. Introduction to EJP 7
2.1.1. Overview 7
2.1.2. Fundamentals of mass-transfer 8
2.1.3. Defining EJP techniques 12
2.1.4. Energy distribution in EJP 14
2.1.5. Role of the electrolyte 19
2.1.6. Summary of research gaps 22
2.2. Topography in EJP – *machining* 23
2.2.1. Introduction 23
2.2.2. Process parameter influence on topography 24
2.2.3. Material influence on topography 35
2.2.4. Summary of research gaps 46

2.3. Macroscale EJP feature geometry – *machining* 47

2.3.1. Introduction 47

2.3.2. Process parameter influence on feature geometry 48

2.3.3. Material influence on the deterministic feature 61

2.3.4. Summary of research gaps 62

2.4. Material deposition in EJP 64

2.4.1. Introduction 64

2.4.2. Jet electrodeposition 64

2.4.3. Jet co-deposition of particulates 69

2.4.4. Anodic oxidation 71

2.4.5. Summary of research gaps 73

3. Experimental 75

3.1. Substrate preparation 75

3.1.1. Influence of microstructural precondition and orientation on the topography in single-phase materials. 75

3.1.2. Influence of grain size and phase ratio in multiple-phase materials 76

3.1.3. Influence of electrolytes on the removal geometry 77

3.1.4. Substrates for EJP coating 78

3.2. Sample processing 78

3.2.1. Static EJP platform 78

3.2.2. Dynamic EJP platform 80

3.3. EJP parameters and electrolytes 81

3.3.1. Influence of microstructural precondition and orientation on the topography in single-phase materials. 81

3.3.2. Influence of grain size and phase ratio in multiple-phase materials 82

3.3.3. Parameters for electrolyte experiments 83

3.3.4. EJP coating parameters 84
3.4. Prior EJP material characterisation 85
3.4.1. Etching and optical microscopy 85
3.4.2. Electron backscatter diffraction 86
3.4.3. Spatially resolved acoustic spectroscopy 87
3.5. Post-EJP characterisation 89
3.5.1. Scanning electron microscopy 89
3.5.2. Focus-variation microscopy 91
3.5.3. Coherence scanning interferometry 93
3.5.4. Hardness testing 94
3.6. Data analysis 94
3.6.1. MountainsMap 94
3.6.2. ImageJ 95
3.7. Chemical analysis 96
3.7.1. Energy dispersive X-ray spectroscopy 96
3.7.2. Raman spectroscopy 97
3.7.3. Electrolyte conductivity and pH 99
3.7.4. Particle surface charge 99
3.8. Microscale topography quantification 100
3.9. Removal and form characterisation 103
4. Characterisation of microstructure-dependent topography in EJP 108
4.1. Introduction 108
4.2. Microstructure-topography dependence in Cu 110
4.2.1. Effect of material precondition on the microstructure 110
4.2.2. Topography observations 114
4.2.3. Topography generation mechanisms 121

4.2.4. Application as a tool to assess material deformation. 127
4.3. Correlating topography with orientation 129
4.3.1. Preliminary microstructures 129
4.3.2. EJP generates orientation characteristic topographies 130
4.3.3. Manipulating orientation-dependent topographies 137
4.3.4. Surface Analytics 144
4.3.5. Crystallographic orientation mapping and validation 150
4.4. Summary 154
5. EJP of multiple-phase materials 156
5.1. Introduction 156
5.2. Effect of annealing treatments 156
5.3. Point processing topographies 160
5.4. Striation processing topographies 165
5.5. Relative phase etching 168
5.6. Near-surface chemistry 170
5.7. Removal rates 172
5.8. Form observations 178
5.9. Summary 180
6. Redefining the removal geometry in EJP 181
6.1. Introduction 181
6.2. Enhancing dimensional accuracy 182
6.2.1. Novel electrolyte systems 182
6.2.2. Current filtering mechanism 188
6.2.3. Scalability of micro-striations 196
6.3. EJP micromachining of titanium 200
6.3.1. Surface generation in titanium 201

6.3.2. Processing strategies in titanium 207
6.3.3. Dimensional accuracy and fidelity 213
6.4. Novel material removal mechanisms 221
6.4.1. Periodic electrochemical oscillations 222
6.4.2. Propagating individual pits 232
6.5. Summary 243
7. EJP coating and surface modification 246
7.1. Introduction 246
7.2. Jet electrodeposition 247
7.2.1. Considerations for jet electrodeposition 247
7.2.2. Nodule size modulation 254
7.2.3. Thiourea doping 262
7.2.4. Silica codeposition 268
7.3. Jet plasma electrolytic oxidation 275
7.3.1. Control of jet plasma electrolytic oxidation 275
7.3.2. Interrogation of jet-PEO coatings 288
7.4. Summary 294
8. Conclusions 297
9. Future work 302
References 306
Appendices 316

Abbreviations

BSE	Backscatter electron	MMT	Manufacturing Metrology Team
CAM	Computer aided manufacturing	MRR	Material removal rate
CCD	Charge coupled device	ND	Normal direction
CNC	Computer numerical control	NMRC	Nanoscale and Microscale Research Centre
CSI	Coherence scanning interferometry	OHP	Outer Helmholtz plane
DC	Direct current	OM	Optical microscopy
EBSD	Electron backscatter diffraction	PEO	Plasma electrolytic oxidation
EBSP	Electron backscatter pattern	RD	Reverse direction
ECE	Electrochemical equivalent	SAW	Surface acoustic wave
ECM	Electrochemical machining	SE	Secondary electron
EDS	Energy dispersive X-ray spectroscopy	SEM	Scanning electron microscopy
EJD	Electrochemical jet deposition	SHE	Standard hydrogen electrode
EJM	Electrolyte jet machining	SRAS	Spatially resolved acoustic spectroscopy
EJP	Electrochemical jet processing	TEM	Transmission electron microscopy
FVM	Focus variation microscopy	TD	Transverse direction
FWHM	Full width at half maximum	TP	Throwing power
HSSJE	High-speed selective jet electroplating	UAEJP	Ultrasonic-assisted EJP
HV	Vickers hardness	Vmc	Core material volume
ID	Internal diameter	Vmp	Peak material volume
IDC	Incident dopant concentration	Vvc	Core void volume
IEG	Inter-electrode gap	Vvv	Valley void volume
IR	Infrared	WC	Tungsten carbide
LAEJP	Laser-assisted EJP	WLI	White light interferometry
ISO	International Organization for Standardization	XRD	X-ray diffraction
JED	Jet electrodeposition	ZOPD	Zero optical path difference

Nomenclature

A	Area, μm²	λ	Wavelength, nm
A_m	Machined area, μm²	λ_g	Grating period, nm
A_p	Profile area, μm²	$\overline{\lambda_q}$	Linear charge density, C/m
A_s	Sample area, μm²	M	Molar mass, g/mol
$at.\ \%$	Atomic percent	M_s^0	Workpiece metal atom
A_{aq}^{x-}	Aqueous anion	M_{aq}^{n+}	Solvated metal cation
B	Passivation breakdown potential, V	MA_{ads}^{x-}	Adsorbed anion species
C_B	Bulk electrolyte concentration, mol/l	m	Mass transferred, g
C_e	Concentration at electrode, mol/l	v_h	Translation velocity, mm/s
D	Diffusion coefficient, m²/s	v_j	Electrolyte jet velocity, m/s
dev_c	Contour deviation, μm²	$\dot{v}_j$	Volumetric flow rate, ml/s
dev_p	Profile deviation, %	v_s	Surface acoustic wave velocity, m/s
d_M	Maximum depth, μm	P	Passivation potential
d_N	Nozzle internal diameter, μm	Q	Total charge transfer, C
d_n	Distance, m	R	Resistance, Ω
Δf	Frequency shift	Sa	Areal surface roughness, μm
δ_N	Diffusion layer thickness, m	Sq	Root mean square surface roughness, μm
F	Faraday constant, 96,485.33 C/mol	T_B	Boiling point, °C
f_s	Characteristic frequency, Hz	T_M	Melting point, °C
I	Current, A	t	Time, s
I_C	Ionic strength, M	t_0	Initial time, s
J	Current density, A/cm²	θ	Angle, degrees
J_{lim}	Limiting current density, A/cm²	V	Electrode potential
J_{noz}	Supply current density, A/cm²	$wt.\ \%$	Weight percent
κ	Electrolyte conductivity, mS/cm	$\overline{x}$	Arithmetic mean average

1. Introduction

Within high-value manufacturing processes, there is a perpetual desire to increase efficiency, in addition to enhancing the quality, applicability and performance of the finished part. In light of current trends in manufacturing, wherein the means to form components of complex geometry and inhomogeneous material properties are being realised, the desire to process the total part to equivalent finish remains paramount. The latter is a salient theme, as increasing part complexity at both the macroscale, *geometry*, and the microscale, *microstructure*, will affect the processing strategies to maintain equivalent finish as required by the part design intent.

Precise finishing of high-value parts therefore presents a technical challenge, especially if there is also a desire to preserve the thermal or stress condition. In this thesis, electrochemical jet processing (EJP) is presented as a novel athermal technique to undertake precise removal and surface processing in conductive materials, independent of global material properties, whilst retaining the stress profile. EJP is defined here as any electrochemical mass-transfer reaction performed selectively upon impingement of an electrolytic jet from a nozzle onto a workpiece material held at opposite electrical potential. The polarity of the workpiece defines whether the electrochemical mass-transfer reaction is a reduction, such as metal deposition from the electrolyte, or an oxidation, such as removal of workpiece material.

Currently, research in anodic dissolution (material removal) EJP is generally limited to homogeneous material systems, such as austenitic stainless steel grades and conventional electrolyte systems, such as sodium nitrate. The result

of this is an apparent knowledge gap surrounding the process, including resulting topographies and material removal phenomena, of precipitate-heavy materials, of which complex aerospace alloys are a prominent example. Considering the difficulty in processing such materials through conventional shear-based methods, such as grinding and milling, EJP represents a route through which high-value materials can be selectively processed in a facile manner. In addition, the precision of EJP is considered to be defined and restricted by the Gaussian current density distribution within the jet. Manipulation of the applied current density distribution has so far been largely overlooked, thus the sum of deterministic featuring in EJP is largely similar in geometric limitation. This thesis intends to enhance the value of EJP as a manufacturing tool. The process is presented as a route through which complex topographies can be generated easily and rapidly in a range of materials. In addition, EJP is characterised, in terms of material removal and topography, for complex material systems resulting from complicated preparation strategies. Furthermore, there is an intent to enhance precision in EJP, through reducing the dependence of the resulting geometry from the applied current density distribution. In addition, EJP is employed as a deposition process to generate surfaces with high surface area topographies compared with the substrate.

1.1. Aims and objectives

The overall aim of this thesis is to enhance the industrial applicability of EJP-generated features on metals, both at the microscale and the macroscale. Work towards this aim is achieved through a series of targeted objectives, which have been identified as potential areas of improvement considering the current state-

of-the-art in the scientific literature and the wider cost and efficiency requirements in high-value manufacturing. The objectives are detailed below, but relate both to the characterisation and generation of surface topographies, as well as material removal characteristics, upon which the dimensional accuracy and resulting form depend. Objectives are hereby identified to enhance the value of EJP:

Objective 1: understanding the role of material precondition in defining topography and form. This is important considering the wider context of developing complex material systems industrially, such as for use in high-stress applications. Limited research has been conducted in understanding material response to EJP, i.e. material removal, form, and surface finish, in materials other than austenitic stainless steel. While a body of work has been undertaken in the area of material dependence in conventional electrochemical machining (ECM), the response to the broader range of processing parameters in EJP needs to be investigated. Therefore, there is a requirement to define the response of EJP across the total operating window, particularly in complicated material systems.

Objective 2: Enhancing the applicability of EJP towards materials characterisation. Anodic dissolution is known to generate orientation-specific topographies, the geometries of which directly relate to the underlying crystallography. Despite this, limited effort has been made to apply this information to characterise material structures. This information is incredibly valuable to the materials science community as it defines the mechanical, physical, and chemical properties of the underlying material. Therefore, the applicability of EJP is investigated in this thesis as a route through which

microstructural information can be obtained from a material, through information-rich topography generation, when applied with topographic measurement.

Objective 3: To reduce feature geometry dependence on the current density distribution. Feature generation in EJP is understood to be dependent on both the Gaussian current density distribution within the electrolytic jet, and the size of the nozzle through which the electrolyte is delivered. An objective of the thesis is to challenge this conventional, and somewhat simple model, in order to be able to generate macroscale features which are beyond the currently considered geometric limitations. This could be achieved through manipulating the electrochemical reactions that occur at the surface during processing.

Objective 4: To increase the process efficiency and versatility of EJP coating. An objective of this thesis is to apply different coating mechanisms whilst retaining the standard operating condition, and the associated processing speed and cost effectiveness. Selective coatings strategies would be enhanced by increasing the localised deposition rates, whereby novel electrolyte design is presented as a route through which this objective could be achieved.

In order to achieve these objectives, a detailed literature review was undertaken to identify gaps in the current knowledge in EJP. The work presented here is centred on investigations into the following research areas, which address gaps in either knowledge or application, or both.

1.2. Thesis outline

To execute the objectives in Section 1.1, the thesis is set out in the following chapters. A detailed literature review is carried out in Chapter 2, to determine the process state of the art and justify the requirements for the succeeding results chapters. Details of the experimental and characterisation methods used in the thesis are given in Chapter 3.

Chapter 4, the first results chapter, investigates the role that material precondition plays in defining the surface topography of simple, commercially pure materials. Further to this, discrete topographies are correlated with underlying crystallographic orientation. This enables EJP to be applied towards orientation-dependent topography generation as part of a broader materials characterisation technique. Since topography generation is rapid, the process is compatible with on-line manufacturing, unlike conventional methods like EBSD.

Chapter 5 assess the role of precondition in determining the topography, form, chemistry and removal characteristics in more complex material systems, from the same feedstock with the identical nominal compositions.

Chapter 6 demonstrates how simple changes to the electrolyte and processing strategy can significantly affect not only the resultant geometric profile, but can radically affect the removal mechanism. It is shown that using a controlled processing strategy, discrete corrosion pits can be propagated to generate sub-nozzle scale geometric features, with interesting and controllable geometries.

Chapter 7 relates to different coating strategies achievable through EJP. Here, it is demonstrated that through electrolyte consideration, electrodeposition

stability and morphology can be modulated, allowing processing at greater current densities. In addition, well dispersed codeposition is demonstrated for unstable nanoparticle suspensions, through chemical consideration. Finally, EJP is shown to be a route through which hard-facing surfaces can be generated through the mechanism of plasma electrolytic oxidation.

2. Literature review

The objective of this chapter is to define the scope of the work presented in this thesis. This was achieved through a comprehensive review of the current and past literature regarding EJP as both a removal and coating technique, including the fundamental surface-modifying phenomena. Through this appraisal of relevant prior literature, research challenges and gaps are identified.

2.1. Introduction to EJP

2.1.1. Overview

EJP, along with other ECM techniques, holds significant advantages over conventional shear-based techniques such as retention of the microstructural integrity and no explicit dependence on hardness. This is because removal occurs through anodic dissolution, defined by Faraday's laws [1]. Machining independence from hardness makes anodic dissolution-based techniques ideal for processing difficult-to-machine materials, such as turbomachinery materials, for example Inconel 718 [2, 3] and cobalt-chrome alloys [4].

In addition, ECM is an athermal process, avoiding heat affected zones (HAZs) at the near-surface. HAZs are thermally-induced microstructural changes, some of which may have detrimental effects on the material properties and can lead to component cracking, due to induced residual stresses [5]. Operational temperature in a conventional electrolysis process is regulated by the electrolyte, with an upper limit defined by the boiling point, (≈100 °C for commonly used electrolytes), since anodic dissolution ceases or is impeded upon electrolyte boiling [6]. Operation beyond the electrolyte boiling point leads

to vaporisation, increasing jet resistance and can lead to spark discharges, which thermally affect the workpiece [7].

As a non-conventional and non-contact machining process, ECM technologies benefit from negligible tool-wear and associated costs, compared with conventional shear-based material removal processes, for example grinding and milling. ECM techniques also result in burr-free surfaces, hence the elimination of a deburring post-processing step. ECM has in fact previously been adapted as a deburring technique [8]. EJP can selectively remove or deposit material without masking [9], removing a processing step. The electrolyte supply is defined by the shape and diameter of the nozzle, usually in the order of 100s of microns [10], therefore the electrical current density of the electrolyte jet is intense, with some studies reporting stable machining regimes in the order of 1000s A/cm^2 in some electrolytes [11]. This leads to high-speed localised removal compared to conventional ECM, with surface dissolution velocities of 10s of microns per second.

2.1.2. Fundamentals of mass-transfer

Electrochemical jet processing (EJP), along with electrochemical machining (ECM) and electroplating, involve a change of oxidation state of workpiece or electrolyte atoms. This either occurs as an oxidation reaction of an anodic workpiece to effect dissolution or passivation (hampering material removal), or the reduction of a cation-containing electrolyte at a cathodic workpiece to effect material deposition [12]. Electrochemical oxidation and reduction are physico-chemical processes directly governed by laws first explored by Faraday in 1833 [13]. Equation 1 shows the relationship between mass transfer, *m*, and the

charge passed, *Q*, as well as the material properties of molar mass, *M*, and valence, *z*.

$$m = \frac{Q}{F} \cdot \frac{M}{z} \qquad \textit{Equation 1}$$

Here, *F* is the Faraday constant. In a constant current scenario, often employed in EJP, *Q* is therefore the product of current, *I*, and time, *t*. In effect, increasing *Q* will increase the material removal or deposition rate. The electrochemical equivalent (ECE) of a given material, which is the mass liberated by a mole of electrons, is therefore calculated according to Equation 2:

$$ECE = \frac{M}{Fz} \qquad \textit{Equation 2}$$

A generalised overall equation for the mass transfer reaction is given in Equation 3. Anodic dissolution (left to right) is the process through which workpiece atoms are oxidised from an anode through an applied potential difference and current, and solvated by an electrolyte. Conversely, jet electrodeposition (right to left) occurs where solvated metal cations within the electrolyte are reduced at the surface of the cathodic workpiece, depositing a metallic film.

$$M_s^0 \rightleftharpoons M_{aq}^{n+} + ne^- \qquad \textit{Equation 3}$$

The overall mass transfer reaction appears to disregard the role of the electrolyte, however even in his seminal studies, Faraday himself noted that the dissolution of iron, for example, was heavily influenced by oxygen and hydroxyl (OH^-) concentrations within the electrolyte. This was further explored in subsequent studies on iron [14], from which the generalised mechanism of anodic dissolution can be taken. These are explored in Equation 4-Equation 6,

involving anionic adsorption (through the outer Helmholtz plane, OHP [15]) onto the workpiece surface forming an unstable species which then undergoes an electron transfer reaction, (*see* Equation 5); the liberation of an electron into the anode bulk, followed by the ejection of the species from the interface into the bulk electrolyte, which is irreversible. Equation 6 is generally succeeded by a hydrolysis step within the electrolyte, in the case of iron, hydroxides are subsequently formed [16] and precipitation reactions occur within the electrolyte waste [17].

$$M_s + A_{aq}^{x-} \rightleftharpoons MA_{ads}^{x-} \qquad \textit{Equation 4}$$

$$MA_{ads}^{x-} \rightleftharpoons MA_{ads}^{(x-n)} + ne^- \qquad \textit{Equation 5}$$

$$MA_{ads}^{(x-n)} \rightarrow MA_{aq} \qquad \textit{Equation 6}$$

The overall observed result of this oxidation process is the removal of material from the surface of the workpiece. Conversely, an electrode polarity reversal in the system will lead to a reduction process at the workpiece, the observable result being material deposition. The near-surface of the workpiece material is understood to be covered by a thin film of dissolution products or gas under anodic dissolution conditions. Jacquet (1936) [18] predicted, based on experimental observations in Cu, that this layer was responsible for electropolishing. In this work, he suggested that this film collected in depressions at the surface, through which either diffusion of an acceptor ion (*noting* Equation 4), or the removal of dissolution products (*noting* Equation 6) is inhibited, localising material removal around the asperities and polishing the surface. Increasing the material removal rate, through increasing the current density, leads to an effective build-up of these dissolution products, thus

delocalising removal from microstructural inhomogeneity [19, 20]. The current at which surface topography becomes independent of microstructure and the electropolishing mechanism begins to dominate is termed the limiting current density, J_{lim} (*see* Equation 7). At this point, the rate of material removal is limited by mass transfer through the diffusion layer of the electrode [21].

$$J_{lim} = \frac{nFD(C_B - C_e)}{\delta_N}, \qquad \textit{Equation 7}$$

Here, n is the charge number, D the diffusion coefficient, C_B the bulk concentration of the reacting species, C_e the concentration of the reacting species at the electrode and δ_N the diffusion layer thickness. δ_N is determined by the anodic current density, convective electrolyte supply forces and bulk concentration. Within conventional electropolishing theory, Landolt (1987) [22] wrote that *'it is common to distinguish anodic levelling or smoothing from brightening. The former refers to the elimination of surface roughness of height >1 μm, the latter to the elimination of surface roughness <1 μm'.* The two processes are defined by discrete mechanisms. In the case of levelling, current is localised at geometric inhomogeneity, decreasing the surface height, however a level surface may not always be bright (roughness <1 μm). Brightening relies on compact salt film development in the process, where the dissolution of a given metal atom becomes dependent on stochastically distributed cation vacancies in the salt film. This delocalises removal from ordered metal lattice positions [23], thus levelling at a much reduced length scale.

2.1.3. Defining EJP techniques

EJP (for machining, see also: EJM [24], ECJM [25], JECM [11] and EJD [26]; for deposition see also: jet plating [21], jet electrodeposition [9], HSSJE [27], HSJE [28]) is defined in this thesis as an overall term encompassing a range of electrolyte jet processing techniques for material removal, deposition and surface modification. The myriad of nomenclature appearing to have arisen from the convergent development of separate studies being conducted for different potential applications, exploiting equivalent in-jet phenomena.

Fundamentally, processing selectivity in EJP techniques relies on the impingement of a conductive electrolyte solution at high velocity onto an unsubmerged, polarised workpiece, from an oppositely polarised nozzle, shown in the schematic in Figure 2.1 (left). Mass transfer from or to the workpiece is proportional to the charge passed in the process, as defined by Faraday (*see* Equation 1) [13, 29], which is localised by the development of a highly resistive radial thin film of radial flowing electrolyte. The development of the radial thin film is a well-understood phenomenon in flow science and terminates in a hydraulic jump [30], whereby the fluid regime transitions from supercritical to subcritical flow, where supercritical flow denotes a Froude number, *Fr*, of greater than 1. The Froude number is a dimensionless quantity evaluated by Equation 8,

$$Fr = \frac{v_j}{\sqrt{g_0 l_0}}, \qquad \textit{Equation 8}$$

where v_j is the flow velocity, g_0 is an external field, in this case gravity, and l_0 is the flow length. Flow analysis was not the objective of this thesis, however flow conditions were controlled such that in this thesis, a hydraulic jump was always

observed, for example shown in Figure 2.1 (right). Typically, jet velocities applied in EJP are ≥20 m/s [31]. Further reference on associated fluid mechanics can be found in White (2010) [32]. Within EJP the result of the thin film is to restrict mass transfer to directly below the nozzle, whereby charge transfer is negligible in the laminar fast-flow area in comparison to the low-resistance stagnation region directly below the nozzle. In a situation without sufficient impingement velocity, where *Fr*>1 across the impingement region, the process would become submerged, as the steady-state height of the film would be greater than the inter-electrode gap (IEG), conventionally <1 mm in EJP [33]; this can be observed in the height of the hydraulic jump in Figure 2.1 (right), which is significantly greater than the IEG (500 µm in this case). Localisation of mass-transfer can also be enhanced through the application of an air-shroud, which further constricts the jet and increases the process precision [31, 33].

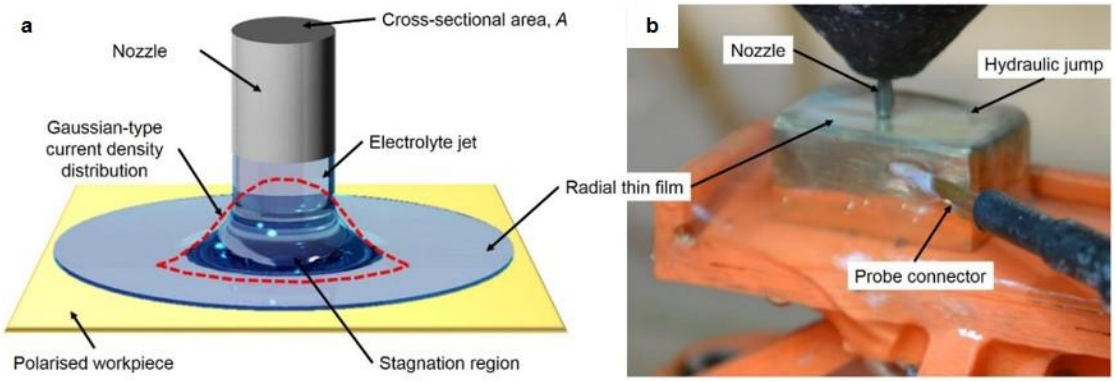


Figure 2.1: a) EJP schematic. Electrolyte impingement at supercritical velocity forms a resistive radial thin film, localising mass transfer below the nozzle, following a Gaussian current density distribution. b) This flow regime terminates at a hydraulic jump, the height of which is greater than the IEG, thus jet velocity is required to be high enough to sweep the jump away from the working region.

2.1.4. Energy distribution in EJP

Material is removed or deposited approximately proportional to the current density distribution, shown in the schematic in Figure 2.1a, which is indicative of the local charge flux at a given point on the workpiece surface. Considering this, an understanding of the distribution is of vital importance to the EJP practitioner, as it defines the selectivity of mass transfer. Translation of this current density distribution allows planar features to be generated in a maskless fashion. Normally within EJP, applied energy is compared through the metric of supply current density, J_{noz}, which is generally defined through Equation 9. Charge passed, Q, the product of supply current, I, and time, t, can be simply correlated with material removal, which is important from a machining perspective. J is the ratio between I, and A the planar area of the nozzle [24],

$$J_{noz} = \frac{I}{A}, \qquad \textit{Equation 9}$$

thus, for an electrode with a circular orifice,

$$\pi \frac{d_N^2}{4} JR \equiv IR = V, \qquad \textit{Equation 10}$$

where d_N is the internal diameter of the nozzle, R is the electrolytic resistance, and V is the potential difference. In EJP, J_{noz} can only be treated as a simplified comparative metric, with a large error factor, as the distribution is generally Gaussian. In EJP electrodeposition, Alkire and Chen (1982) [34] explored the current density distribution in a mathematical model, which was shown to be Gaussian, experimentally verified using the ferricyanide reduction reaction. Succeeding investigations in jet plating, for example by Karakus and Chin (1994) [21], and Kunieda et al. (1998) [9] (among others), confirmed through

experimentation, the Gaussian nature of the in-jet current density distribution reported by Alkire and Chen (1982), through observations of deposit distribution and morphology. This is consistent with the energy distribution in other energy beam processes, such as laser beam machining [35].

A following investigation undertaken in jet deposition by Li and Walker (1996) [36] considered how manipulating the angle of address would affect the current density distribution. Their study found that decreasing the angle of address (towards horizontal 0°) distorted the current density distribution from the normal Gaussian reported by Alkire and Chen (1982), through a field-focussing effect at the part of the nozzle adjacent to the cathode workpiece, (*see* Figure 2.2). This is of special importance in EJP, as the study investigated a simple method of manipulating the input current density distribution, and therefore the mass-transfer area, without altering the tooling. Rajput et al. (2015) [27], investigated the potential distribution in jet plating with respect to the applied voltage, cation concentration and IEG, in order to enhance control of deposition rate and height.

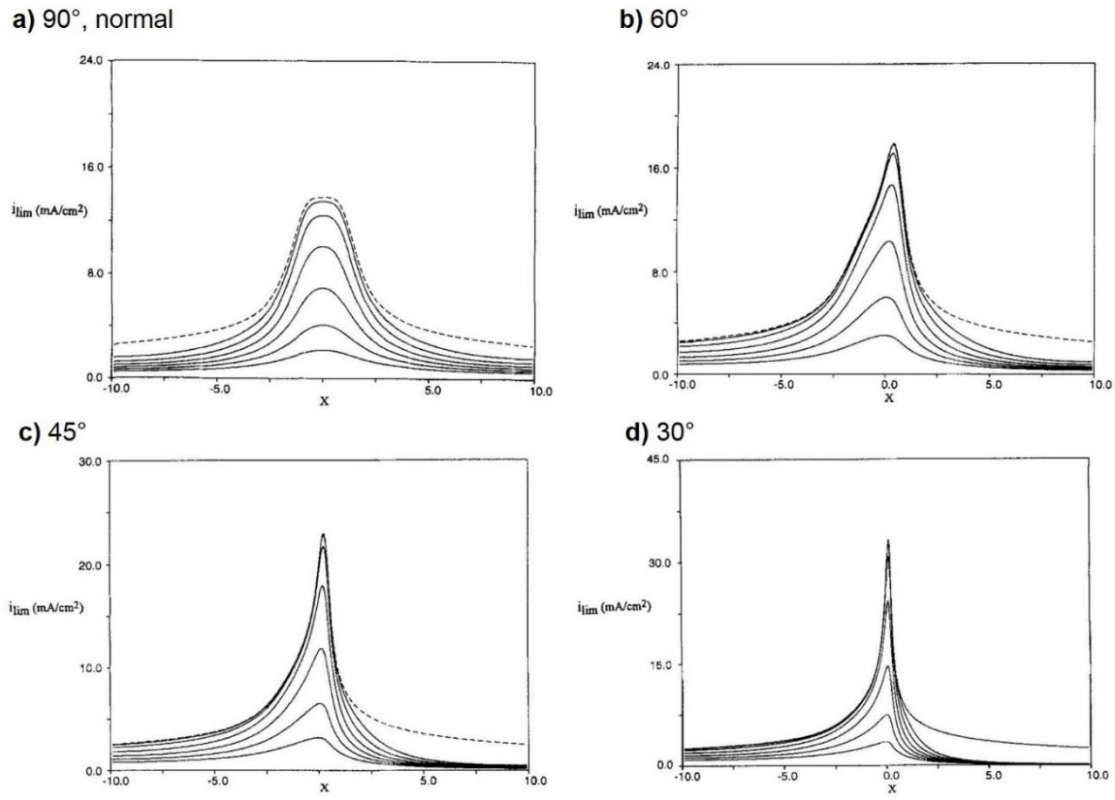


Figure 2.2: Taken from Li and Walker (1996) [36]. Simulating the current density distribution over a cathode surface at different impingement angles. Peak current density is increased through field-focussing. Abscissa represents nozzle radii.

In EJP (anodic dissolution), Datta et al. (1989) [37] noted the discrepancy between the supplied current density and the effective surface-defining current density. The authors experimentally observed surface finishes that were inconsistent with those expected considering operation around the limiting current density and the predicted electropolishing condition. Instead, observed topographies were significantly rougher than expected. In this investigation the authors estimated, based on machined profiles that were significantly larger than the nozzle diameter, that the effective current density, J, experienced by the machined surface could have been as low as 20 A/cm^2, when the applied current density, J_{noz}, was 75 A/cm^2. This discrepancy was subsequently mathematically simulated by Yoneda and Kunieda (1995) [38], in EJP, for a

standard cylindrical nozzle, where a Gaussian current density distribution is observed across the electrolyte jet (*see* Figure 2.1). This was determined by firstly calculating the electrical potential distribution within the jet using the finite element method, shown in Figure 2.3. The large error factor associated with quoting J_{noz} is evident from the calculated current density distribution (*see* Figure 2.3b), where J_{noz} = ≈470 A/cm^2. Peak current density, achieved at the centre of the processed feature, was calculated to be ≈340 A/cm^2.

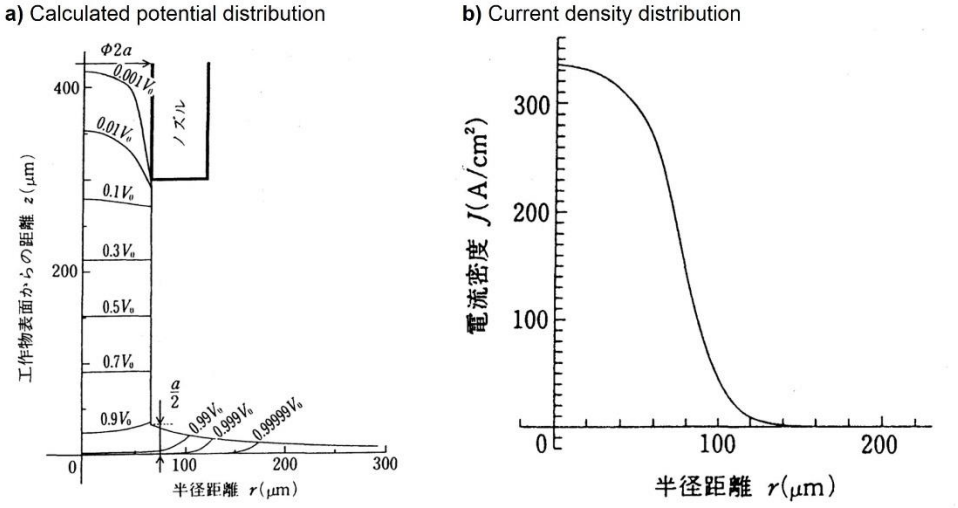


Figure 2.3: a) Calculated potential gradient in EJP. b) The resulting current density distribution, both taken from Yoneda and Kunieda (1995) [38]. The distribution is approximately Gaussian in nature. Calculated for: 0.13 mm nozzle, I = 0.62 A, resulting in J_{noz} ≈470 A/cm^2. IEG = 0.3 mm.

The description presented by Yoneda and Kunieda did not evaluate changes in the electrical potential across the jet with respect to the IEG. The potential gradient at the anode surface at different gap widths was simulated by Kozak et al. (1996) [39], wherein the shape of the distribution was noted to change significantly from the aforementioned Gaussian distribution as the IEG was decreased, see Figure 2.4a (*L* is the IEG in mm, d_{noz} = 0.8 mm). Where IEG ≤ d_{noz}, the peak of the potential distribution was localised to directly below the

cylindrical electrode wall of the nozzle. The authors simulated the resulting current density distribution for a case where IEG > d_N (2 mm, *see* Figure 2.4b), correlating with the observations of Yoneda and Kunieda (1995), while also noting that significant increases in applied voltage had negligible effect on the dissolution area where there was a machining threshold current density. The latter point is important as it mathematically demonstrated a route through which profile aspect ratio could be significantly increased, using conventional power supply process parameters.

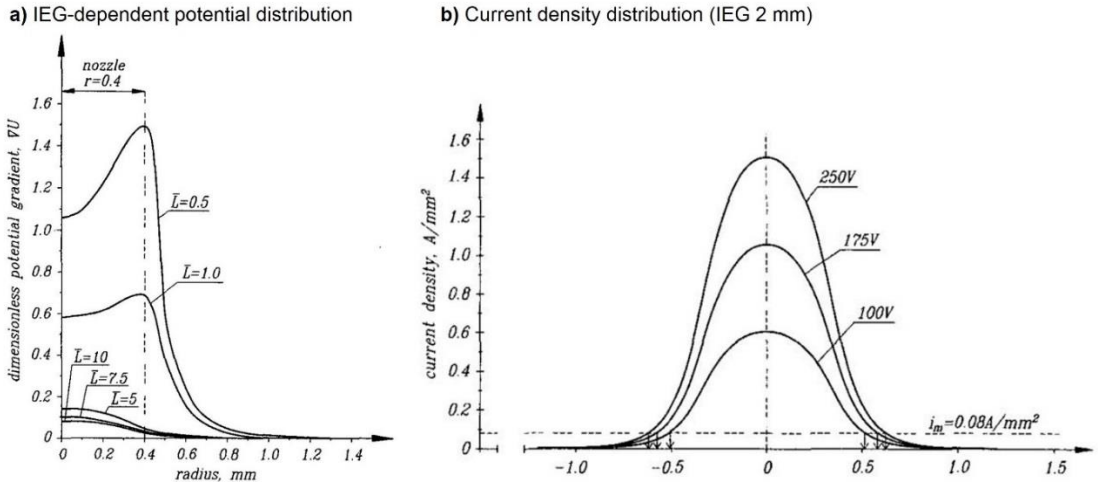


Figure 2.4: a) Potential distribution gradient with respect to IEG. Where IEG ≤ d_{noz}, the electric-field gradient is localised below the nozzle and preferential removal occurs as a reflection of the cathode. b) Current density was simulated for a case where IEG > d_{noz}, where increases in applied potential do not greatly increase dissolution area.

The model provided by Kozak et al. (1996), considered the conductivity of the electrolytic medium, wherein localised temperature increases due to resistive (Joule) heating will affect the performance. The authors concluded that the performance of EJP, in terms of material removal, was effectively limited by electrolyte boiling. Furthermore, the simulation presented showed good correlation with experimental verification. The current density distribution in EJP

was also simulated in stainless steel by Hackert et al. (2008) [40] for a pit processing operation. This was a simple, computationally efficient profile generation model that ignored resistive heating effects during processing. Thus resulted in an efficient simulation that showed good correlation with the material, within the processing conditions tested.

2.1.5. Role of the electrolyte

In addition to being the charge carrier within ECM and EJP, the electrolyte stream is responsible for removal of machining debris (in anodic dissolution) and evolved gas (in dissolution and deposition), refreshing electrolyte at the machining surface, and regulating the temperature through convective heat transfer [41, 42]. In addition, the choice of electrolyte has been shown affect the surface texture, dimensional accuracy, and removal rate in ECM [43]. Within ECM, the choice of appropriate electrolyte is largely dependent on the workpiece material, the passivation resistance and the engineering specification of the part (*see* section 2.2.3.1), as well as the process intent (bulk material removal or finishing) [44]. Acidified electrolytes are generally employed in ECM, as these improve the solubility of metal hydroxides in aqueous solution [17], reducing sludge build-up, therefore improving effective debris removal from the IEG. In addition, lowering the pH of electrolyte solutions (pH <7) drastically changes the surface electrochemistry of the workpiece. This was notably explored by Marcel Pourbaix throughout his career [45, 46]. As an example, the behaviour of iron in electrolytes of different acidities, investigated by Pourbaix (1970) [47], is shown in Figure 2.5a. In this case, lowering the pH is shown to destabilise the passivating films, corresponding to the difference between the passivation potential, *P*, and the passivation breakdown potential,

B, which decreases upon acidification. The works of Pourbaix and his associates informed early practitioners of EJP, who used acidified electrolytes, such as Nannichi (1962) [48] for drilling micro-holes in copper, and Booker and Stickler (1962) [49], who used a sulfuric/hydrofluoric acid mixture to jet-polish semiconductor materials.

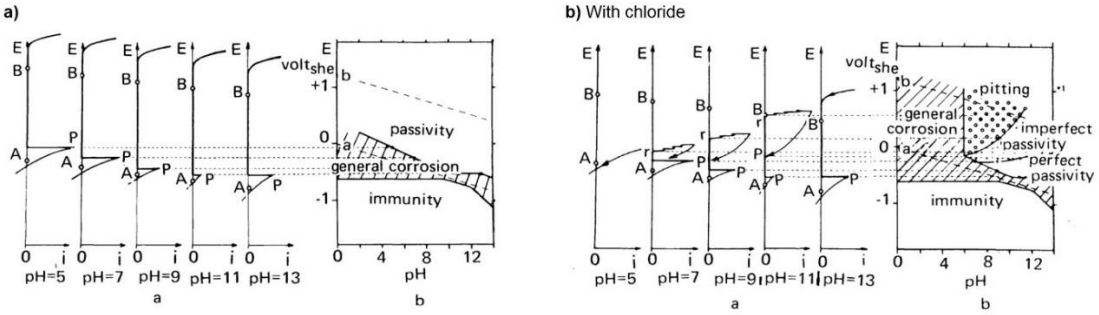


Figure 2.5: Pourbaix diagram derivation (potential/pH) for iron in a) chloride-free solutions, and b) with 355 ppm chloride. Taken from Pourbaix (1970) [47].

Electrolytes in ECM are generally separated into two categories: passivating and aggressive [50, 51]. Considering Figure 2.5a, passivating electrolytes reduce the passivation potential at a given pH, increasing the difference between *P* and *B*, which increases the stability of the passivating films. Conversely, aggressive electrolytes are able to rupture the passivating films (*see* Figure 2.5b), which destabilises passivation, leading to pitting, even at relatively high pH. In ECM, passivating electrolytes, such as those containing nitrate, are understood to allow greater dimensional accuracy [52], which is due to passivation in the area of the workpiece held at low anodic potential (also referred to as stray-cutting resulting in overcut). In the presence of aggressive anions, destabilisation of passivity in this region occurs through film rupture, leading to pitting and stray cutting. The spatial response with regards to IEG can be quantified by the term throwing power, *TP*, used in both electroplating

[53] and electrochemical machining [54], which can be experimentally determined for a given electrolyte-material system, with two anodes held at different IEGs, following Equation 11:

$$TP = \frac{(L - M) * 100}{L + M + 2} \qquad \textit{Equation 11}$$

where length ratio between the two anodes, *L*, and mass-loss ratio, *M*. Using this experimental and quantification, Landolt (1972) [55] showed that when using chloride electrolytes, mass removal is inversely proportional to the IEG, however using passivating electrolytes (in this case $NaClO_3$), mass-loss was greatly reduced at larger IEG than with chloride. Considering Equation 11, throwing power is also related to the electrolyte conductivity, whereby increases (through increasing concentration), will increase throwing power and reduce dimensional accuracy.

It has been shown that electrolytes can be doped with anions to impart desirable properties of constituent anions to the electrolyte. For example, in titanium, this was shown by Bannard (1976) [56], who demonstrated that small additions of bromide to chloride-containing electrolytes can significantly reduce the energy requirements in terms of anodic potential required for material removal in ECM. This is a significant process improvement considering the high corrosion resistance of the material. The investigation considered earlier work undertaken by Cotton and Dugdale (1964) [57], which indicated that the aggressiveness, in terms of the suppression of the breakdown potential of the oxide film, of halides towards titanium was Br^- (3.5 V) > I^- (4.2 V) > Cl^- (14.2 V) > F^- (92.0 V).

Electrolyte doping has been the subject of limited investigation in EJP, except for the purpose of processing tungsten containing materials. Hackert-

Oschätzen et al. (2013) [58] successfully machined different tungsten carbide (WC) materials using a $NaNO_3$/NaOH mixture at a 2:1 molar ratio. The role of basic hydroxide in destabilising insulating tungsten oxides has been well-understood at least since studies undertaken by Kelsey (1977) [59], justifying the addition of the chemical to the electrolytes employed by Hackert-Oschätzen et al. The high alkalinity of caustic hydroxide-containing electrolytes complicates handling and increases risk to the user. To enhance industrial application of the technique, ECM research groups are currently attempting to employ electrolytes of lower toxicity [60]. A small amount of research has been accomplished employing novel electrolytes, such as mineral water [61], and citric acid [62]. However, the high energy localisation in-jet would inhibit the application of mineral water-based electrolytes to EJP, except at very low current density or applied potential. In addition, work is being undertaken within the ECM community to remove toxic contaminants from the electrolyte waste stream [63].

2.1.6. Summary of research gaps

The greatest scope for research resulting from this section involves the electrolytes applied to EJP. NaCl and $NaNO_3$ electrolytes dominate the literature, due to cost and toxicity considerations, however practitioners may benefit from less studied electrolyte systems in terms of dimensional accuracy and material removal rate.

- **Processing with different electrolytes**. Beyond $NaNO_3$, electrolytes that enhance dimensional accuracy in EJP have yet to be explored. Considering the mechanism of precision enhancement in the $NaNO_3$ system (oxide generation in the low current density area), there are likely

to be other, more efficient chemistries that can better this effect. An exploration of this effect is required.

- **Processing difficult to machine alloys**. In light of the high corrosion resistance and poor electrochemical machinability of titanium and its alloys, processing of this material system, which has widespread application in high-value aerospace component manufacture, could benefit from the exploration of different electrolyte systems. In ECM, different halide salts have been shown to alter the material electrochemistry; within EJP this has yet to be exploited, and is directly aligned with the thesis objectives in terms of exploring deterministic feature processing and topography generation.

2.2. Topography in EJP – *machining*

2.2.1. Introduction

The surface topography of a given part or material can have a significant impact upon functional properties, such as fatigue life [4], hydrophobicity and hydrophilicity, [64-66] fluid dynamics and the transfer of heat [67]. Therefore topographic evaluation, however primitive, is necessary for all parts designed for high-stress or fluid-facing applications, regardless of the process employed to generate the part. Thus, it is necessary to understand and explore the factors that determine topographic response of a given material to the process. Within EJP and ECM, the resulting topography after processing is understood to be influenced by both the processing parameters, and the material microstructure, shown in Figure 2.6. These directly relate to the first two targeted thesis objectives (*see* Section 1.1), corresponding to the impact of material

precondition and the characterisation of material-specific topographies after EJP. Therefore, topography-defining properties are explored in detail in the following section.

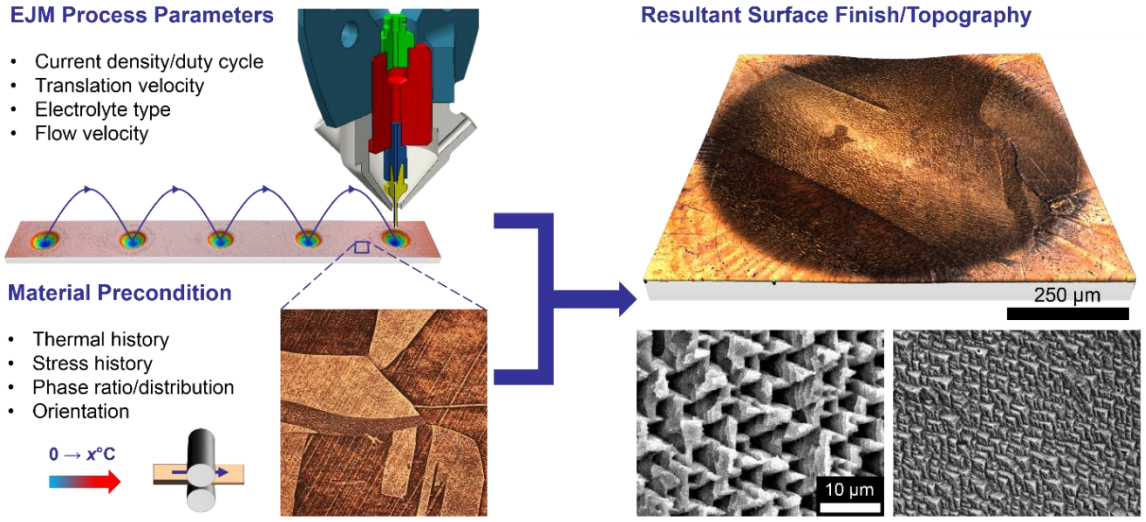


Figure 2.6: Process and material parameters (both lists illustrative and non-exhaustive) contribute to the topographic response after EJP.

2.2.2. Process parameter influence on topography

2.2.2.1. Applied energy

Within EJP techniques, changing the applied process energy is one of the most consistently employed methods to exercise control over the surface topography [68, 69], as such adjustments can be easily undertaken through manipulating the conventional power supply parameters of applied potential and supply current, either manually or as part of an numerically controlled (NC) operation.

Considering a single-phase material, such as austenitic stainless steel, the current density effect on the topography is well-understood in pit processing, in terms of topographic amplitude, shown by Sen and Shan (2005) [70], Ikeda et al. (2006) [71], and Natsu et al. (2007) [24]. The latter is shown in Figure 2.7, where increasing current density ≤108 A/cm^2 increases the surface reflectivity

in addition to decreasing the measured surface amplitude. Beyond this current density, further increases were not reported in the study to decrease the profile amplitude parameter, *Rz*, further >216 A/cm^2; resulting in an apparent power-law regression. Lower surface amplitudes are generally sought in mechanical applications, as low quality surfaces can decrease part performance [72].

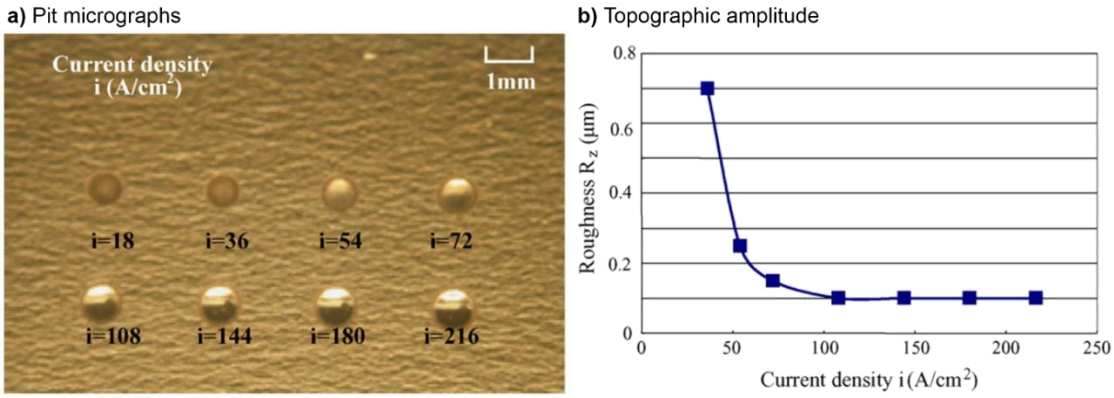


Figure 2.7: a) Pits machined at increasing current density. b) This is correlated with topographic amplitude, (Rz is the average of the peak-to-valley height [73]). Both images from Natsu et al. (2007) [24].

The effect of the low current density region of the distribution in EJP pitting operations was investigated by Ikeda et al. (2006) [71], who measured an order of magnitude greater roughness amplitudes, *Rz*, at the edges of discrete pits processed at high current density (>100 A/cm^2). Where the central region was recorded at <0.2 μm, the amplitude of the edge region was recorded >2 μm. Following this, Kawanaka et al. (2013) [74], correlated topography with current density in Cu and brass, in addition to stainless steel, wherein increasing supplied current density (between 8-79 A/cm^2) generated smoother surface morphologies, regardless of total charge transfer. This investigation first explored the notion that EJP could be employed as a means of selective surface texturing, whereby careful control over microscale topography could increase

the applicability of the surface. Enhancing cell ingress in biomedical applications, and altering surface tribological properties were suggested in this work, decoupling from the *lower-the-better* (Sen and Shan, 2007 [75]) approach to surface amplitude as a performance metric in EJP. Kawanka et al. (2014) [68], explored this further, noting that low current density machining employing EJP is capable of generating complicated surfaces that are difficult to obtain with other machining processes. In addition, the surface roughness dependence on current density is shown to differ somewhat to that presented by Natsu et al. 2007 [24], in that rather than remaining static beyond ≈100 A/cm^2, an increase is observed after 87 A/cm^2 up to the highest current density tested (187 A/cm^2), shown in Figure 2.8, despite processing in the same material (SUS 304), with the same electrolyte ($NaNO_3$, 20 wt.%).

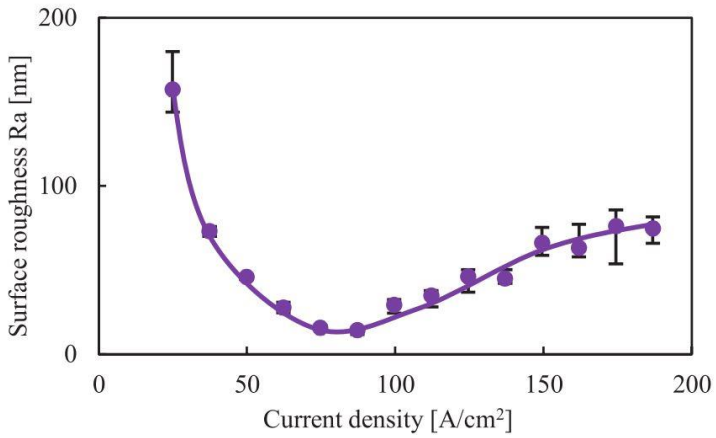


Figure 2.8: Surface roughness dependence on current density (stainless steel in $NaNO_3$), taken from Kawanaka et al. (2014) [68]. Surface roughness increases >87 A/cm^2.

Superficially, slight increases in roughness upon increasing current densities >100 A/cm^2 may not appear important, however it is suggestive of a change in the dissolution mechanism, therefore comprehension of this phenomenon is of considerable importance if practitioners are serious about the application of

EJP. Considering section 2.1.1, these observations were attributed to the thickness of the diffusion layer in EJP by Kawanaka and Kunieda (2015) [76] (*see* Figure 2.9), whereby processing >87 A/cm^2 (stainless steel with $NaNO_3$) implies operation within the mechanism described in Figure 2.9c. In this range, the diffusion layer is proposed to be too thick to localise electrochemical dissolution at surface asperities, thus the polishing effect is reduced. The high current densities achieved in EJP in comparison to ECM and anodic electropolishing [77], and therefore a large associated mass-transport diffusion layer, implies that this effect could be possible.

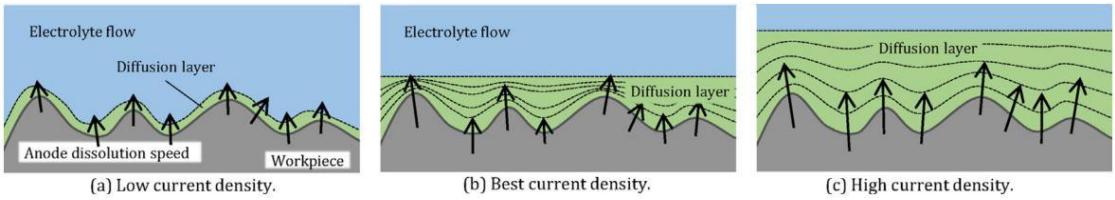


Figure 2.9: Schematic representation diffusion layer thickness in EJP changing resulting surface topographies, a) at low current density, the diffusion layer is too small to delocalise removal away from surface asperities. b) Increasing current density allows brightening. c) Further increases equilibrate removal across the surface, therefore delocalising removal from the surface asperities. Taken from Kawanaka and Kunieda (2015) [76].

The difference between the roughness curves in the same material acquired by Natsu et al. (2007) (*see* Figure 2.7b) and Kawanka et al. (2014) (*see* Figure 2.8) could be a result of this effect. Considering the experimental parameters detailed in the latter study (d_N: 1.43 mm, flow rate: 5.4 mL/s), the supplied electrolyte flow velocity would be 3.36 m/s. Direct comparison with the former investigation is not possible, as no flow rate is listed (only supply tank pressure: 0.5 MPa), however nozzle diameters employed in this study were significantly narrower (0.42, 0.26 mm), therefore it is possible that electrolyte jet velocities

were faster. Within ECM, it is considered that the smoothest finishes are achievable at the limiting current density [78, 79], which is partially dependent on convective mass transport. Relatively low jet velocities may therefore lead to a roughening of the surface, should the limiting current density be exceeded (*see* Equation 7), whereas increasing jet velocity could lead to an increase in the limiting current density, and thus the operating range of the technique [80].

2.2.2.2. Dwell time and translation velocity

Regarding the memory effect in ECM, described by Rajurkar et al. (1998) [81] as the transfer of initial surface undulation to the final surface topography, it is necessary in electrochemical processing to remove the starting roughness. This is dependent on the processing conditions and the material, which the authors acknowledge increases the amount of machining waste. Considering the high charge localisation in EJP, this memory effect can be overcome rapidly, which was investigated by Natsu et al. (2007) [24]. In this study concerning typical EJP parameter sets in determining the influence of dwell time on topography in a pit machining case (zero nozzle translation), the authors found no correlation between roughness and dwell time at low and high current densities (J_{noz} = 36 and 108 A/cm^2, respectively), over depth ranges from 10-40 µm, corresponding to dwell times of between 2-8 s at low, and 0.8-2.8 s at high current densities. In this investigation, the authors summarised that any influence of dwell time on the resulting topography, and therefore the memory effect, was negligible in comparison to the effect of current density distribution.

Considering the Gaussian current density distribution in EJP, translation as part of a planar machining operation means that the workpiece is affected by a current density lower than the peak of the *J* distribution. Sen and Shan (2005)

[70] translated the electrolyte jet and found negligible influence of feed rate on the resulting surface roughness, although this was undertaken at relatively slow translation velocities in comparison to other EJP practitioners (0.2-0.8 mm/min were tested in this study). Pits and striation processing were directly compared by Ikeda et al. (2006) [71], where it can be seen in Figure 2.10, that the amplitude is significantly greater in planar processing mode, due to interaction of the workpiece with low current density. In addition, it can be seen that the resulting roughness relationship is decoupled from the power-law regression in pit processing; the effect of jet translation on the surface roughness therefore is also an equilibration, whereby significant increases in current density have little effect on the resulting amplitude (*Rz* ≈0.5 μm at 78 A/cm^2, ≈0.4 μm at 216 A/cm^2). A similar effect was observed by Hackert et al. (2007) [31], whereby grain boundary etching was observed upon multiple reciprocations of the electrolyte jet over a Ni-superalloy workpiece material (Nimonic 80A).

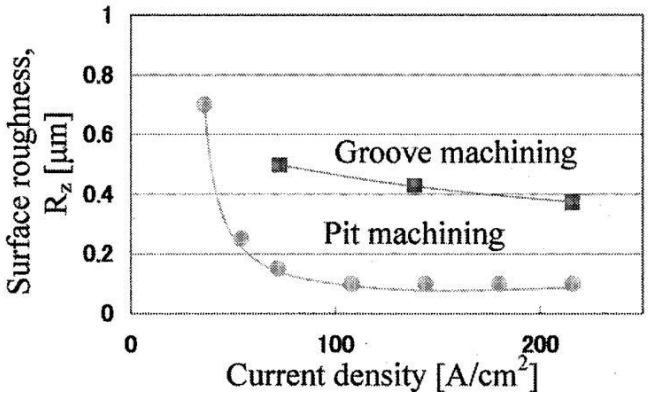


Figure 2.10: Topographical differences between pit and striation processing in EJP. Interaction between low current density regions and the workpiece increases topographic amplitude and the relationship is discrete from the power-law regression observed with pits. Taken from Ikeda et al. (2006) [71].

The effect of nozzle translation velocity on surface topography was investigated by Hackert et al. (2011) [82], in different steel workpieces (10 reciprocations,

anode potential 56 V). In all cases, the profile roughness parameters, *Ra* and *Rz*, were observed to decrease as the translation velocity was increased from 200 µm/s to 1000 µm/s. This effect was also observed by Mitchell-Smith et al. (2014) [2] in Ni-superalloy Inconel 718, in which decreasing the translation velocity significantly increased the surface undulation from 10 mm/s to 1 mm/s, shown in the secondary electron micrographs in Figure 2.11.

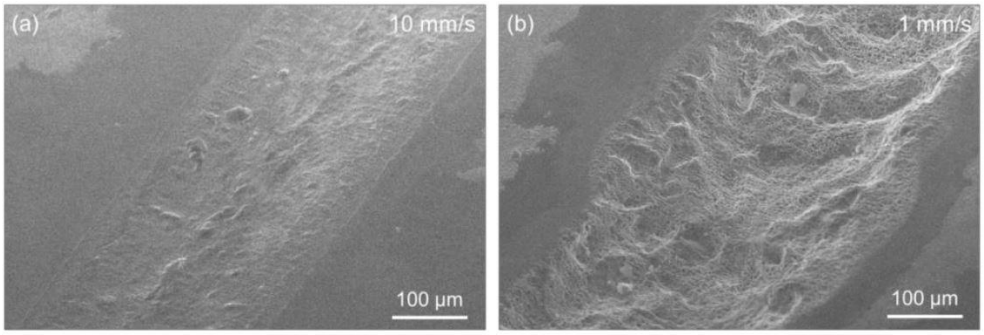


Figure 2.11: Increasing undulation by reducing translation velocity. a) Smoother surfaces are observed at high translation velocity, b) whereas at slower translation velocities surface is porosity observed. Taken from Mitchell-Smith et al. (2014) [2].

The theory of decreasing surface roughness through increasing the translation velocity was explored by Kawanaka and Kunieda (2015) [76], who proposed that this effect was the result of a smaller exposure time to the low current density region of the reciprocating jet for a given point on the surface (*see* Figure 2.12a). This was verified experimentally, whereby similar topographies were achieved at different current density values (62-156 A/cm^2) at the highest translation velocity tested (100 mm/s, *see* Figure 2.12b). The authors observed that through translation at the highest velocity, the effect of planar manipulation could be completely overcome and in some cases exceeded at all of the current densities investigated. This enables EJP to be used for both ‘bulk’ material removal, translating at low velocity (thus increasing the linear charge density),

and subsequently used for finishing, through increasing the translation velocity. Through pre-programming of toolpaths, this can be completed in one process step, as was performed by Miyoshi and Kunieda (2016) [83], in an EJP turning operation.

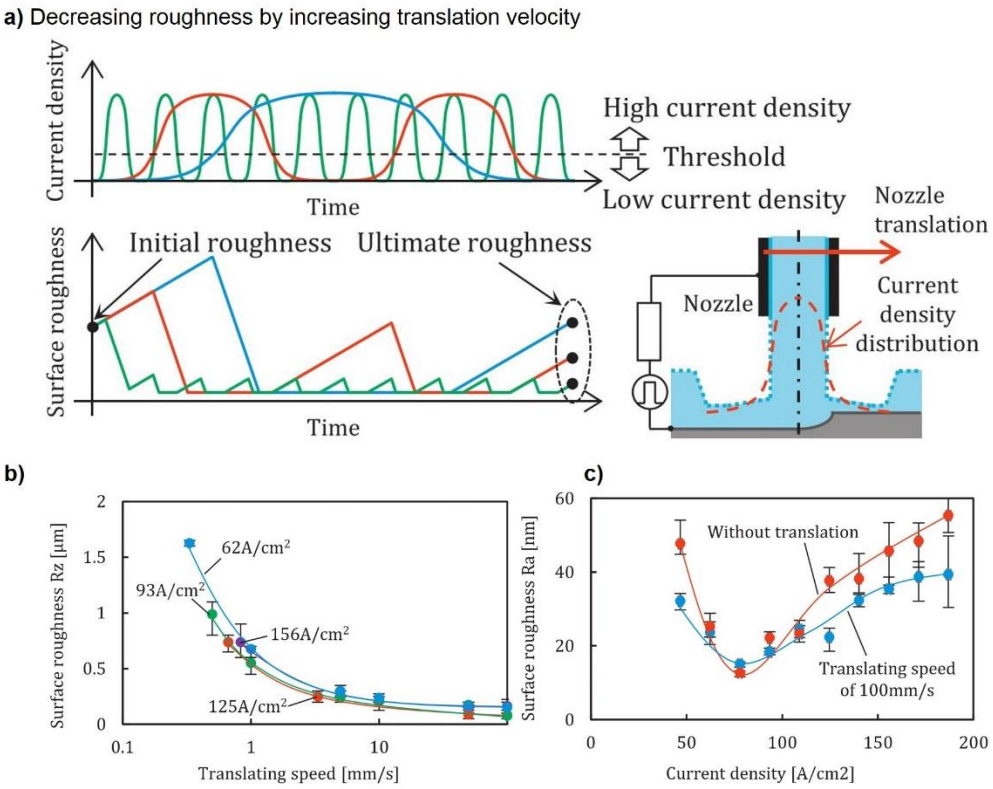


Figure 2.12: a) At high translation velocity, the time point is exposed to low current densities, thus the ultimate roughness, is reduced. b-c) Experimental data showing increasing translation velocity overcoming current density effects in this range. Taken from Kawanaka and Kunieda (2015) [76].

The inverse relationship between translation velocity and surface amplitude is not followed in all material cases. Liu et al. (2017) [84] showed that in a titanium alloy (TB6), the opposite effect was true. This is due to the highly passivating nature of the material system, and will be discussed in detail in section 2.2.3.1 (page 35).

2.2.2.3. *Application of pulse power*

Pulsing power supplies are conventionally applied in ECM for the purpose of removing machining debris and gases in the IEG through resupply of electrolyte [85]. Kawanaka and Kunieda (2015) [76] explored how changing not only the magnitude of the current density and the translation velocity, but the nature of the power supply could lead to a high degree of control over the surface topography in EJP to generate mirror-like finishes. This was achieved through the application of ultra-short (ns) pulsing, instead of a conventional direct current (DC) power supply. The principle is analogous to that observed in electrochemical micromachining (EMM) [86], whereby the greater resistance away from the proximity of the cathode tool increases the charging time of the electrical double layer [87]. When the pulse duration is lower than the charging time, no material removal occurs beyond the proximal area (*see* Figure 2.13a).

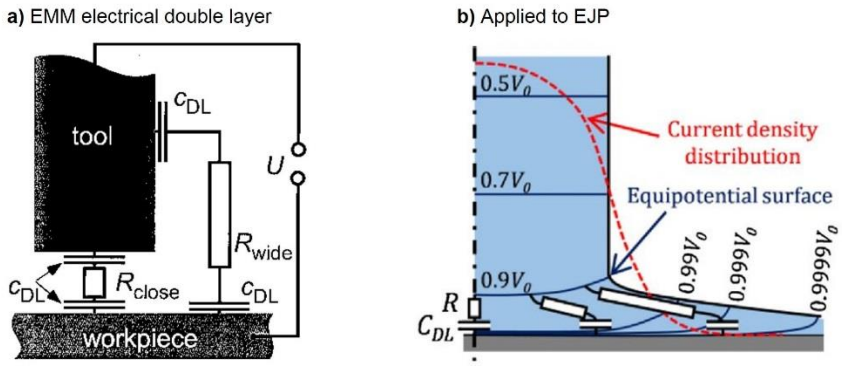


Figure 2.13: a) Schematic of the electrical double layer in EMM, where anodic effects only occur in close proximity to the tool, at short pulse intervals (ns), due to spatial dependence on resistance. Here, charging time outside the proximal area is greater than the pulse duration. Taken from Schuster et al. (2000) [87]. b) The double layer model applied to EJP, from Kawanaka and Kunieda (2015) [76].

Applying this to EJP, the authors proposed that this would eliminate part of the low current density distribution, where the resistance is greater (*see* Figure 2.13b), thus would provide an effective spatial machining threshold. It was found

that through application of a duty factor of 1%, deleterious translation effects could effectively be overcome to achieve a mirror-finish on stainless steel.

To counter the subsequent low removal rate (considering low duty factors), the authors proposed a bipolar finishing method to more rapidly discharge the capacitance, and could achieve mirror-finishes with duty factors greater than five times higher than monopolar pulsing, although nozzle erosion resulting from anodic dissolution was reported.

2.2.2.4. Flow velocity

Different effects of electrolyte flow in conventional modes of ECM have been reported, whereby increasing this factor can reduce or increase surface roughness, depending on the electrolyte-material relationship. Roughness reductions occur due to increasing flow velocities aiding debris and gas evacuation from the IEG [44, 88], subsequently reducing current localisation [89]. However, Datta and Landolt (1975) [90], reported the opposite effect in Ni processed with acidified (HNO_3) sodium nitrate-based electrolytes. This was due to the suppression of the mass-transport diffusion layer, described in section 2.2.2.1 (page 24), which effectively raised the limiting current density for a given flow rate. The acidified nature of the electrolyte probably negated the possibility of the formation of insoluble dissolution products of Ni in the waste stream, reducing any current distribution inhomogeneity caused by debris in the electrolyte stream. Considering this, there are relatively few published investigations into the effects of flow velocity in EJP, which tend to be somewhat greater (≤30 m/s, compared with ≤10 m/s in ECM). Sen and Shan (2005) [70] investigated the effect of changing the inlet pressure, which correlates with jet velocity, across a range of nozzle diameters, reporting a

smoothing of the resulting surface of a Ni-superalloy workpiece (SuperNi 263A) as the pressure was increased (*see* Figure 2.14a), apparently in line with prior investigations in ECM. However, the opposite effect was observed by Liu et al. (2014) [91], as part of a comparative study between EJP and electrochemical slurry-jet machining (ESJM) of Stellite 12, wherein a positive correlation between surface topography and jet pressure between 1.5-3.0 MPa, through a 0.18 mm jet nozzle was observed (*see* Figure 2.14b). This could be a result of the large difference in the range of inlet jet pressures investigated in the study, or the processing potentials applied to the anode workpiece: Sen and Shan (2005): 340 V, Liu et al. (2014): 30 V. Such large differences in applied energy may indicate differing electrochemical removal mechanisms in either investigation, which complicates direct comparison. However, both studies indicate that any observed differences in topography with flow velocity are insignificant in comparison to the effects of applied energy density.

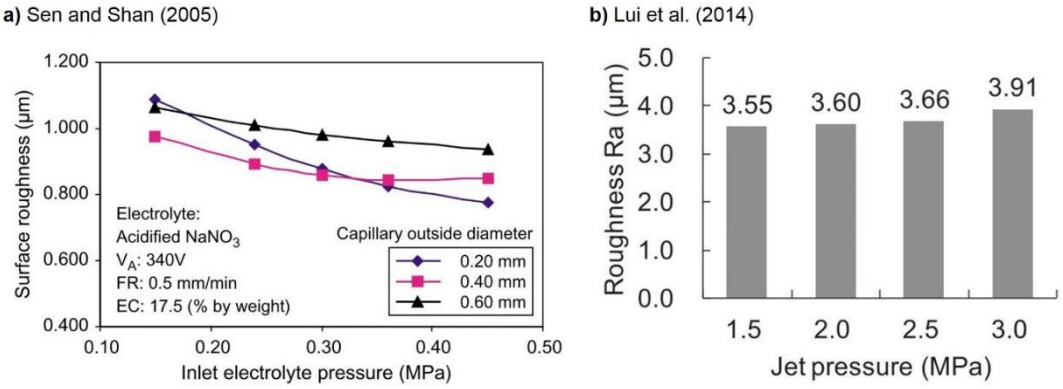


Figure 2.14: Jet pressure (related to flow velocity) and surface roughness in EJP. Although different trends are observed in both investigations, neither the jet pressures, nor the working potentials were tested in the same range, therefore direct comparison is impossible. a) From Sen and Shan (2005) [70], b) from Liu et al. (2014) [91].

2.2.2.5. Electrolyte

The effect of electrolyte of the surface topography after EJP has been largely under-reported (*see* section 2.1.5). This is surprising considering solution chemistry has been shown to have a direct effect on the surface generation mechanism in ECM [88, 92], however it may arise from a reluctance to employ electrolytes of higher toxicity than conventional $NaNO_3$, widely used in EJP. This is pertinent considering the probable atomisation and misting of some of the solution as it is impinged onto the workpiece at high velocities.

2.2.3. Material influence on topography

2.2.3.1. Material passivation

In ECM, the corrosion resistance of the material is understood to affect the resulting surface topography as this defines the localised dissolution process [93]. The passivation of a metal or alloy system describes the affinity to oxidising agents, such as oxygen, which is ubiquitous in aqueous nitrate-based electrolytes conventionally used in ECM. An effort was made by Lohrengel et al. (2016) [93] to classify metals according to the structure and composition of these passivating oxide films, when processed in neutral nitrate-based electrolytes under ECM conditions (*see* Figure 2.15). Notable is the absence of the key engineering materials, titanium and tungsten from this study; these were observed to be electrochemically inert under the process parameters investigated (<30 A/cm^2). Titanium however can be successfully processed with other electrolytes, such as bromide, and at greater current densities [56, 82].

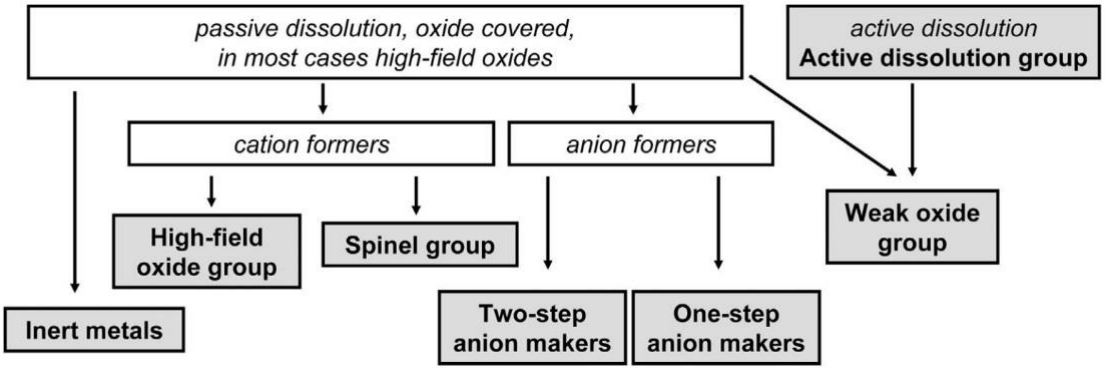


Figure 2.15: Classification of materials in ECM. Taken from Lohrengel et al. (2016) [93].

Generally within prior EJP investigations, austenitic stainless steel has often been used as the workpiece material [24, 71, 82, 94]. This is a result of the well-defined and beneficial characteristic of the material to form polishing oxide films in the dissolution process [95], which lead to a high level of control over the surface topography (*see* section 2.2.2.1, page 24). Referring to Figure 2.15, Lohrengel et al. (2016) classified iron and its alloys into the spinel group, and ECM processing conditions lead to discrete and controllable layers: Fe/Fe_3O_4/supersaturated Fe-nitrates/electrolyte bulk. In addition, as a single-phase material system, austenitic stainless steels do not have large volumes of inert phases, or phases with differing electrochemical equivalent (*see* sections 2.2.3.3, page 42 and 2.2.3.4, page 44 respectively). Kawanaka et al. (2013) [74] processed copper with EJP, which led to highly porous microscale topographies across relatively broad operating conditions. This exploited the poorly controllable passivation characteristics of copper under anodic dissolution conditions, where sporadic pitting is observed under transpassive operating regimes, for example by Landolt et al. (1969) [96]. Lohrengel et al. (2016) classified copper as a weak oxide former (*see* Figure 2.15), where the authors observed that 10-20 % of charge was transferred through oxygen evolution,

which requires oxide film coverage. Instead, sections of the anode oscillate between passivation and active dissolution, followed by re-passivation; the authors projecting that no stable ECM process is possible using a nitrate electrolyte.

Titanium alloys, which are subject to widespread usage in high-value manufacturing sectors, such as aerospace and biomedical [66], represent a material class that could benefit from micro-machining and surface texturing using EJP. However, the response of Ti alloys to electrochemical machining is known to be poor in terms of topography control. This is due to the formation of thick, electrically insulating passivating oxide films upon processing [97]. A number of different processing strategies have been explored in EJP to minimise this effect.

Pajak et al. (2006) [98] used a hybrid process termed laser-assisted jet electrochemical machining (LAJECM), based on previous work undertaken by the same research group [99, 100], and observed roughness reductions in comparison to the conventional mode of EJP operation using $NaNO_3$. This was confirmed in a succeeding investigation by the same research group, De Silva et al. (2011) [7], and was proposed to be due to the heating effect of the coaxially applied laser energy, which locally increased electrical conductivity of the electrolyte at the central impingement point, and therefore the local current density [37, 101]. In addition, Zhang et al. (2013) [102] stated that pulsed lasers could remove electrolytic products from the surface, through highly localised ablation, which would be beneficial for titanium alloys forming passivating oxide layers. Separately, Mitchell-Smith and Clare (2016) [25] attempted to subject Ti-6Al-4V alloy to EJP with $NaNO_3$ using ultrasonically-assisted sample staging

(direct ultra-sonication [103]), described by Skoczypiec (2011) [104]. In their investigation, UA-EJP was reported to reduce the profile roughness, *Ra*, of processed striations by 31% in comparison to the conventional mode of operation. This was attributed to the mechanical breakdown of the brittle oxide films by the applied ultrasonic frequency, which exposed more of the surface to the action of the anodic dissolution process.

Considering section 2.2.2.5 (page 35), changing the electrolyte type represents a route through which electrochemically generated topographies in titanium can be controlled. This has been exploited in electrochemical micromachining, for example by Madore and Landolt (1997) [105], who investigated both bromide and sulfuric acid – methanol mixtures, and Baehre et al. (2016) [106], who varied the acidity of $NaNO_3$-based electrolytes and compared them with neutral NaCl and KBr. In spite of this, changing electrolyte has been the subject of less investigation in EJP, possibly due to concerns over potential exposure to electrolyte systems of higher toxicity. Lu and Leng (2005) [107] used jet-electrochemical micromachining to process Ti-6Al-4V using a NaBr electrolyte of high concentration (5 M), similar to the range of KBr solutions investigated by Bannard (1976) [56], although the authors didn't compare topographic response to other electrolytes in the investigation. Liu et al. (2017b) [108] explored the difference in surface topography between $NaNO_3$ and NaCl, in EJP of TB6 (>10 wt.% vanadium), building on an ECM study in the same material by Wang et al. (2017) [109]. Liu et al. (2017b) reported significantly brighter surfaces and lower roughness upon processing with the aggressive chloride electrolyte.

2.2.3.2. Orientation anisotropy topography

It has been reported in many electrochemical studies that processing at low applied energy can lead to anisotropic material removal, dictated by orientation-dependent passivation characteristics [110]. Crystallographic corrosion has been reported in a large number of metals, providing they are kinetically stable in aqueous solutions. Examples include, but are not limited to; aluminium [111], copper [112], iron [113], gold [114], nickel [115] and titanium [116]. To satisfy crystallographic etching conditions, and generate anisotropic topographies, there must be adequate removal selectivity between the different atomic planes within the material. This is defined by the precise anode reaction. In the case of copper processed with $NaNO_3$, Schneider et al. (2011) [112] reported high dissolution selectivity between {100}, and {111} planes at low current density (17.5 A/cm^2), wherein the less-packed family of planes dissolved at a faster rate and generated bright surfaces (*see* Figure 2.16). In addition, the authors observed preferential gas evolution, likely to be oxygen, from the {111} planes. Martinez-Lombardia et al. (2014) [117], reported the opposite trend in copper, suggesting that {111}-type planes were removed faster than those corresponding to the other principal cubic orientations, however similar orientation-dependent topographies were observed to those reported by Schneider et al. (2011). In addition, the investigation was performed in a hydrochloric acid-based electrolyte, which will reduce the formation of insulating passivating films in the anodic dissolution process (*see* section 2.1.5), which is likely to affect the comparative dissolution characteristics.

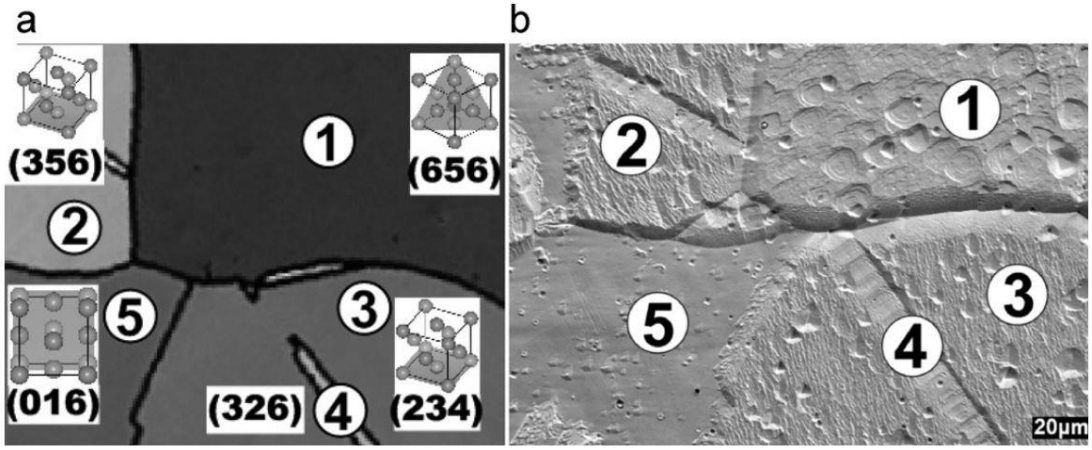


Figure 2.16: Processing Cu with $NaNO_3$ in active dissolution modes (17.5 A/cm^2), where the orientation defines the surface texture. a) Prior EBSD map, b) same field of view after etching. Numbers denote identified grain orientation: 1 [656], 2 [356], 3 [234], 4 [326], 5 [016]. Image from Schneider et al. (2011) [112].

In succeeding investigations, Schneider et al. (2012a) (2012b) [118, 119], showed that orientation-specific topographies were eliminated by processing away from the active, and into the transpassive dissolution mode where oxide films break down and dissolution occurs more rapidly (>20 A/cm^2 in Cu), confirming prior investigations by Landolt et al. (1969) [96] and Kinoshita et al. (1970) [120]. Anodic dissolution anisotropy, dependent on orientation, in aluminium has been well-reported in the literature. For example, Kaesch et al. (1988) [121] observed faceting and micro-tunnelling when processing with halide electrolytes (*see* Figure 2.17a). In this work the authors suggested that the environment within the micro-tunnelled pits was highly acidic, and therefore the rate formation of crystallographic pitting could be suppressed upon increasing pH. Seo et al. (2003) [111] correlated the anisotropic dissolution characteristics in aluminium with the stability of the passive oxide film at different orientations, where {100}-type planes have been shown to passivate

readily in halide-containing electrolytes. This leads to preferential removal of {111} and {101} planes, evolving greater current densities (*see* Figure 2.17b).

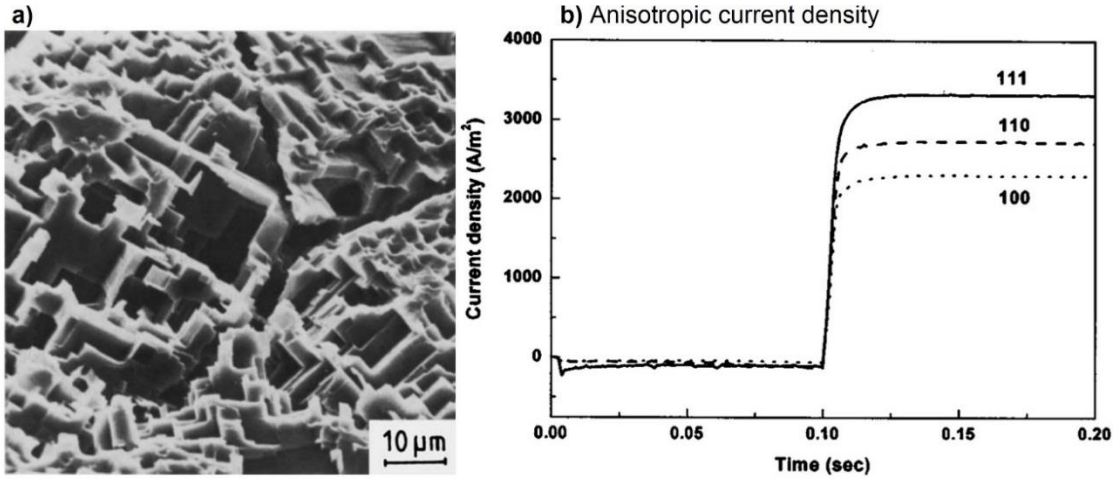


Figure 2.17: a) Crystallographic micro-tunnelling of aluminium. From Kaesch et al. (1988) [121]. b) Anisotropic current density evolution, where {100} directions dissolve more slowly, taken from Seo et al. (2003) [111].

Therefore, the exact dissolution characteristics in the generation of crystallographic-etch pitting has been shown to be dependent on the electrolyte-material relationship. These crystallographic topographies have not been reported in EJP. This is due to two reasons; i) materials are generally processed at higher current densities, at which point dissolution is effectively isotropic, ii) passivating electrolytes, such as nitrate, are most often used in EJP. These are characterised by a tendency to generate oxide films during processing (*see* section 2.1.5) [23, 43, 122], which allows enhanced dimensional accuracy and brighter, pit-free surfaces [90]. This is in direct opposition to aggressive electrolytes, such as chloride, which promote passivity breakdown, pitting, and reduced dimensional accuracy [123-125].

2.2.3.3. Electrochemically inert phases

Materials containing electrochemically inert phases such as metal-matrix composites (MMCs) feature widespread application where the design intent is mechanically robust or hard-facing parts. Conventional machining of hard materials is time-consuming and can require expensive diamond tooling, therefore ECM methods could be exploited in these material systems. Hardening phases commonly used in MMCs or formed in steels, such as tungsten carbide (WC) and cementite (Fe_3C), are generally more ceramic than the matrix. As such, they often have a worse response than the matrix or binder metal to the electrochemical treatment [44], however in some cases, such as the investigation presented by Coughanowr et al. (1986) [126], the binder may be more resistant to the electrochemical treatment. This defines the resulting surface topography after an electrochemical processing treatment.

In ECM, Haisch et al. (2002) [127] reported that cementite does not dissolve anodically, even using aggressive chloride-based electrolytes, within the potential ranges that were tested. This meant that in the case of a range of steels containing pearlite colonies, the resulting topography was dominated by protruding carbide lamellae, which were removed through 'wash-out' mechanisms. Considering this erosive removal mechanism, recent work has been undertaken simulating the localisation of current density and therefore material removal around the lamellae by Klocke et al. (2017) [128], which concentrates material removal in the ferrite adjacent to the cementite grain boundary. Walther et al. (2007) [129] explored the anodic dissolution of hard refractory ceramics, such as TiC and TiN in sodium nitrate, where the presented voltammograms indicate the dissolution of the binders (Co, Fe, Ni) at lower

anode potentials. Anodic dissolution was reported for all specimens of TiC and TiN, however this study considered these separately from binder metals. In addition, the ceramic grains were themselves observed to dissolve in an inhomogeneous manner, explained by the passive films that formed on the grain surfaces during the sintering process employed to generate the samples.

Specifically within EJP, Hackert-Oschatzchen et al. (2013) [58] successfully processed pure WC and WC-Co alloys using NaOH-based electrolytes. In order to eliminate NaOH from the input electrolyte stream, Mizugai et al. (2013) [130] demonstrated that processing could be undertaken using simple $NaNO_3$ solutions, due to the cathodic reduction of water in the jet nozzle prior to impingement, which evolves hydrogen gas and generates hydroxide in the solution. Following this, Miyoshi and Kunieda (2016) [83] proposed that hydroxide could be generated at the workpiece through the application of a bipolar pulse. In this case, the water reduction during the cathodic cycle leads to the generation of hydroxide at the workpiece. This destabilises the tungsten oxide and allows the workpiece to be electrochemically machined during the anodic cycle. Without a bipolar power supply, Liu et al. (2015) [131] successful processed WC through application of Al_2O_3 particles (10 μm diameter) to a neutral NaCl electrolyte in order to mechanically abrade the insulating oxide upon impingement at high jet pressure and anodic potential (4 MPa, 120 V), which removed substantially more material than the abrasive water jet alone at equivalent jet pressure. In terms of applications, Walker et al. (2017) [132], performed EJP on Al-Si materials, generating hard-facing silicon colonies at the surface in order to increase the wear resistance for cylinder liner applications.

2.2.3.4. Grain characteristics

Considering Equation 2, the electrochemical equivalent (ECE) dictates the mass and therefore the volume of a substance removed in an ECM process. For polycrystalline materials composed of multiple phases, this will result in inhomogeneous topography as phases with greater volume-corrected ECE will appear to remove at a faster rate, assuming equivalent current density distribution [79]. This has been investigated in ECM, but the effect in EJP has largely been ignored as most research groups tend to investigate single-phase materials, such as austenitic stainless steel, or composite materials where one phase is electrochemically inert. An investigation into the effect of differential phases on the resulting surface topography in electropolishing of brass was presented by Rotty et al. (2016) [133], where the authors observed the zinc-rich β-phase to be preferentially removed under non-optimised polarisation potentials.

Burger et al. (2012) [134] studied selective element depletion in the precise electrochemical machining (PECM) of a single crystal Ni-alloy. It was indicated that low current density machining leads to inhomogeneous elemental dissolution, which resulted in topographic undulations in the investigation. This effect was also investigated in a different additively manufactured Ni-alloy by Wang et al. (2017) [135], where undulations were observed to correlate with dendritic structures and layer bands, although topographic sensitivity to microstructure was reduced at increased current density. As part of an effort to define a process signature, Klocke et al. (2018) [136] identified different causes of material modifications at the near-surface resulting from ECM, relating both to electrolyte flow and material microstructural properties, such as passivation,

selective dissolution, and pitting, summarising within the investigation that achievable surface topographies strongly depend on microstructure.

Prior ECM investigation in steels undertaken by Krishnaiah-Chetty and Radhakrishnan (1981) [137] established importantly that the post-machined surface is defined by the underlying grain structure, not only the ECE of the component phases. In this investigation, surface roughness was observed to increase with grain size. This effect has been reported in EJP in different metal matrix composite materials by Hackert-Oschatzchen et al. (2012) [58], and Miyoshi and Kunieda (2016) [83], who both reported that the surface roughness was positively correlated with the size of the WC grains within the workpiece. Further study by Hackert-Oschatzchen et al. (2016) [138] simulated the evolution of the machined surface around an electrochemically inert SiC particle, whereby current flow and material removal is proposed to increase around the periphery of the particle, leading to undermining.

The effect of thermal loading and stress distributions in defining the resulting surface topography have largely been underreported in electrochemical technologies, despite surfaces being sensitive to material defects under certain operating conditions [112]. It is understood that this is the result of a desire to eliminate the effect of microstructural inhomogeneity from the surface topography, considering mechanical applications. Since investigations by Landolt [86] among others, identified the effect of microstructural inhomogeneity in defining the resulting surface can be almost entirely overcome through processing at the limiting current density, further investigation is largely inane as a research avenue under conventionally applied electrochemical conditions, unless topographies representative of the underlying microstructure are

desirable. An example of this is presented in work by Melisova et al. (1997) [139], where persistent slip bands in copper were revealed by sequential electropolishing and imaging. The relatively extreme flow regimes in EJP however, will significantly increase the limiting current density through suppression of the mass-transport diffusion layer.

2.2.4. Summary of research gaps

Considering topography generation in EJP, applied energy has generally been considered as the main process parameter influencing the resulting surface. The effect of current density for a single-phase, homogeneous material system is largely understood. Research gaps identified in terms of processing parameter influence generally involve the topographic response to changes in the electrolyte system, which has largely been under-explored in EJP. This is especially important in the processing of titanium alloys, which generally respond poorly to electrochemical processing, but could benefit greatly from EJP. The effect of electrolyte flow velocity in defining the surface topography in jet processing techniques remains to be investigated. In addition, the vast majority of EJP research has been undertaken in one type of material system, austenitic stainless steel. The resulting topography from this material system during EJP is easy to control, largely a result of the single-phase composition, and favourable passivation characteristics, which help to polish the surface during processing. To be applied in an industrial application, the process response for more complex material systems needs to be characterised. Other material systems present additional complexities and hence research challenges. Research gaps highlighted in this section of the literature review concern mainly the process response to material properties:

- ***The impact of changing the microstructural precondition of the workpiece material*** – the topographic response to changing the grain size, phase ratio, phase machinability in complex alloys, as well as thermal treatment and stress history in EJP is not understood. This is important considering the complex microstructures of materials that are employed in high-value engineering applications to which EJP could be applied. In addition, surface topography is well understood to have an impact on a range of properties, including fatigue life, corrosion resistance, drag, and fluid- and biological-facing properties.
- ***Orientation topographies – generation and characterisation*** – while orientation-dependent microscale topographies have been reported in a range of materials as a result of anodic dissolution and etching, limited attempts have been made to apply this knowledge as a viable materials characterisation technique. Translational EJP could allow the process to be employed for the generation of large-area selective generation of these topographies, that could be calibrated for given orientations against a conventional technique, such as electron back-scatter diffraction (*see* section 3.4.2). This would create a low-cost method capable of appraising orientation in polycrystalline metallic samples and could lead to widespread impact beyond this work.

2.3. Macroscale EJP feature geometry – *machining*

2.3.1. Introduction

Considering the ongoing drive towards technological miniaturisation, greater levels of control over the machined feature in terms of size reduction and

enhanced dimensional accuracy remain important pursuits in any machining process. To this end, the influence of process parameters and workpiece material are investigated in this section of the literature review, correlating with the third targeted thesis objectives (*see* section 1.1), corresponding to improving control over the macroscale removal geometry in EJP.

2.3.2. Process parameter influence on feature geometry

2.3.2.1. Applied energy and translation

While the charge passed influences the scale of the machined feature in EJP [24, 39, 70, 99, 140], the most significant parameter controlling the geometry of the deterministic feature (where the resulting profile is not dependent on randomness) is the current density distribution, described in detail in section 2.1.4 [38]. This variable defines the localised charge flow and thus local mass transfer/material removal characteristics, according to Faraday's law (*see* Equation 1). For a cylindrical nozzle setup as conventionally employed in EJP, this has a Gaussian current density distribution, thus material is removed as an apparent reflection of this.

Considering the application of energy density in EJP, the majority of investigations have been undertaken using continuous DC operating conditions (100% duty), maximising MRR for a given current [24, 37, 39, 40, 70]. Despite the extensive application of pulse power in electrochemical micromachining (EMM) to enhance dimensional accuracy and machining precision [16, 60, 87], this has been the subject of limited investigation in EJP. Miyoshi and Kunieda (2016) [83] changed the supply from DC to a bipolar pulse in an EJ-turning operation in WC-Co micro-rods, where they reported decreasing width with decreasing duty cycle and anode pulse time. The bipolar pulse led to significant

nozzle wear through anodic dissolution during the reverse pulse; the authors therefore devised an insulated glass nozzle as a solution.

Aside from the applied energy defining the geometric profile by dictating the MRR [40, 70], the effect of applied potential on the dimensional accuracy of the machined feature was explored by Sen and Shan (2005a) [70], whereby the authors reported increasing roundness error between potentials 200-480 V. The study presented by Pajak et al. (2006) [98], agrees with these findings, wherein overcut and taper are observed to increase with potential from 80-180 V. The effect of changing processing potential on feature widths was explored by Schubert et al. (2011) [141]. Where a hydraulic jump could be successfully generated (IEG >30 µm, *see* section 2.3.2.2, page 50), widths were reported as approximately 1.5 nozzle diameters at potentials between 10-80 V. However, by processing at lower potential (5 V), widths approaching nozzle diameter were observed, accompanied by expected reductions in MRR. In addition, processing >80 V increased the widths >1.5 nozzle diameter. Hackert-Oschätzchen et al. (2013) [58] investigated WC-Co composite materials, reporting a positive correlation between feature widths and applied potential (20-60 V), although the feature depth/applied potential relationship was less obvious and the authors reported no correlation.

The lateral translation velocity, v_h, of the electrolyte jet affects the resulting geometric profile through changing the linear charge density, $\overline{\lambda_q}$, making MRR inversely proportional to v_h [37], which has been well-reported by many EJP practitioners [24, 82, 142]. The relationship between v_h and the feature geometry was explored by Mitchell-Smith et al. (2014) [2], who reported feature widths processed at v_h = 100 mm/s (≈400 µm) to be approximately 30% of those

achieved at v_h = 0.01 mm/s (≈1400 µm) in Inconel 718 processed using nitrate (150 µm nozzle I.D.). This was also reported by Wang et al. (2017) [109], investigated in a titanium alloy (Ti-10V-2Fe-3Al) using a hybrid NaCl/$NaNO_3$ electrolyte, across a significantly narrower v_h range (0.01-0.036 mm/s). In the same alloy, Liu et al. (2017) [84] reported this trend across a broader translation velocity range (0.01-0.250 mm/s), although noting that stray corrosion increased as well.

2.3.2.2. Nozzle diameter and inter-electrode gap

The nozzle diameter dictates the scale of the processed feature in EJP, through directly influencing the size of the stagnation region upon impingement and therefore the minimum radius of the electrolyte thin film (*see* section 2.1.3). This represents the limit at which sufficient electrical potential can evolve to effect adequate passage of charge and material removal. Considering localisation of mass transfer in EJP was understood by Datta et al. (1989) [37] to be dependent on the constrictive effect of the high-velocity resistive thin film, this variable is important in terms of defining the geometric profile.

The importance of the hydrodynamic stagnation region has been understood in jet-processing techniques at least since Chin and Tsang (1978) [143] who observed that this region, within a jet plating system, corresponds to a radius of approximately 0.6-1.4 nozzle diameters, d_N (*see* Figure 2.18a). Subsequent EJP investigations by: Natsu et al. (2007), d_N = 0.42 mm [24], Hackert-Oschätzchen et al. (2011) , d_N = 0.1 mm [82] and Liu et al. (2014) , d_N = 0.18 mm [91] among others, appear to correlate and fall well in this range in a variety of stainless steels and Stellite 12 (*see* Figure 2.18b). This ratio however appears to be satisfied when processing simple material systems, such as

stainless steels and varies when EJP is applied to more complex material systems. This is explored in detail in section 2.3.3. The effect of changing the nozzle diameter on overcut and taper was investigated by Pajak et al. (2006) [98], who reported significantly greater overcut in drilling operations using 0.3 mm nozzles than 1 mm nozzles. In addition, taper was shown to be reduced under equivalent conditions.

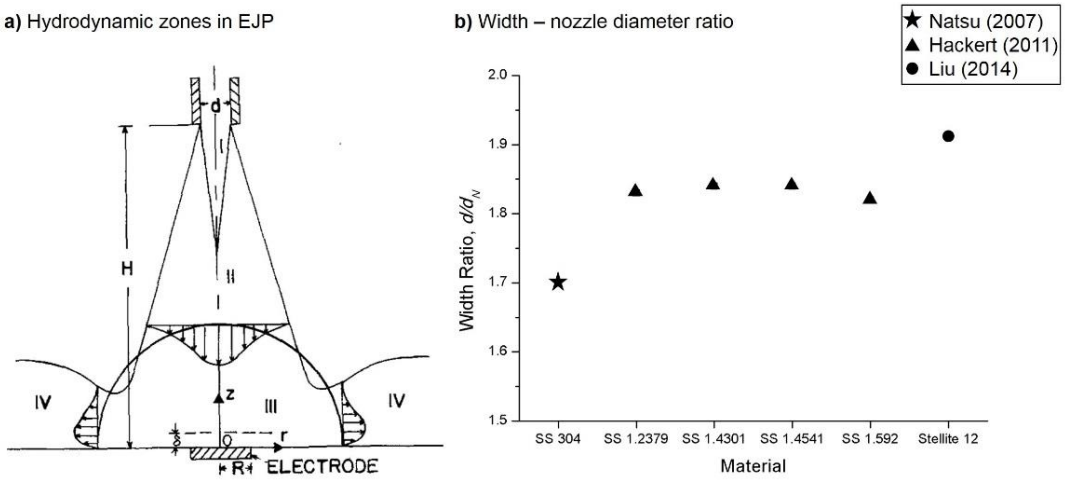


Figure 2.18: a) Schematic hydrodynamic zones in EJP. Material removal is concentrated in the stagnation zone (III), from Chin and Tsang (1978). b) Feature width – nozzle diameter ratio taken from Natsu et al. (2007) [24], Hackert-Oschatzchen et al. [82] and Liu et al. (2014) [91].

Changing the length of the inter-electrode gap (IEG) can affect the removal rate and thus, the resulting geometric profile from a given operation [144]. This results from a change in electrolyte jet resistance with path length and is especially important for potentiostatic processing, such as that employed by Kozak et al. (1996) [39], where increasing the IEG reduces the supply current in accordance with Ohm's law. In this investigation the authors presented ≈35% reduction in the dissolution velocity at both 100 and 250 V (jet pressure: 0.6 MPa) between 2 and 4 mm IEG, which correlated well with the prior simulation. Similar relationships were observed by Pajak et al. in (2004) [100], and (2006)

[98] in both Hasteloy and Ti-6Al-4V and by Goel and Pandey (2016) [10] in copper. Schubert et al. (2011) [141] reported large feature widths at very low IEG (< 30 μm, <30% nozzle I.D.), which the authors demonstrated was the result of the inability of the process to develop a radial thin-film and hydraulic jump at very small IEGs. This has led to ongoing studies aimed at enhancing the level of control over the IEG in EJP. Minimising IEG is required to maximise charge flow and removal, although is required to be large enough to avoid electrode contact, flashover and to maintain the hydraulic jump. Notably, this has been explored by Hackert-Oschätzchen et al. (2014) [144], who evaluated current feedback to maintain the IEG, in addition to prior electrical probing and laser scanning, constructing topography maps to inform the EJP scanning strategy. The latter technique was investigated by Zanjani et al. (2017) [145], from the same research group, where an on-line laser pre-scanning strategy was employed in a prototype setup to map a complex surface (in this case a coin) prior to EJP. This is essentially the application of an existing surface metrology approach.

Recently, Liu et al. (2018) [146] also reported the reduction of the mass removal rate with increasing IEG as part of an abrasive-assisted EJP operation, where the authors correlate this with the effective reduction in current density, rather than the reduction in the kinetic energy of the abrasive particles. In addition Martin et al. (2018) [140] investigated the effect of sequentially increasing the effective IEG over multiple passes during an electrochemical jet turning operation on the removal rates, and Malik and Manna (2018) [147] simulated this inverse relationship between IEG removal rate in EJP. Considering a fixed current scenario, increasing IEG will lead to an increase in machining potential,

dictated by Ohm's law. Providing the power supply can accommodate these variations, the removal rate should not be impacted to the same extent compared with the fixed voltage case, as removal is directly proportional to the charge transferred (*see* Equation 1) [29]. The localisation of material removal with increasing IEG at constant current was investigated by Ikeda et al. (2006) [71], where the roundness of pits drilled with a multi-nozzle system was shown to reduce upon increasing the IEG beyond 0.25 mm (0.26 mm nozzle). Kunieda et al. (2011) [148], notably decreased kerf widths of the processed features below 'nozzle size' in EJP upon increasing the IEG. This however, was achieved using an adaption of conventional EJP apparatus, whereby a flat jet (2032x37 μm) was employed through electrolyte ejection from a linear orifice. By careful design of the orifice geometry, the electrolyte jet expands in line with the orifice and contracts in the perpendicular direction. Through application of this setup, slots were drilled into stainless steel reported to have widths <37 μm. Mitchell-Smith et al. (2014) [2] reported a small reduction in depth through increasing the IEG from 50-250 μm, although this was accompanied by an increase in pit width. Therefore, no conclusions can be drawn regarding a difference in MRR, however the precision and dimensional accuracy would appear to have been reduced across this range.

2.3.2.3. Electrolyte

From prior ECM investigations, it is understood that changing the electrolyte can significantly alter the dimensional accuracy of the processed feature [50, 60, 87, 92]. This generally relates to the spatial passivation characteristics with regards to the applied current density distribution and is therefore discrete for a given electrolyte-material combination. For a conventional ECM setup, this

relationship is detailed in section 2.1.5. Within EJP, the effect of changing the electrolyte on the material removal was first explored by Datta et al. (1989) [37], who reported a significant difference in current efficiency between equimolar (5 M) $NaNO_3$ and NaCl electrolytes. In this study, the current efficiency using NaCl was observed to be independent of current density, while current efficiency with $NaNO_3$ was observed to increase across the same current density range (12-75 A/cm^2), which correlated well with previous ECM studies [44]. The difference in current efficiency was correlated with oxygen evolution at the workpiece in nitrate electrolytes. Oxygen evolution as a sacrificial anodic reaction in nitrate electrolytes was investigated (among others) by Lohrengel et al. (2016) [93] in a range of materials and was observed in-situ using a transparent electrode and identified as a reaction product by Garg et al. (2018) [149], using gas chromatography.

Considering prior ECM studies by Zhu et al. (1983) [150] and De Silva et al. (2003) [151], reducing the electrolyte concentration generally increases the dimensional accuracy of the processed feature through decreasing the throwing power (*see* section 2.1.5). Both Pajak et al. (2004) [98] and (2006) [100], and Sen and Shan (2005) [70] investigated the effect of changing the concentration of $NaNO_3$ on material removal in EJP, where increasing this variable increased the MRR in a fixed potential processing operation, considering a reduction in resistance. The investigation by Sen and Shan (2005) [70] reported an increasing roundness error of pits processed at increasing electrolyte concentration, although this was alleviated through processing at higher inlet pressures (correlating with jet velocity, *see* section 2.3.2.4). In apparent contrast, Hackert-Oschätzchen et al. (2013) [58] observed width reductions

through increasing electrolyte concentration as part of a fixed potential process, although this was in WC-Co composite materials. In this case, increasing the concentration of the NaOH component of the electrolyte mixture, which is able to decompose passivating tungsten oxides [59], was proposed to control the mechanism behind the reported results. Wang et al. (2017) [109] investigated both NaCl, $NaNO_3$ and a 1:1 hybrid electrolyte of the two, showing greater control over dimensional accuracy and higher MRR in the hybrid than both base electrolytes.

2.3.2.4. Flow velocity and dynamics

In ECM, increasing the flow velocity increases the evacuation of debris, such as sludge and evolved gases [43, 152]. Considering a fixed potential operation, this would impact the effective current density because suspended debris and gases decrease the electrolytic conductivity, therefore this would directly affect the resulting geometric profile. In EJP, Sen and Shan (2005) [70] reported that increasing electrolyte inlet pressure increased MRR between the ranges of 0.15-0.35 MPa (0.4 mm nozzle I.D.), although increasing beyond 0.35 MPa reduced MRR. The reduction in flow velocities >0.35 MPa was proposed to be a result of a decrease in the interaction time between the electrolyte and the workpiece, reducing Joule heating and thus conductivity, upon increasing the refresh rate of the electrolyte. No explanation was given as to why the MRR increased in the lower pressure range tested, although it is likely to be a result of increasing debris evacuation efficacy. Ikeda et al. (2006) [71] reported a slight reduction in pit width upon increasing electrolyte tank pressure between 0.2 and 0.3 MPa, although no further reduction upon increasing the flow velocity beyond this. In this study however, a multi-nozzle setup was tested; here the flow fields

from each nozzle interact with one another, creating a hydrodynamic scenario more complex than the standard operating condition. When employing a slot-jet EJP setup, Kunieda et al. (2011) [148] reported decreases in cut width resulting from increases across the range of 0.2-0.5 MPa tank pressure, which the authors observed was a result of increasing parallelism of the applied jet at higher velocities. Goel and Pandey (2016) [10] also reported increasing MRR with inlet jet pressure, proposing that this was the result of greater evacuation of machining debris and evolved gas, which decreased the resistance of the electrolyte used.

As part of an effort to further understand the effect of electrolyte flow on geometry generation in EJP, Hackert-Oschätzchen and co-authors have attempted to incorporate electrolyte flow field effects into numerical simulations of EJP. This is largely because Hackert-Oschätzchen et al. (2008) [40], (2010) [153], and (2012) [69] observed an increasing divergence between their numerical model and the experimentally observed geometric profiles as machining time was increased. In all investigations, the profiles were deeper and narrower than accompanying simulations, which did not incorporate fluid effects. In addition, the latter study modelled the effective current density, which was greater than that experimentally observed. Through incorporating fluid effects, Hackert-Oschätzchen et al. (2015a) [77] and (2015b) [154] successfully simulated the jet shape and modify the current density distribution to account for local flow differences. In both of these studies, the authors' successfully correlated mean current density with that experimentally observed, within the time frame investigated (≤2 s). While the diameters of the processed features in the latter simulations (incorporating fluid effects) showed better correlation

with the experimental observations, processing times >1 s lead to chamfering and therefore greater divergence, due to a secondary machining effect that was not included in the model. The authors proposed that this resulted from the reflected electrolyte that contacted the sides of the pit and lead to removal at the edges and remains the subject of further investigation within the research group.

2.3.2.5. Hybrid processing strategies in EJP

Hybrid processing strategies have been investigated repeatedly through adapting standard EJP apparatus for the purpose of offsetting perceived disadvantages with the process generation of macroscale features, such as low removal rates compared with shear-based techniques, unfavourable passivation effects in certain materials, and stray current machining. It is therefore important to note these adaptions when undertaking EJP investigations that aim to overcome the same problems. Hybrid processing in general was broadly described by Lauwers et al. (2014) [155] as being *'based on the simultaneous and controlled interaction of process mechanisms and/or energy sources/tools having a significant effect on the process performance'.* For a successful hybrid process strategy, the objective is to generate a synergistic effect from each contributory mechanism, such that the product of performance enhancement (MRR, precision etc.) is greater than the sum of each mechanism. In EJP (machining), a hybrid strategy was first explored by Datta et al. (1989) [37], who applied a laser (laser-assisted EJP – LAEJP). This was inspired by prior research in jet plating undertaken by both von Gutfeld (1983) [101] and Gelchinski et al. (1985) [156], where laser-assist increased the localised deposition rates, as well as smoothing the deposit topography. This

resulted from localised laser-induced heating of the workpiece, which increases the electrolyte conductivity in the vicinity, intensifies diffusion transport and lowers the activation energy for ECM interactions. Datta et al. (1989) [37] observed no increase in global removal volume with LAEJP when using NaCl as the electrolyte in either steel or nickel. In addition, the authors reported a significant reduction in removal for both materials when processed with LAEJP compared with a conventional setup using $NaNO_3$ electrolyte. The authors concluded that the laser stimulated oxygen evolution from the anode in the case of nitrate-containing electrolytes, thus increasing resistance in the IEG. In this investigation, the authors reported that the feature depth (when using NaCl) was increased and the pit widths were reduced. In addition, the resulting profile changed from the calotte form to a more complex geometry, shown also by De Silva et al. (2011) [7] in Figure 2.19, characterised by a central dimple within the processed feature.

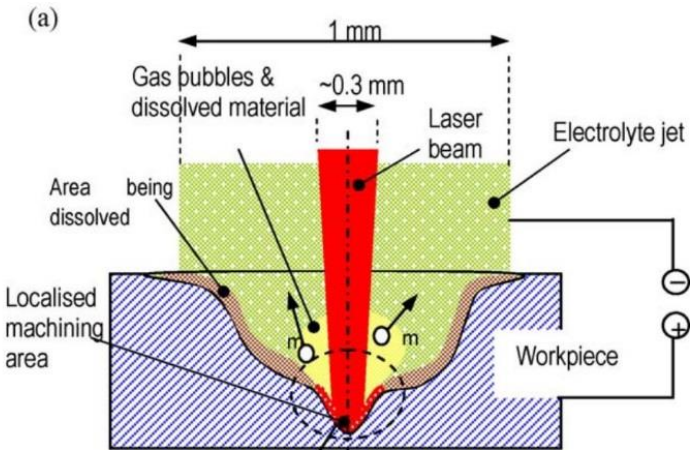


Figure 2.19: Laser-assisted EJP overview, showing the localisation of material removal at the pit centre. Taken from De Silva et al. (2011) [7].

De Silva et al. (2004) [99] reported greater MRR when applying LAEJP. While this appears to contradict the work of Datta et al. (1989) [37], the latter

investigation was undertaken under potentiostatic conditions, whereby lowering resistance (by local heating) increases effective machining current in accordance with Ohm's law. In addition, the former investigation was performed at laser power of 22 W, in comparison to 0.375 W applied by De Silva et al. Surprisingly, considering the findings of the earlier study, no details regarding the electrolyte type (nitrate or chloride) were detailed by De Silva et al., although succeeding research by the same group, Pajak et al. (2004) [100], employed a $NaNO_3$ electrolyte at identical process parameters. Therefore, the discrepancy in MMR was likely a result of the difference in laser power. Aside from MRR enhancements, in both studies, the authors reported significant improvements to pit taper. Pajak et al. (2006) [98] reported that LAEJP could successfully process passivating materials such as titanium by breaking down oxide layers, which the authors suggested was the result of surface acoustic waves. De Silva et al. (2011) [7], elucidated that the localised temperature increase at the workpiece surface was inversely proportional to the thermal conductivity of the workpiece, therefore proposing that the efficacy of LAEJP in enhancing MRR and taper was material dependent. An identical simulation was applied by Malik and Manna (2017) [157], to a slightly different Ni-superalloy (Inconel 718 instead of Hasteloy). Independently, Zhang et al. in (2009) [94] and (2010) [158] investigated the effect of electrolyte concentration on laser attenuation, and also observed the complete removal of the recast layer associated with the laser-drilling process.

Investigations by Liu and co-authors have sought to improve MRR, and improve the performance of EJP towards materials not amenable to anodic dissolution in aqueous environments. In 2014, Liu et al. [91] proposed the addition of

abrasive slurry into the electrolyte jet. In this investigation, alumina particles were applied into the electrolyte feedstock (both NaCl and $NaNO_3$), where the MRR was shown to significantly increase beyond that expected by EJP alone due to synergistic effects of erosion and corrosion (increases of >80% at 2 MPa pressure, >160% at 3 MPa pressure using 0.5 wt.% particle loading). Aspect ratio of the processed feature in Stellite 12 was also observed to increase. In a follow-up study, Liu et al. (2015) [131] reported significant increases in aspect ratio (532%) and interestingly current density (659%) applying abrasive assisted EJP in comparison to standard EJP. The latter was proposed to be a result of the mechanical removal of the passivation tungsten oxides, allowing anodic dissolution of the underlying tungsten carbide. Recently, Liu et al. (2018) [146] explored the process in stainless steel for the purpose of creating complex microchannel geometries, showing that increasing jet velocity and abrasive concentration reduced the removal contribution from anodic dissolution.

Mitchell-Smith and Clare (2016) [25] applied ultrasonic assistance to the process (UAEJP) of highly passivating Ti-6Al-4V. The authors reported identical increases in depth and reductions in width (7% over multiple passes and 6% over single passes), resulting from the mechanical breakdown of passivating oxide films (*see* section 2.2.3.1, page 35). These oxide films were proposed to shield the basal areas of the machined feature and lead to sideways material removal. Goel and Pandey (2016) [10] also successfully demonstrated an increase in MRR using UAEJP compared with EJP, this time using a copper workpiece, which was proposed to aid in the breakdown and evacuation of anodic films resulting from the process.

2.3.3. Material influence on the deterministic feature

2.3.3.1. Material and microstructure

Considering material removal in EJP, Pajak et al. (2006) [98] investigated current efficiency for different engineering materials, reporting an independence of this factor on physical material properties, rather depending on the physical properties and ability to dissolve. In this study, the authors reported the current efficiency relationship with regards to material as: stainless steel<aluminium alloys<titanium alloys<Hasteloy. Relatively few investigations have been undertaken characterising the effect of the material on the resulting geometric profile in EJP and the majority of published literature in this regard has been presented by Hackert-Oschätzchen and co-authors. Hackert-Oschätzchen et al. (2011) [82] subjected four different stainless steel grades to identical EJP operations and reported negligible difference in feature width, however the depth was reported to correlate with the differing specific dissolution volume, calculated from the weighted alloy ECE. Kawanaka et al. (2013) [74] reported a decrease in pit diameter in a dual-phase brass after heat treatment (750 °C, 1 hr) when compared with the as-received material, which was correlated with grain size increases. Contributions to the literature in this area are limited.

2.3.3.2. Precipitates and composite materials

Hackert-Oschätzchen et al. (2013) [58] investigated the effect of the tungsten-carbide (WC) cobalt composite materials across three different WC grain sizes (1, 2 and 4 µm). In this study machined depth and width were observed to increase with grain size, although no explanation for this observation was reported. Miyoshi and Kunieda (2016) [83] also investigated WC-Co composite materials and reported that MRR was inversely proportional to WC grain size

between 2-10 μm, which the authors considered to be a result of an erosive removal mechanism complementing corrosive anodic dissolution. Regarding the loading of particles, Hackert-Oschätzchen et al. (2016) [159] reported no significant difference in machining characteristics, such as feature depth and width, in aluminium-silicon carbide (SiC) composite materials of 5 wt.% and 10 wt.% SiC. In a follow up study from within the same research group, Lehnert et al. (2018) [160] reported similar results in equivalent material compositions, although this time comparing with the non-composite matrix alloy (0 wt.% SiC). In this investigation, the presence of SiC was shown to increase the removal depth in NaCl electrolyte, which the authors proposed to be a result of erosive effects and the presence of SiC was observed to decrease the width of the processed feature. The latter was suggested to result from current density focussing around the SiC particles, which was proposed to increase passivation, although the mechanism behind this remains unclear.

2.3.4. Summary of research gaps

Within this section, it has been outlined that the applied current density distribution is the most significant factor in determining the geometry of the resulting profile, while the charge passed and nozzle diameter determine the scale of the processed feature. A series of different hybrid processing strategies have been adopted to try to reduce the significance of these constraining factors. A large number of EJP studies rely on fixed potential processing, where the machining current, defining removal, is left to float dependent on process resistance. Through processing under fixed potential conditions, variables such as the IEG, electrolyte concentration and electrolyte flow rate inevitably affect the resulting geometry. Material removal becomes extremely sensitive to

electrolyte conductivity, although this is only one factor governing the electrolyte-workpiece interaction, and detaches from an understanding of discrete reactions at the anode. Considering this, the investigations undertaken in this thesis have been undertaken using a fixed current processing regimen.

Research gaps that have been highlighted in this section of the literature review include:

- ***The effect of electrolyte on dimensional accuracy and MRR in a fixed current setup.*** This has not been investigated thoroughly in EJP, however dimensional accuracy and MRR are key performance indicators for any industrial machining process. In addition, materials such as titanium alloys, which are difficult to process electrochemically could benefit from research into changing the electrolyte type for the purpose of overcoming passivation.
- ***The effect of microstructural inhomogeneity on the resulting geometric profile.*** Prior investigations have reported that the level of passivation and the size of microstructural features affect not only the resulting topography but the geometric profile. This been the subject of very limited investigation in metallic materials with dual-phase microstructures, although knowledge in this regard is important considering materials are generally selected based on the suitability towards the end application, rather than machining performance.

2.4. Material deposition in EJP

2.4.1. Introduction

The ability to coat materials remains of vital importance to the engineering community and represents a route through which the response of a material to its environment may be modified, while retaining the beneficial characteristics of the underlying bulk material, for example: strength, toughness, cost and creep-resistance. Superior surface properties may be imparted onto a workpiece or varied, for example; hard-facing (such as increased wear resistance in mechanical applications) [161] and fluid-facing properties (such as self-cleaning surfaces) [65], corrosion resistance [162], thermal insulation [163], or to alter a biological response (such as implant favourable or anti-microbial surfaces) [105]. Through the ability to execute multiple coating strategies, EJP represents a route by which component surfaces can be altered in a selective fashion, as part of an athermal process that does not alter the application-defining properties of the underlying material. Different in-jet processing strategies are explored in the detailed review below, and directly relate to the thesis objective outlined in section 1.1, referring to surface elaboration as part of a selective processing strategy.

2.4.2. Jet electrodeposition

Jet electrodeposition (JED) is the reduction of metallic cations onto the surface of a component and physically is analogous to electroplating (*see* section 2.1.2) [164]. The in-jet nature of the deposition process is by definition selective and high local deposition rates relative to conventional electroplating can be achieved, without masking or auxiliary electrodes. Planar CNC JED was proposed as a technique by Fletcher and Oliver (1974) [165], who patented a

jet plating setup with compressed air assist for deposition on metallic workpieces, which was at least partially inspired by earlier patents, for example by Polichette (1969) [166], without numerical control. Alkire and Chen (1982) [34] described the electrochemical kinetics of the impingement region with regards to electrolyte concentration, applied energy and flow velocity in order to determine experimental conditions for successful selective JED. This was compared with a slot-jet setup, by Alkire and Ju (1987) [167]. In this investigation, the authors presented the slot jet as a route through which large surface areas could be plated, whilst retaining high selectivity, wherein increasing current density increases the selectivity between plating in the impingement region in comparison to the wall-jet (thin-film) region. This selectivity was directly measured for copper deposits in EJP by Karakus and Chin (1994) [21], and was shown to delocalise at increasing IEG.

Considering process parameters for minimising topographic amplitude, electroplating techniques are in direct contrast to electropolishing. In the latter family of techniques, operating at or above the limiting current density (indicating mass-transport limited processing conditions) is understood to lead to the smoothest surface topographies, however in electroplating, the smoothest topographies are generated well below the limiting current density [168]. Winand (1992) [169] related this to the $\frac{J}{C_B}$ ratio, where C_B is the bulk cation concentration. The greater this ratio, the more dendritic the deposit, shown in Figure 2.20.

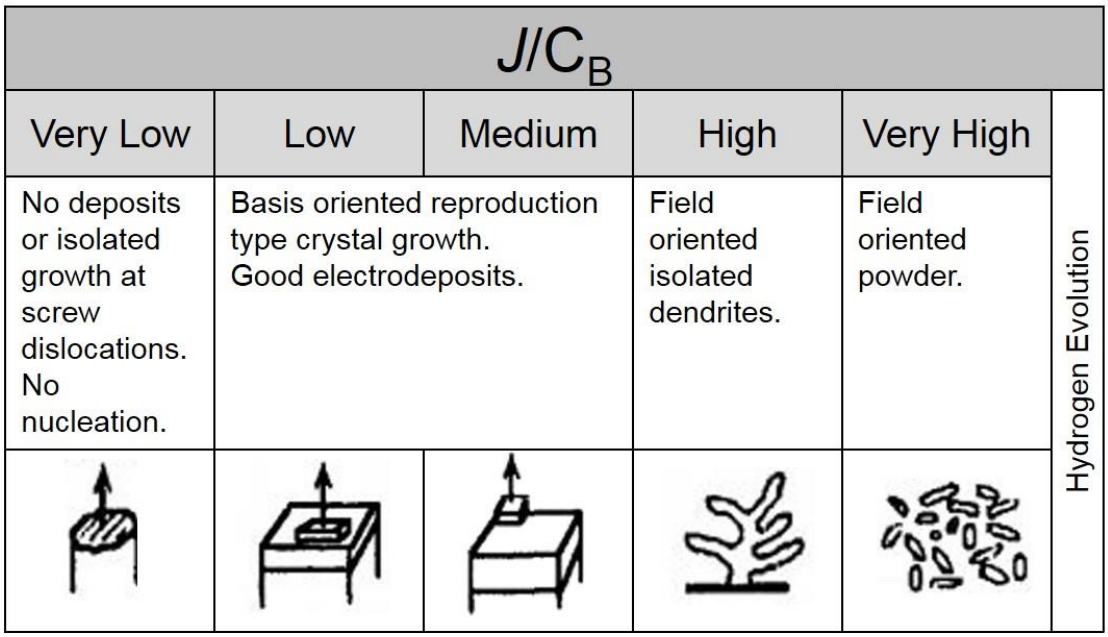


Figure 2.20: In electroplating, the ratio between current density and bulk concentration determines the morphology of the final deposit. Adapted from reference [169].

This is because under conventional electroplating conditions, the reverse of the ECM levelling effect is observed. Therefore, undulations in the topography i) localise charge transfer, and ii) protrude into the diffusion layer into an electrolyte composition more representative of the bulk concentration (i.e. more metallic cations). These increase the localised plating rate and exacerbate the scale of the protrusion, resulting in nodulation [170]. This was confirmed in JED by von Gutfeld et al. (1983) [101] who observed brittle columnar gold electrodeposits resulting from processing at 16 A/cm^2 (above the limiting current density), with poor adhesion. Considering the aforementioned study undertaken by Alkire and Ju (1987) [167], there is evidently a compromise between increasing dimensional accuracy, and enhancing topography and deposit integrity.

Subsequent investigation by Bocking and Cameron (1994) [171] also demonstrated increased deposit integrity at smaller current densities, drawing

from work presented in Bocking's thesis (1994) [172], indicating deposit hardness was enhanced at low current densities. In this study, the authors co-deposited gold and nickel, showing that increasing the current density reduced the fraction of nickel within the deposit, likely to relate to difference in standard electrode potential between the elements. Nickel was added to the electrolyte to increase deposit hardness. In addition, many striking nodular morphologies were presented by Bocking, when plating gold $>J_{lim}$ (*see* Figure 2.21a, b).

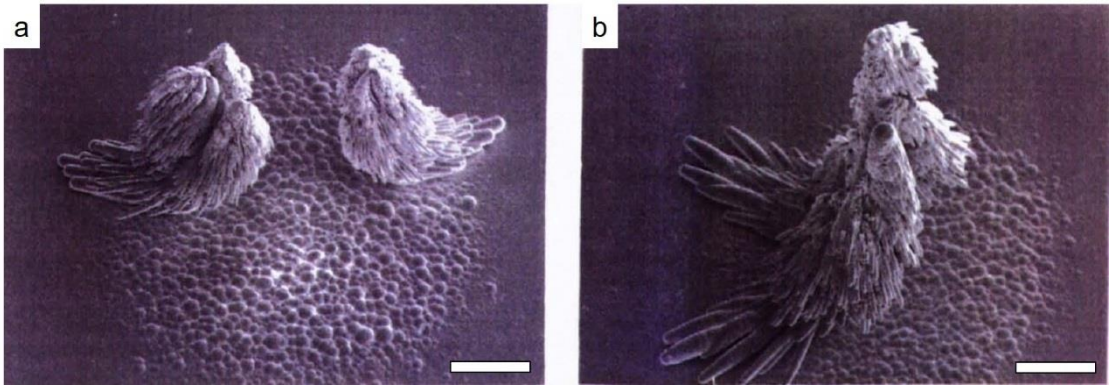


Figure 2.21: SE micrographs showing structures achieved in gold where $J>J_{lim}$ (10 A/cm^2). a) after 6 s, b) after 8 s. Taken from Bocking [172]. Scale bars are 100 µm.

Dover et al. (1996) [170] attempted to prototype tooling for electrical discharge machining (EDM) by superimposing striations generated with JED of copper processed at low current density (5.68 A/cm^2, 40 layers). Although the authors presented micrographs of the tooling correlating with the prior CAD file, they reported some nodulation of the deposit, for which they gave three explanations: i) inappropriate current density, ii) each deposition run results in a non-flat surface, amplified with each pass, iii) edge effects due to acceleration/deceleration of the nozzle, which changes the linear charge density. The first explanation was excluded as the authors repeated the pattern at lower current density (3.79 A/cm^2, 60 layers) and observed identical

nodulation. The application of JED as a rapid prototyping tool was further investigated by Kunieda et al. (1998) [9], who employed a lapping step to level any surface protrusions after each plating pass in copper (*see* Figure 2.22). Through applying this extra step, the authors addressed explanations ii) and iii) presented by Dover et al. (1996). Although the global processing time was significantly increased, JED was successfully employed to generate sloped walls at angles ≤45 ° and a large deposit of 2 mm height (20 hour process time). Jet electrodeposition has subsequently been industrially applied to generate printed circuit boards using masking, although retaining low plating rates [173]. Qiao et al. (2005) [174] applied EJP to co-deposit a cobalt and nickel alloy. Alloy electrodeposition presents interesting challenges due to the unique standard electrode potentials of different elements, which means electrodeposition of one element will always be favoured. In this study, the authors used an electrolyte with a Ni concentration an order of magnitude greater than Co.

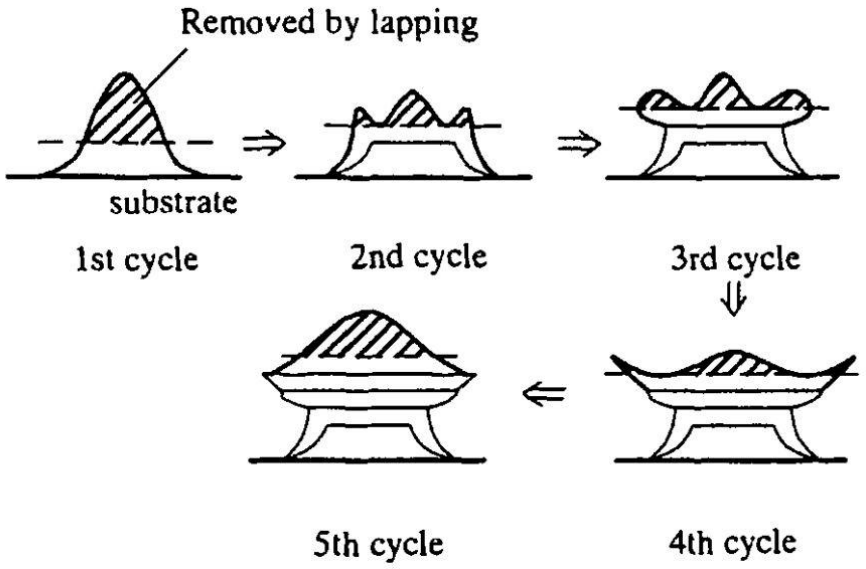


Figure 2.22: The lapping step developed to remove surface perturbations, taken from Kuneida et al. (1998) [9].

2.4.3. Jet co-deposition of particulates

EJP can be exploited for the generation of metal matrix composite coatings, whereby suspended particulate matter within the electrolyte is deposited with the matrix former (generally a metal), to generate a co-deposit [175, 176]. The objective of any co-deposition process is to synergistically combine beneficial properties of both the matrix former and the particle reinforcement [177]. Conventional bath co-deposition has been exploited to this effect since Sautter (1963) [178] generated Ni-Al_2O_3 composites with significantly greater yield strength than electrodeposited Ni. Guglielmi (1972) [12] explored the process kinetics, proposing that co-deposition was based on i) loose particle adsorption to the cathode and equilibrium with the particle suspension followed by ii) irreversible incorporation. In the first mechanism, particles are screened by solvent molecules and adsorbed ions. This transitions to a stronger field assisted adsorption, once the particle is dehydrated, followed by progressive matrix incorporation. Further to this, Celis et al. (1987) [175] proposed that the first step was aided by the adsorption of ionic species around the inert particle. In this study, the authors proposed five discrete stages of incorporation: i) ionic adsorption in the electrolyte, ii) forced convection towards the boundary layer, iii) particle diffusion through the diffusion layer, iv) particle adsorption onto the cathode, v) reduction of the adsorbed ionic species to incorporate inert particle.

Co-deposition in EJP was first exploited by Takeuchi et al. (1997) [179], where compositionally graded Ni-P SiC was coated onto aluminium substrates. In this investigation, jet velocity was adapted to optimise electrodeposition of Ni-P, which requires higher velocities for limiting current density maximisation, and codeposition of SiC, which is greater at low velocity. The inverse relationship

between jet velocity and particle incorporation results from wash-out before sufficient entrapment, which is consistent with the retardation of mechanism i) proposed by Guglielmi's model [12]. The objective of the study was to identify processing conditions whereby the composition ratio could be modulated at limited expense to deposition rate.

Subsequently, Osbourne et al. (2007) [180] co-deposited Cu-Al_2O_3 using EJP at 0.1-3 A/cm^2. Higher suspension concentrations were shown to increase the incorporated particle concentration, while flow velocity was again shown to inhibit co-deposition, where the flow rate was determined to influence alumina incorporation to a greater extent than suspension concentration and current density. Micro-hardness was shown to increase with alumina incorporation. This investigation built on prior work undertaken in the thesis of Osbourne (2006) [181], who studied the modulation of conventional EJP parameters on the hardness, resistivity and crystallisation of Cu-Al_2O_3 matrix composites. Thiemig et al. (2007), (2008a) [182, 183] co-deposited Ni-Al_2O_3 composites with EJP, whereby incorporation of Al_2O_3 not only increased the micro-hardness, but crystallisation textures were shown to change from (100) for pure Ni to enhanced (111), (220) and (311) textures. Thiemig et al. (2008b) [184] discovered that the effects of particle buoyancy and gravity on incorporation, which are important parameters in conventional co-deposition, were negligible in EJP for particles <50 nm, where incorporation is dependent on convectional diffusion.

The role of the electrolyte in governing particle incorporation in conventional bath deposition was explored by Bund and Theimig (2007) [185] for the Ni-Al_2O_3 co-deposition system. In this investigation zeta potential, ζ, was introduced as

an important parameter determining incorporation levels. Greater magnitudes of ζ decrease agglomeration within the electrolyte and aid the dispersion of particles within the deposit. It was discovered that strong negative charges are favourable for co-deposition rather than strong positive charges, which confirmed prior investigations by Celis at al. (1987) [175]. While counterintuitive considering cathodic charge, this was proposed to be a result of the greater cation cloud surrounding nanoparticles. Considering Guglielmi's model [12], this enhances the first adsorption mechanism, prior to incorporation. This finding was confirmed by Man et al. (2014) [186] in brush plating co-deposition, where the authors also observed a reduction in Ni grain size with increasing Al_2O_3 incorporation.

2.4.4. Anodic oxidation

EJP has been applied towards anodization of titanium by Mori and Kunieda (1997) [187] and aluminium by Kuhn et al. (2017) [188]. Coating thickness ≤500 nm were realized in the latter investigation at large applied potentials (160 V) and processing times (600 s). Beyond these preliminary studies, no other work has been undertaken regarding EJP anodic oxidation. An oxidation method which has been industrially applied to generate useful, hardwearing and corrosion resistant coatings is plasma electrolytic oxidation (PEO). This has not yet been subject to EJP investigation, but may enable selective modification of aerospace materials such as titanium [189], aluminium [190] and magnesium [191].

PEO exploits well understood electrochemical processes, such as gas liberation and metal oxidation (*see* Figure 2.23) [192]. Considering the 'b'-type mechanism shown in Figure 2.23, anodization occurs during processing,

thickening up to the dielectric breakdown potential of the oxide film, U_5, where breakdown results from tunnelling ionisation [193]. Beyond U_6, this mechanism is supported by thermal ionisation processes, which lead to micro-arcing, wherein the film is alloyed with elements contained within the electrolyte. At point U_7, arcs are powerful enough to discharge into the workpiece and damage the material. Considering the large range of energy densities that can be applied using EJP, this technique could be easily adapted to perform PEO.

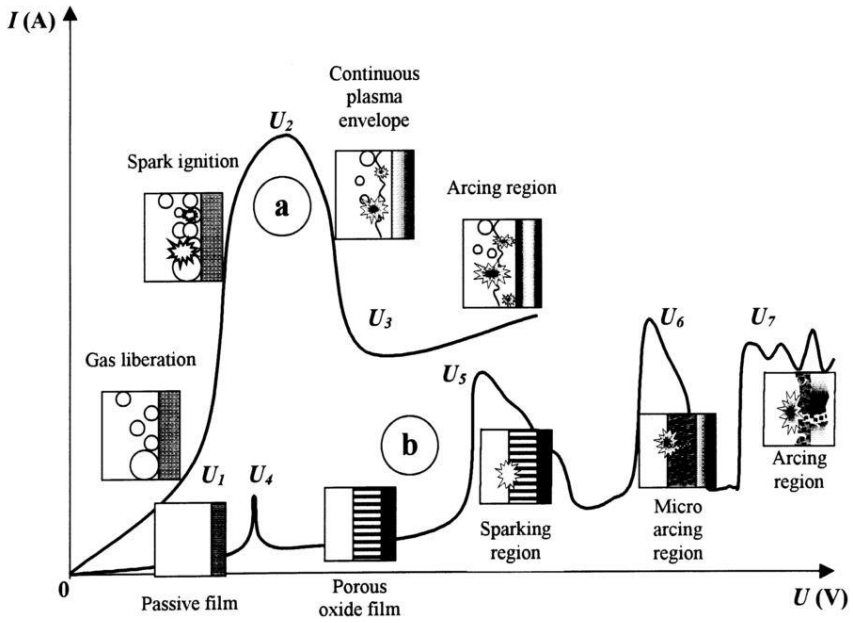


Figure 2.23: Discrete anodic plasma generation phenomena. a) From gas liberation, b) from oxide layer breakdown. Taken from Yerokhin et al. (1999) [192].

PEO coatings have been exploited for a number of different industrial applications, such as corrosion resistance [162], thermal stability [194], photocatalytic activity [195] and bio-compatibility [196]. The versatility results from advantageous mechanical, chemical and physical properties of the oxide films, which are understood to be a function of the high temperatures generated by the plasma (≤10,000 K [66]) that sinter, melt and affect the crystallisation of the ceramic coating.

2.4.5. Summary of research gaps

In this section, it has been shown that EJP has been successfully adapted to selectively coat materials through electro-reductive deposition of metallic coatings through application of a cathodic potential to the workpiece. The literature has shown that deposition stability and quality is largely inversely proportional to the input energy density. This inhibits industrial application as the low mass transfer rates (hours per mm^3) required to generate suitable deposits significantly increase the processing time. Co-deposition of nanoparticles through EJP has largely been restricted to the Ni-Al_2O_3 material system, whereby these have been shown to enhance deposition material properties in comparison to jet-electrodeposited nickel. In addition, anodic oxidation techniques are largely underexplored in EJP, whereby simple anodization mechanisms have been exploited in aluminium alloys. Considering the utility of plasma electrolytic oxidation (PEO) in generating robust, corrosion resistant coatings in valve metals, it is surprising that no EJP research group has explored this avenue. This is pertinent considering the large energy densities EJP is capable of achieving. Research gaps that have been highlighted in this section of the literature review include:

- ***Increasing mass transfer rates whilst retaining deposition stability.*** For EJP to be applied as a coating technique, mass transfer rates must be substantially increased. This can only be achieved through increasing energy density, which currently decreases deposit quality. However, electrolyte chemistry has been largely neglected regarding its impact in EJP-electrodeposition studies. This is pertinent considering the

widespread application of chemical additives in conventional bath-based electroplating for the purpose of increasing deposition rates and quality.

- ***Co-deposition of poorly stable nanoparticle suspensions*.** To date, nanoparticle co-deposition in EJP has been largely limited to stable suspensions within electrolyte nanoparticle systems, such as Ni-Al_2O_3. EJP response towards the co-deposition of unstable suspensions, such as SiO_2 in Cu (where silica is unstable in the acidic media required for Cu electrodeposition) is undocumented, but knowledge in this regard would benefit EJP practitioners through expanding or at least defining the usable palette within co-deposition.
- ***Feasibility of EJP to execute PEO-type surface modifications.*** PEO is conventionally undertaken on valve metals to enhance material and corrosion properties. To date, this has not been reported in EJP, despite the large energy densities which should make such mechanisms achievable in jet processing. The lack of literature may be a result of negative results, such as the mechanism being incompatible with EJP, considering general bias towards reporting positive results. Mechanistic incompatibility with EJP may arise from the enhanced evacuation of anodic gases in the high-velocity electrolyte jet stream. It is these gases that are broken down in the electric field to generate the plasma, so this factor could retard the PEO mechanism. The importance of such coatings towards surface and application functionalisation dictates that the feasibility of selective PEO needs to be explored.

3. Experimental

This chapter describes the sample generation, EJP parameters and characterisation techniques, data analysis routines, as well as performance metrics applied throughout the succeeding results chapters. Investigation-specific processing parameters can be found in the Appendices.

3.1. Substrate preparation

3.1.1. Influence of microstructural precondition and orientation on the topography in single-phase materials.

To appraise the effect of deformation and annealing, commercially pure Cu (≥99.9% purity), was cut from sheet (3 mm) into six 20x100 mm lengths. The lengths were then separated into two sets, called prior-annealed and non-annealed, correlating with the thermal history prior to EJP. The three prior-annealed lengths were subjected to heat treatment at ≈0.7 Tm (750 °C, 3 hrs), in order to coarsen the microstructure and obtain a neutral stress condition. Samples were removed from the furnace and left to air-cool. The second preparation step involved both sets of samples, whereby defects were induced into the material, which was achieved through cold-rolling the lengths to thickness reductions of 0% (no reduction, control set), 26% and 52%. Samples (20x20 mm) were then cut from each of the lengths corresponding to the six discrete preconditions, before being resin mounted in the normal direction. Subsequently, the resin-mounted samples were ground and polished manually to 1 μm diamond and washed with deionised water prior to EJP. Material removal from the original surface in EJP will reduce topographical dependence

on near-surface induced stresses caused by grinding and polishing, however every care was taken in these preparation steps to limit the amount of manual polishing force.

To correlate topography with crystallographic orientation, samples of polycrystalline Al (1050, 1.5 mm sheet), Ni (201, 3 mm sheet) (>98% purity) and Al-alloy (6080, 6 mm plate) were cut into pieces 20x20 mm. All materials were subsequently annealed ≈0.7 Tm (Al alloys = 465 °C, Ni = 1020 °C) for three hours in order to neutralise the stress condition, before extraction from the furnace and air-cooling. Samples were resin mounted, ground and polished to 1 μm diamond and washed with deionised water prior to EJP. For samples subjected to prior EBSD, additional polishing was undertaken using colloidal silica (0.3 μm) and samples were successively washed in ethyl lactate, acetone, methanol and isopropanol prior to characterisation [197].

3.1.2. Influence of grain size and phase ratio in multiple-phase materials

Brass (Cu39Zn2Pb) was selected as the feedstock in the study concerning multiple-phase materials. In this regard brass was selected as an ideal material system, whereby a high degree of control is possible over the microstructure during heat treatment, as well as well-researched anodic dissolution phenomena in this material system. All samples were generated from the same feedstock, of nominal composition outlined in Appendix 1, from which the weighted alloy electrochemical equivalent (ECE) was calculated, according to Equation 2. For simplification, each element is assumed to dissolve into one valence state, where z: Cu (II), Zn (II), Pb (II). Difference in corrosion resistance

between Cu and Zn components was appraised considering standard oxidation potential ($Cu \rightarrow Cu^{2+} + 2e^- = -0.340$ V; $Zn \rightarrow Zn^{2+} + 2e^- = 0.763$ V, *vs* SHE), taken from Lange (1999) [198], indicating that Zn is significantly easier to oxidise than Cu. Separate sample pieces were cut from this feedstock and heat-treated for 60 minutes over a range of temperatures (450, 550, 650, 700°C), before being removed and water quenched. In addition, another sample was processed in an identical fashion at 800°C, and subsequently tempered for 30 minutes (500°C). These samples were resin mounted for grinding and polishing to 1 µm diamond prior to EJP.

3.1.3. Influence of electrolytes on the removal geometry

Inconel 718 (3/8 inch plate, Unicorn Metals) was the workpiece used in the dimensional accuracy enhancement investigation. The nominal composition of the material is given in Appendix 2 (median value, wt. %, quoted for each alloying element), along with the inferred ECE. Current efficiency was calculated considering the weighted average of these values. Inconel 718 was selected due to the ease of electrochemical machinability (and poor conventional machinability), prior research on this material system within the research group, and the application of this material to high-value industry, such as aerospace gas turbines. Samples (15x15 mm) were cut, ground and polished, and washed in deionised water before EJP.

Ti-6Al-4V sheet (3 mm, Unicorn Metals) was used in the titanium micromachining study of nominal composition given in Appendix 3. Ti-6Al-4V was selected as an alloy of titanium, due to its extensive application in aerospace, which has both poor electrochemical and conventional machinability, and would therefore benefit from processing improvements.

Samples (20x20 mm) were cut from the plate, mounted in resin, subsequently ground and polished (>1 μm diamond), and washed sequentially in deionised water before EJP.

3.1.4. Substrates for EJP coating

Samples of pure copper (≥99.9% purity), previously described (*see* section 3.1.1), were cut from sheet into pieces (20x20 mm) and were used as electrodeposition substrates. Surfaces were ground using 1000 grit paper, and washed with deionised water prior to EJP.

Pieces of Ti-6Al-4V sheet, previously described in section 3.1.3 (20x20 mm) were used in jet plasma electrolytic oxidation (PEO) studies. This material was selected due to the high elemental affinity towards oxygen, which makes the material amenable to PEO, as well as the widespread application of titanium alloys to aerospace applications.

3.2. Sample processing

3.2.1. Static EJP platform

Research regarding electrolyte selection was undertaken using a static EJP platform, designed and built at the University of Nottingham by Jonathon Mitchell-Smith. This is differentiated from a conventional EJP platform by the fixed end-effector, upon which the nozzle is located. Instead, the workpiece is positioned relative to the nozzle and therefore impinging jet. Planar manipulation of the workpiece is achieved through manual high-precision optical staging and a telescopic stage is used to alter the working height, shown in the photo in Figure 3.1. The inter-electrode gap (IEG) between the sample

and the nozzle was also set manually, through the use of feeler gauges. Compressed air is supplied through the end-effector creating a coaxial air-shroud around the electrolyte jet, which constricts the impingement area. Material transfer (removal or deposition) is enacted using a DC power supply, while a numerical controlled (NC) pump supplies fresh electrolyte from a reservoir tank.

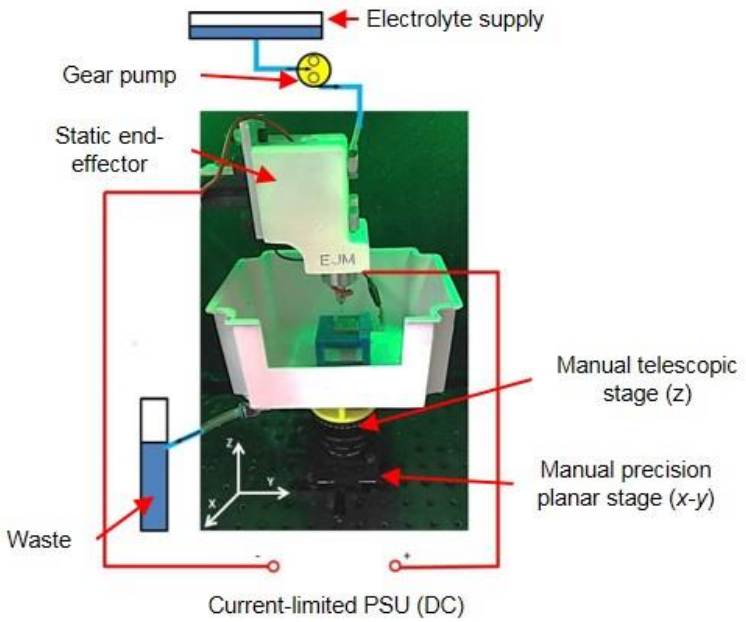


Figure 3.1: Static EJP platform used in this thesis. The end-effector is fixed to the frame, while the workpiece is manipulated prior to processing through manual precision staging. The electrolyte collector (white box) feeds waste into a disposal tank, preventing contact with staging.

The platform is controlled through a simple Arduino setup encoded and built at the University of Nottingham by Dr Matthias Hirsch, whereby process time, current, and pump supply voltage are manually adjustable. This setup was intended to be a simple test-bed to appraise the impact of multiple electrolytes in EJP. This was achieved through employing a small reservoir tank, which allows low volumes of different electrolytes to be tested and exchanged rapidly. The platform simplicity allows for rapid maintenance and adaptation. Nozzle

translation is not possible using this platform, as this requires a dynamic end-effector, or workpiece movement; instead the processing regime is limited to pit machining (anodic workpiece) and spot material deposition (cathodic workpiece).

3.2.2. Dynamic EJP platform

A dynamic EJP platform was also used here, designed and built at the University of Nottingham by Jonathon Mitchell-Smith (*see* Figure 3.2). In this setup, the end-effector is translatable through precision numerical control servos and the workpiece is fixed to a bed in comparison to the static platform. This enables planar processing operations as well as pits and spot deposits. In addition, multiple supply tanks are used in this setup allowing for fast electrolyte changeover and in-process mixing [199]. Numerical control is exercised over the supply current, translation velocity, pump voltage and electrolyte draw. A DC power supply is used in this platform, connected to the workpiece with a Cu probe. The power supply was limited by voltage to 300 V and by current to 7 A, with total power output limited to 750 W.

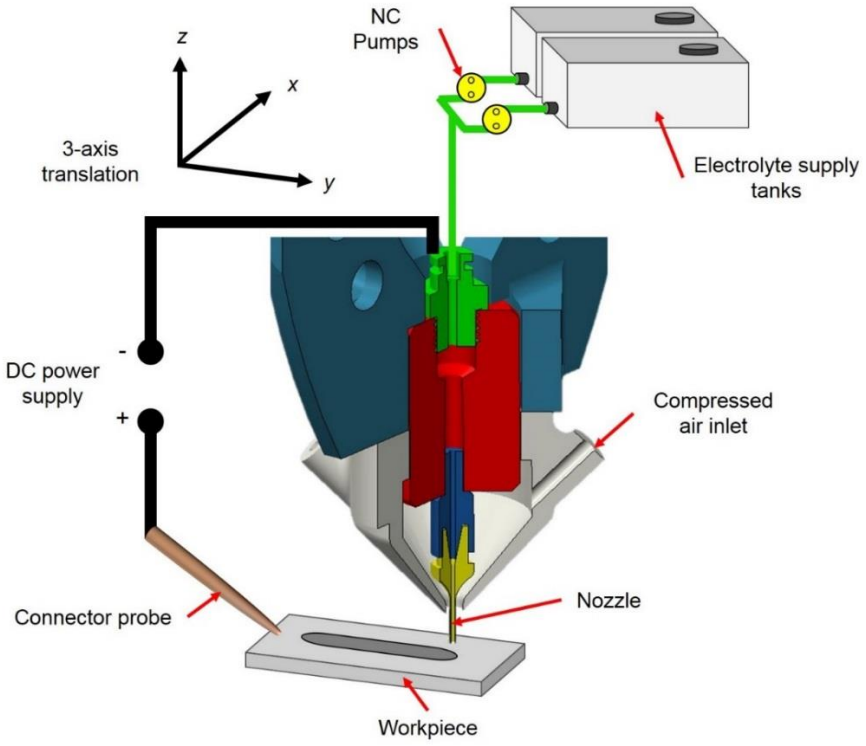


Figure 3.2: Schematic showing the dynamic rig used in this thesis. This enables three axes nozzle translation and planar machining operations, as well as the ability to draw electrolyte from multiple tanks.

3.3. EJP parameters and electrolytes

3.3.1. Influence of microstructural precondition and orientation on the topography in single-phase materials.

EJP parameters for these experiments are listed in Appendix 4, where a broad range of current densities were tested (J_{noz} = 20-450 A/cm^2). IEG was maintained at 0.5 mm. For the appraisal of the effect of annealing and stress condition in Cu, $NaNO_3$ (2.3 M) was used. As outlined in the literature review (*see* section 2.2.2.2, page 28), surface topography is shown to be dependent on the translation of the electrolyte jet, whereby the surface is affected by the low current density part of the Gaussian distribution, when a standard nozzle

and normal machining convention are applied. In order to conduct preliminary studies into the effect of microstructure on the resulting EJP topography, translation velocity was removed through pit processing, whereby a given point on the surface is exposed to the same current density in the machining cycle. Three pits were machined at each current density value to increase the statistical significance of the resulting datasets.

To correlate crystallographic orientation with surface topography, NaCl was tested as well as $NaNO_3$, as the literature indicated that corrosion is more likely to be anisotropic in more aggressive solutions, such as those containing chloride anions. The ionic strength of this electrolyte was fixed with that of the $NaNO_3$ electrolyte (2.3 M), and the conductivity of the NaCl electrolyte is given in Appendix 4. To correlate surface topography with orientation across large areas, surfaces were processed with a raster pattern. In such instances, the jet translation velocity was fixed at 0.5 mm/s.

3.3.2. Influence of grain size and phase ratio in multiple-phase materials

To appraise the effect of current density on the resulting EJP surface for each brass material precondition, two modes of machining were undertaken: the point approach and the vector approach. An array of pits and striations were machined for each material condition. Parameters are listed in Appendix 5, where IEG was maintained at 0.5 mm. As the resulting surface after EJP is known to be affected by the low current density area of the distribution as the electrolyte jet traverses the workpiece, the point approach was considered important to understanding the mechanisms of surface generation as well as

material removal. Three pits were drilled into each material precondition at each current density. The total charge passed, Q, was controlled in the process (uncertainty ±1.95 μC) as the product of applied current, I, and time, t, and is listed adjacent to the approximate supplied current density. The vector approach, commonly employed by EJP practitioners, was also appraised through the machining of striations, in order to characterise surface generation in a more applicable machining environment. Nozzle traverse velocity was maintained throughout striation machining at 0.5 mm/s.

3.3.3. Parameters for electrolyte experiments

All salts used were ≥98% pure. The percentage identifier for a given doped electrolyte represents the molar contribution of the dopant to the total ionic strength, for example NaI 40% indicates an effective NaI concentration of 0.92 M, where I_C = 2.3 M. The remaining contribution being met by the base electrolyte, for example $NaNO_3$ or NaCl: 1.38 M, where I_C = 2.3 M. IEG was maintained at 0.5 mm.

Regarding the dimensional accuracy enhancement experiments whereby Inconel 718 was processed, $NaNO_3$-based electrolytes were mainly used, as well as a NaCl solution, as detailed in Appendix 6. All doped electrolytes were matched by ionic strength, I_C, (2.3 M). Electrolyte electrical conductivities were measured as described in the methodology (section 3.7.3, page 99).

The preliminary machinability study in titanium was performed using the electrolytes listed in Appendix 7. Electrolytes were compared with $NaNO_3$, where the literature review indicated poor electrochemical machinability of the material in this electrolyte type. Considering the relatively low molar solubility of

NaF in aqueous solutions compared with the other salts tested in this study, a lower concentration (0.5 M) un-doped solution was tested in this study, along with a NaCl-doped electrolyte (3:1 composition ratio). Halide electrolytes were developed from this preliminary study, using NaCl as the base electrolyte in all cases, to enhance processing of the titanium alloy and to innovate the removal mechanisms allowed in EJP. The ionic strength of all electrolytes was matched (2.3 M). These are listed in Appendix 8.

EJP was performed using both the static and the dynamic apparatus detailed in sections 3.2.1 and 3.2.2 respectively. Pit and striation processing of Inconel 718 was undertaken according to the parameters listed in Appendix 9, while the titanium micromachining studies were executed according to Appendix 10.

3.3.4. EJP coating parameters

In all coating experiments, IEG was set to 0.5 mm and a 510 µm diameter nozzle was used, to limit the number of variables. In comparison to conventional anodic dissolution conditions, a cathodic potential (≤100 V) was applied to the workpiece in jet electrodeposition experiments, to effect material deposition. Current density, J_{noz}, was varied in this study between 5-100 A/cm^2.

$CuSO_4.5H_2O$ (Fisher), Na_2SO_4 (Fisher), H_2SO_4 (Fisher), thiourea (Sigma Aldrich) and silica nanoparticles (200-300 nm, Sigma Aldrich) were used in this investigation. All chemicals were analytical reagent grade or higher (>99% purity). Where silica containing electrolytes were employed in processing, the electrolyte reservoir tank was magnetically stirred to maximise suspension stability. Electrolytes used in this investigation are detailed in Appendix 11. In all experiments apart from Zeta potential measurements, silica additions

remained constant at 0.3 g/L. Zeta potential was measured using laser Doppler electrophoresis (*see* section 3.7.4). Since this characterisation process is sensitive to elevated suspension concentrations and pH level, these were attenuated in order to evaluate the behaviour of more dilute solutions than those used for deposition.

In the jet-plasma electrolytic oxidation studies, the workpiece was biased with large anodic potentials (≤200 V), although current limitation was still employed. Sodium sulfate (1 M) was the sole electrolyte in this feasibility study, although acidity was varied (pH 2, 7, 13), where buffering was undertaken using NaOH and H_2SO_4. To generate striations, the jet was translated at 0.05 and 0.1 mm/s.

3.4. Prior EJP material characterisation

3.4.1. Etching and optical microscopy

Material microstructures were appraised through optical microscopy, and acquired after appropriate material preparation (in all cases grinding and subsequent polishing to 1 μm diamond). Samples were then etched after polishing. For Cu and brass samples investigated in this thesis, grain contrast was achieved through chemical etching using acidified (HCl) ferric chloride, detailed by Walker and Tarn (1991) [200]. For Ni, Al and Ti-alloys investigated here, satisfactory grain contrast was generated using EJP with NaCl under appropriate processing regimes (listed throughout the thesis and supplied in appendices). This avoided the use of hydrofluoric acid-containing etchants, such as Kroll's, conventionally used to generate grain contrast in Al and Ti-alloys [200]. The exact EJP parameters are listed with each acquired

micrograph throughout the thesis. Surfaces were subsequently characterised either with a Nikon LV100ND optical microscope (50x objective), or an Alicona G5 Infinitefocus focus-variation microscope (50x and 100x objectives).

3.4.2. Electron backscatter diffraction

Electron backscatter diffraction (EBSD) was used to appraise the orientations of large areas of Cu and Ni, using an Oxford Instruments HKL Advanced EBSD system, with NordlysMax3, located at the Nanoscale and Microscale Research Centre (NMRC), University of Nottingham. Data was subsequently manipulated using Oxford Instruments Aztec proprietary software. The acquisition area (field of view, FOV) and spatial resolution used in these investigations was FOV 4.85*x*3.63 mm, 4.5 μm/pixel (for Ni). EBSD allows for rapid high-resolution spatial appraisal of grain orientation, size and phase identification of crystalline materials. The spatial resolution is intrinsically governed by the resolution of the scanning electron beam, with a nominal angular resolution of approximately 0.5°. The high spatial and angular resolution, when coupled with rapid online data processing and pattern identification mean that EBSD is widely applied in academia and industry for orientation measurement [201]. A typical schematic is shown in Figure 3.3, whereby the sample is mounted at 70° relative to horizontal. The electron beam passes over the sample, where electrons are diffracted by the near-surface atoms of the sample and are measured by an electron backscatter pattern (EBSP) detector, typically a phosphor screen connected to a charge-coupled device (CCD) for data transfer. This technique relies on diffraction, thus is governed by Bragg diffraction rules.

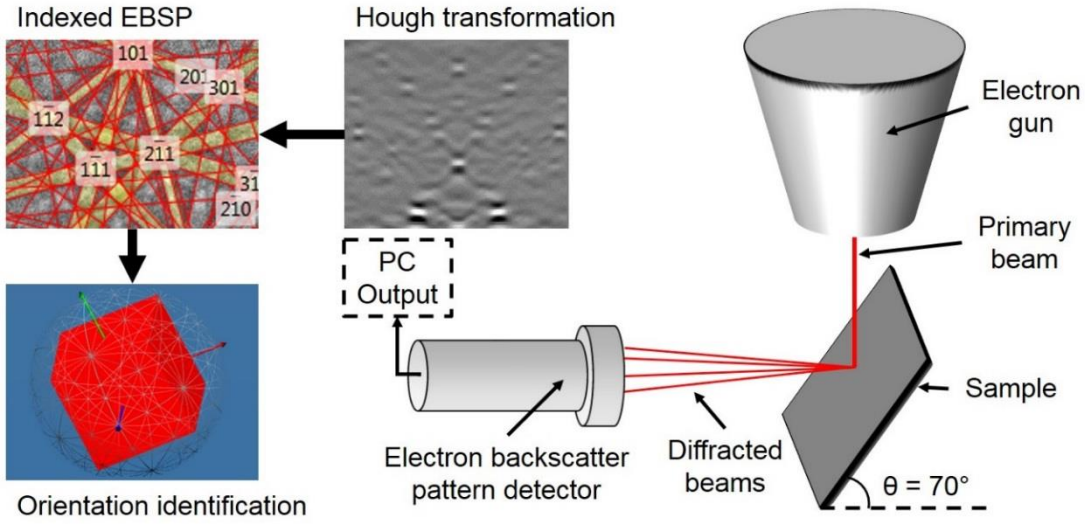


Figure 3.3: A schematic showing a typical EBSD sample setup, whereby the primary beam is incident at the surface of a sample oriented 70° relative to horizontal.

A given EBSP (Kikuchi pattern) is unique to a crystal (defined by the lattice parameters), the relative orientation of the crystal, the wavelength of the primary beam, and proximity of the sample to the phosphor detector [202]. After Kikuchi pattern acquisition, band identification of the patterns is automated through the application of a Hough transformation; converting observable bands into points, which increases computational efficacy. Peak positions within this Hough transformation are located and compared with a predefined database to determine the crystallographic orientation. Due to the surface-sensitive nature of EBSD (≤1 nm), a highly polished surface is necessary for a good data acquisition.

3.4.3. Spatially resolved acoustic spectroscopy

A custom-built spatially-resolved acoustic spectroscopy (SRAS) setup was used to characterise the orientations of large areas of polycrystalline Al and Ni in this thesis. This technique holds several benefits over conventional orientation analysis techniques, such as electron backscatter diffraction

(EBSD). SRAS is not as sensitive to surface roughness as EBSD, so data can be acquired with less sample preparation time and effort. In addition, it can be undertaken under ambient conditions, negating the use of high-vacuum equipment. Data acquisition is fast in comparison to EBSD, however post-processing is currently computationally expensive, whereas modern EBSD systems are able to achieve this online.

In this SRAS setup, a broadband Q-switched laser (1064 nm, generation laser) and an optical mask, a grating pattern of known period, λ_g, were imaged onto each sample, matching the temporal frequency and spatial frequency of the laser and sample for narrow band excitation. The thermo-elastic effect caused by laser irradiance produces a packet of surface acoustic waves (SAWs) with a characteristic frequency, f_s. Thus, the velocity of the SAW, which is a function of the mechanical properties of the sample is found by $v_s = f_s\lambda_g$ [203]. The surface perturbation due to the SAW packet was detected by a knife-edge detector, using a second continuous wave laser (532 nm, detection laser). The velocity at which a SAW packet propagates through a crystalline lattice is dependent on the orientation of the lattice. All scans in this work were conducted at 24 μm wavelength, λ_g, giving a patch size of ≈200 μm and a nominal resolution of ≈100 μm. The current outlined setup is unfortunately incompatible with Cu, which is an excellent reflector of red, and absorber of green wavelengths of light. Enhancing the quality of output data in SRAS involves maximising generation laser absorption and detection laser reflection.

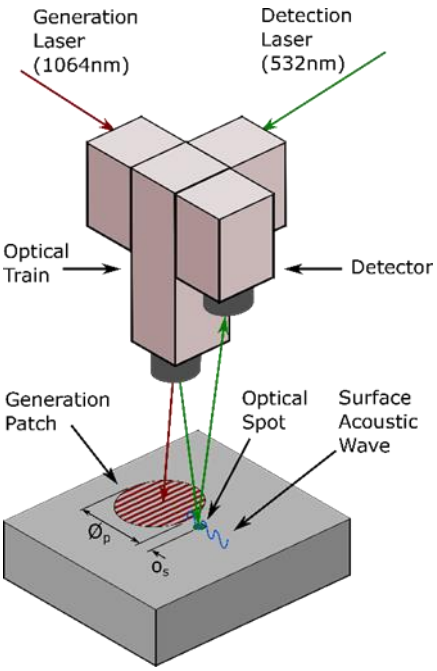


Figure 3.4: Schematic of the SRAS setup used in this thesis. A red (1064 nm) generation laser is imaged onto a sample to generate SAWs; the perturbations from which can be appraised using a green (532 nm) detection laser. Figure taken from Li et al. (2014) [204].

3.5. Post-EJP characterisation

3.5.1. Scanning electron microscopy

Scanning electron microscopy (SEM) was used for imaging EJP topography. This was undertaken using both a Philips XL-30 system (thermionic source), located at the NMRC, and a Hitachi HS-2000N system located at the Precision Manufacturing Centre, both at the University of Nottingham. SEM allows for imaging features across multiple length scales (mm to nm), with a significantly greater depth of field than OM techniques. Within a typical thermionic source SEM, electrons are accelerated from a tungsten source at potentials generally between 10-40 kV (10-20 kV used in this thesis), using an electron 'optical'

column; a typical SEM setup is shown in Figure 3.5, including an energy-dispersive X-ray (EDS) detector, described in section 3.7.1 (page 96).

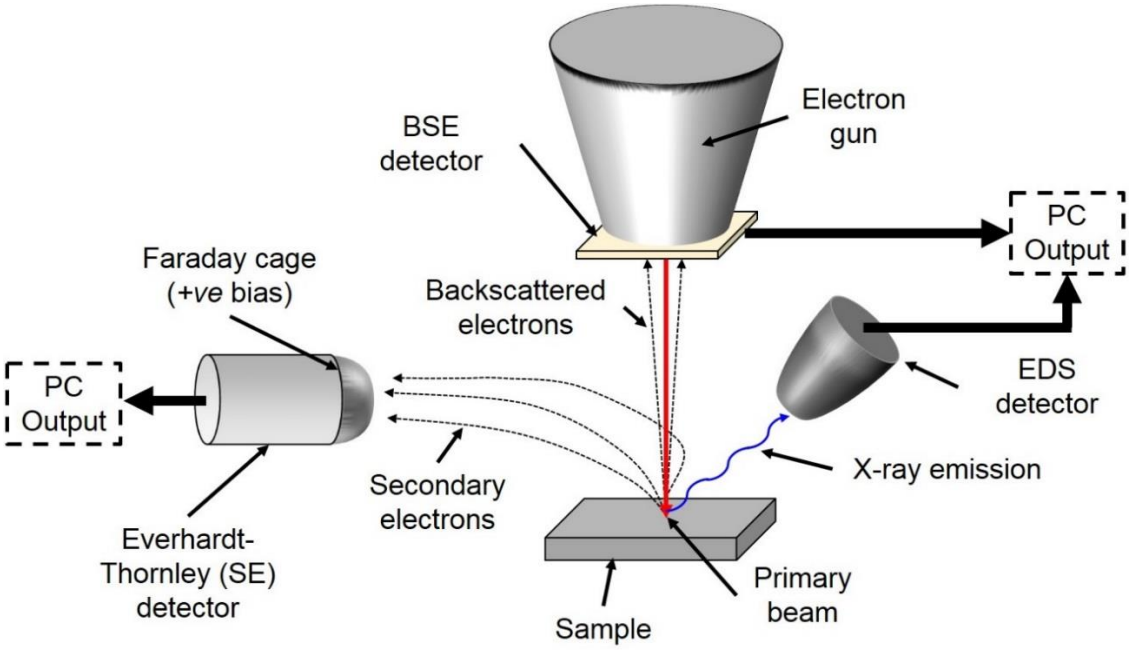


Figure 3.5: Schematic of a typical SEM. Low-energy secondary electrons (SEs) are detected with an Everhardt-Thornley detector, where SEs are deflected towards a scintillator through a Faraday cage held at small positive potential. Backscattered electrons (BSEs) are effectively reflected and detected normally to primary beam.

SEM imaging is achieved through the detection of electrons, which are differentiated by the nature of the interaction between the primary electron beam and the near-surface of the sample. The majority of imaging within this thesis was undertaken using secondary electrons (SEs). To generate a SE, a primary beam electron (of high energy) interacts with a sample atom, transferring some of this kinetic energy to a valence band (outer-shell) electron, which results in inelastic scattering. The emitted SE has a much lower energy relative to the primary beam, thus the escape-depth of SEs from metals is shallow (≤1.5 nm), considering the mean free path of an electron is intrinsically related to the kinetic energy. This makes SE microscopy highly surface

sensitive and ideal for topography appraisal. Images are constructed in the SEM through rastering the primary beam over a defined area, and magnification is achieved through decreasing this area.

The second type of electron imaging used in this thesis involves backscattered electrons (BSEs). In this interaction, primary beam electrons are elastically scattered by the atomic nuclei within the sample and are effectively reflected at high energy, normal to the sample surface. The high energy nature means the escape-depth is significantly greater than that of SEs, thus when imaging with BSEs, the noise level is generally increased, and the surface sensitivity is decreased, as a result of effective sub-surface imaging. In addition, large energies means BSEs cannot be deflected by an Everhardt-Thornley detector, therefore a dedicated detector has to be used, mounted onto the electron gun (*see* Figure 3.5). Primary beam interaction probability with atomic nuclei depends on the scattering cross-section of a given atom, intrinsically related to the atomic mass; therefore mass-contrast imaging is achievable using this technique, yielding information regarding the dispersion of different elements within a sample.

3.5.2. Focus-variation microscopy

Topography was characterised in this thesis using a focus-variation microscope (FVM) (Alicona G5 Infinitefocus, Manufacturing Metrology Team (MMT)) at the University of Nottingham, which is an optical measurement technique, for the purpose of topography quantification (deterministic form and microscale roughness) and for the generation of geometrically accurate three-dimensional surface renderings. FVM takes advantage of the shallow depth of field of visible wavelengths of light, whereby topographic height is measured through the

acquisition of a series of images at differing height (achieved by moving the objective along the optical axis). Through characterising the contrast level between neighbouring pixels, a focus value can be calculated. The *z* height at which this value is maximised is the detected height for a given planar (*x,y*) position. Large areas can be assessed by acquiring multiple fields of view through inputting a local coordinate system into the FVM; these are then automatically stitched together by the proprietary Alicona measurement software, allowing for rapid data collection [205]. A complementary focus stacked optical micrograph of the measured surface is also output in addition to the topographic dataset.

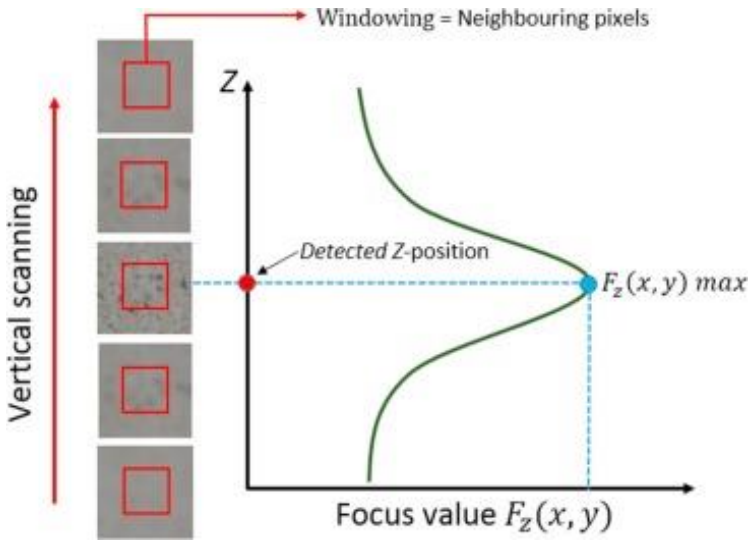


Figure 3.6: Working principle of FVM. Through vertical image acquisition, the focus value, $F_z(x,y)$, for a given planar coordinate can be maximised, through neighbouring pixel contrast. This becomes the detected topographic height. Taken from Moroni et al. (2018) [205].

The quality of the topographic dataset is correlated with the magnification of the objective lens used in the analysis (10, 20, 50, 100x objectives used in this thesis), whereby a higher magnification allows for topographic data to be returned at smaller length scales, increasing the surface resolution of the

resulting data. The applied objective depends on the type of information required, such as microscale topographic information (100x and 50x), or geometric information (10x or 20x). Applied objectives are stated throughout the thesis. Due to the maximisation of the focus value depending on neighbouring pixel contrast, pixel saturation needs to be avoided for successful analysis. This means very smooth surfaces, which are likely to reflect large amounts of the illumination light, are difficult to measure. Consequently, FVM is not capable of reliably measuring surfaces where the arithmetic mean amplitude is <50 nm. In addition, as an optical technique, unobstructed line-of-sight is required between the surface and the objective, which limits the measurement of high-angle slopes.

3.5.3. Coherence scanning interferometry

For the quantification of smaller scale surface structuring than is possible using the FVM system, a coherence scanning interferometry (CSI) system was used in this thesis (Zygo NewView 8300, MMT, University of Nottingham), using a 50x objective. CSI is also an optical technique and therefore reliant on line-of-sight, so that high-angle slopes are difficult to measure. In this system, white light is split into two paths: the reference light path and the experimental light path, which interacts with the same surface. CSI relies on the coherence between different wavelengths of light, where the coherence is the ability to interfere in an observable way. As the bandwidth of the light increases, the coherence length between different wavelengths decreases. An interference signal (or fringe) is only constructed when the path difference between the experimental and reference light paths is less than the coherence length. Therefore, white light is used in CSI, as the broadband nature makes the

coherence length, and subsequently the optical path difference, very small. The low coherence length increases the surface sensitivity of CSI, where the highest intensity central fringe (zero optical path difference, ZOPD) represents the topography probe. Through scanning the objective along the optical column and characterising the resulting interference fringes, the ZOPD point represents the *z* height of a given pixel.

3.5.4. Hardness testing

Hardness was appraised using a Buehler Vickers hardness tester (300 gf load for titanium oxides). The apparatus measures hardness by driving a diamond tipped indenter into the top surface of the interrogated material at a predetermined force. The dimensions of the generated indent are subsequently measured and the hardness value can be determined through the ratio of force to indent area. In all cases in this thesis, the hardness value of the processed surface was compared with unprocessed control samples.

3.6. Data analysis

3.6.1. MountainsMap

MountainsMap is surface analysis software that has been used throughout this thesis to aid the analysis of information and characterise topographies acquired using SEM (*see* section 3.5.1), FVM (*see* section 3.5.2, page 91) and CSI (*see* section 3.5.3, page 93). Surfaces were quantified according to the methodology outlined in section 3.6.1 (page 94) in accordance with ISO 25178. The datasets obtained using FVM and CSI can also be reconstructed digitally, this was done throughout the thesis to aid visualisation of the topographical differences

resulting from EJP, for the purpose of qualitative appraisal. The complementary optical micrograph (in the case of FVM), or independently acquired SEM micrographs can be applied over a reconstructed surface, to overlay the microscale texture to the feature form, depending on the intention of the figure. In addition, MountainsMap was used to colourise SEM micrographs throughout the thesis for the purpose of aiding the visualisation of topographic contrast.

3.6.2. ImageJ

ImageJ is an open source software package that is used throughout this thesis for image manipulation and characterising materials and surfaces before and after EJP. This software was used as a convenient method of measuring surface pore size after material removal and nodule size after material deposition in EJP. As most of these features are too small to be measured by optical metrological methods, this was achieved through the characterisation of SEM micrographs. The methodology for measuring pore surface areas from a raw micrograph is shown in Figure 3.7. The micrograph is input into ImageJ software, after which the scale is set (μm per pixel) manually based on the SEM scale bar. Through acquiring all micrographs at identical magnification, providing the specimens are in focus, the scale and the subsequent methodology are transferrable. A micrograph can be subjected to a binary threshold operation, where the porous recesses appear saturated black (*see* Figure 3.7c). This operation can mis-assign certain parts of the surface, based on the manual binary thresholding operation; this can be seen as isolated black pixels (*see* Figure 3.7d). To eliminate this noise, only pore sizes larger than 0.2 μm^2 were measured, from which pore size histograms, such as Figure 3.7e, can be constructed (noting the 0.2 μm^2 threshold).

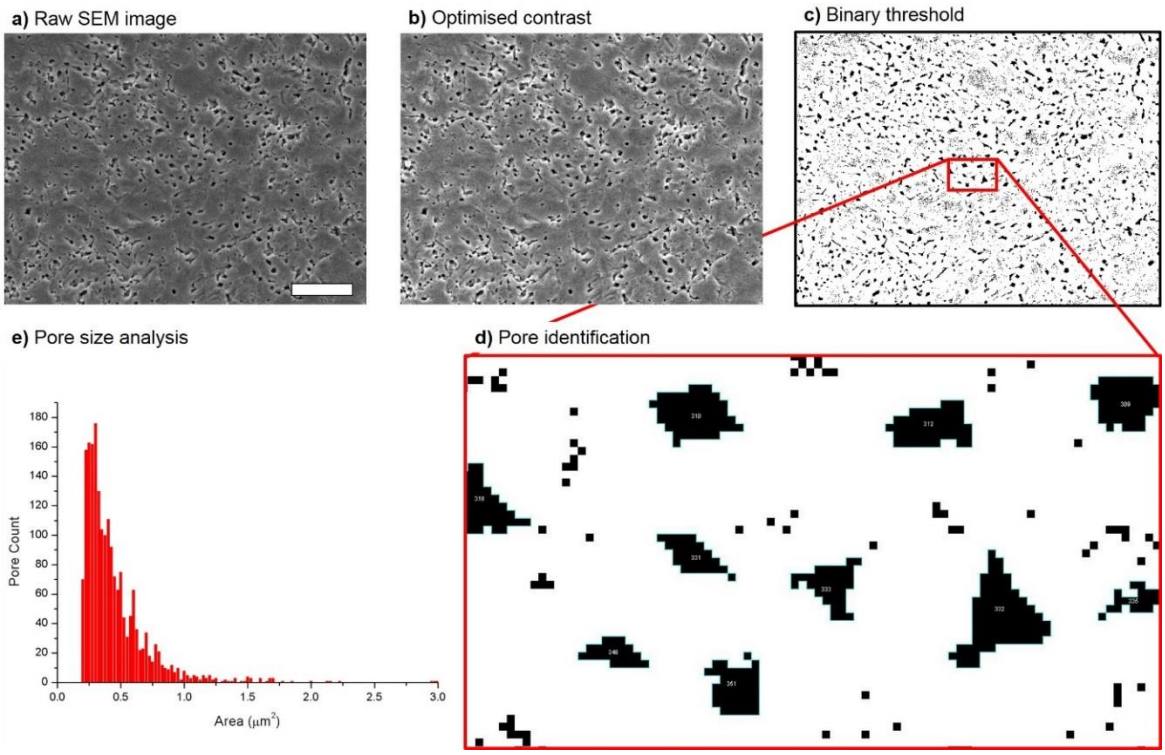


Figure 3.7: Pore size analysis. a) Micrograph uploaded to ImageJ, scale set (pixels per μm). b) Micrograph after automated brightness and contrast enhancement, and c) after binary thresholding. d) Noise (lone black pixels) is visible in the image, so for surface porosity measurement, only features >0.2 μm^2 are appraised, from which size histograms, e) are generated. SEM scale bar is 10 μm.

3.7. Chemical analysis

3.7.1. Energy dispersive X-ray spectroscopy

Energy dispersive X-ray spectroscopy (EDS) is a technique used throughout this thesis to appraise near-surface chemical composition, using an Oxford Instruments XMax 80 silicon drift X-ray detector (NMRC, University of Nottingham), with proprietary Inca analysis software. In EDS, a sample is bombarded with a high-energy electron beam, normally within an SEM, where in some cases the interaction of the primary beam with an atom will eject an electron from a core-shell. This generates an unstable intermediate species,

which is stabilised through the de-excitation of an outer-shell electron into the core-shell vacancy. There is an X-ray emission associated with this transition, the energy (wavelength) of which is characteristic for a given transition (such as *K* or *L*) within a given element. The coupling of SEM and EDS within the same system allows for imaging and chemical analysis to be performed simultaneously, thus information-rich local chemical data can be acquired.

The emitted X-rays are detected by a CCD detector (*see* Figure 3.5) and the wavelength is indexed against a database within the software to determine elemental presence. The relative peak intensities can be compared to yield information regarding the local chemical composition. X-rays have a large mean-free path in metals in comparison to electrons, thus EDS surface sensitivity is effectively limited by the penetration depth of the primary electron beam into the sample. This is typically <5 μm, although this is dependent on the beam energy and the scattering cross-section of the material (*see* section 3.5.1). This means that when X-rays are generated, they will escape the sample bulk and can therefore be detected, reducing the surface sensitivity.

3.7.2. Raman spectroscopy

Raman spectroscopy is a type of spectroscopy that characterises the interactions of light with materials. Raman scattering is dependent on the material symmetry and can consequently be predicted for a given structure based on predefined selection rules. Therefore bonding information can be obtained through this technique, thus when coupled with elemental analysis such as EDS, surface structure and chemistry can be appraised. In Raman spectroscopy, the sample surface is illuminated with a monochromatic laser, which for the most part interacts elastically with the surface chemistry. This

effect is called Rayleigh scattering (*see* Figure 3.8), and yields no information regarding the bonding interactions within the analysed surface. A very small fraction of the incident light is inelastically scattered, either losing or gaining energy (Stokes or anti-Stokes), through the interaction of the light with the molecular vibrations. If the energy change during scattering is large, this typically means strong chemical bonds are present in the sample, conversely the energy change is small when weak chemical bonds are present [206]. A typical Raman spectrum is composed of peaks corresponding to a different vibrational '*phonon*' mode. For a material to be Raman active, this mode must involve a change in molecular polarizability [202].

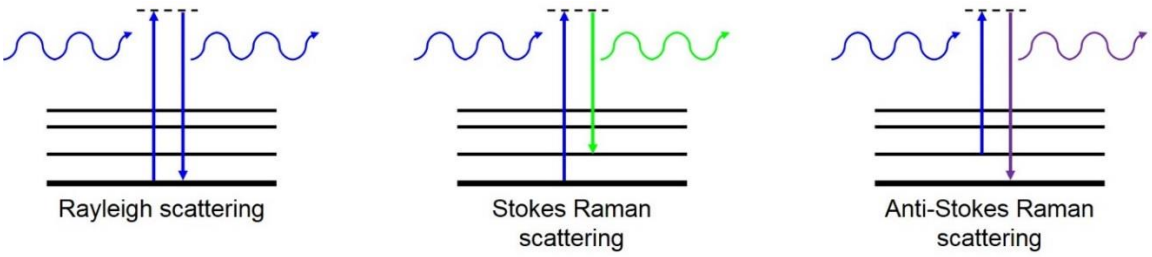


Figure 3.8: Schematic of discrete molecule-light interactions: elastic (Rayleigh) scattering, and inelastic Raman (Stokes) scattering, where energy is transferred to a higher molecular energy level, and Raman (anti-Stokes), where energy is transferred to a lower molecular energy level.

Raman vibrational spectra in this thesis were recorded on a Horiba–Jobin–Yvon LabRAM HR Raman microscope, with an excitation laser wave-length of 532 nm (power = ≈16 mW) and a 600 lines/mm grating using a Synapse CCD detector. The Raman shift was calibrated using the Rayleigh line and a Si (100) reference sample (520 cm^{-1} Si-Si peak). Typical spectra were acquired over 30–60 s, with 8 accumulations to reduce the signal to noise ratio.

3.7.3. Electrolyte conductivity and pH

Electrolyte conductivity was measured using a Mettler Toledo Seven2Go S3 conductivity meter. Conductivity is characterised by electrical resistance through the electrolyte, where the method is based on a Wheatstone bridge, which balances resistors of known resistance with the electrolyte. Calibration was achieved with a pre-supplied sachet of calibration solution (12.88 mS/cm). Electrolyte pH was characterised using a Hanna Instruments Checker Plus HI-98100 pH tester, where the probe has a proton sensitive bulb (glass doped with alkali metal ions) and a reference electrode. In this case, ion exchange occurs between the proton and the alkali metal, which generates an electrical potential. This potential is proportional to the acidity. Calibration was achieved using the pre-supplied sachets of calibration solution at pH 4, 7, 10.

3.7.4. Particle surface charge

Electric surface potential or zeta potential, ζ, is a useful method for evaluating the propensity of colloids to agglomerate in a given fluid. Ideally a high magnitude zeta potential (ζ >+25 mV or ζ <-25 mV) would create the optimum dispersion within an electrolyte, whereby large electrostatic repulsion can overcome Van der Waals attractive forces. The zeta potential of nanoparticle silica deposited in Chapter 7 was characterised using a Malvern Zetasizer Nano ZS across a range of electrolytes and acidities. This process utilises the laser Doppler electrophoresis technique. The movement of the silica particles in a given electrolyte within an electric field is assessed through measurement of small frequency shifts, Δf, in the scattered laser light (of a wavelength λ) according to Equation 13. From the frequency shift (θ), the velocity, v, and

therefore the magnitude of surface charge of the silica nanoparticles within a given solution can be appraised.

$$\Delta f = 2v \sin\frac{\theta}{2} / \lambda \qquad \textit{Equation 12}$$

3.8. Microscale topography quantification

Topographic datasets, acquired after EJP using FVM and CSI microscopy were analysed in MountainsMap software (*see* section 3.6.1), in order to analyse and compare surfaces and the effect of changing EJP parameters. All data presented in this thesis were appraised using three-dimensional areal measurements; these are significantly more robust than two-dimensional measurements due to the large increase in the analytical size of the dataset, and can also yield more characteristic topography information. The primary metric in this thesis is the areal amplitude indicator, *arithmetic mean surface height*, *Sa*. *Sa* considers the average height of the surface features, and is evaluated over an area, following Equation 13.

$$Sa = \frac{1}{A}\iint_A |z(x,y)|dxdy \qquad \textit{Equation 13}$$

Sa is employed within this thesis as a general comparative metric between similar EJ-processed surfaces, where a lower returned value represents low average surface amplitude, and consequently a smoother finish. *Sa* was only used to compare similar surfaces, as the metric does not consider the localisation of height differences, thus very different topographies may return similar amplitude values. Microscale roughness, *Sa*, was acquired from EJP

surfaces after separation from the form and the waviness according to ISO 25178, following the steps outlined in Figure 3.9.

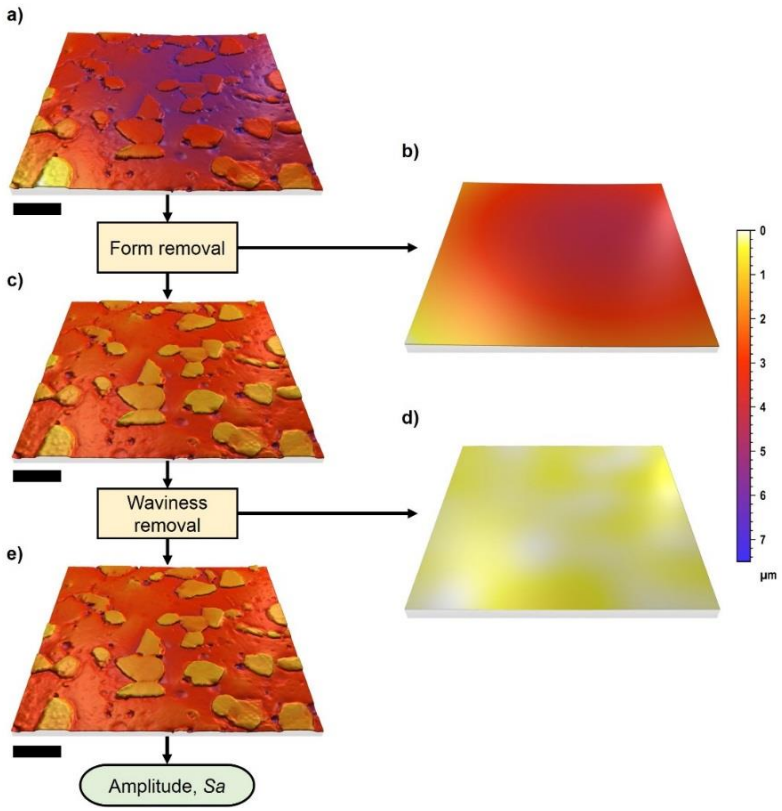


Figure 3.9: FVM reconstructions (100x objective) showing a) EJ-processed surface topography. Through application of a 2nd order polynomial filter, b) form is subtracted to give surface c). Roughness is separated from d) waviness using a cut-off index, resulting in roughness surface, e) to appraise amplitude, Sa. Scale bars 25 µm.

Here, the raw topography (*see* Figure 3.9a) was input into MountainsMap, after which the geometric form (resulting from EJ-processing) was removed through application of a 2nd order polynomial *low-pass* filter (applied in the software, Figure 3.9b). The waviness was removed from this surface through the application of a cut-off *high-pass* filter to separate the roughness surface (*see* Figure 3.9e), from which the microscale amplitude can be taken. These steps were repeated by the software; the exact cut-off filter used for each dataset is listed where such data is presented throughout the thesis.

Height localisation on the roughness surfaces (after the aforementioned filtering steps) was appraised using the volume parameters: *Vmp*, *Vmc*, Vvc, and *Vvv*, shown in Figure 3.10. Peak material volume (*Vmp*) was measured from the top 10% of the surface height; valley void volume (*Vvv*) was measured as the vacant void-space of the bottom 20% of the surface height; core material volume (*Vmc*) was measured as the bulk material volume between the top 10% and the bottom 20% of the surface height, and core void volume (*Vvc*) as the void-space between the same height values. These parameters simplify the identification of height localisation, such as large areas of equal depth, or small protruding peaks.

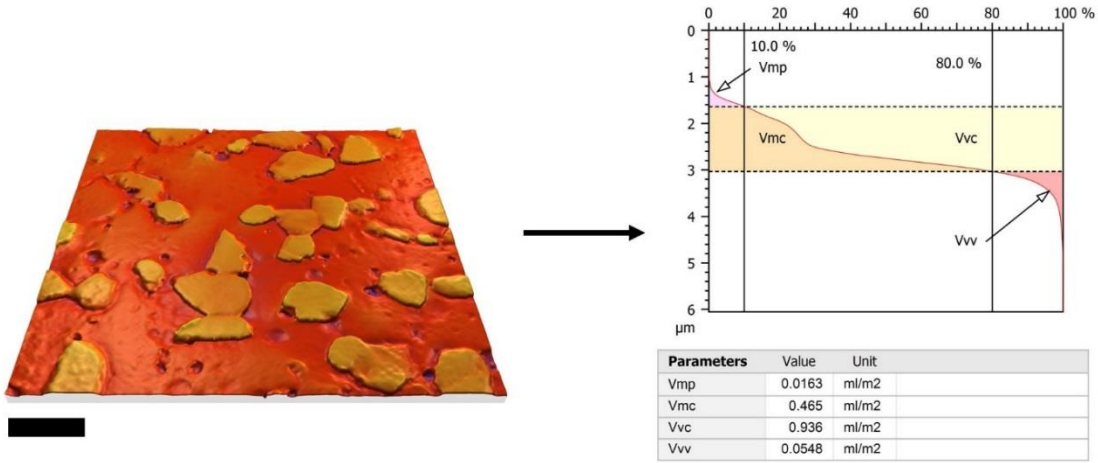


Figure 3.10: From filtered surfaces, volume parameters can be extracted, considering peak material defined as the top 10% of surface height and valley material defined as bottom 20%. Scale bar 25 µm.

In some cases, such as the characterisation of orientation-dependent surfaces, the gradient and the direction of the gradient of the topography was analysed. This was performed on CSI datasets by Rong Su (MMT, University of Nottingham). Provided accurate topography measurement, the gradient vector

of the surface can be obtained from the directional derivatives of the height map by following Equation 14,

$$grad(h) = \begin{bmatrix} g_x \\ g_y \end{bmatrix} = \begin{bmatrix} \delta h/\delta x \\ \delta h/\delta y \end{bmatrix}, \qquad \textit{Equation 14}$$

where *h* is the height function of a surface, g_x and g_y are the partial derivatives of the height function in *x* and *y* directions, respectively. The direction of the gradient, calculated following Equation 15

$$\theta = \tan^{-1}\left(\frac{g_x}{g_y}\right), \qquad \textit{Equation 15}$$

is the orientation in which the gradient has the largest value, i.e. the magnitude of the gradient, calculated following Equation 16.

$$|\mathrm{grad}(h)| = \sqrt{{g_x}^2 + {g_y}^2}. \qquad \textit{Equation 16}$$

In this work, the calculation of the gradient is done by numerically convolving the Sobel kernel [207] with the height map of the surface. The gradient direction, θ, ranges from −180° to 180° measured anticlockwise from the positive *x*-axis. Then the two-dimensional map of the surface slope angle is calculated from the magnitude of the gradient as, $\tan^{-1}(|grad_h|)$. In this thesis, these calculations were undertaken in Matlab, for the purpose of correlating topography with characteristic orientation-specific dissolution.

3.9. Removal and form characterisation

Material removal in anodic dissolution is governed by Faraday's laws of electrolysis, summarised in section 2.1, and is dependent on the charge

transferred, Q, and the electrochemical equivalent (ECE) of the sample. The literature survey indicated that multiple valence states are achievable in transition metals, and material removal in ECM processes can be enhanced by wash-away of electrochemically inert particles, such that the concept of current efficiency (which assumes dissolution into one valence state) commonly applied within ECM research, cannot reliably provide information regarding the process electrochemistry. To counter this, charge specific mass removal, M_σ, was measured as a mass removal per unit charge. This was analysed using FVM datasets (20x objective) of pit or striation features at varying current densities into a specimen of the sample material. Volume data was extracted in MountainsMap software, where the mass removed in a discrete machining process is the product of the removal volume, V and the material density, ρ. M_σ can subsequently be calculated through division by Q. In this thesis, M_σ was compared with the ECE for different valence states depending on the material electrochemistry; whenever ECE is displayed graphically, the assumed valence state is also listed.

For alloys, a weighted ECE is necessary to compare with M_σ. This is complicated by material compositions in alloys, which are generally stated as a range. Where material removal is characterised in alloys, ECE is calculated as an upper and lower bound; considering the upper bound, the elemental composition is assumed to be the highest value of the range, with the balancing element reducing to make up the percentage. Conversely, this is reversed considering the lower bound.

Dimensional accuracy of EJ-processed features was appraised through multiple performance metrics. Considering a two-dimensional profile acquired

from a striation (*see* Figure 3.11), the maximum cut width (kerf) can be measured and consequently, through consideration of the nozzle diameter, the overcut, *O*, can be determined. *O* is a commonly applied metric in EJP literature, used for characterisation of dimensional accuracy and precision. Maximum machining depth, d_M, is simply the deepest point along a profile from a levelled surface, and full width at half maximum (FWHM) is the profile width at 0.5 d_M. The profile gradient can be characterised when the FWHM is divided by kerf.

$$O = \frac{kerf}{Nozzle\ I.D.}$$

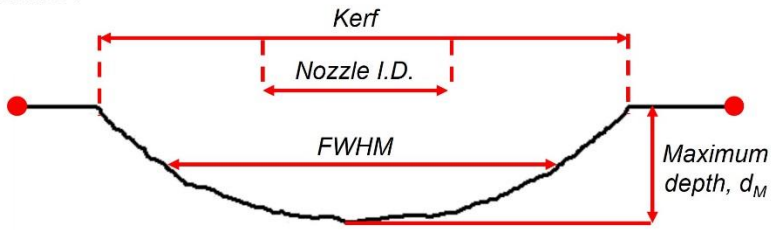


Figure 3.11: Performance metrics for extracted profiles, showing the derivation of overcut, O, and full width and half maximum/kerf.

EJ-processed area, A_m, determines the extent to which the original surface has been removed from a defined sample area. This metric was analysed using MountainsMap software, wherein a levelled surface was set from an extracted sampling area, A_s, of controlled dimensions. In this thesis, A_s was kept constant ($l = 1\ mm,\ w = 1.5\ mm$). The surface was then subjected to a binary height threshold (*see* Figure 3.12b), where only the levelled top surface is considered. A_m is subsequently calculated as the sampling area minus the sum of the un-machined areas of the levelled top surface; increasing A_m means a larger proportion of the original surface has been removed, within the predefined window and vice-versa.

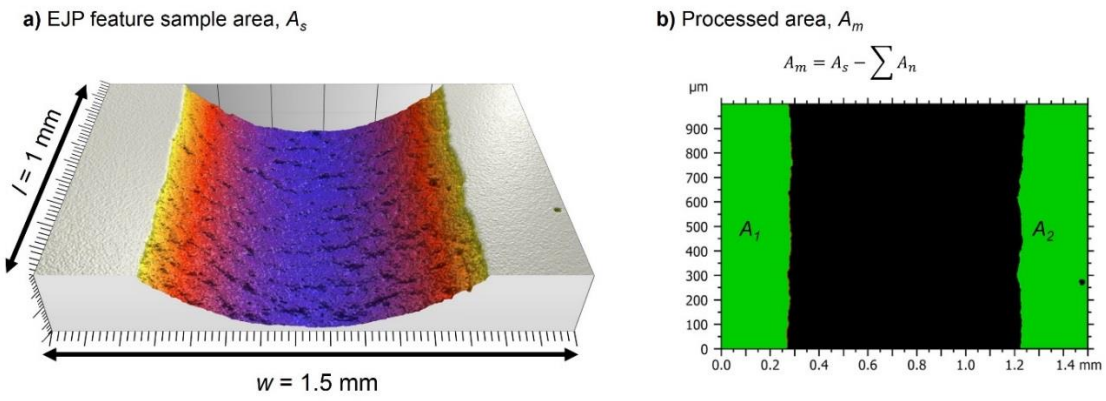


Figure 3.12: To calculate jet-processed area, a sample window of controlled dimensions (l = 1 mm, w = 1.5 mm) was extracted from a levelled source surface, shown in a). A binary height threshold was set from this levelled surface, b) where the processed area is the sample area minus the sum of the un-machined, levelled top surface.

Dimensional accuracy was further appraised with two metrics regarding both the edge definition, dev_c, and the profile definition dev_p. To characterise edge definition, the edge contour was extracted from the length of the sample area, to which a best-fit line was applied. The resulting deviation area could then be appraised across the controlled sample length (1 mm) for each electrolyte tested, a greater deviation area is indicative of reduced cut edge definition (*see* Figure 3.13a). Profile definition was appraised through applying a best-fit arc to an extracted profile, from the opposing edges of the kerf. The total deviation between the profile and the best-fit arc was measured, considering the total profile area, A_p, ensuring measurement fidelity. This metric is then expressed as a percentage of A_p. Without considering profile area, deeper cuts yield a greater total deviation (*see* Figure 3.13b), not representative of the actual dimensional accuracy.

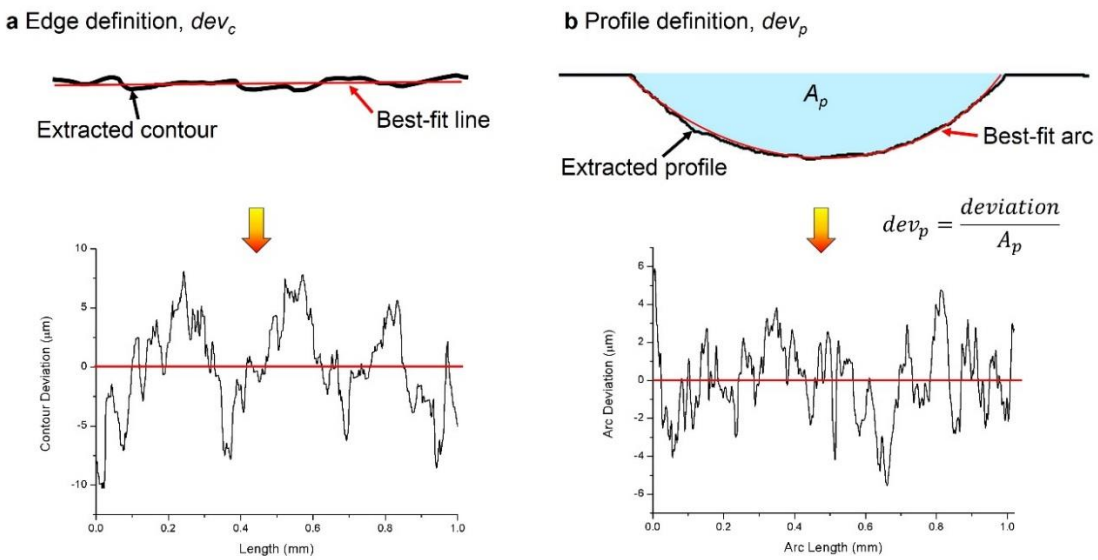


Figure 3.13: a) Edge definition is calculated from the deviation of the edge contour from the best fit line across the sample length (1 mm). b) Profile definition is calculated through considering the deviation from a best fit arc and division by the total profile area.

4. Characterisation of microstructure-dependent topography in EJP

4.1. Introduction

The literature review (*see* section 2.2.4) indicated that surface topographies resulting from electrochemical techniques are influenced by microstructural inhomogeneity within conventional processing regimes, however this has been the subject of limited investigation in EJP. This is a concern considering the potential application of the technique towards high-value manufacturing, wherein complex material systems feature increasing usage, for example those produced by additive manufacturing techniques. Such workpieces could exploit functional grading, whereby the microstructure may change spatially throughout the part, therefore knowledge regarding material-EJP interactions across broad operating regimes is valuable to the practitioner. This is especially pertinent considering the role of surface topography in dictating the lifespan of a part in service, affecting safety factors such as fatigue life [72].

The literature review showed that the topographies of electrochemically processed surfaces could be largely determined by the orientations of the underlying grains within parameters achievable using EJP (*see* section 2.2.3.2, page 39). Considering: the automatable nature of the technique, the selectivity, as well as execution under ambient conditions, it is proposed that EJP could be used to generate orientation-dependent topographies over predetermined surface areas of polycrystalline materials. Such topographies, if analysed appropriately, could yield valuable information pertaining to the underlying crystallography of a materials system. In materials, the microstructure

determines many of the properties that are unique to a given system [208], whereby the absolute and relative orientation of grains has a profound impact on material performance, affecting factors such as fatigue [209], ultimate tensile strength [210] and creep [211], even in single crystal systems. Therefore, information in this regard is highly prized by both the materials scientist and the engineer as they serve to verify materials processing technologies. This understanding is especially important, particularly with the emergence of new manufacturing processes, seeking to further exploit orientation-specific material properties [212].

At present, the range of tools for determining the texture and orientation of material microstructure is limited. Orientation characterisation is commonly undertaken through diffraction-based techniques, such as electron back-scatter diffraction (EBSD) [213, 214] and X-ray diffraction [215]. The former relies on electron diffraction and can characterise space group symmetries in an unambiguous manner at high spatial resolution (<20 nm) [216]. However, their industrial application is limited due the nature of analysis, and the use of electrons requiring high-vacuum equipment. In addition, sample preparation time and cost for EBSD and TEM specimens is often prohibitive and characterisation efficacy is dependent upon specimen quality. Large area analyses (mm scale) are impractical using TEM and encumbered by significant processing times in EBSD, despite increasing computational and processing efficiency. In light of this, creation of novel characterisation processes have the potential to revolutionise microstructural interrogation of materials and therefore represent valuable contributions to the field. To contribute towards a solution to

this efficiency problem, EJP could be applied to reveal microstructural detail that could be characterised by interpreting the topography.

4.2. Microstructure-topography dependence in Cu

4.2.1. Effect of material precondition on the microstructure

Samples were prepared as per the experimental section 3.1.1. A sample from each precondition observed in cross-section (transverse direction normal to observer, *see* Figure 4.1), to view the microstructure through which the EJP features would be machined. This was achieved through conventional chemical etching in acidified (HCl) ferric chloride solution, where optical micrographs of the resulting microstructures are shown in Figure 4.1. Consistent with well-understood annealing theory, grain size is observed to have significantly increased in the pre-annealed set (right column), with a large number of parallel growths, likely to be annealing twins. In addition, expected grain refinement upon cold-rolling (Hall-Petch hardening) is observed in both non-annealed and pre-annealed sample sets. Deformation of the existing grains is clearly visible in the prior-annealed sample set, considering the bowing of the grains that are likely to have been parallel growths (26% reduction, *see* Figure 4.1), and the severe deformation, likely slipping, upon further rolling thickness reduction (52% reduction, *see* Figure 4.1).

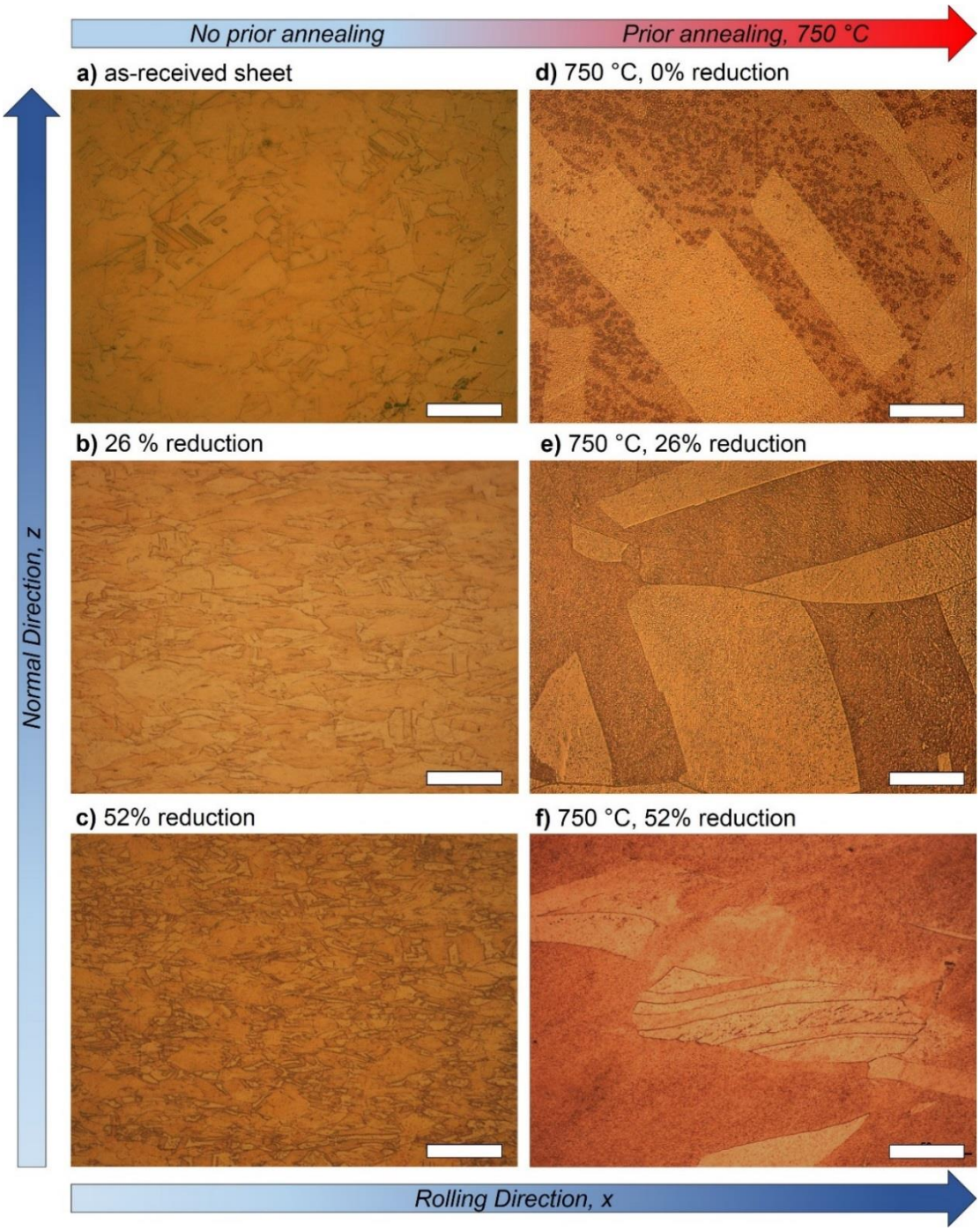


Figure 4.1: Optical micrographs of chemically etched microstructural preconditions investigated: a) as-received, b) 26% reduction, c) 52% reduction, d) 750 °C, e) 750 °C, 26% reduction and f) 750 °C, 52% reduction. Expected grain size increases with annealing and cold-rolling grain-refinement are observed. Scale bars 50 µm.

It is acknowledged that the effective surface-defining current density will be reduced from the supplied current density at the nozzle as the jet translates. In addition, material removal, based on total charge transfer, should be controlled

in order to achieve a depth at which the entirety of the original, polished surface is removed. To this end, charge-specific removal was characterised (according to the routine outlined in the methodology) in the two different electrolytes for Cu, Al and Ni, shown in Figure 4.2. For Cu and Ni, processing with NaCl is shown to enhance material removal, which is consistent with the literature, whereas no difference is shown for Al (*see* Figure 4.2b). Al appears to dissolve into the Al (III) oxidation state regardless of current density, despite reports of some dissolution through Al (I) species [217]. For Cu and Ni, processed using $NaNO_3$, increasing current density increases the charge-specific removal [44]. For Cu, this was determined to be the result of a gradual shift in the valence state from Cu^{2+} to Cu^{1+} as current density is increased. For Cu processed with NaCl, the apparent removal efficiency is shown to decrease inversely with current density. This may be the result of the reducing efficiency of dissolution waste removal as the rate of generation increases. The collected data was used to inform processing strategies to fix the removal depth across large areas to ≈60 µm. To this end, considering a fixed translation velocity (v_h = 0.5 mm/s), surfaces were processed at 50 A/cm^2 for Al 6080 and 30 A/cm^2 for Ni 201 in NaCl. Consistency of depth-matched surfaces are shown for these materials, whereby maximum removal depth is shown not to exceed 60 µm, aside from focussed trenches adjacent to non-conductive resin. After EJP, samples were cleaned in deionised water in an ultrasonic bath and characterised without further surface preparation.

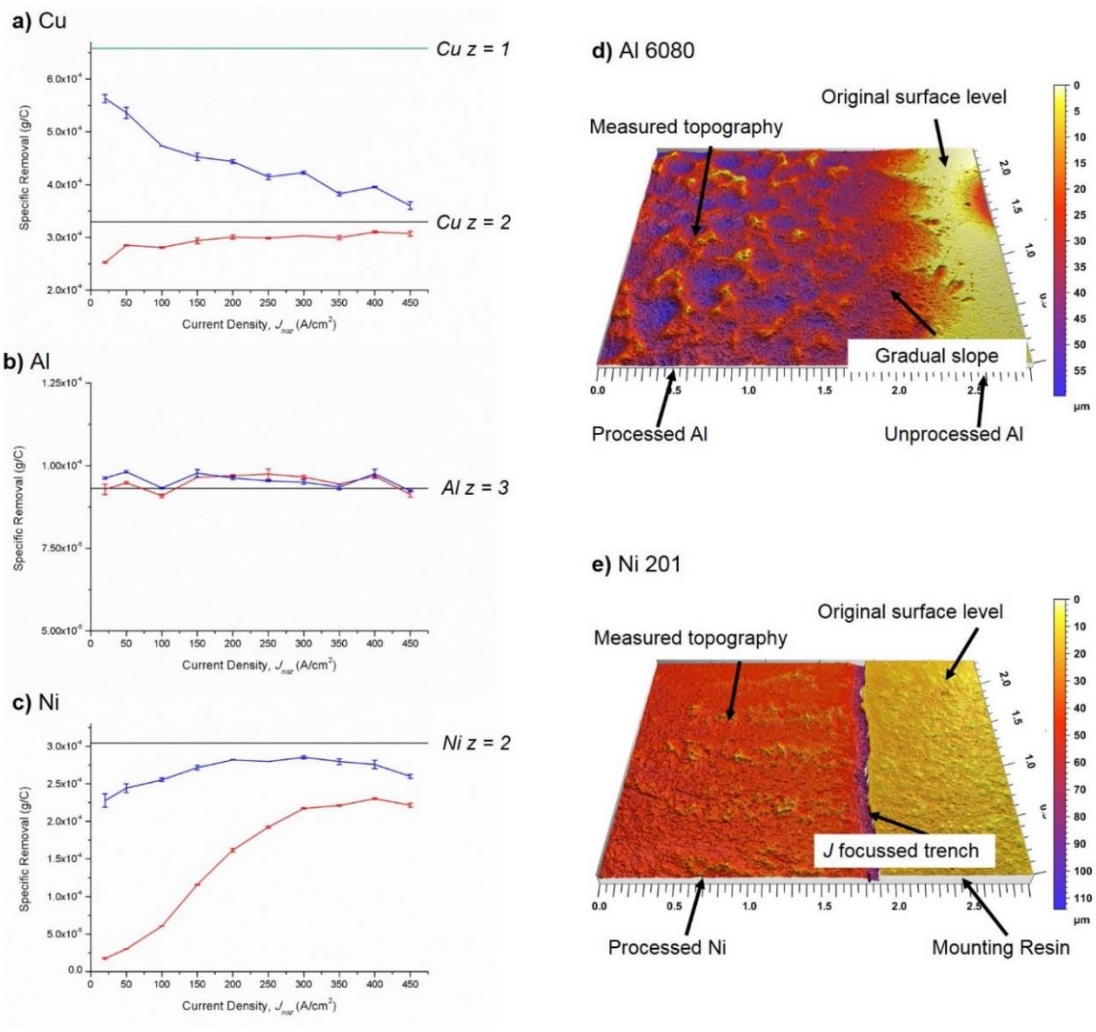


Figure 4.2: Charge-specific removal: a) Cu, b) Al, and c) Ni in $NaNO_3$ (red) and NaCl (blue). Horizontal bars represent valence states listed adjacent. Generally, processing with NaCl increases material removal, except for Al, appearing to dissolve to Al (III), regardless of current density. Reconstructed surfaces showing material removal depth in Al 6080 and Ni 201, from the processed area to the unprocessed area of each surface, from which the output orientation texture maps were generated. Where processing area is terminated by resin, translation of the jet across the resin focusses removal at the interface, generating trench features <115 μm in depth. Removal depth, outside of trenches, is <60 μm for Ni. Where the area is terminated by the toolpath, such as for Al 6080, the jet movement creates a gradual tapering effect. In this case, the maximum depth of the surface is approximately 60 μm for Al.

4.2.2. Topography observations

Cu sheet was prepared as described in methodology, differentiated into two sample sets, indicating the thermal condition of the material prior to the cold-rolling treatment. EJP pitting operations were subsequently undertaken using $NaNO_3$ (2.3 M) across a broad range of current densities (20-450 A/cm^2, 4 s dwell), outlined in Appendix 4. The most notable difference with regards to the two aforementioned sample sets is the apparent brightness of the processed surfaces, shown in Figure 4.3a and b (J_{noz} = 20 A/cm^2, no prior cold-rolling). The non-annealed pit (Figure 4.3a) appears dull and non-reflective in comparison to the bright prior-annealed pit (Figure 4.3b), from which the microscale topography following the EJP treatment can be considered. Bright surfaces are a notable observation, as these are not consistent with the norm expected from EJP at low current densities.

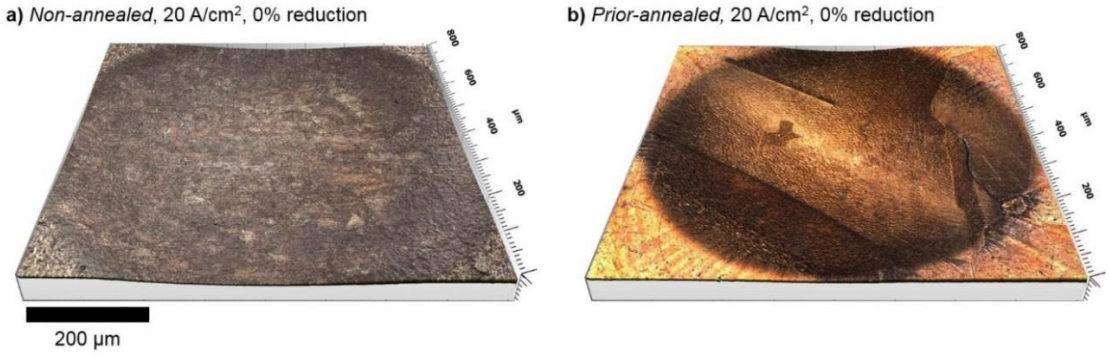


Figure 4.3: Surface reconstructions overlaid with optical micrographs of pits processed using identical parameters (20 A/cm^2, 4 s). a) Non-annealed pit is optically dull, b) prior-annealed pits are more reflective.

This qualitative difference in brightness between the sample sets with different thermal histories appears to occur regardless of the amount of post-annealing cold-work, within the ranges tested (<52% reduction). As the significant difference in apparent reflectivity is indicative of a difference in microscale

topography, the samples were observed using secondary electron (SE) microscopy, shown in Figure 4.4, where each surface has been processed with identical processing parameters (50 A/cm^2, 4 s). For the samples not subject to annealing before cold-rolling and EJP (Figure 4.4a, c), typical surfaces appear highly porous, where the pores generally appear cubic in morphology, reflecting the crystal symmetry of Cu. Crystallographic pitting is not unexpected from low-rate anodic dissolution, and has been investigated substantially in Cu. Pore size appears to be reduced slightly for the sample subjected to the greatest rolling treatment (52 % thickness reduction), shown in Figure 4.4c. For the samples annealed at 750 °C prior to EJP (*see* Figure 4.4b, d), surfaces appear to have negligible porosity, and highly ordered periodic step structuring is revealed, again indicative of the symmetry of the discrete crystallite. Upon cold-rolling (Figure 4.4d), the exposed lattice appears less ordered, and band-type features can be observed, leading to a discontinuous resulting topography.

Highly porous topographies in the non-annealed sample set, compared with the annealed samples, are directly responsible for the difference in apparent reflectivity as light is scattered in multiple directions by microscale pores. This compares with pore-free directionally-aligned step structures, caused by prior annealing, which reflect incident light to the observer in a more efficient manner.

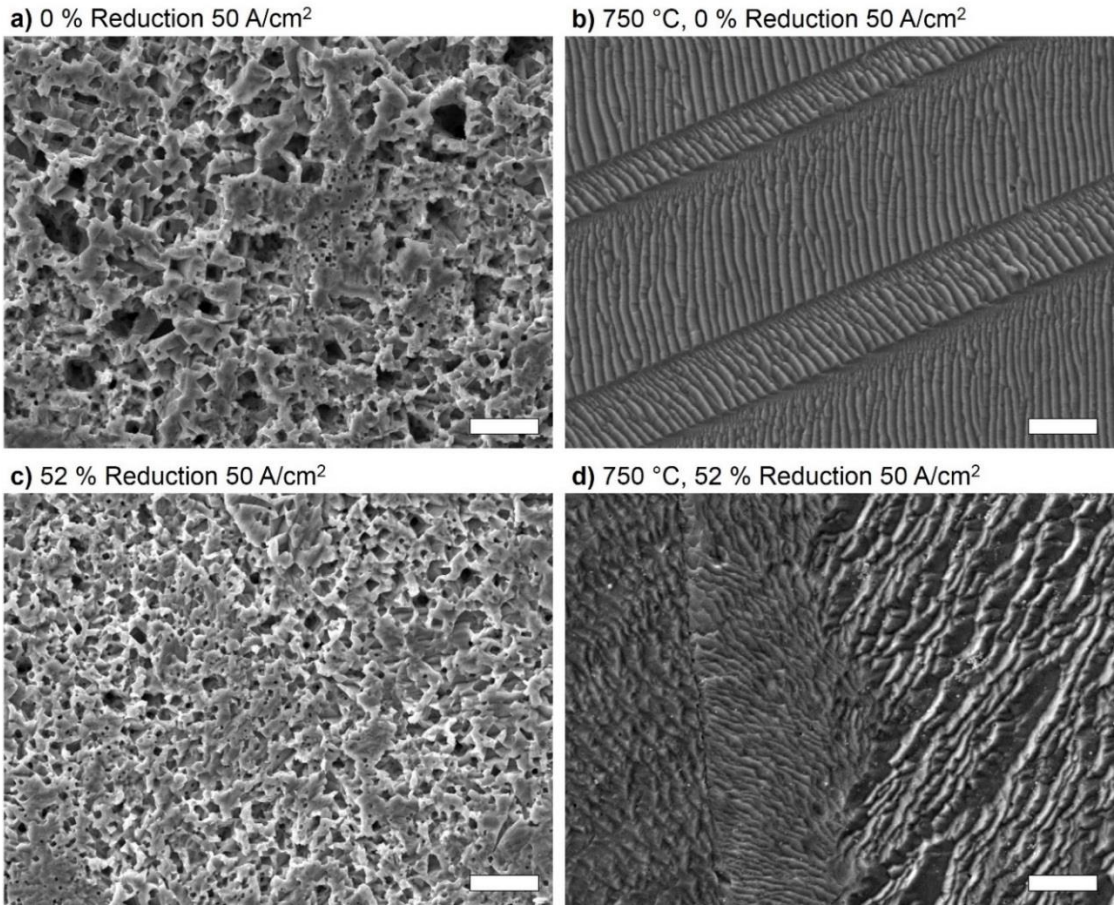


Figure 4.4: SE micrographs of identically processed surfaces (50 A/cm^2, 4 s), showing topographical differences between samples without annealing (left column) and with annealing (right column). a) In non-annealed, un-worked specimens (feedstock precondition), numerous large surface pores are observed. b) Prior annealing all but eliminates porosity, revealing highly ordered structuring, consistent with underlying crystallite symmetry. c) Cold-rolling (52% reduction) without prior annealing again results in a porous surface, although porosity appears finer than the as-received precondition. d) For prior-annealed Cu subjected to cold-rolling, the exposed lattice is less ordered, and banding is visible within single-grain areas. Scale bars 10 µm.

Pore sizes of the non-annealed samples were appraised through image processing of SE micrographs, at equivalent magnification, across a range of current densities (20, 50, 100, 300 A/cm^2), according to the routine outlined in the methodology, and the data are shown in the histograms in Figure 4.5. Pore sizes were not appraised for the pre-annealed samples, as the apparent density of discrete pores was considered too low for meaningful analysis.

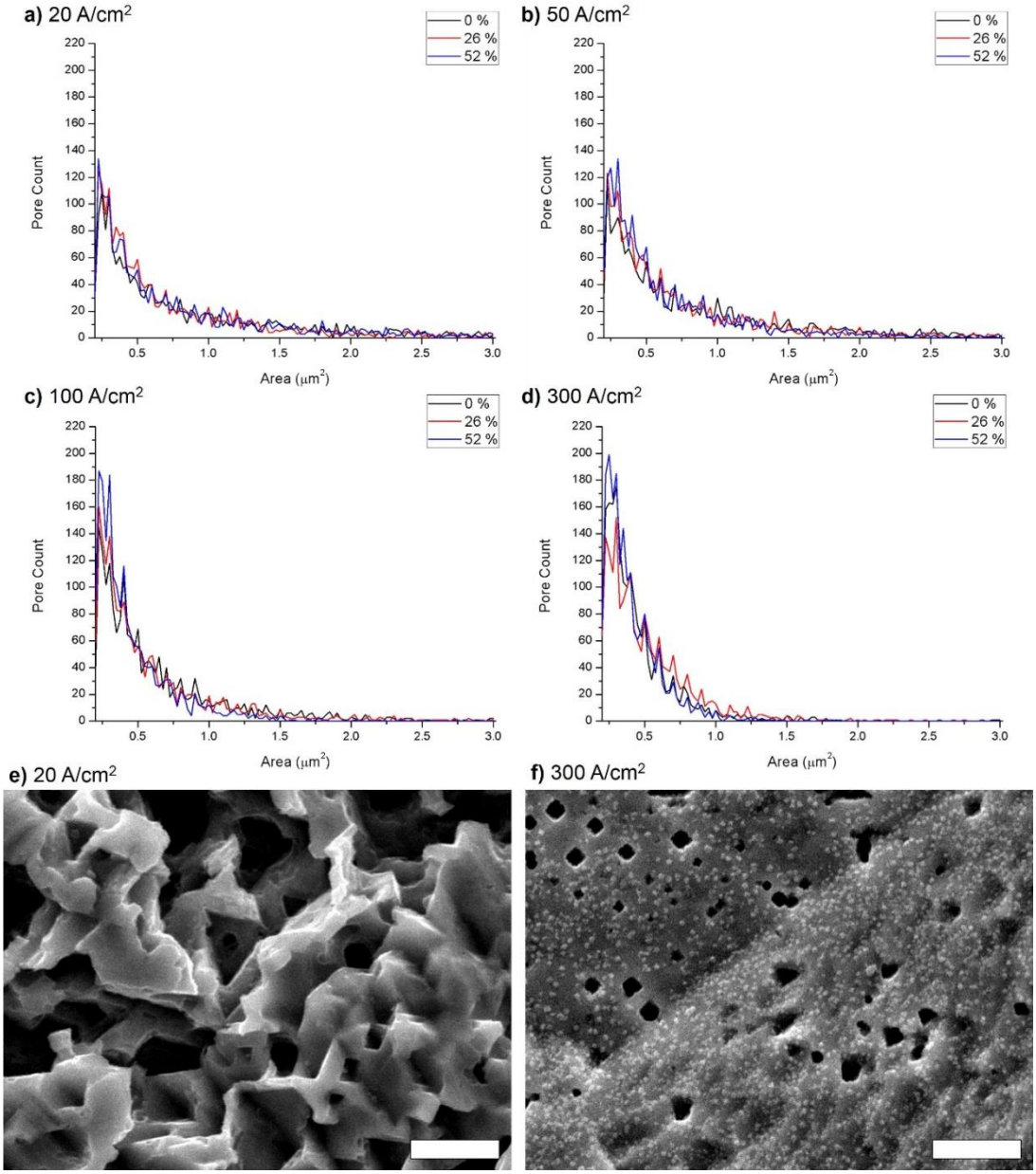


Figure 4.5: a-d) Pore size (<3 μm^2) in non-annealed samples is inversely dependent on applied current density. In addition, pore size decreases with rolling treatment. e) SE micrographs showing large crystallographic pores across the surface (20 A/cm^2), f) while increasing current density decreases the pore sizes, the morphology is still dependent on underlying crystallography. SEM scale bars are 2 μm.

Pore size is evidently strongly influenced by the current density, with the histogram range narrowing as the current density is increased, however the pore morphology is defined by the crystallography of the underlying grain (*see* Figure 4.5e), apparently independent of the applied current density. This is

interesting, as while orientation-defined pitting has been reported extensively at low current densities [113], it is unusual to observe anisotropic microstructure-defined pitting geometries at high current densities (*see* Figure 4.5f) and associated large anodic potentials. In addition, at all current densities, a slight reduction in the size of the pores with rolling treatment can be seen.

Specifically, the size of the largest pores (>3 μm^2), appears to be acutely dependent on the rolling treatment at low current density, following the same trend as the smaller pores (*see* Figure 4.6). The amount of pores >3 μm^2, out of the total sample measured (2000), can be expressed as a percentage. For the data acquired in this study, at the lowest current density tested (20 A/cm^2), 21.45 % of the total pores were >3 μm^2. This decreased to 10.10 % at 50 A/cm^2, and further decreased to 2.15 % at 100 A/cm^2. At the highest mean current density tested (300 A/cm^2), only 0.25 % of the measured pores were greater than 3 μm^2. Information in this regard is important, as high surface porosity is considered undesirable for some mechanical applications, as even small flaws can act as localised stress concentrators, thus affecting the service life of a component.

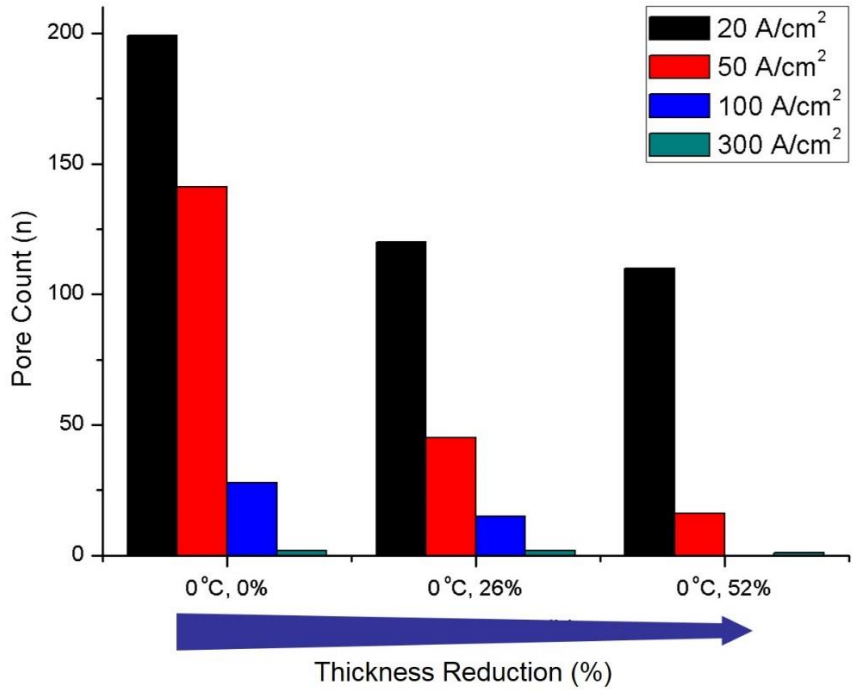


Figure 4.6: Pore dependence (>3 μm^2) on current density and material precondition. Greater reductions reduce the frequency of pores >3 μm^2. Sample size 2000 pores.

Surface amplitude (areal roughness, *Sa*) was appraised for the basal areas of the processed pit features of all material preconditions in an attempt to quantify the evident topographic differences (following the routine outlined in the methodology section), where the data is presented in Figure 4.7. A significant difference in amplitude between the non-annealed (*see* Figure 4.7a) and prior-annealed (*see* Figure 4.7b) sample sets is determinable at low current densities (<100 A/cm^2). In this case, the sample sets subjected to prior annealing have lower surface amplitudes; at J_{noz} = 20 A/cm^2 and 0% reduction, the non-annealed workpiece has a roughness of 0.384 μm (σ = 9.8%), significantly greater than the roughness of the prior-annealed workpiece at identical parameters (0.089 μm, σ = 11.5%). This observation is consistent with the understanding that increasing the level of order within a crystalline lattice, such

as through annealing, reduces the amplitude of the surface for a given set of EJP processing conditions at low current density.

For the non-annealed series (*see* Figure 4.7a), where the feedstock sheet was rolled as-received, the roughness appears to follow a similar (power-law) trend described in a range of materials, such as austenitic grades of stainless steel [24] and Ni-superalloys [2]. Interestingly, no quantifiable difference in roughness can be seen with regards to rolling treatment, at the majority of the current densities tested, even though SE micrographs suggest a decrease in the pore size with rolling reduction. This is understood to be partially a result of the apparatus measurement limits (*see* section 3.5.2). On the contrary, for the series annealed prior to cold-rolling, a different trend is followed for most preconditions (*see* Figure 4.7b). For the lowest reduction conditions (0% reduction), the roughness – current density relationship is decoupled from the expected power-law; instead appearing more linear (prior-annealed, R^2 = 0.80; non-annealed, R^2 = 0.30). The decrease in the dependency of surface roughness on current density, can also be shown through the comparison between the greatest *Sa* (low current density) and the smallest *Sa* (high current density). Expressed as a percentage, the smallest amplitude is a relatively large proportion of the greatest amplitude for the 0% and 26% reductions (54% and 56%, respectively). This proportion decreases significantly for the 52% reduced precondition (21%), which is comparable to the values observed in the non-annealed precondition at 0% reduction (22%). In addition, an incremental difference in roughness with rolling treatment can be seen across the range between 100-300 A/cm^2, increasing in amplitude as the workpiece becomes more deformed and more banding is observed. No difference in roughness was

observed for current densities greater than 300 A/cm^2, beyond the range of error, likely to be a result of increasing efficacy of the electropolishing.

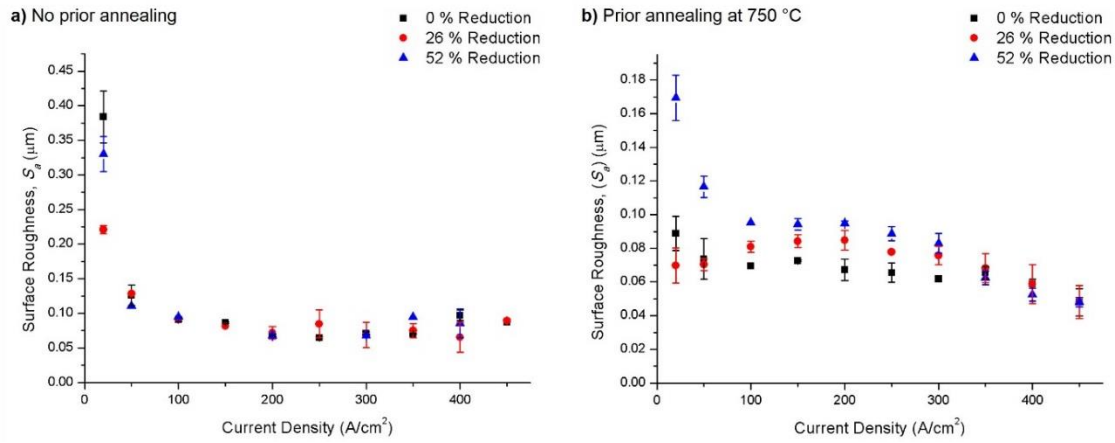


Figure 4.7: Roughness, Sa, acquired from central pit areas. In experiments where the feedstock was rolled without prior annealing, a), no difference was observed in roughness after EJP, within these experimental ranges, however for the samples annealed at 750 °C prior to cold-rolling and EJP, b), roughness generally increases with rolling treatment <300 A/cm^2. Error bars are the standard deviation from the mean.

While the surface roughness may not appear to vary greatly in absolute terms depending on the precondition, the topographic morphologies for both sample sets appear to be different after prior rolling. This shows that many of the surface discontinuities, such as sub-micron diameter pores, are beyond the detection limit of the FV microscope (≥1.75 µm using 100x objective), and approaching the physical diffraction limit of visible wavelengths of light. In addition, while it can be seen that all surfaces have superficially similar roughness values, the surfaces appear different, depending on the material precondition, therefore highlighting the limitations of arithmetic mean roughness measurements.

4.2.3. Topography generation mechanisms

The most dramatic microscale topographical difference in EJ-processed Cu is observable between the two different thermal histories presented in this study,

shown in Figure 4.4. Where the material has not been subjected to prior annealing, porous surfaces are always observed and although the size of these surface defects is largely controlled by the current density, increasing this parameter (up to 450 A/cm^2) does not completely eliminate their formation, even in a static processing scenario. The relationship between pore size and current density is likely caused by current equalization across larger surface areas, caused by increased diffusion layer thickness [76]. Therefore, a mechanism through which the size of surface pores can be controlled, independent of material precondition, through adjustments to the processing parameters, can be proposed. This could be applied to the EJM of inhomogeneous microstructural systems, although dynamic processing strategies could only be possible with intimate knowledge of the localised material precondition and resulting response to process. Anodic dissolution is well-understood to be initiated at defect sites in the lattice [112] or the passivating oxide layer [116], whereby complex stress distributions around defects increase the probability of localised removal, shown in Figure 4.8. Therefore, it is unsurprising that through high-temperature annealing (≈0.7 T_m, 3 hr) and eliminating defects from large volumes of the workpiece, the number of discrete initiation points is reduced, *ergo* porosity is reduced.

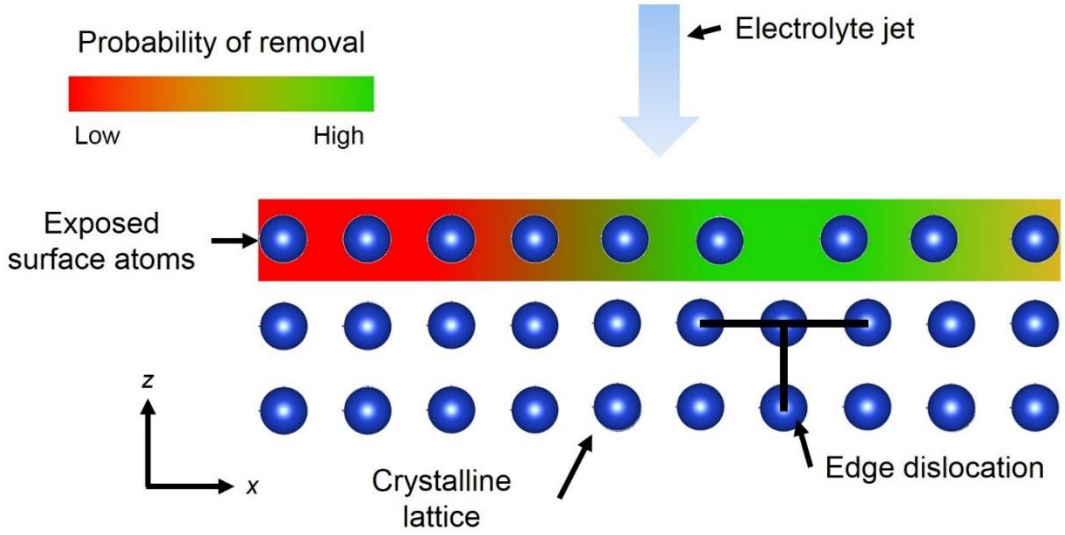


Figure 4.8: Schematic showing illustrating pore initiation in the vicinity of lattice defects, such as edge dislocations. Sectional view of an ordered lattice, whereby removal probability of a given surface atom is influenced by surrounding stress distributions. Within unstressed lattice (red area), removal probability is constant across the discrete atoms, however altering the stress distribution will increase the removal probability through decreasing the removal activation threshold.

What is unusual is the apparent independence of pore morphology (not size) on current density between the pits processed across the complete current density range. Pores in the non-annealed specimens always appear crystallographic in shape. While this appears to be counterintuitive in high current density anodic dissolution, such topographies have previously been reported in the literature [96], whereby the electrochemical dissolution phenomena of copper are unstable and parts of the surface undergo active dissolution, regardless of current density [93].

The inverse relationship between apparent pore size and rolling treatment, for the samples not subjected to prior annealing could be a result of the refinement of the grains due to the cold-rolling treatment (*see* Figure 4.1). As crystallographic pores are only able to propagate within single, similarly oriented

domains, whilst retaining their geometric identity, it is logical that reducing the grain size will reduce the effective lattice volume through which a discrete pore will grow. This is especially pertinent considering the number of large-area pores (>3 μm^2), wherein the size of many grains within the highest stressed sample tested (52% reduction) appear to be within the same order of magnitude as the large-area pores. In addition, as the microstructure is refined by increasing rolling treatments, the effective grain boundary density will increase. This is important because boundary zones will constrain the propagation of a crystallographic pore, effectively arresting propagation; a crystallographic pore cannot propagate across a grain boundary *and* retain the same geometry. This is shown in Figure 4.9, processed at high current density (350 A/cm^2).

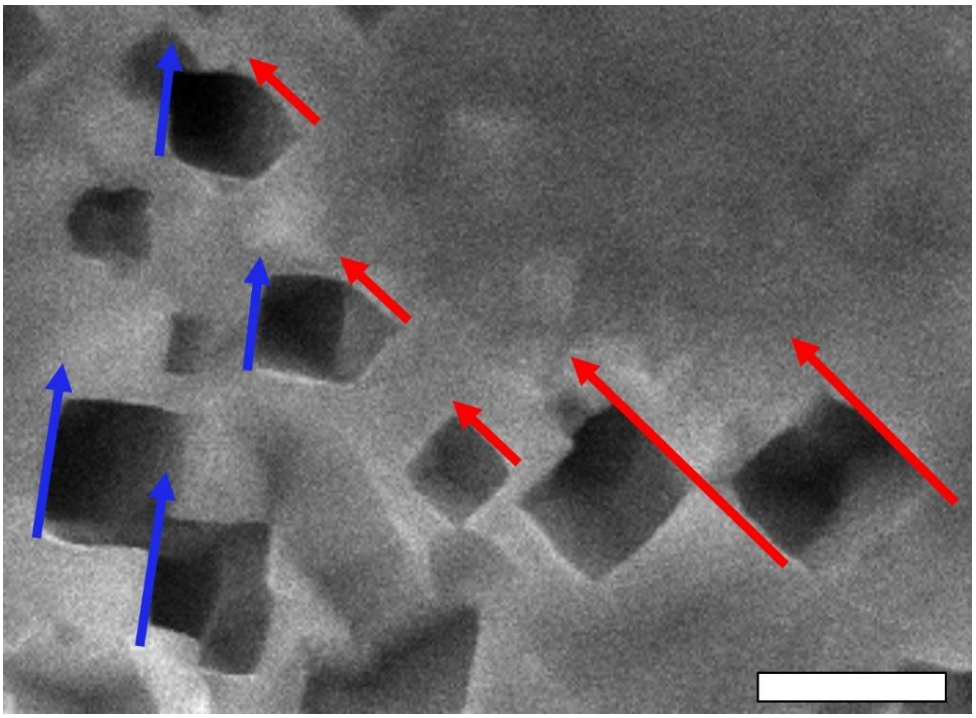


Figure 4.9: SE micrograph (0% reduction, 350 A/cm^2), showing a grain boundary. Crystallographic pores align with the lattice. Pore growth is largely constrained by the grain boundary. In some cases, pores are able to propagate across boundaries, however morphology becomes a convoluted hybrid of both orientations. Scale bar 1 µm. Blue and red arrows demarking two individual crystals.

The growth of a crystallographic pore is generally constrained by the grain boundary, although in some cases, propagation can occur across the crystallographic domains, the result of which are pores of hybridised morphology.

For the annealed samples, EJP revealed stepped surfaces (*see* Figure 4.4b, d). After annealing, the grain boundary density is considerably reduced compared with the feedstock and it is proposed that in this precondition, material removal occurs without pore-growth being arrested by the grain boundaries, to the same extent. Without growth inhibition, pore-type features, which reflect the symmetry of the Cu lattice, are able to equalize over the discretely orientated domain of a single grain, leading to the stepped morphology seen in the SE micrographs. This stepped morphology, like that of the cubic pores, is also intrinsically related to the symmetry of the material lattice, therefore the two seemingly different morphologies (cubic pores and cubic steps) are likely formed by equivalent phenomena. This is also supported by equivalent machining conditions used to generate all surfaces in Figure 4.4.

The step featuring in the annealed samples is too fine to be appraised using FV microscopy, however, differences in measurable surface roughness with rolling treatment (*see* Figure 4.7b) for the annealed samples appear to be caused by band-type features on the surface. This surface banding results from the plastic deformation of copper grains, probably through shearing-type mechanisms, illustrated in the schematic in Figure 4.10. With no cold-rolling treatment, highly ordered lattice structures are revealed (*see* Figure 4.10a). During cold-rolling, shearing phenomena occur, leading to banding in Figure 4.10b. The magnitude of these topographical phenomena are large enough to be measured by FVM,

therefore the effect of rolling treatments on roughness can be quantified between 100-300 A/cm^2. Above 300 A/cm^2, the effect of plastic deformation on the resulting surface amplitude appears to be overcome, resulting from increased asperity attack at higher current densities (electropolishing).

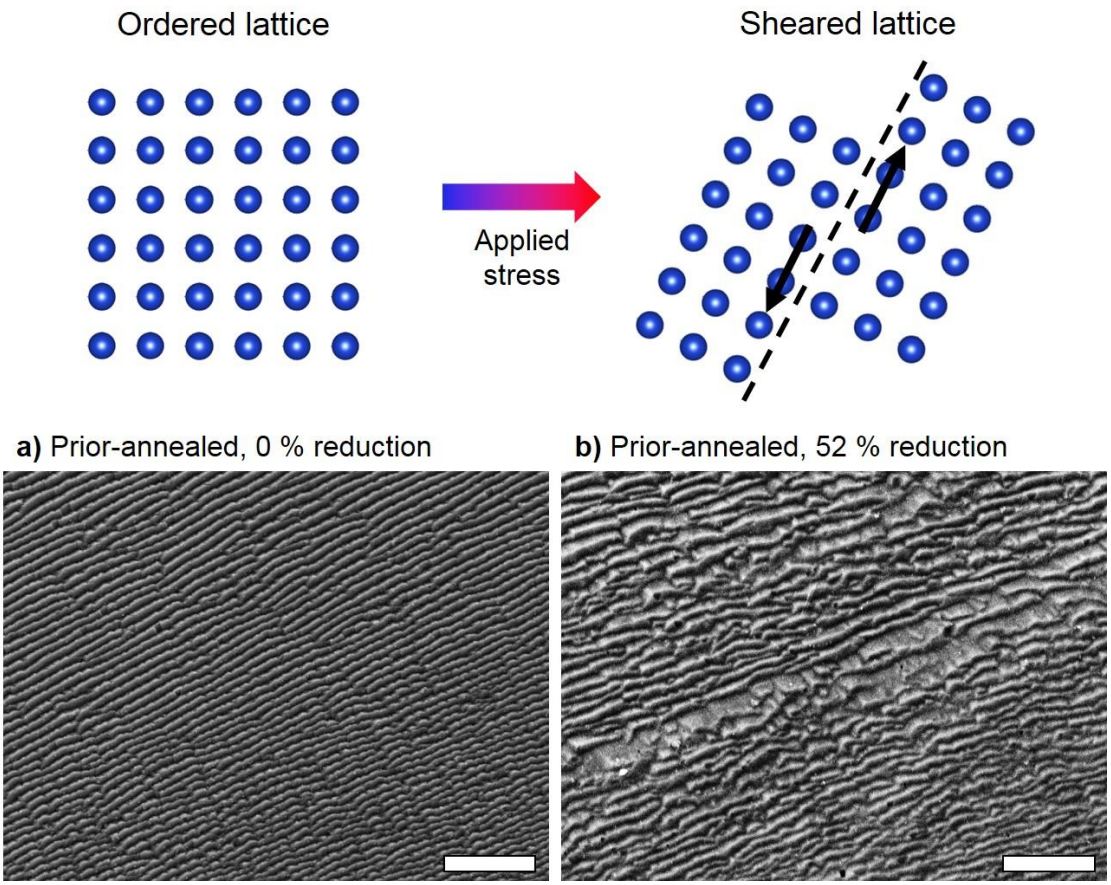


Figure 4.10: Schema showing an ordered lattice and a sheared lattice after cold-work. a) Processing of annealed samples reveal ordered topographies consistent with the orientation. b) Upon cold-rolling, textural discontinuities are revealed, caused by shearing mechanisms during plastic deformation, leading to surface banding and higher measurable roughness. SEM scale bars 10 µm.

Annealed Cu samples show ordered surface structuring, acutely dependent on the grain orientation normal to the electrolyte jet and consistent with well understood principles of chemical etching. For polycrystalline materials, such as those studied here, the orientations of the grains within the material will be

stochastic in nature. This could complicate deterministic feature processing, where smooth and repeatable surfaces across areas larger than the material grain size are required. The result of non-optimised processing parameters are shown in the grain boundary interface (between grains ‘a’ and ‘b’) in Figure 4.11a. Through increasing the current density beyond 300 A/cm^2, the textural dependence on orientation is reduced, leading to a smooth finish (*see* Figure 4.11b) across adjacent grains ‘c’ and ‘d’.

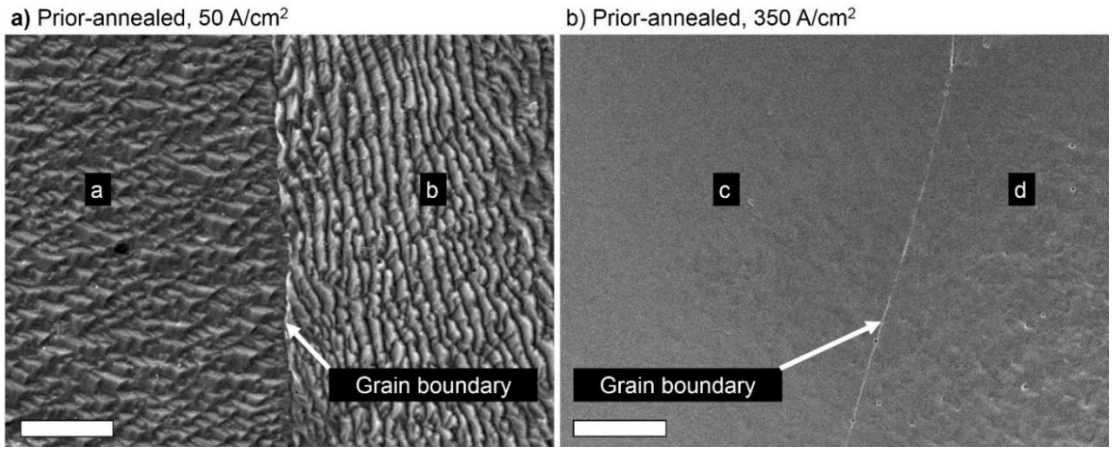


Figure 4.11: SE micrographs of the prior-annealed specimen (0% reduction) processed at a) low (50 A/cm^2) and b) high (350 A/cm^2) current densities, overcoming orientation-specific roughness. SEM scale bars are 10 µm.

4.2.4. Application as a tool to assess material deformation.

The sensitivity of EJP-generated topography to induced material defects within certain processing conditions (<100 A/cm^2) could enable the technique to be applied as part of a selective probing device to investigate material deformation when coupled with appropriate surface analysis such as metrology or microscopy. This application is analogous to conventional chemical etching, however when applied to this effect, EJP holds several significant benefits. Primarily, the analytical surface is generated by the process within seconds. This all but eliminates metallurgical preparation steps, for example grinding and

polishing; in EJP, surface preparation and etching occur simultaneously within the same process step. In addition, there is no thermal or stress input during the surface generation process. This means the integrity of the near-surface microstructure can *always* be ensured. This is of special importance, where the near-surface microstructure may be plastically deformed as a result of inappropriate surface preparation, for example very soft materials.

Secondly, the selective nature of EJP means that an area of a discrete component can be targeted and analysed, without affecting the integrity of the rest of the part. Furthermore, control can be achieved over the depth of the analytical surface, as this is intrinsically related to the charge passed in the process. This precise control can allow surfaces to be sequentially prepared and analysed, and repeated, in order to achieve three-dimensional microstructural information. This would represent a protracted process if conventional surface preparation and etching were applied, but could feasibly be accomplished within seconds using EJP.

Finally, surfaces can be generated in a facile manner using solutions of common, non-toxic salts, such as $NaNO_3$ (used here) and NaCl, which reduces the complexity of resulting waste streams, in comparison to conventional chemical etching. An example of a prepared analytical surface is shown in Figure 4.12. Here, a sample of Cu, which has undergone sever plastic deformation (52% reduction) has been subjected to EJP to generate a microstructural topography, and characterised with focus-variation and SE microscopies.

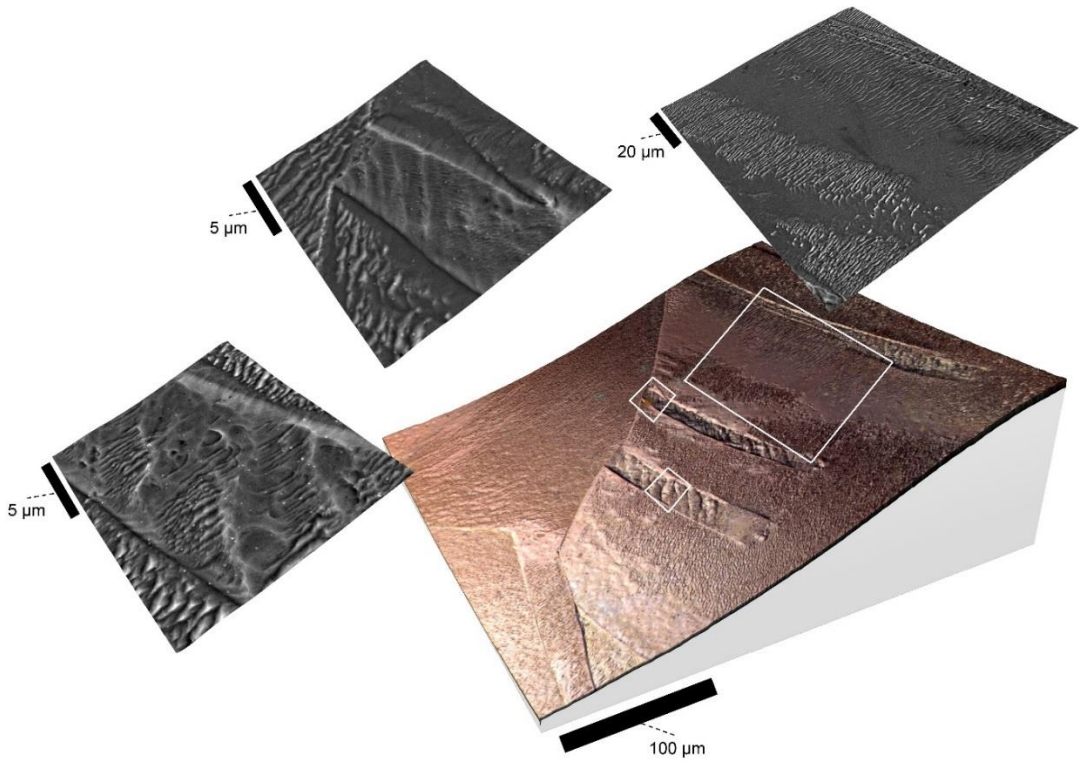


Figure 4.12: EJP as part of an investigatory tool to appraise material deformation. Targeted, selective, precisely controlled material removal reveals the characteristic slip planes in the Cu workpiece.

4.3. Correlating topography with orientation

4.3.1. Preliminary microstructures

For this set of experiments, samples of Ni and Al alloys were prepared as per experimental section 3.1.1 (page 75). The resulting etched microstructures are shown in Figure 4.13, which have been taken from the basal areas of pits machined into the materials using EJP. All samples are shown to be polycrystalline with a distribution of grain orientations, correlating with differential optical contrast.

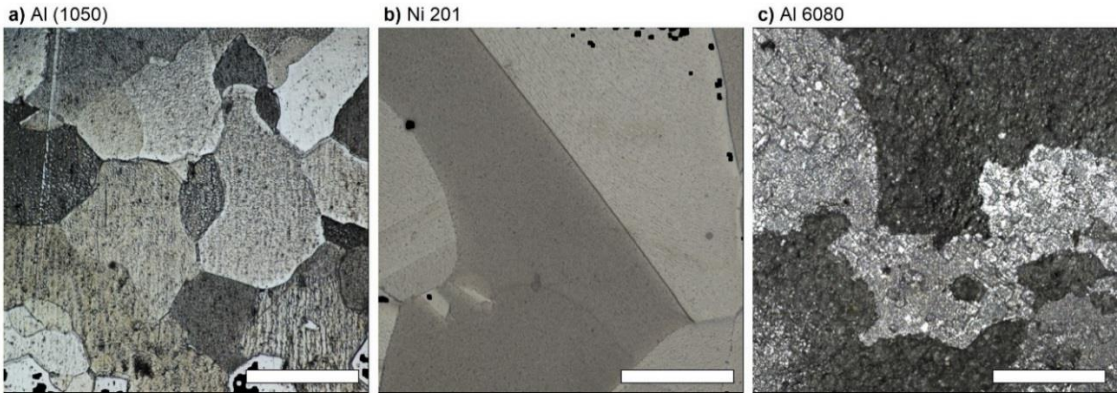


Figure 4.13: FV optical micrographs (50x objective, 324 µm FOV) of annealed material microstructures appraised after EJP treatment with NaCl a) Al 1050 (450 A/cm^2), b) Ni 201 (150 A/cm^2) and Al 6080 (50 A/cm^2). Scale bars 100 µm.

4.3.2. EJP generates orientation characteristic topographies

Considering the repeating surface structuring in Figure 4.11a, it is evident that crystallographic orientation can define the topography under appropriate processing regimes. Correlating topographical information with orientation therefore could represent a route through which spatial orientation information can be attained as part of a simple, low-cost operation.

To further investigate this, EJP-generated orientation-dependent surfaces in fcc materials were characterised, wherein samples of polycrystalline Al and Ni were appraised using spatially-resolved acoustic spectroscopy (SRAS), to output crystallographic orientation maps [203], shown in Figure 4.14b, c. Cu was not characterised in this set of experiments, as it is not compatible with the applied iteration of the SRAS set-up; whereby an infrared (1064 nm) generation laser is used to generate a packet of surface acoustic waves (SAWs), and the resulting surface perturbation measured by a green (532 nm) 'detection laser'. Hence for enhancing data quality, it is desirable for the analysed material to maximise absorption of the generation laser and reflection of the detection laser.

Unfortunately, Cu is excellent at both reflecting red, and absorbing green wavelengths. From the extracted datasets, discrete grains were identified, such that a pit was selectively machined into a grain vicinal to each of the three principal cubic orientations relative to normal direction (*see* Figure 4.14a), using NaCl at a constant current density (20 A/cm^2). Location coordinates (labelled d-i) were imported into computer aided manufacturing (CAM) software to generate a machine toolpath, with which the samples were subsequently processed.

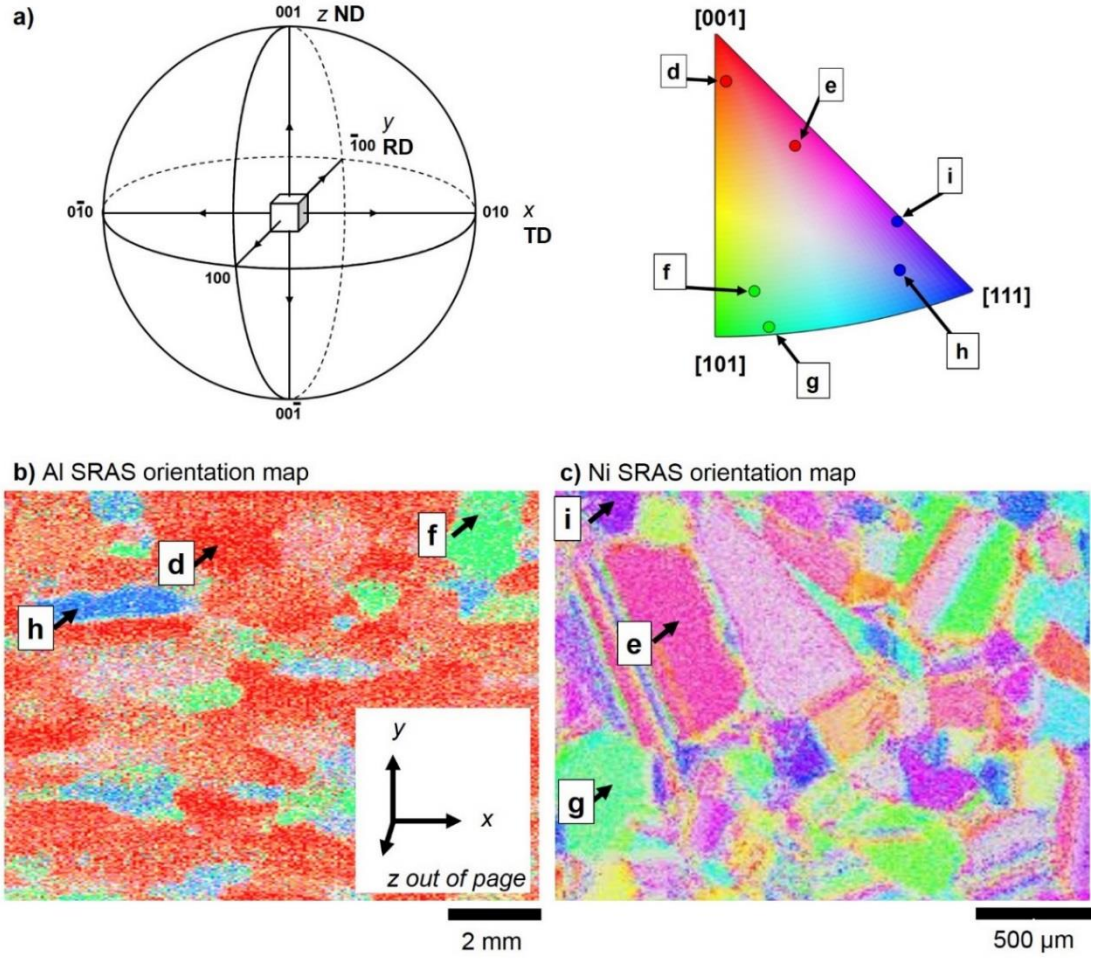


Figure 4.14: a) For cubic crystal systems defined by Bunge notation [201]. From prior SRAS, orientation maps are generated for both b) Al (50x100 µm/pixel), and c) Ni (10x20 µm/pixel). From these maps, grains were targeted (labelled d-i), by inputting planar coordinates into computer aided manufacturing software, to observe topographies resulting from EJP oriented grains (relative ND), vicinal to the three principal cubic orientations ([001], [101], and [111]), at 20 A/cm^2.

Secondary electron micrographs show textural variation associated with different orientations. Where grain orientation tends towards <001>, smooth surfaces are generated in Al in the central pit region of *grain d* (*see* Figure 4.15a) and a small number of cubic crystallographic pits are observed. Large gradients, approaching 90°, relative to the transverse direction (*see* Figure 4.15b) are seen in this orientation, resulting from retardation of dissolution in <001> directions, correlating with previous studies [121, 218]. Here, resulting topography is defined by inhibited-etching directions, dictated to be the slowest dissolving surfaces.

In Ni, observed surfaces are generated from repeating inverted square-pyramidal pits, when grains vicinal to [001] are machined (*see* Figure 4.15c). Immediately, it can be determined that in Ni, pore growth is inhibited by directions other than <001> and is therefore discrete from Al. The pyramidal walls generally feature gradients of between 30-40°, relative to the normal direction (ND). This is shown firstly by tilting the sample in the SEM chamber, whilst observing the same crystallographic pit (*see* Figure 4.15d). The closest exposed faces of the pits can be observed at a specimen tilt of 30°, however most of these faces cannot be seen upon further tilting to 35°. This indicates that the angles, from the vertical ND, fall between 30°-35°. This correlates well with the angle of the <111> directions, theoretically, $\tan^{-1}\frac{1}{\sqrt{2}}$ (≈35.25°), from normal direction. This is further supported by the cross-sectional profile across a pyramidal pit (acquired using CSI), where opposing walls feature slopes of 34° and 39° (*see* Figure 4.15e). That the side walls are not all exactly 35.25° is predictable because: *1)* considering Figure 4.14c, *grain e* is shown to have an orientation vicinal, but not identical to [001], and *2)* material removal at this

length scale, whilst determined primarily by the underlying crystallography, will be strongly affected by microstructural inhomogeneity. This evidence indicates that for Ni ≈[001], material removal is likely to be arrested by <111> directions, shown in Figure 4.15f. For removal arrested mainly by <101>, gradients approaching 45° would be expected. This is not observed.

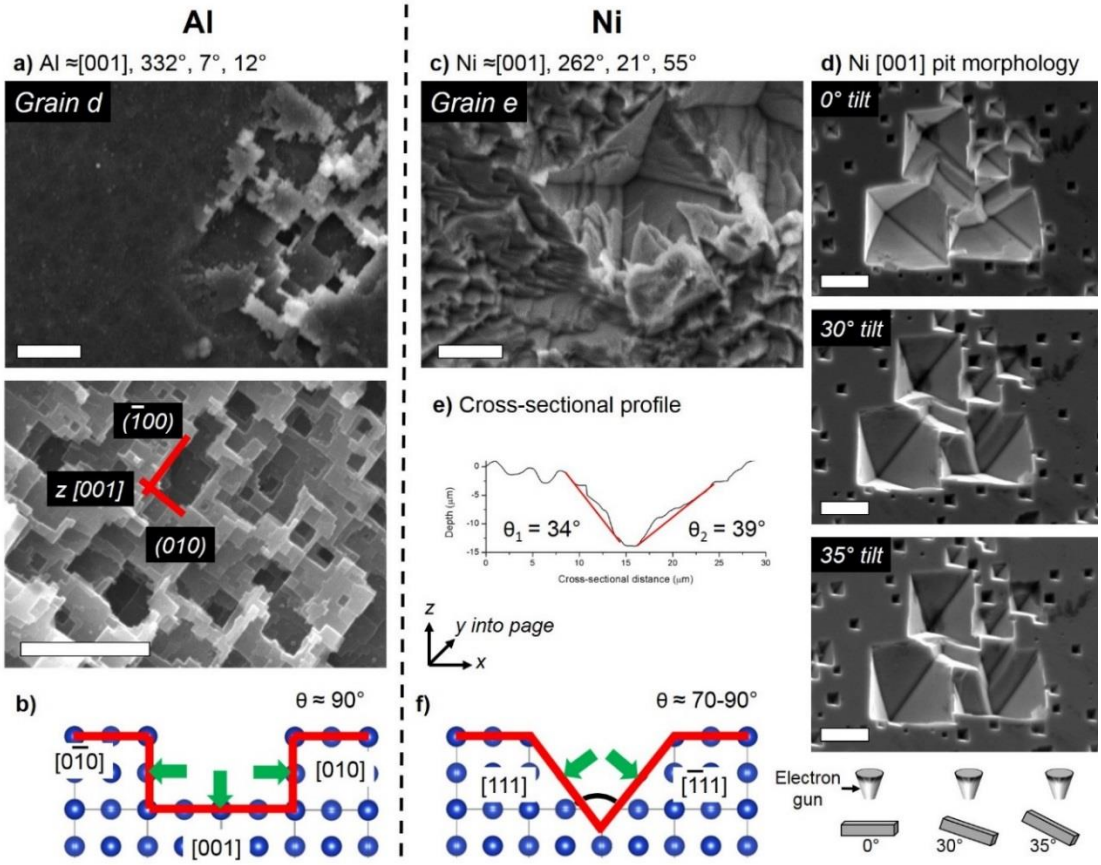


Figure 4.15: For Al (left) and Ni (right), drilling pits into grains d and e (both ≈[001]) respectively (20 A/cm^2). SE micrographs all acquired from ND, cross-sectional profiles and schema are represented from RD. Green arrows indicate suggested slow-etch directions. a) For 'Grain d' (Al), smooth surfaces dispersed with cubic pits are observed, b) indicating slow-etch directions <001>. c) square-pyramidal pits observed in similarly oriented Ni 'Grain e'. d) SEM specimen tilting shows the gradient is ≈35° from ND, correlating with <111>. e) This is supported by cross-sectional profiles across pyramidal pits, where gradients fall between 34°-39°, suggesting that etch-inhibited directions align with <111> in Ni. SEM scale bars are 5 μm.

For grains oriented towards <101> relative to the normal direction, repeating stepped features are generated in both Al and Ni (*see* Figure 4.16a), however the topographies are characteristic for each material. In Al, the stepped structuring generally appears to be orthogonal with an inter-step angle of approximately 90° in this orientation, again indicating material removal retardation in the <001> directions, shown in the cross-sectional schematic in Figure 4.16b.

Conversely for Ni, steps are not obviously orthogonal and grains tending towards [101] feature relatively large plateaux, which are indicative of a tendency towards an equilibrium removal condition. These areas are truncated by stepped features (*see* Figure 4.16c), the angle between the two surfaces being >90°, generally between 125-140°. Blunted diamond-like pits shown for Ni ≈[101] surfaces (*see* Figure 4.16d), previously reported in Ni [219], appearing to result from inhibited dissolution along <111> directions, theoretically $\tan^{-1}\frac{1}{\sqrt{0.5}}$ (≈54.74°) from ND. This indicates that dominant material removal follows <001>, and dissolution is inhibited along the <111>, and possibly <101> directions. Lower selectivity between <111> and <101> directions complicates surface topographies of Ni compared with Al, although the surfaces remain characteristic. The different etch selectivity between Al and Ni is indicative of the etching defined by different mechanisms. In both materials, the <111> directions are close-packed and therefore the effective ECE is greater. Intuitively this should result in a slow-etch direction, which is the case in Ni. However for Al, oxide passivation is stronger for <001> directions and the evolved current density is smaller [121], thus this defines the etch topography.

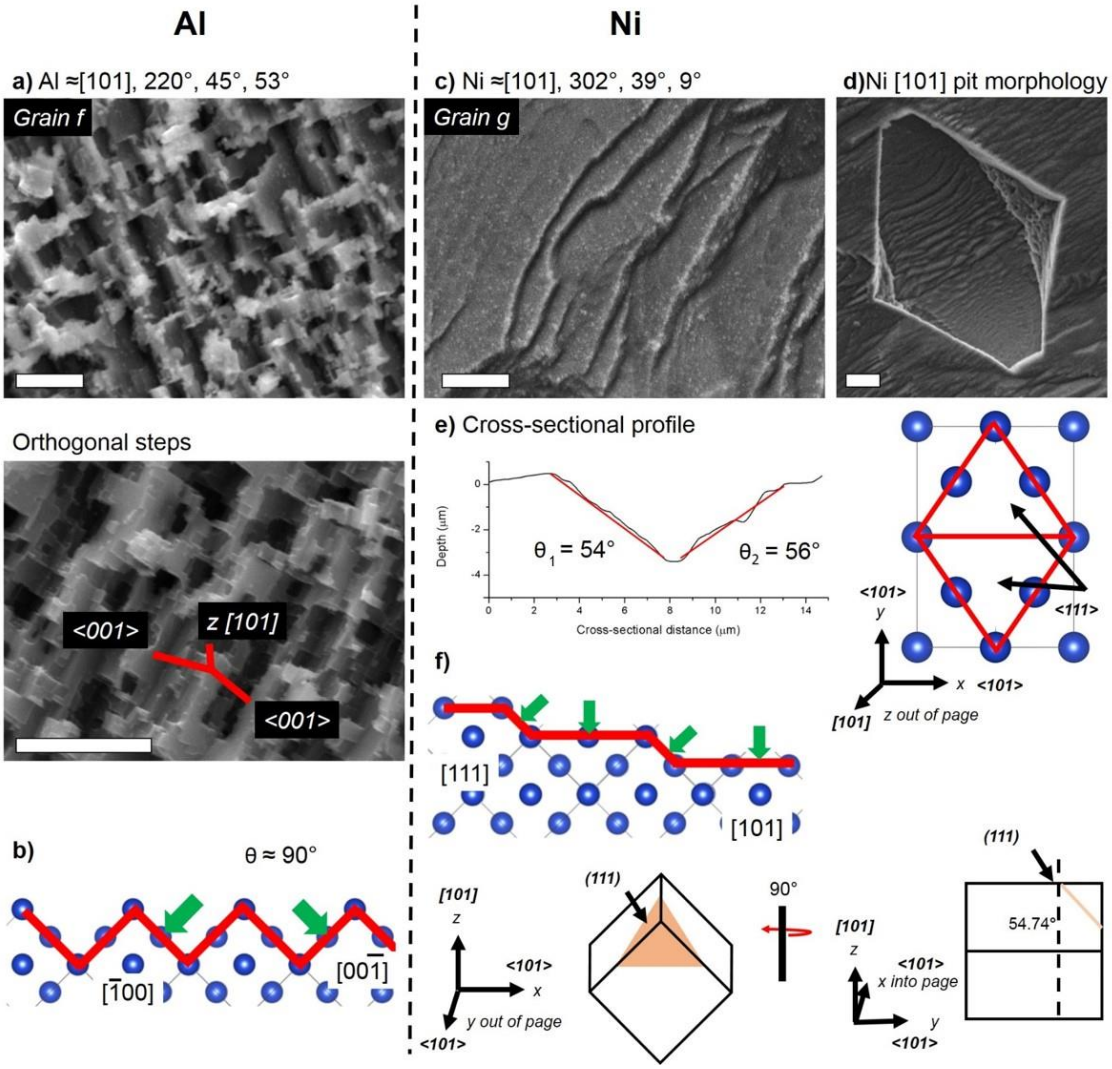


Figure 4.16: For Al (left) and Ni (right), drilling pits into grains f and g (both ≈[101]) respectively (20 A/cm^2). Cross-sectional profiles and schema are represented from the RD unless different axes are included. a) The base of the pit processed in 'Grain f' (Al) has orthogonal steps, aligning with <001>, again indicating slow-etch directions in Al follow <001>. c) For Ni, stepped features are also observed, however these are not orthogonal. d) In addition, processed surfaces are dispersed with blunted diamond pits, geometrically allowed by fcc <101> orientations, if removal is inhibited by <111>. e) This is supported by cross-sectional profiles acquired across a diamond pit, whereby the gradient is observed to be between 54°-56° from the ND, correlating with the theoretical angle of these directions (≈54.74°). All SEM scale bars are 5 μm.

For grains tending towards <111> relative to the ND, repeating pyramidal-type textures are observed in Al (*see* Figure 4.17a), which is expected considering slowest etching directions aligning with <001> (*see* Figure 4.17b). For a periodic

pyramidal surface, three dominant slopes with 120° inter-separation would be expected. For Ni, surfaces are composed of plateaued triangular features (*see* Figure 4.17c), where the angle of each triangular plate ≈60°. This corresponds to removal arrested by <111> faces, which are equilateral when sectioned through this orientation. Hexagonal pit morphologies, reflective of the packing of this orientation, are dispersed throughout the surface; a typical example is shown in Figure 4.17d, supporting <111> slow-etch directions in Ni. Interestingly, material removal is prohibited along the faces to the degree where undermining of crystallographic pits occurs, an example of which is given in Figure 4.17f, where the pit retains geometric identity at subsurface level.

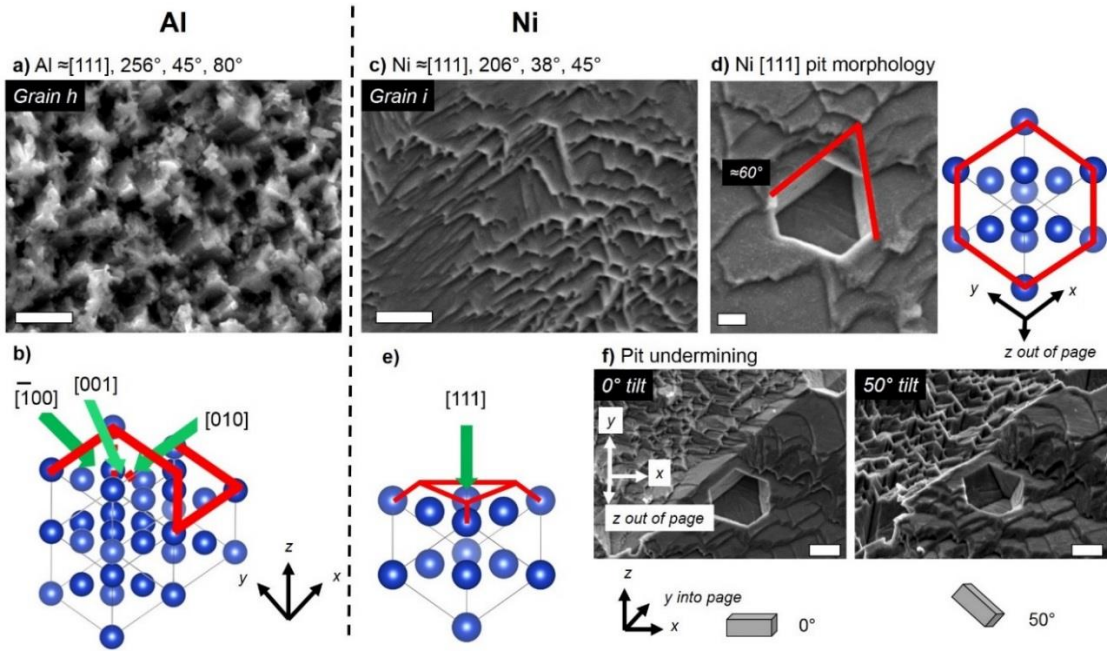


Figure 4.17: For Al (left) and Ni (right), drilling pits into grains h and i (both ≈[111]) respectively (20 A/cm^2). a) In Al, repeating orthogonal pyramidal textures are observed. Removal is inhibited along <001> directions. c) Triangular plateaux are observed, featuring angles of 60°, correlating with the (111) plane, which is equilateral when sectioned through this orientation. Pits exhibit hexagonal morphologies, geometrically allowed in this orientation and f) material removal along this orientation appears to be inhibited, to the extent that propagating pits undermine the (111) surface, ahead of conventional top-down removal modes. All SEM scale bars are 5 µm.

The surface textures generated in both materials here are intuitive, when considering their origins in the respective geometries of the principal orientations, and are therefore characteristic for a given parent-grain orientation. In Al, implicit in the exposure of cubic and pyramidal features is arrested material removal along <001> crystallographic directions, defined by the stronger passivation characteristics [220]. For Ni, characteristic topographies can be explained considering removal arrested mainly by <111> directions, defined as the close-packed directions. These relationships can be quantified in a repeatable manner and underlying orientation information can be output, relating the apparent topography to the principal cubic orientations.

4.3.3. Manipulating orientation-dependent topographies

Grain-dependent topography succinctly demonstrates anisotropic material removal and is dependent on the material, applied energy, and electrolyte used. For Al and Ni, it is shown that the result of using an aggressive NaCl electrolyte in EJP, is grain-dependent texturing at low applied current density (J_{noz} = <100 A/cm^2). Grain-dependent texturing here results from crystallographic corrosion phenomena across the machined area. The textural relationship with current density is demonstrated by differential surface texturing (root mean square height, *Sq*, over multiple grains), in an identical manner to Cu (*see* Figure 4.7), which was measured for both Al and Ni in aggressive NaCl and passivating $NaNO_3$ electrolytes (*see* Figure 4.18a, b). For Al and Ni processed with NaCl, a power-type regression between surface amplitude and current density is followed, across J_{noz} = 20-450 A/cm^2. Amplitude depends on diffusion layer thickness in anodic dissolution, whereby electropolishing is achieved at high current densities, and asperities act as field-focussing elements, increasing

localised current to enhance their dissolution rate (*see* section 2.2.2.1) [22, 76]. At low current densities (<100 A/cm^2), where the surface resulting from EJP is dominated by microstructure effects, relatively large amplitudes are generated using NaCl, indicative of the increasing scale of microstructure-defined topography. The scale of grain-dependent texturing is inversely proportional to the applied current density in EJP, between 20-200 A/cm^2, beyond which the amplitude does not decrease significantly. For Al and Ni, lattice-defined texturing can be enhanced at current densities <100 A/cm^2, hence operation within this domain is preferred. No equivalent amplitude relationships for these materials processed with $NaNO_3$ were observed, indicative of reduced dependence on the specimen microstructure. Topographic reconstructions, acquired after processing across current densities: 20-300 A/cm^2 using NaCl (*see* Figure 4.18c-q), correlate with the amplitude analysis, resulting in a gradual transition from microstructure-defined removal to electropolishing.

The SE micrographs (*see* Figure 4.18d-r) acquired at identical current densities (20-300 A/cm^2), show single grain topographies. Lattice-defined removal, resulting in cubic geometric structuring at current densities (<100 A/cm^2) is demonstrated for both materials, the scale of which decreases inversely with current density. For both materials studied here, processing at high current density (≥300 A/cm^2) results in negligible periodic topography at this length scale. Transpassive dissolution (processing beyond the passivation potential) of materials has previously been shown to have limited dependence on microstructural factors, such as orientation [118]. It is assistive to the technique that lattice-defined topography is largely insensitive to applied current density

over a broad range (20-100 A/cm^2), even where transpassive dissolution modes are predicted, (Ni, J ≤20 A/cm^2) [37].

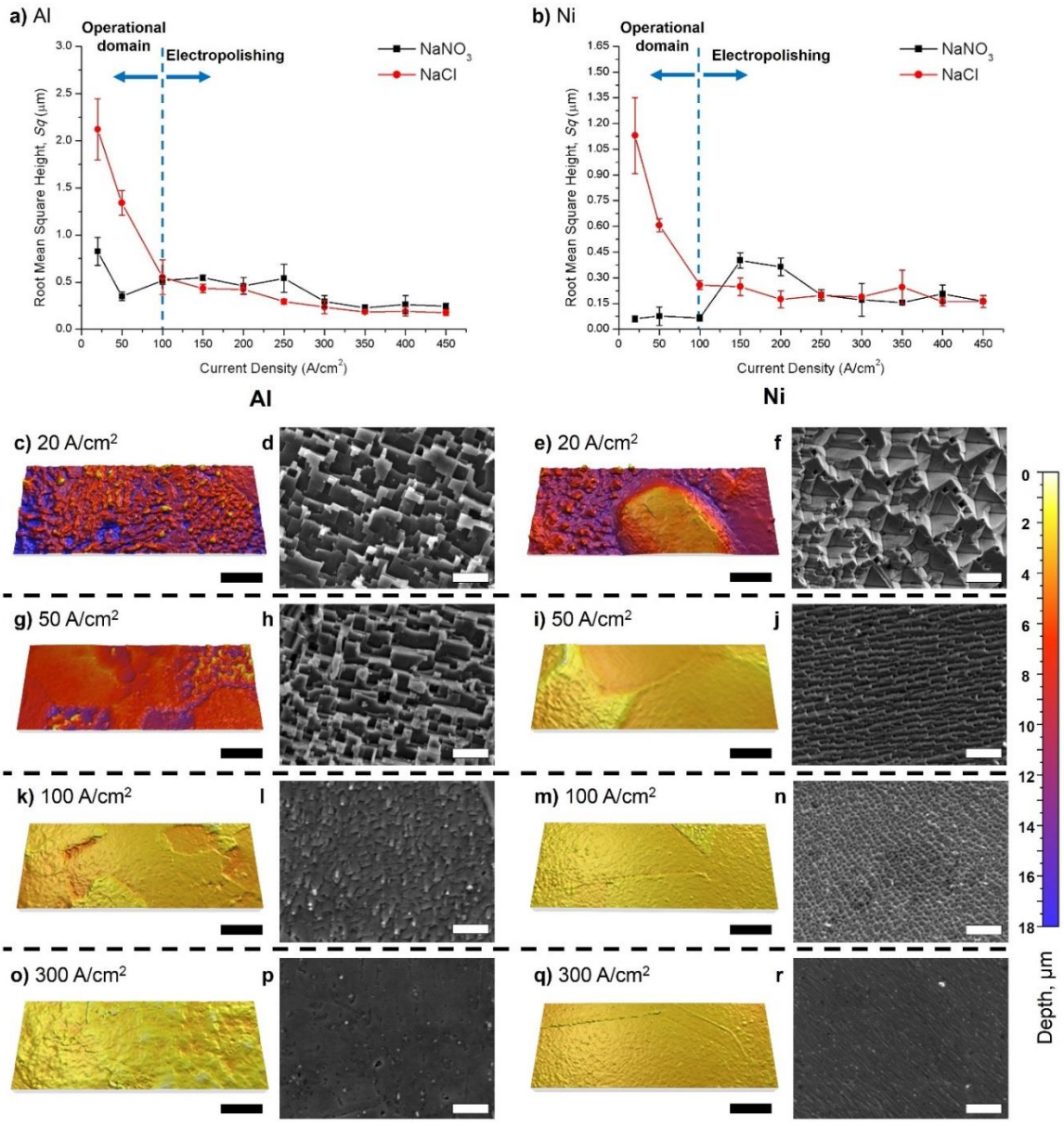


Figure 4.18: RMS roughness, Sq, is approximately power regression with J_{noz}, for a) Al machined with NaCl, but not with $NaNO_3$, b) also observed with Ni. Reconstructions of processed areas acquired using FVM (50x objective), and subjected to 2nd order polynomial form filter [221]. SE micrographs of single-grain areas, machined with NaCl. c, e) At low current density (20 A/cm^2), grain-dependent topography is generated in both materials and d, f) repeating microscale structuring is observed. Upon increasing current density (50 A/cm^2), g, i) grain-dependent topographic contrast is still evident in both materials, although finer in scale, with h, j) ordered surface structuring. At higher

current density (100 A/cm^2), topography amplitude is reduced, k, m) but still apparent in both materials and l, n) finer-scale repeatable surfaces are shown in SEM, although appearing to delocalise from high-level ordering associated with lower current densities. At higher current densities (300 A/cm^2), o) no grain-dependent topography is observed in Al, and p) smooth surface textures are observed, the same is shown for Ni, although q) intergranular attack is evident, and r) some ordering is apparent. Electropolishing mechanisms dominate ≥100 A/cm^2. Error bars are the standard deviation of the mean, from three discrete pits for each data point. Black scale bars are 50 µm, white scale bars are 10 µm.

Using $NaNO_3$ under equivalent processing conditions, no lattice-defined topography in Al was observed, and a limited extent in Ni, although less than with NaCl, shown in the surface reconstructions in Figure 4.19, where differential reflectivity is indicative of differing microscale topographies. This is likely to be a result of the more positive oxidation potential: Cu<Ni<Al (*vs.* standard hydrogen electrode) [198]. In Al, anodic oxide-generating $NaNO_3$ delocalises material removal from the microstructure, hence etching appears isotropic within this parameter set. In effect, if orientation-dependent topographies are to be generated in a passivating material, such as Al, an aggressive electrolyte is recommended. However more noble materials, such as Cu, do not appear to generate orientation-dependent topographies with aggressive electrolytes (*see* Figure 4.19e), within the parameter set applied here. Therefore for Al and Ni, aggressive electrolytes, stimulating anisotropic removal in EJP, are preferable in orientation topography generation.

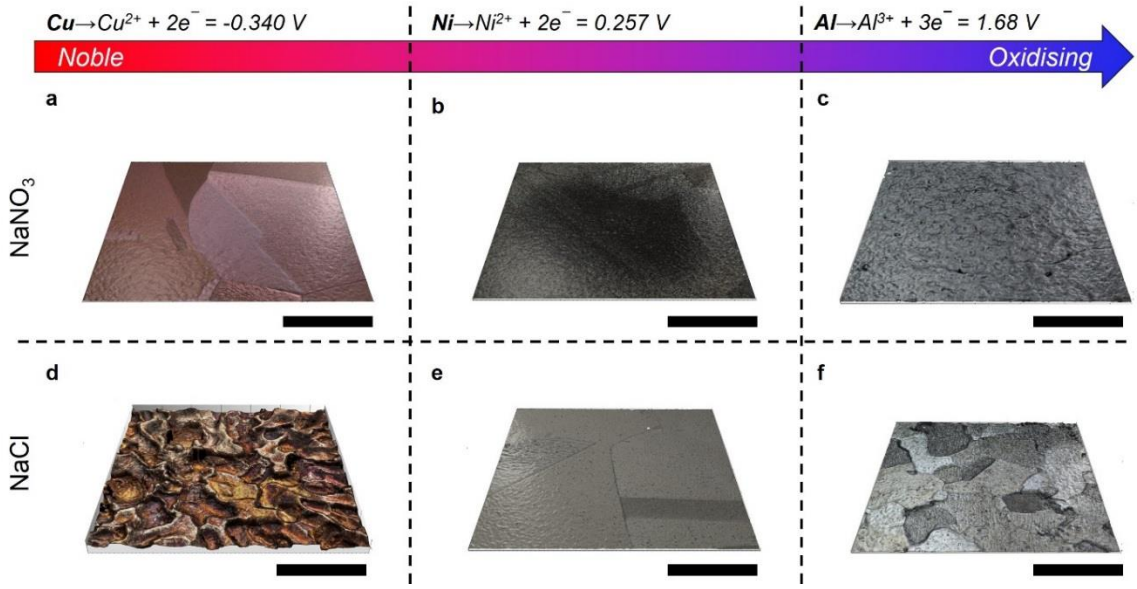


Figure 4.19: Reconstructions showing the effect of electrolytes on surface topography (100 A/cm^2). a) With Cu, orientation-dependent contrast is generated using $NaNO_3$, b) to a lesser extent in Ni, and c) not at all in Al. Using NaCl, d) removal is discontinuous, undulating, and inconsistent with underlying crystallography in Cu, however, orientation-dependent topographies are observed in e) Ni, and f) Al. This appears to correlate with the standard oxidation potential, Cu<Ni<Al. Scale bars 100 µm.

When processing, the dissolution profile is dictated by the current density distribution. Classically, this appears Gaussian for a cylindrical nozzle, (*see* Figure 2.1a). Localised variation in microscale topography is observed as a result of the feature form, such as for Al vicinal to [001], where inhibited-etching directions, defined by the material-process response, follow <001>. A pit section is shown in Figure 4.20a, where the central region appears reflective, indicative of lower surface amplitude, compared with the walls (*see* Figure 4.20b). At low current density, smooth surfaces are not generally expected in EJP [24]. Despite differential amplitudes, similarities in the textural morphologies at the pit base and the side wall are observed (*see* Figure 4.20c, d).

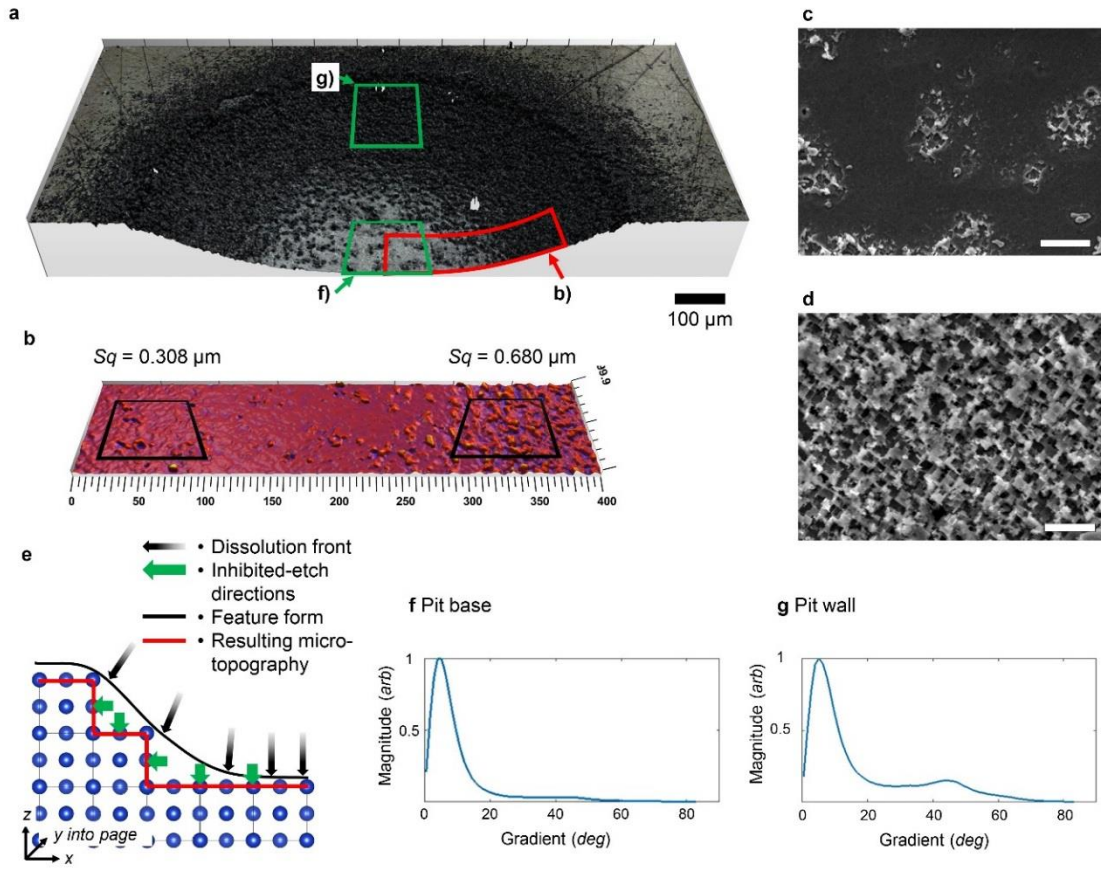


Figure 4.20: Characteristic topography generation is independent of dissolution front. a) Reconstructed pit section, with optical micrograph (FVM, 50x objective) drilled at low current density (20 A/cm^2, 14 s dwell) into a single-grain area of Al (NaCl), orientation ≈[001], showing greater reflectivity at the base, (extracted surface red box). b) From extracted surface (after form removal, 2nd order polynomial) different roughness is shown, where the central regions have lower amplitudes. Complementary SE micrographs, showing differential texturing at: c) pit bases, d) and sides, where equivalent cubic recesses are observed, albeit at a finer surface dispersion in the pit base. e) This can be correlated with the relationship between the dissolution front and the preferential removal vector. f, g) Consequently, topographic response is similar at both locations. SEM scale bars 10 µm.

An interpretation of the surface-generation mechanism for Al is shown in the idealised schematic in Figure 4.20e. As dissolution achieves steady-state and a side wall of the pit becomes exposed, additional <001> inhibited-etch directions are exposed. Therefore, the topography generated is inconsistent with that subject to attack from the normal direction. The single-grain

topographies created throughout the pit are not uniform, therefore an orientation mapping routine based upon EJP-generated topographies cannot rely on roughness (amplitude) differences alone, and must accommodate this variation. Material removal does not occur in the normal direction in this case, leads to periodic surface stepping, having a scattering effect, therefore appearing dull to the observer. Dominant slope angles are equivalent at the pit base and the side walls, as these are defined by equivalent inhibited-etch directions, however surface dispersion of cubic pits is lower at the base. Since characteristic slope angles are the same at the base and side of the pit, they remain representative of the underlying grain orientation. The dependency of the micro-topography on the feature form is therefore reduced, under anisotropic etching conditions.

When creating striations through jet translation, the same effect is observed, shown for Ni, orientation evaluated by SRAS prior to etching (*see* Figure 4.21a). Translation EJP reveals grain-dependent topography (*see* Figure 4.21b), where periodic form over the surface correlates with jet movement (*see* Figure 4.21c). Surfaces from single-grain areas show equivalent characteristic texturing at central (*see* Figure 4.21d), and edge regions of the resulting slot (*see* Figure 4.21e), although the total amplitude is greater in the low current density region. Consistency of micro-topography generated, independent of form, allows large areas to be rapidly processed and characterised.

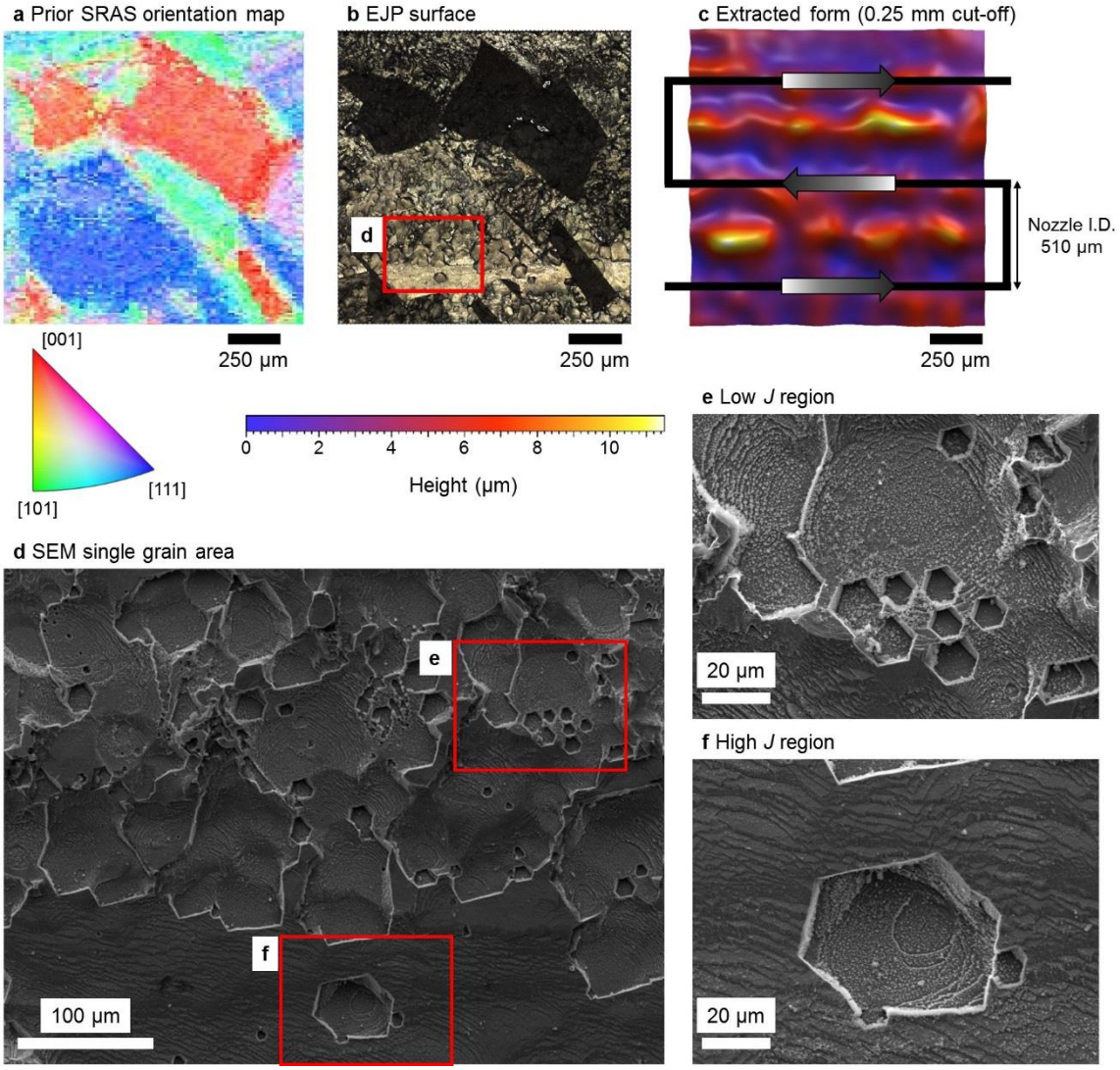


Figure 4.21: Anisotropic microscale topographies are largely independent of form for planar toolpaths. a) Comparing with prior SRAS orientation data (18 directions, 20x10 µm/pixel), b) after EJP (30 A/cm^2, v_h = 0.5 mm/s), grain-dependent texturing is observed (FVM, 20x objective), c) despite the form resulting from jet translation. SE micrographs, from the same grain taken at d) central and e) edge regions of the translating jet show equivalent characteristic morphologies, albeit with a greater pit frequency at the edges.

4.3.4. Surface Analytics

The topography of jet processed surfaces varies significantly within single-grains, due to the lattice orientation relative to the dissolution front. However, surface characteristics unique to given orientations in both Al and Ni, are revealed by the gradients of the resulting topography. Provided an accurate

topographic representation is acquired, coherence scanning interferometry was used in this work [222], the gradient vectors and directions of the surface can be obtained according to Equation 14 and Equation 15, to show a statistical distribution of the characteristic slopes for a given surface.

From this distribution, the gradient directions can be quantified, yielding a distribution of peaks unique for an orientation in a given material. For Al grains oriented vicinal [001], micro-topographies comprised of cubic recesses are generated under anisotropic electrochemical etching conditions, (repeating flat areas). This means small slope angles (<10°) are prominent (*see* Figure 4.22c). In this case, the gradient direction varies and trend observation is difficult. For orientations vicinal to [101] and [111], further analysis is necessary for differentiation, through analysis of slope direction, as the histograms for both of these surfaces show similar prominent slope angles which are >45°. For a stepped topography representative of that observed for etched grains orientated vicinal [101], the theoretical difference of peaks is 180° (*see* Figure 4.22e). When grains vicinal [111] are subjected to EJP, periodic pyramidal topographies are observed. The theoretical angle in this case will be 120° (*see* Figure 4.22e).

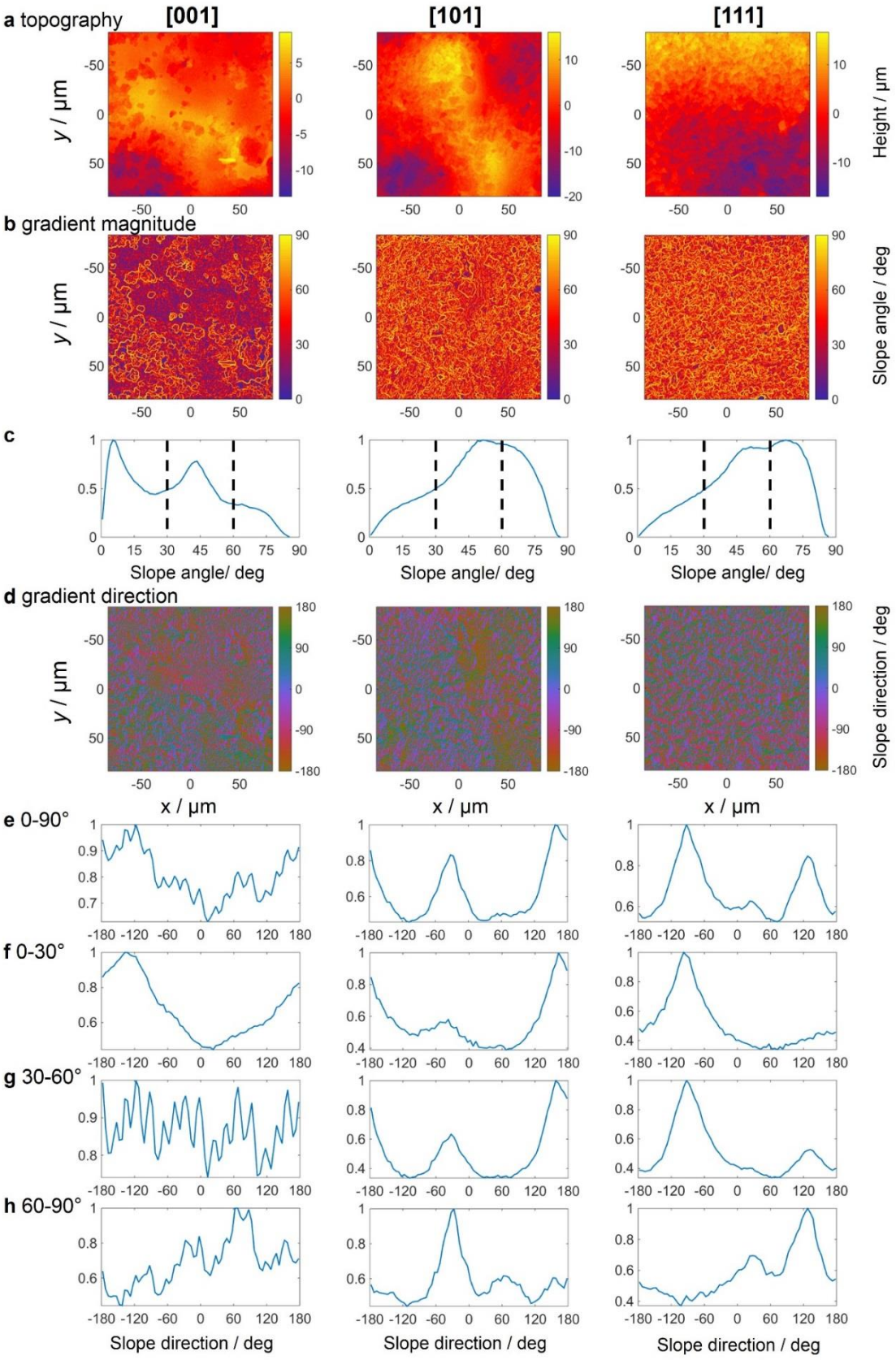


Figure 4.22: Surface analytical correlation in Al. For grains oriented vicinal to the three principal cubic orientations. Datasets showing raw CSI topography (50x objective), shown for ≈[001], ≈[101] and ≈[111] (a). From these datasets, slope magnitude can be

appraised, revealing the gradient maps for the prior topographies vicinal to: [001], [101] and [111] (b). Corresponding statistical analysis shows a low angle peak for grains oriented ≈[001] (significant flat surface), and similar dominant slope angles >45° for orientations vicinal to [101] and [111] (c). These textures are separable through analysis of the slope direction, which reveals two-dimensional gradient direction maps for vicinal [001], [101] and [111] respectively (d). Statistical analysis of this data shows that for ≈[001] oriented grains, the distribution is unstable (due to the plateaued topography of the surface), for grains ≈[101], where stepped surfaces are generated, two dominant peaks are observed, the difference between the directions is 180°, and for grains vicinal to [111], three dominant peaks are observed, the direction separated by 120° (e). Sampling of the gradient distribution can reveal more topographic information, for low angles (0-30°): ≈[001] shows one dominant direction, while ≈[101] and ≈[111] show two dominant directions (f). For higher angle gradients (30-60°), periodicity, defined by the cubic geometry of the surface is observed for ≈[001], although no significant difference in the dominant peaks is shown for ≈[101], or ≈[111] (g). Sampling high-angle gradients (60-90°), periodicity is still apparent for ≈[001] grains, a third peak is apparent for ≈[101] grains (supplementary figure 1b) and for ≈[111] oriented grains, two dominant peaks are observed, still separated by 120° (h).

For Ni, EJP-generated surfaces are more complex, resulting from lower anisotropic etching, hence contrasting is more challenging. The inverted square-pyramidal pitting seen resulting from EJP of orientations vicinal [001], means that the dominant slope angle will be ≤45°. In addition, the slope directions of the pyramidal features are separated by 90°. For grains oriented vicinal to [101], the histogram shows a dominant peak between 10-20°, along with a smaller peak between 30-40°. In addition, the separation of the slope directions is >120°. For grains oriented vicinal to the [111], the histogram shows a dominant slope angle <10°, corresponding to plateaued areas. Characterisation of the slope directions in this case shows three directions with a separation of 120°. Both [101] and [111] surfaces show six major slope directions for high-slope surfaces (60-90°).

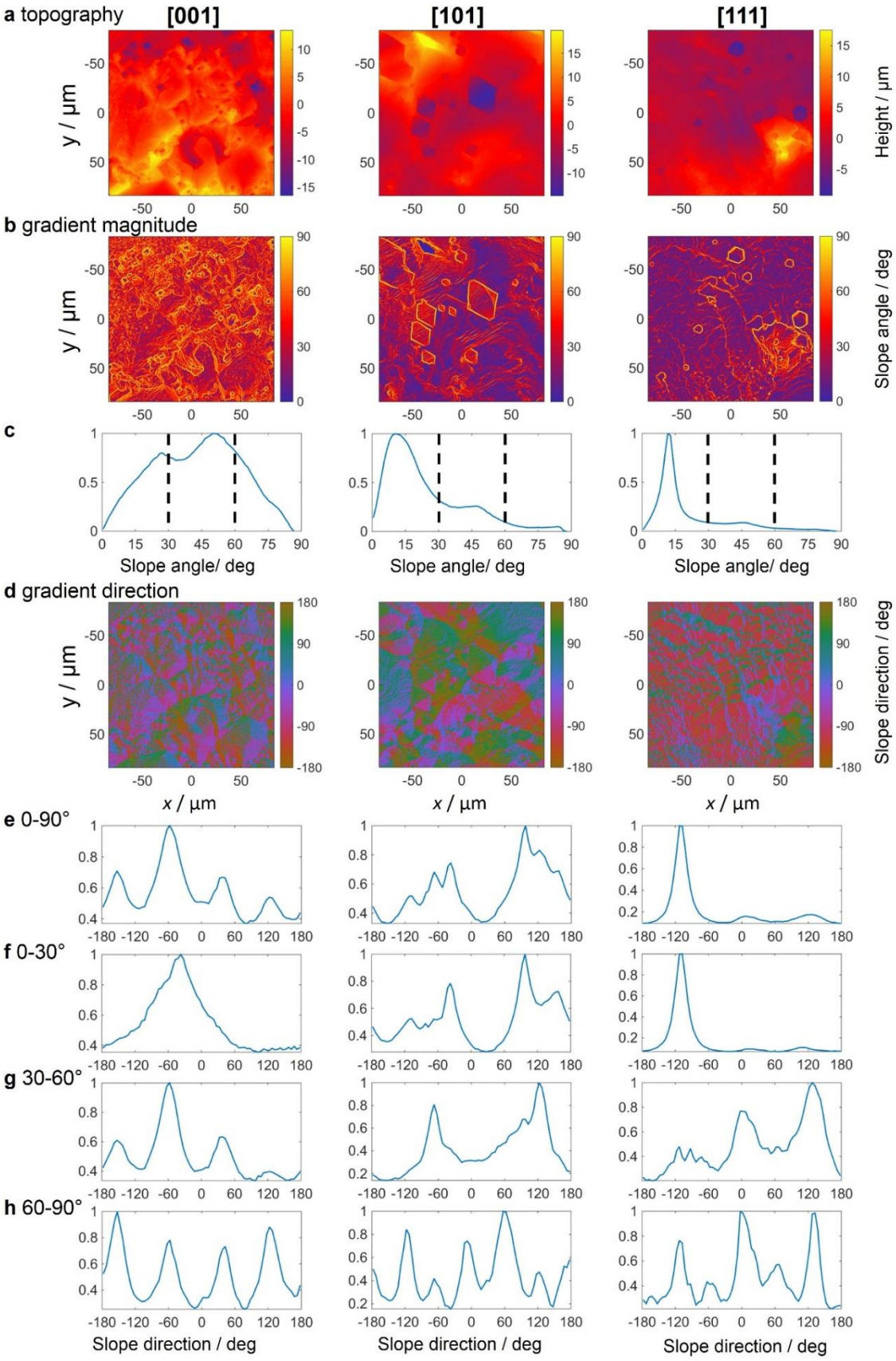


Figure 4.23: Surface analytical correlation in Ni. For Ni, grains oriented vicinal to the three principal cubic orientations. Datasets of raw CSI topography (50x objective),

shown for ≈[001], ≈[101] and ≈[111] oriented grains (a). Slope magnitude can be appraised reveal gradient maps for orientations vicinal to [001], [101] and [111] (b). Corresponding statistical analysis shows two broad gradients with angles of ≈30° and ≈50° for grains oriented ≈[001] (pyramidal topography). Orientations vicinal to [101] show a broad low-angle slope and a small peak ≈30-40° (correlating with periodic stepping). A similar distribution is shown for [111], although the low-angle slope is significantly narrower corresponding to large plateaus (c). Analysis of the slope direction, generates maps for [001], [101] and [111] (d). Statistical analysis shows for ≈[001] oriented grains, pyramidal slopes are separated by 90°, for grains ≈[101], where stepped surfaces with are generated, two dominant peaks are observed, the difference between the directions is >120°, and for grains vicinal to [111], three dominant peaks are observed, the direction separated by ≈120° (e). Sampling of the gradient distribution, for low angles (0-30°): ≈[001] shows one broad direction, while ≈[101] and ≈[111] surfaces show dominant directions statistically representative of the non-segmented direction distribution, as these cases, the majority of the slopes are low-angle (f). For higher angle gradients (30-60°), periodicity, defined by the pyramidal geometry of the surface is observed for ≈[001], for ≈[101] surfaces, ≈180° peak separation is apparent, and for ≈[111], the ≈120° peak separation is shown (g). Sampling high-angle gradients (60-90°), strong periodicity for ≈[001] grains is shown (reflective of the four-fold rotational symmetry of pyramidal features, six periodic peaks are apparent for ≈[101], and for ≈[111], reflective of the hexagonal packing of the inhibited-etch directions <111>, leading to the six-walled [101] (blunt diamond) and [111] (hexagonal) pits (h).

From this method, a grain of Al or Ni can be readily assigned to the closest principal orientation. Automating data acquisition and splitting topographical information (*see* flowchart Figure 4.24) allows planar response profiles to be plotted to generate three-colour orientation maps. Equivalent orientations generate identical characteristic slopes from identical EJP treatment and the aforementioned topographical analysis. However, since this characterisation intervention is far less than conventional methods, the technique is deployable upon high-value assets beyond the laboratory. Nonetheless, it is intuitive that reciprocal orientations lead to machined surfaces with characteristic alignment

relative to the normal and transverse directions. Analysis of absolute gradient directions may be applied to increase the measurement fidelity.

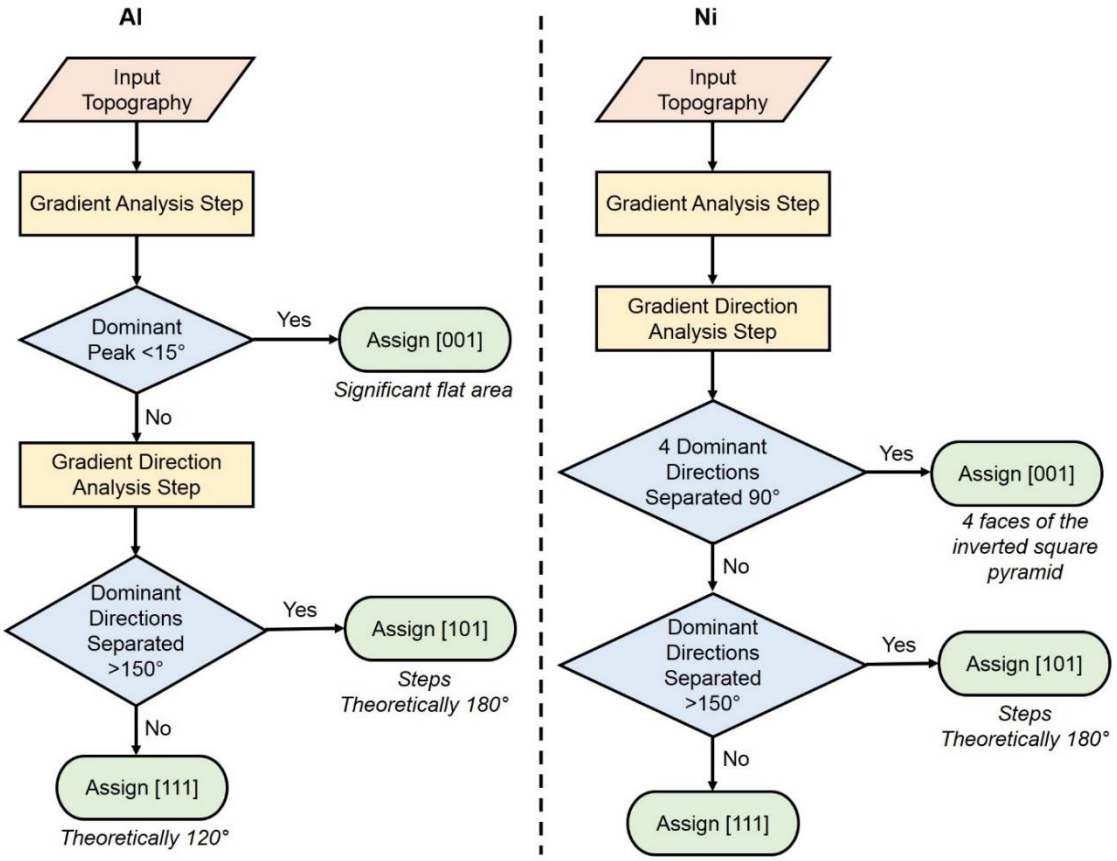


Figure 4.24: Topography analysis flowcharts to assign orientations for Al (left) and Ni (right), through correlation of topography observations with CSI datasets.

4.3.5. Crystallographic orientation mapping and validation

Grain orientation texture maps were generated for Al and Ni specimens, through EJP large-area analysis, and are shown in Figure 4.25 and Figure 4.26 respectively. Comparing with prior SRAS orientation data (*see* Figure 4.25a) in Al, EJP large-area surface processing (50 A/cm^2, v_h = 0.5 mm/s) reveals grain-dependent reflectivity (*see* Figure 4.25b). This surface was measured (<20 s per 160x160 µm acquisition), to output an orientation contrast map (*see* Figure 4.25c). SEM analysis of grain topographies show textures expected from the respective assignments in Al (*see* Figure 4.25d-g), demonstrating large-area

method repeatability. In addition, clear boundaries are observed, where intergranular corrosion is <2 µm wide (*see* Figure 4.25h, i), significantly less than the sampling distance used in this technique (42 µm per pixel).

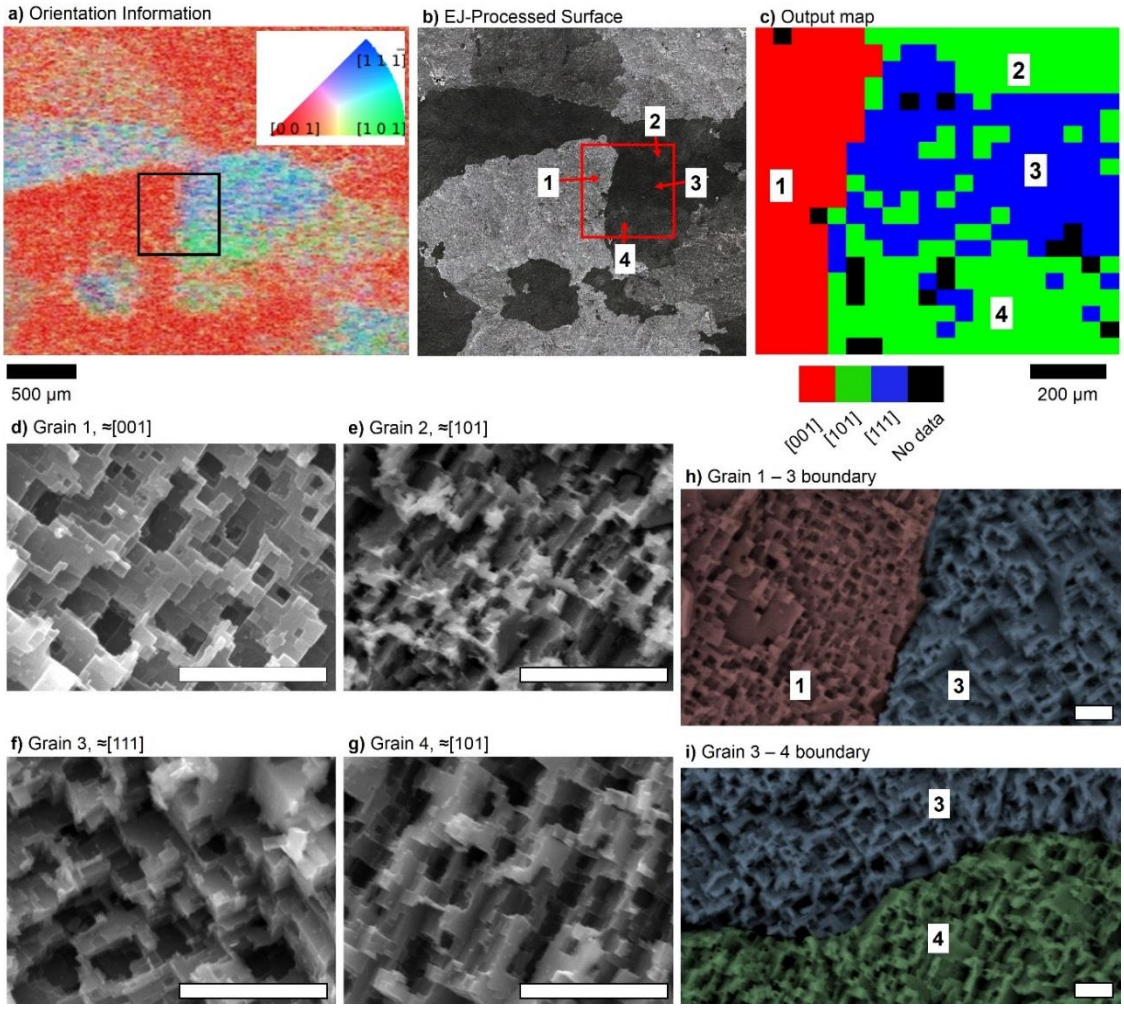


Figure 4.25: For Al, a) subjected to prior SRAS orientation analysis (50/100 µm per pixel). b) FVM (20x objective) of large-area processed surface (inset red, CSI acquisition area). c) Topography orientation output map (42 µm/pixel), following the surface-analytical process (red [001], green [101], blue [111], black – no data), where grains are assigned to closest principal orientations. SE micrographs showing d) grain 1 topography, assigned [001], e) 2, assigned [101], f) 3, assigned [111], g) 4, assigned [101] (f). Tinted micrographs showing boundary zones between h) grain 1 and 3, and i) grain 3 and 4, in both cases, the intergranular crevice (where topography is not representative of the underlying orientation) is <2 µm wide. SEM scale bars are 2 µm.

For Ni, prior EBSD data (*see* Figure 4.26a) was down sampled to three-colours, against which to benchmark the EJP topography approach (*see* Figure 4.26b). The resulting output orientation map EJP surfaces is shown in Figure 4.26c. The map is in close agreement with prior EBSD data on a pixel-by-pixel basis (68% pixels correctly assigned) (*see* Figure 4.26d). Correlated pixel assignment was greatest for [001] grains (75%), followed by [101] (65%) and [111] (62%), shown in Figure 4.26e. Here, three causes of uncorrelated pixels are observed, resulting in mis-assignment: 1) material removal, where the revealed microstructure is not representative of the near-surface microstructure, measured by EBSD (≤50 μm of Ni was removed, *see* Figure 4.2), leading to shifting boundaries during etching, also the complete corrosion of grains, 2) hybrid topographies of unpolarised grains not vicinal to any principal orientation; surfaces appear representative of the more dominant removal directions (Ni <001>). It is believed this could explain the bias of mis-assigned pixels from [101] grains to [001], ahead of slow-dissolving [111] (*see* Figure 4.26e), 3) grain-boundary effects, such as where stepped edges are generated, exhibiting [101]-characteristic topographies (*micrographs see* Figure 4.26f-i).

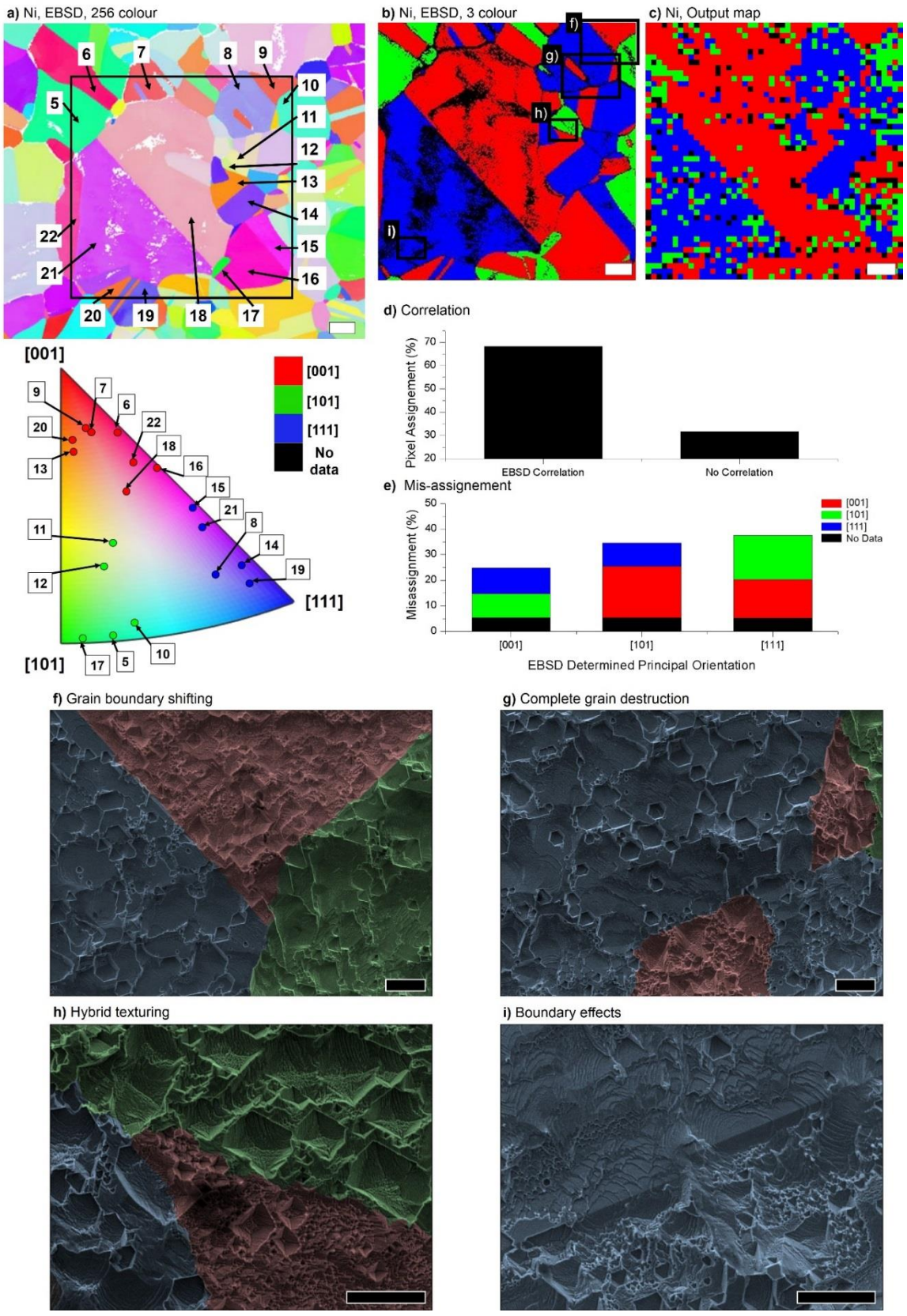


Figure 4.26: For Ni, a) appraised by prior EBSD orientation measurement (256 colour raw dataset), CSI acquisition area black inset (50x objective), with labelled grains. b) EBSD data down-sampled to three-colours, through bin assignment to the closest

principal orientation for comparison, grains labelled as per inverse pole figure. c) Output planar texture map (42 µm/pixel, colour convention as Al, showing orientation contrast and d) good correlation (68%) with prior EBSD data on a pixel-by-pixel basis. Three causes of non-correlated pixels are identified here: surface destruction, f) resulting in apparent grain boundary shifting, and g) complete corrosion of prior measured grains – the annealing twin within grain 8 is removed, and therefore not assigned in output map; h) bisection of parent-grain orientation - texture shown likely to be grain 11 (after complete corrosion of grain 12), which has an orientation bisecting [001] and [101]. Our process has assigned to [001], largely as a consequence of the inverted pyramidal topography. i) Mis-assignment caused by boundary effects: similar ≈[111] grain boundaries mis-assigned to [101]-type texturing, due to the large step between the grains. Orientation map scale bars (white) are 200 µm, SEM scale bars (black) are 50 µm.

4.4. Summary

This chapter demonstrated how surface topographies resulting from EJP are influenced by the microstructure, such as stress and thermal treatment, whereby superficially similar materials can exhibit drastically different topographic response to the same process. Suggestions are made to inform practitioners wishing to avoid operating regimes where discrete material-dependent textures are generated. However, it is acknowledged that such topographies contain potentially valuable information concerning the microstructure and crystallography of the material. Subsequently, EJP is presented as a route through which orientation-dependent topographies can be reliably generated in a range of engineering materials for the purpose of microstructural analysis. The first section of the chapter determined the effect of annealing and cold-rolling on the surface topography of copper over a broad current density range. EJP of copper leads to porous surfaces where the material has not been annealed prior to processing, due to the initiation of pitting

events at discontinuities in the lattice. In addition, severe plastic deformation is shown to affect the resulting surface topography, whereby slipped lattice planes are observed at the surface after processing. EJP, when accompanied with surface analysis is proposed as a route through which defects within a material can be characterised as part of a low-cost, low-intervention process.

The second section characterised the anisotropic orientation dependent topographic response for different engineering materials (Al and Ni) to EJP using an aggressive NaCl electrolyte. The purpose of this investigation was to lead the creation of an entirely novel materials characterisation technique, whereby information pertaining to the crystallographic orientation could be acquired from the topographic interrogation of electrochemical jet processed surfaces. The resulting technique is currently able to bin a given grain of an engineering material, where the process response has been subjected to prior characterisation, into one of the principal orientations. The technique shows a 68% correlation with prior EBSD data. However, it is acknowledged that true comparison is inherently difficult considering material removal in EJP (10s μm, *see* Figure 4.2), when comparing with EBSD surface characterisation that is surface sensitive to the nm scale. Whilst the information is clearly of a lower quality than conventional microstructural characterisation techniques, such as EBSD and SRAS, the capital expenditure of the technique is small in comparison, and the process can be undertaken in ambient conditions, allowing incorporation into on-line processing strategies and factory floor technologies. In addition, increasing the quality of extracted data is the subject of further investigation.

5. EJP of multiple-phase materials

5.1. Introduction

The literature review indicated a lack of fundamental investigation in materials containing multiple phases (*see* section 2.2.3.4, page 44), concerning both the topography and the form of the electrochemically processed feature. As indicated in Chapter 4, this is a concern considering the targeted application of the technique towards highly stressed aerospace parts that could be generated with complicated and inhomogeneous microstructural distributions.

Generally, austenitic stainless steels have been appraised in prior studies, largely due to the excellent response of this material to EJP in terms of highly controllable surface roughness and localisation of oxidation effects. This effectively represents selecting an optimum material for a given machining process, and is useful for process parameter characterisation. Such studies represent valuable contributions to the field as these have unravelled fundamental aspects of the process, providing useful information to the EJP practitioner. Building on this to develop EJP further, it is necessary to interrogate more complex materials systems. This is pertinent considering most materials in high-stress applications are selected for their advantageous material properties and not necessarily machinability. Such investigations therefore have the potential to represent notable contributions towards advancing EJP.

5.2. Effect of annealing treatments

Samples were prepared in accordance with the experimental section 3.1.2. Etched microstructures are shown in the optical micrographs in Figure 5.1.

Predictable increases in grain size with annealing temperature are observed [223], as well as changes in the resulting phase ratio, with α-phase (fcc, lighter colour) concentration decreasing and β-phase (bcc, darker colour) concentration increasing as the annealing temperature is increased.

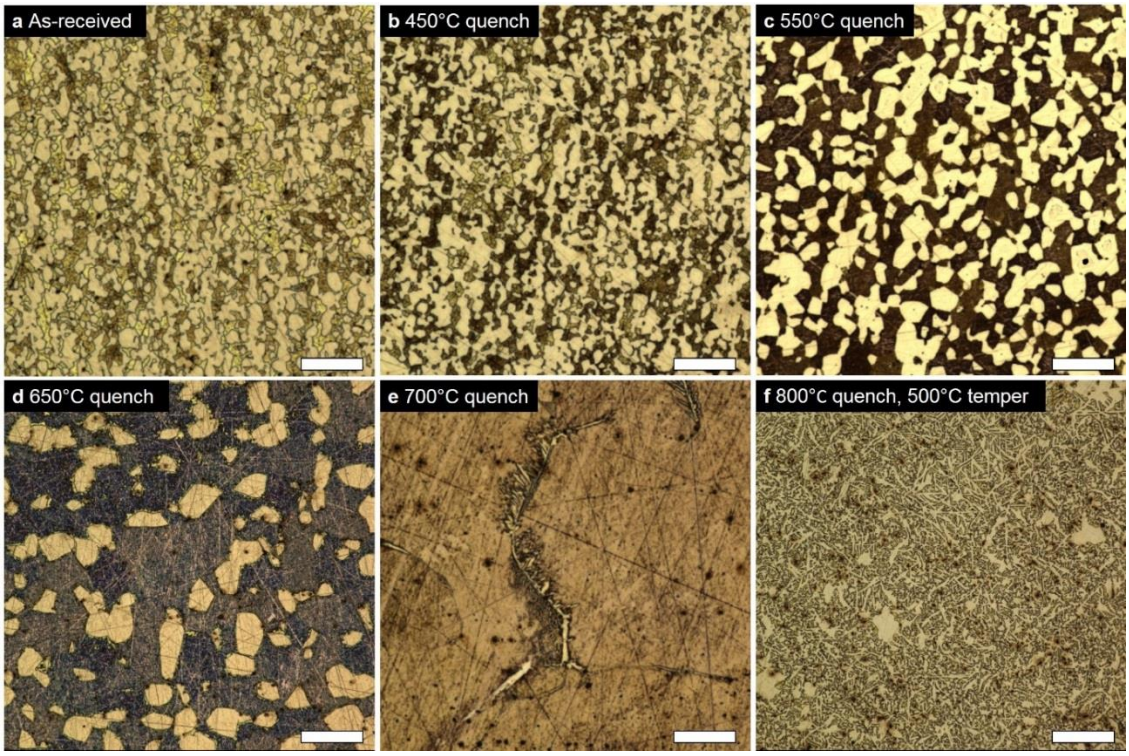


Figure 5.1: Etched microstructures of brass preconditions. An increase in grain size is observed with increasing annealing temperature, as well as a decrease in apparent α-phase. All scale bars 50 μm.

For the sample tempered after annealing (800-T), shown in Figure 5.1f, a finer microstructure than the as-received condition is generated. Samples of each precondition were etched using acidified ferric chloride solution for initial microstructural inspection [200]. Optical micrographs were acquired using a focus-variation microscope (20x objective), and resulting microstructures are shown in Figure 5.1b-f respectively.

The component phase ratio, and grain size, were quantified according to the methodology in Figure 5.2. From an etched surface, shown in the optical micrograph (*see* Figure 5.2a), energy dispersive X-ray spectroscopy (EDS) was performed in order to characterise the phase compositions (Cu and Zn only) in the respective samples (*see* Figure 5.2b). In this study, the contribution to the machined surface from Pb was ignored as this phase is insoluble in brass and is known to form small (1-2 μm) discrete globular particles, which are included to act as chip breakers to enhance conventional machinability. Due to the large atomic mass, the volume fraction of this element is relatively small [224]. EDS was undertaken using the system detailed in section 3.7.1 (20 kV beam, 60s acquisition time, minimum 6 spectra per phase per precondition). Binary images were generated from optical micrographs after thresholding in ImageJ, (*see* Figure 5.2c), where α-phase grains appear white (grayscale, 0), and regions of β-phase black (grayscale, 255). Appraisal of the number of pixels corresponding to each phase in the whole binary image allows for estimation of the phase ratio, shown in Figure 5.2d. From the binary image, line profiles can be acquired (*see* Figure 5.2e), from which the grain sizes were quantified, shown in Figure 5.2f. Profiles were taken at four different orientations for each micrograph in order to negate directional effects associated with rolled materials. This method counts grains through the identification of grain boundaries, and therefore is less accurate when appraising the size of interconnected grain structuring. This is exemplified for the finer microstructure, shown in Figure 5.1f, compared with samples of discrete grains, as it cannot characterise the interconnected nature of the basket-weave matrix. However, it instead gives an approximation of the α-phase lath diameter in the subject.

Applying Equation 2, the ECE of given phases can be calculated through weighting of the pure material ECE, applying the respective phase compositions of Cu and Zn (after conversion to atomic %), observed experimentally by EDS (*see* Figure 5.2b). Thus, β-phase ECE is always greater than α-phase ECE (ECE for as-received precondition: α = 0.3329 mg/C, β = 0.3335 mg/C).

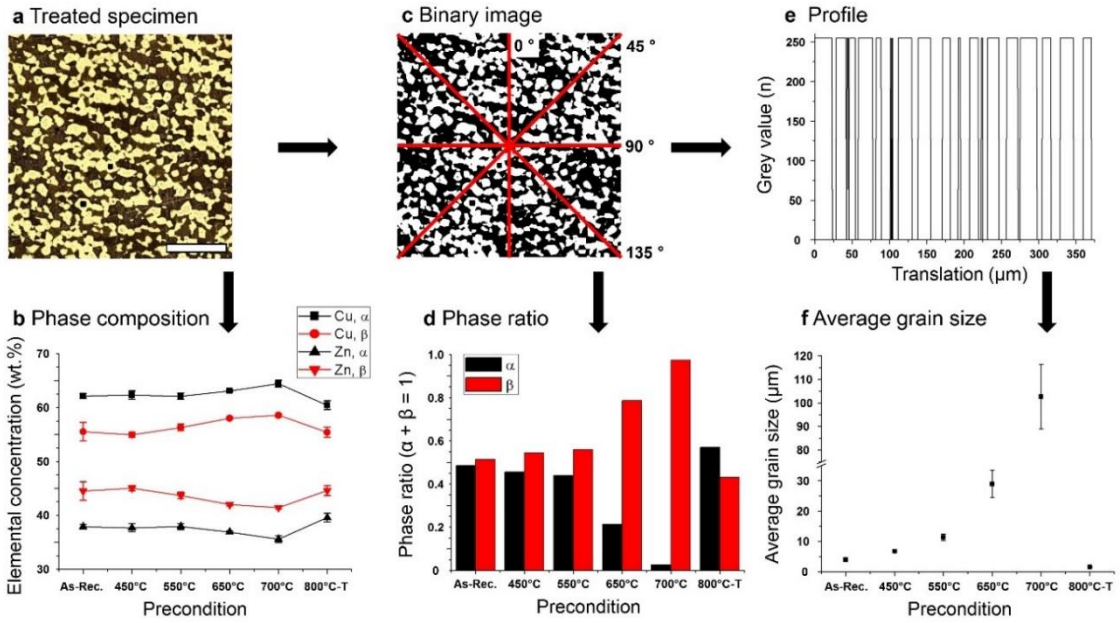


Figure 5.2: Effect of pre-treatment on microstructure and phase composition. a) Optical micrograph of etched surface. b) EDS phase compositions at each precondition. c) Binary image from optical micrograph, from which d) the phase ratio (α/β) can be obtained through pixel counting, α-phase white and β-phase black. e) From the binary image, greyscale profiles can be acquired at different orientations, where each step (0-255) corresponds to a grain boundary. f) Grain boundaries per length, allows average grain size approximation through the linear intercept method. Error bars are the standard deviation from the mean, calculated from the grain sizes returned from at least four profile orientations in each material. Scale bar 100 µm.

5.3. Point processing topographies

The workpieces were subjected to identical EJP point processing treatments, where the parameters are outlined section 3.3.2 and detailed in Appendix 5. A key characteristic of the brass surfaces appraised here, and indeed of multi-phase materials in general when processing with electrochemical techniques, is the preferential machining of one phase relative to another. In this case, the α-phase, which has a marginally lower electrochemical equivalent (ECE, *see* Equation 2) and significantly greater corrosion resistance, considering standard oxidation potentials (*see* section 2.2.3.1, page 35), is retained at the surface, while the β-phase is removed preferentially. Evidence for this is shown in Figure 5.3, for the preconditions machined at identical EJP treatments (100 A/cm^2), whereby the α-phase observed in the optical micrographs in Figure 5.1 correlates with the protruding grains in the SE micrographs and surface reconstructions presented in Figure 5.3. This is expected as a result of the lower ECE and higher corrosion resistance of the α-phase, except for the predominantly single-phase workpiece (700°C, *see* Figure 5.3j). Even in this workpiece however, retained α-phase present at the grain boundaries, is shown to protrude in the accompanying SE micrograph (*see* Figure 5.3i). The SE micrographs and accompanying reconstructions show that the observable surface is closely related to the underlying material microstructure, and larger prior α-grain sizes are retained at the surface after machining. Furthermore, it should be noted that the relative phase machinability is apparently independent of the phase electrical conductivity considering the α-phase (fcc, Cu-rich) is likely to be the most conductive phase in comparison to the β-phase (bcc, Zn rich).

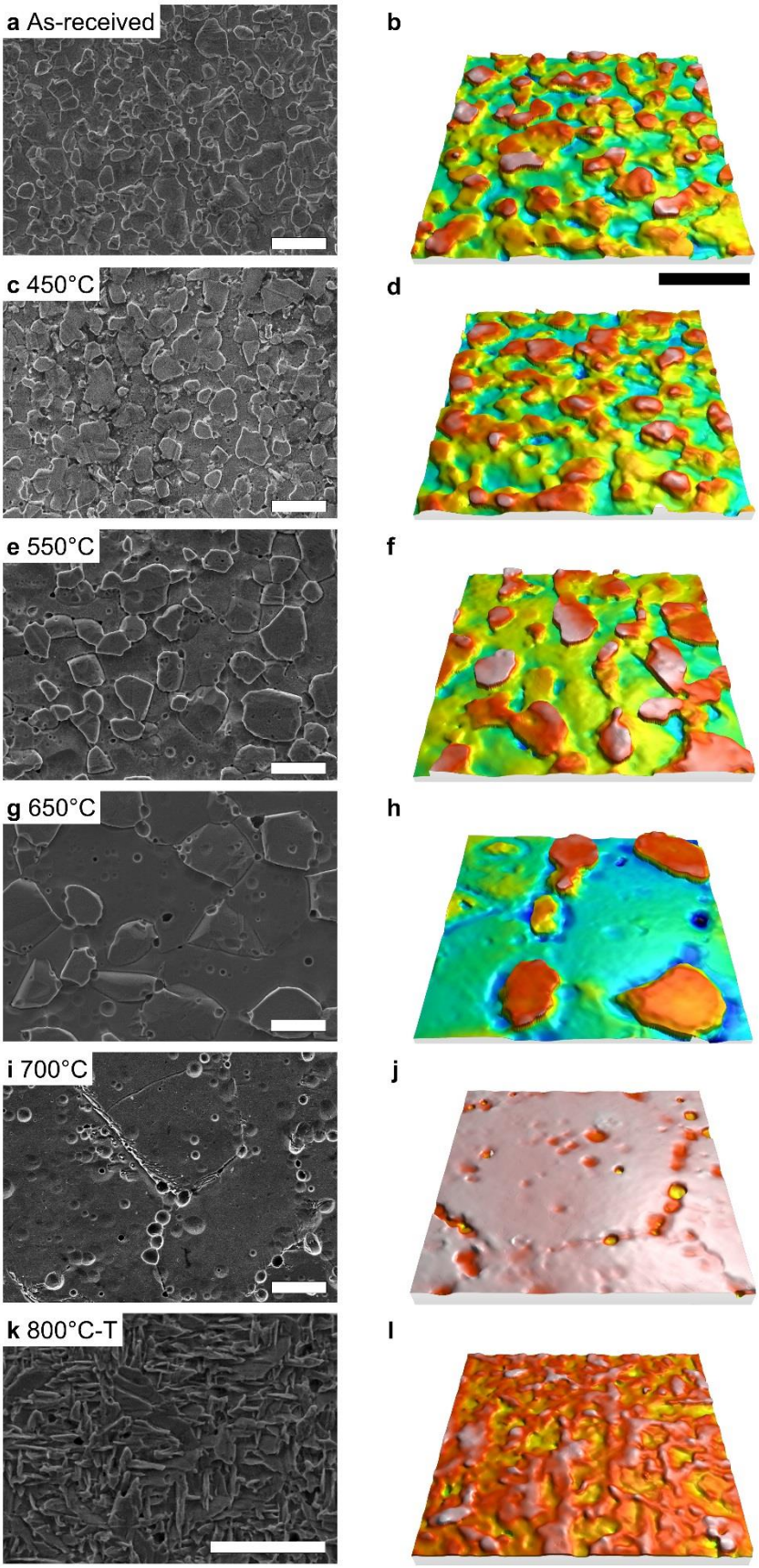

a As-received
b
c 450°C
d
e 550°C
f
g 650°C
h
i 700°C
j
k 800°C-T
l
0
1
2
3
4
5
Depth, µm

Figure 5.3 (Overleaf) Surfaces resulting from equivalent EJP operations (100 A/cm^2) on the workpieces. SE micrographs a, c, e, g, i, k), show the protrusion of α-phase grains after EJP in all cases, including i, where fine α-phase structures are observed in boundary areas. Reconstructions (100x magnification) b, d, f, h, j, l), showing the relative protrusion of surface phases can be quantified. Scale bars 20 μm.

As the material microstructures tend towards single-phase (550, 650, 700°C conditions) and the number of β/β grain boundaries increases (as a proportion of the total boundary length), intergranular attack of β/β grain boundary areas becomes clear. This manifests as multiple hemispherical (isotropic) micro-pits along the length of the grain boundary. This is likely the result of the lower activation energy required for the liberation of a given metal atom as the long-range order of the crystalline lattice is disrupted in this area. The more electrochemically inert nature of the α-phase appears to prevent these isotropic pitting events from occurring at dissimilar α/β grain boundaries. Material removal instead occurs around a given α-phase grain in a homogenous manner, resulting in undermining. This is due to a current-focussing effect, resulting in highly localised current density increases at the edges of α-phase grains. This effect has been simulated for inert ceramic-type phases by Hackert-Oschätzchen et al. (2016) [138] and leads to the depression of the inter-boundary zone on the β-phase side, which is easily observed in the 650°C annealed condition (*see* Figure 5.3h).

Topographies were quantified using FV microscopic data (100x objective), using the metrics of areal arithmetic mean height, *Sa*, and root mean square height, *Sq*, to describe the surface amplitudes. In both datasets, shown in Figure 5.4, the surfaces for all of the workpieces appear to follow similar power-law trends with applied energy, although the magnitude of the height changes

with precondition in some cases. For the as-received, 450°C, and 550°C annealed samples, no difference in height beyond the error range is detected for current densities >50 A/cm^2, although there is some variation at the lowest current density tested (20 A/cm^2). The smallest heights, corresponding to the smoothest surfaces were achieved with the 700°C annealed workpiece, a result of the predominantly single-phase nature of the material, which leads to a significant reduction in the amount of protruding α-phase.

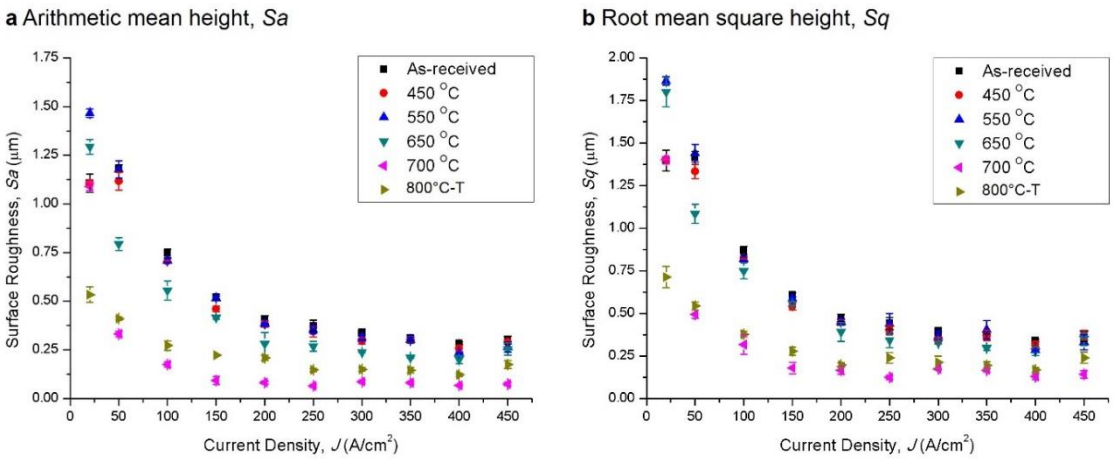


Figure 5.4: Surface roughness analysis for pits. a) Sa, b) Sq. Error bars are the standard deviation from the mean for three processed pits at each data point.

From this data alone, it is not possible to determine the impact of grain size on pit roughness (*Sa*, *Sq*), as the phase fractions of α- and β- have also been varied during pre-treatment. Where the phase ratio tends towards one phase, lower roughness is observed, a consequence of the reduction in the influence of relative machining rates on the resulting surface. However, from the data presented it is clear that grain size does have some effect on the roughness. For example, the 800°C-tempered condition, having the smallest grain size (approximately 1.5 μm) and a similar phase ratio to the as-received, 450°C, and 550°C samples results in lower surface roughness after equivalent processing.

Surfaces were subsequently appraised with respect to their volume parameters; peak material volume (*Vmp*), core material volume (*Vmc*), core void volume (*Vvc*), and valley void volume (*Vvv*), in order to characterise the distribution of surface volume with respect to current density and material precondition. Extracted data are shown in Figure 5.5. For all volume parameters, an inverse relationship is observed with regard to current density, indicating a smoother surface due to electropolishing effects, correlating well with areal height analyses (*see* Figure 5.4). At low current densities, the 650°C annealed condition is shown to have the greatest *Vmp*. This is likely to be the result of the largest α-phase grain size, which protrudes from the surface after EJP. Conversely, the tempered sample (smallest α-phase grain size) and the 700°C annealed condition (predominantly β-phase), show the lowest *Vmp*. In terms of valley void volume, the 700°C annealed condition shows the most, correlating well with Figure 5.3j, representing a quantification of the prior-observed intergranular attack of homogenous β/β boundaries in the predominantly single-phase material. For all surfaces except the 700°C annealed, and 800°C-tempered conditions, *Vmc* data is lower than *Vvc* (*see* Figure 5.4b and c), which indicates a significant fraction of the total surface volume being empty space. This is expected as these workpieces are rich in β-phase, which preferentially etches to leave a topography dominated by protruding α-phase grains. The difference between *Vmc* and *Vvc* is reduced somewhat, as current density is increased, demonstrating flatter surface topographies, likely to result from a tendency towards a more equal removal of α- and β-phases as electropolishing effects increase.

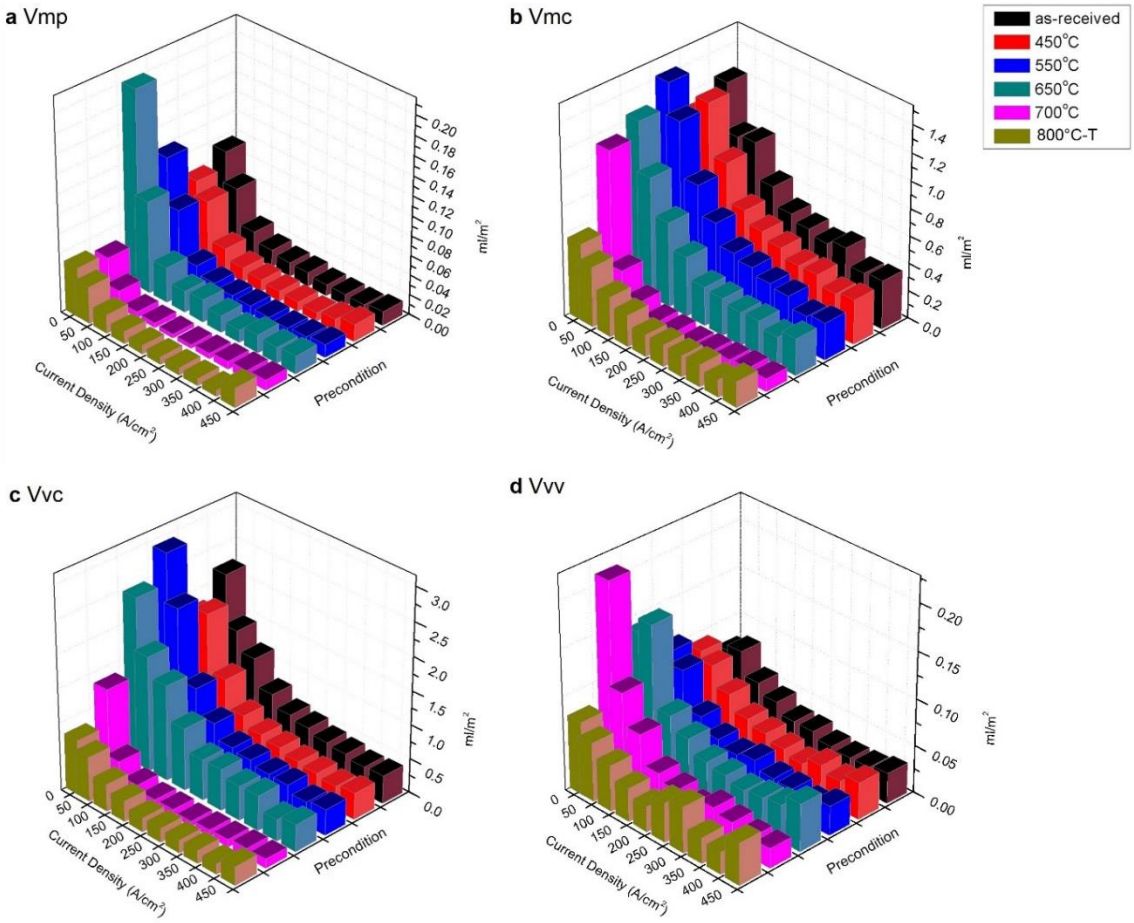


Figure 5.5: Volume parameters from the surfaces of pits machined in the different brass microstructures. a) Vmp (peak material), b) Vmc (core material), c) Vvc (core void), d) Vvc (valley void).

5.4. Striation processing topographies

Surface amplitudes observed in point machining are not representative of the conventional vector approach to EJP, which is most commonly practised. In this case, the electrolyte jet is translated across the workpiece as part of a two-dimensional toolpath, whereby the current density distribution lead-in and lead-out are lower than the central processing regime in the jet. The latter affects the resulting topography, lowering the effective surface defining current density. This implies that microstructural differences that cause insignificant differences

in point processing are likely to affect the topography across a broader J_{noz} range, in vector processing. To appraise the microstructural effects in an environment more similar to conventional electrochemical jet processing, striations were machined in identically treated samples at equivalent feed rate and three current densities (J_{noz} = 20, 100, 300 A/cm^2), detailed in Appendix 5. At all tested current densities, there is a clear increase in surface amplitude with grain size, up to the 550°C annealed condition, at which point surface amplitude decreases, even as grain size is significantly increased (*see* Figure 5.6a). This results from the increasing phase-fraction of the dominant β-phase, leading to a machined surface more typical of a single-phase material. For this material, there is a shift in the surface-defining mechanism becoming less dependent on the grain size, and more dependent on the phase ratio. This effect is shown to be independent of current density within the range tested.

The low surface amplitude (in comparison to point machining) attained at low current density (J_{noz} = 20 A/cm^2) appear uncharacteristic. Here, a fraction of the measured surface is comprised of α-phase grains from the original surface, subjected to the preparatory surface polishing routine, indicating that in this case, the amplitude is defined by the material removal as well as a microstructural characteristic. In contrast, at higher current densities, where all of the prior surface was removed in the process, larger surface amplitudes are observed. Despite this, in vector processing, the dependence on current density of the surface amplitude is reduced in comparison with point machining and microstructural effects dominate the topography. This is due to an equilibration effect, whereby the final current density experienced by a given point of the machined surface is lower (lead-out of the *J* distribution) than that experienced

by the central region of a machined pit. Therefore the surfaces are defined by more equal current densities than implied by the supplied current density (J_{noz}).

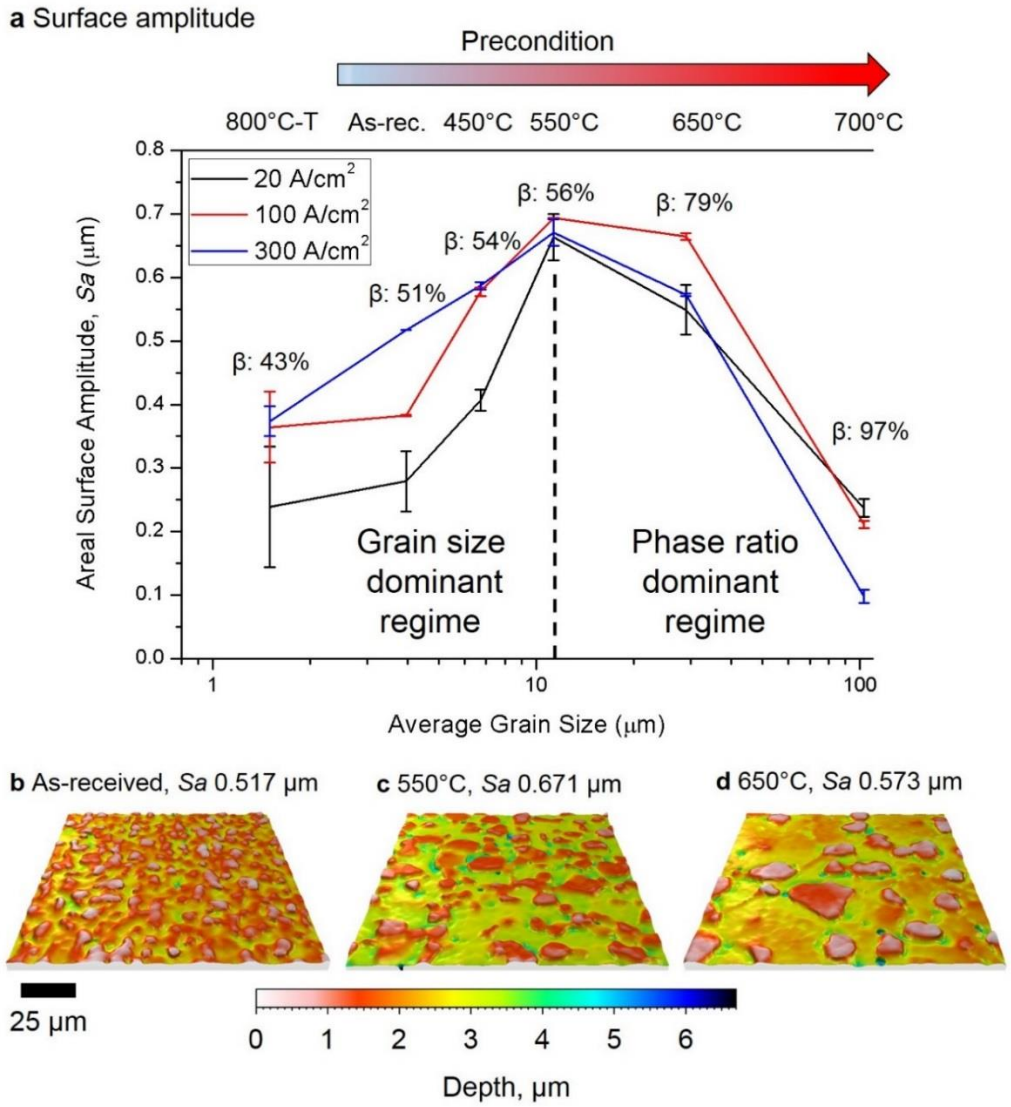


Figure 5.6: a) Roughness, Sa, of striations machined at three current densities (20, 100, 300 A/cm^2) in the different material preconditions (note log scale). Topographic reconstructions from samples machined at high current density (300 A/cm^2), where surface roughness increases with grain size from b) as-received material to c), the 550°C precondition, and then decreases for preconditions beyond, as the surface volume of protruding α-phase decreases, d) shown for the 650°C precondition.

5.5. Relative phase etching

The apparent shift in dominant surface-defining mechanism from grain size to phase ratio in this material can be understood through consideration of the relative phase machinability. This was appraised for the different preconditions, through the quantification of step heights, between α and β-phase of the point-machined sample set. A larger step height is indicative of greater relative machinability of a given phase. In Figure 5.7a, difference in machinability is shown to decrease as the current density is increased, from low J (α<<β), to high J (α<β). This supports the prior appraisal of pit surface roughness, *Sa*, *Sq*, decreasing as the current density is increased (*see* Figure 5.4a, b), which is indicative of the difference in machinability reducing as current density is increased.

In addition, there appears to be a correlation with grain size at low current density, where the difference in etch rate is greatest. Referring back to Figure 5.6 (vector processing), step height increases with grain size, (defining the first regime), increasing roughness. However, the number of discrete steps decreases as the phase ratio becomes more polarised, which leads to a reduction in surface amplitude (defining the second regime). The correlation between grain size and step height is exemplified in the extracted profiles at low (*see* Figure 5.7b) current density (for the two grain size extremes), where steps are demonstrably greater with increasing grain size. At higher current density (*see* Figure 5.7c), grain size has a lesser effect on relative machinability, and profiles are approximately equivalent in step height. At higher current densities, where electropolishing mechanisms dominate in EJP, and the relative machinability tends towards the electrochemical equivalent of the phases, the

amplitude of the machined profiles appears to be more equivalent, although the surface frequency, which is governed by the grain size, is different. This is supported by the data shown in Figure 5.7a, demonstrating that the average step height is smaller than the average grain size.

Grain size itself is not thought to make a significant difference to the relative machinability of given phases, as this is dependent on *J* and the composition of both the material and the electrolyte, however changes in grain size affect the step height between the two phases. The difference in step height with grain size, at J <50 A/cm^2, is proposed to be the result of an anchoring effect, wherein larger α-phase grains are retained in the workpiece for longer as the surface evolves into the material. Larger grains therefore allow greater protrusion.

Where the relative machinability of α<<β, (low current density), step height should tend towards α-phase grain size, however, the quantified result is smaller, with a large data spread. The spread can be partially explained by the stochastic distribution of α-phase grains within the material (*see* Figure 5.7d), where a discrete step height depends on the position of a given α-grain relative to the dissolution front (*see* Figure 5.7e). In addition, the step height will reduce from the average grain size, especially for a large-grained sample. As the dissolution front evolves into the workpiece during dissolution (increasing height difference), exposed α-phase grains will be subject to electrochemical attack regardless of the preferential machinability of the β-phase, as i) they will act as current-focussing features and ii) the α-phase surface area subject to attack will increase (*see* Figure 5.7f).

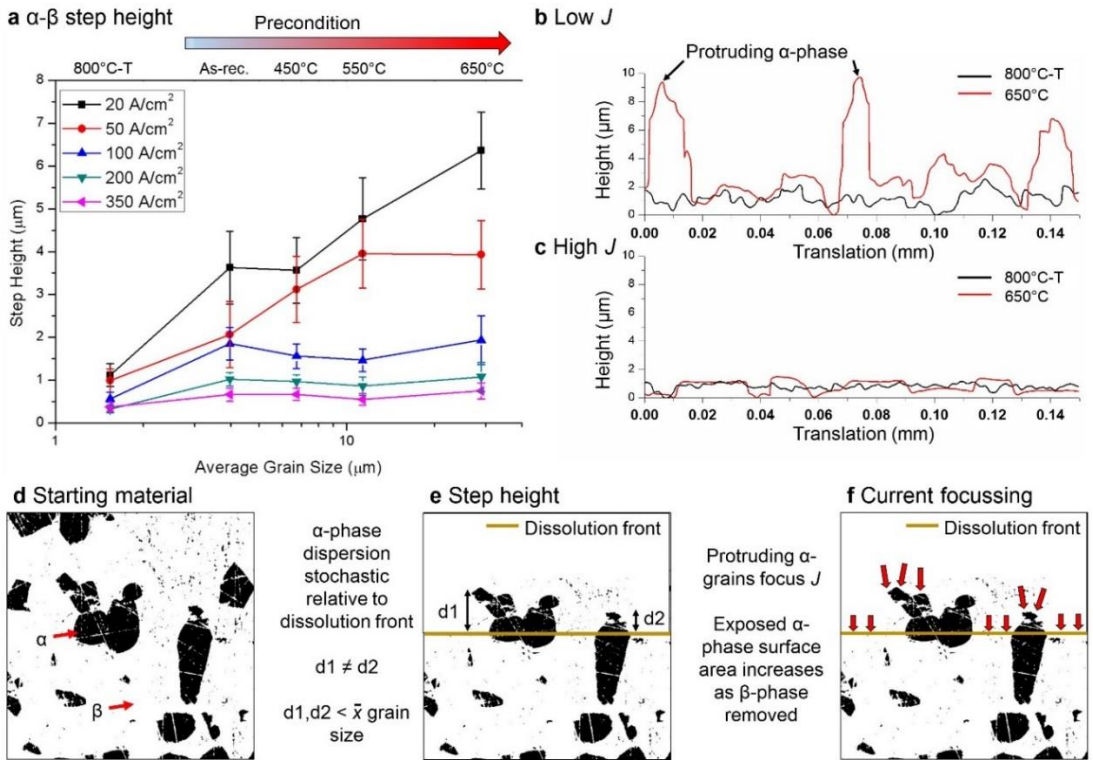


Figure 5.7: Step height measured between α- and β-phase across a range of current densities (20-350 A/cm^2), for all preconditions. Step height increases with grain size, evidenced in the exemplar extracted profiles from the extreme grain sizes in this study at low and high current density, b) and c) respectively. d) Schema viewed in cross section (α-phase black; β-phase white), step height is less than average grain size due to e) stochastic distribution of α-phase within the material and relative to the dissolution front and f) current focussing effects, which limit protrusion. Error bars are the standard deviation of the mean value of steps acquired from at least four profiles at each condition.

5.6. Near-surface chemistry

In addition to difference in machinability between the two phases, compositional changes are observed at the near-surface due to the different oxidation potentials of the elements present. As the more corrodible element in brass, considering oxidation potentials, it is more energetically favourable to liberate Zn from the surface compared with Cu, thus the relative surface concentration of relatively corrosion resistant Cu increases. This was appraised for sectioned

striations across current densities (20, 100 and 300 A/cm^2) and is shown in Figure 5.8. Zn concentration is depleted at the near-surface layer <1.5 μm in depth, especially at the lowest current density tested in this study. At 300 A/cm^2, surface concentration of Zn is more representative of the bulk material, indicating an increased rate (per charge passed) of Cu removal. This is largely thought to result from the surface dissolution rate, which is slow at 20 A/cm^2 (≤ 4 μm/s at jet centre; where the maximum surface dissolution rate is the ratio between the maximum pit depth and the machine time), when compared with a high current density of 300 A/cm^2 (≤ 65 μm/s at jet centre). When the rate of bulk material removal is low, the surface is exposed to the action of the electrolyte for a longer time period, thus selective removal between Cu and Zn is increased. This builds a Cu-rich layer over the β-phase as the Zn is preferentially leached. Conversely, where the dissolution rate is greater, selective removal is significantly reduced, such that the surface composition is more representative of the bulk material (*see* Figure 5.8f and g). The Cu-rich build-up at low current densities is likely to limit the preferential removal of the β-phase as dissolution evolves.

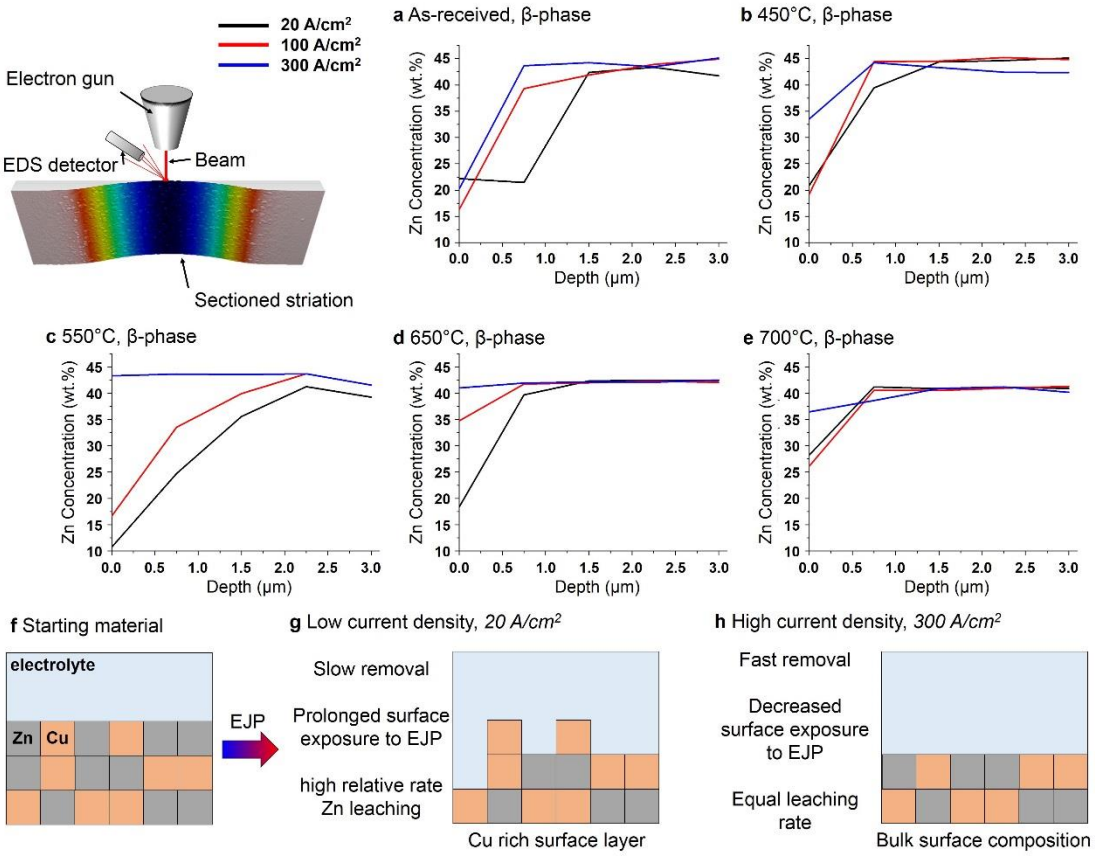


Figure 5.8: Spectral acquisition of β-phase Zn concentration (wt. %) of sectioned tracks (20, 100 and 300 A/cm^2), from EDS line-scans (6 points, 0.75 µm intervals), where β-phase grains were selected at the track centres. Dezincification is observed in all cases, and is more pronounced at low current density. This is shown in the schema f-h), where the leaching rate is dependent on current density.

5.7. Removal rates

A consequence of poor α-phase etching at low current density, is an erosive removal mechanism, whereby the inert phase is removed at a lower rate through anodic dissolution. Instead, as the surface evolves, α-phase grains are undercut and subsequently washed away in the electrolyte jet. Supporting evidence for this effect is shown in the tinted SE micrograph of a sectioned surface in Figure 5.9a, processed at low current density, where α-phase grains are undermined by the preferential machining of the β-phase. In the

reconstructed surface (*see* Figure 5.9b), this undermining effect can be appraised, complemented by the extracted profile (*see* Figure 5.9c), taken across points i-ii, which shows material removal exaggerated at the inter-phase grain boundary in this case, where the interface is up to 2 μm deeper than the adjacent β-phase grains. Evidence for the erosion of α-phase grains through undermining and wash-out mechanisms is shown in Figure 5.9d, of the 550°C annealed condition. Here, a recession where the width corresponds in magnitude to the average α-grain size in this material (11.3 μm, *see* Figure 5.2), can be seen in the central blue (deepest) area of the reconstruction. This is atypical of the surrounding surface and is likely to be the result of α-grain erosion. The accompanying SE micrograph of this area (*see* Figure 5.9e), shows a more irregular surface texture at the base of the recess when compared to the surrounding grains, indicative of a different removal mechanism.

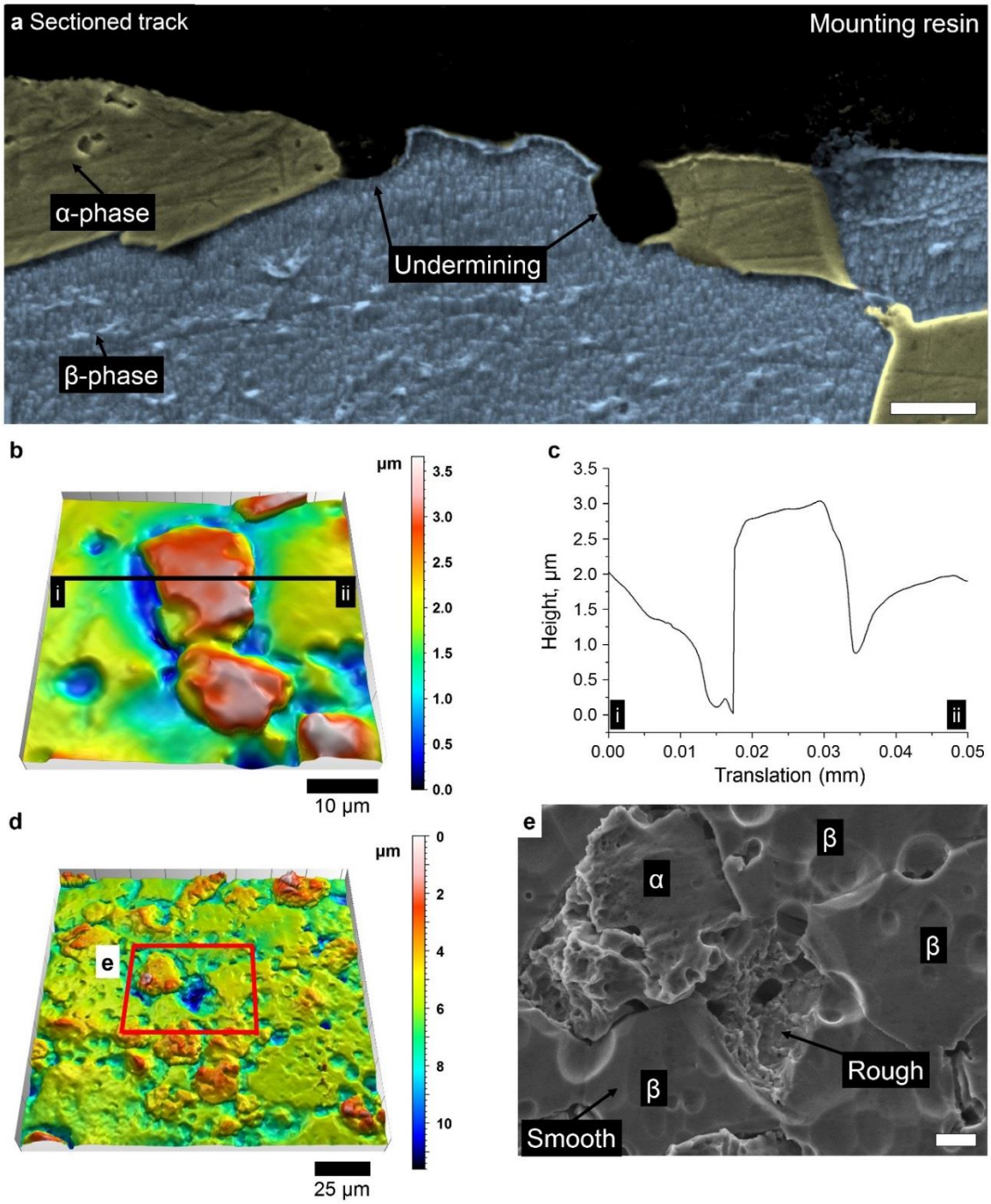


Figure 5.9: a) Tinted SE micrograph (α-phase yellow; β-phase blue) of striation section (650°C, v_h = 500 µm/s, 100 A/cm^2). α-phase grains are undercut. b) Reconstruction showing α-phase undercutting (650 °C, 100 A/cm^2), c) extracted profile d). Recess from probable wash-out event, corresponding in magnitude to the average grain size in this material (550°C, 50 A/cm^2), atypical of surrounding surface, e) SE micrograph showing a different surface texture at the base of this recess. All scale bars 5 µm.

The influence of possible erosive effects on the removal efficiency, was appraised through measuring the removal mass per unit charge (actual ECE) for the pit samples, at each condition, as outlined in the methodology, and shown in Figure 5.10a. This was compared with the theoretical ECE for the feedstock material (lower – light, upper – dark green, *see* Appendix 1). For erosion complementing anodic dissolution, an inverse relationship would be expected between α-phase grain size and removal volume, specifically at low current density. This is because the α-phase, which dissolves slowly at low *J*, (shown previously), is anchored less in the bulk as the grain size is reduced. Thus, the probability of a wash-out event is increased as the grain size is reduced. In addition, a finer dispersion of α-phase grains increases the number of discrete potential wash-out events over equivalent surface area. Large α-phase grains are retained in the bulk for longer periods, whereby they will eventually be subjected to anodic dissolution, once the field-focussing effects are increased, which occurs as the height differential between the protruding phase and the evolving β-phase surface increases. This is supported by the optical micrograph of a sectioned pit machined at low current density (20 A/cm^2) into the 650°C annealed condition (*see* Figure 5.10c), wherein flattened tops of the protruding α-phase grains are visible. This is attributed to field-focussing (described in Figure 5.7). In this instance, α-phase removal occurs predominantly through anodic dissolution – not erosion. This is contrasted by the optical micrograph of an equivalent pit in the as-received condition of supply, whereby cratering can be observed and rough topped α-phase grains can be seen (*see* Figure 5.10b) Figure 5.10a shows a correlation between removal

mass with grain size at low (20 A/cm^2) current density, except for finest-grained sample (800°C-T).

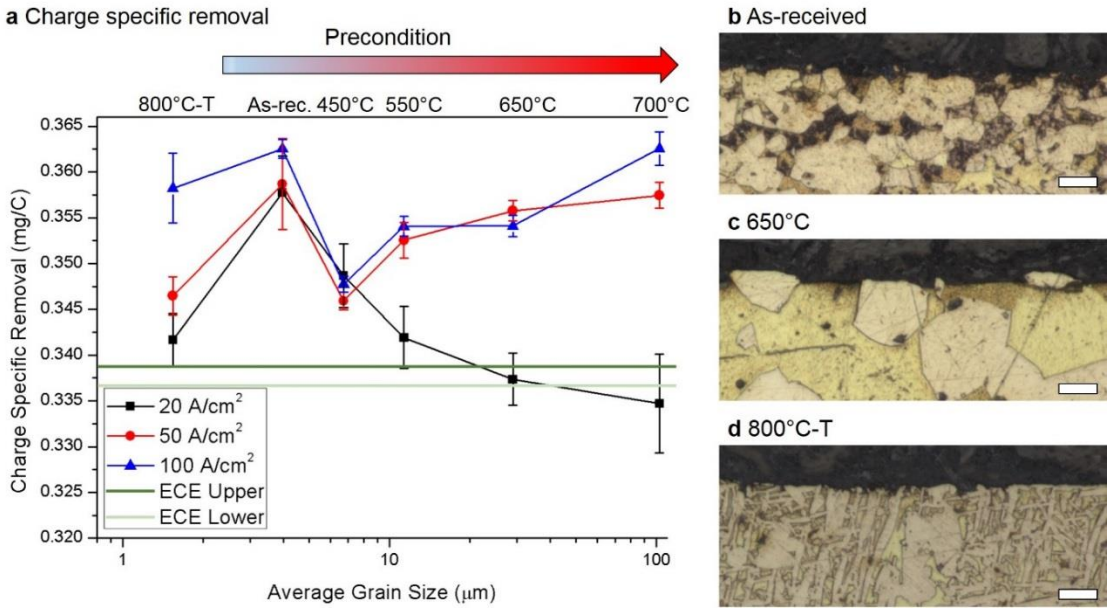


Figure 5.10: a) Charge specific removal (mg/C), shown for low, medium and high current densities (20, 100, 300 A/cm^2). Sectioned low current density (20 A/cm^2) pits machined into b) as-received, c) 650°C, d) 800°C-T conditions of supply. Error bars are the standard deviation from the mean of three discrete pits. Scale bars 10 μm.

For the as-received and 450°C annealed conditions, the charge specific removal at low current density is approximately the same as the higher current densities tested, within the range of error. Bhattacharyya (2015) [78], described the expected increase in material removal efficiency with current density in ECM. For Cu (the main element of this brass), Kinoshita et al. (1970) [120] showed the efficiency to be dependent on the valence state of dissolution. In active modes of dissolution (J ≤20 A/cm^2), liberated copper species tend towards Cu (II) (cupric). Schneider et al. (2012) [118] demonstrated that increasing the current density into the transpassive regime (J >20 A/cm^2), results in a gradual valence shift towards Cu (I) (cuprous), requiring a lower charge equivalent for liberation. In light of this expected valence change, it is

interesting that the two aforementioned conditions show similar charge-specific removal at all current densities tested. It is possible that this uncharacteristic removal behaviour is a result of erosive removal. As the current density is increased, anodic material removal is also increased, but the contribution from erosion is reduced, reducing expected removal gains. The correlation between grain size and material removal at low current density is broken by the precondition with the smallest measured grain size and basket-weave microstructure (800°C-tempered). This is thought to be a result of the conjoined nature of the α-phase grains, whereby each grain is anchored into a matrix microstructure, (*see* Figure 5.10d). This inhibits discrete wash-out events from occurring during processing, therefore the apparent removal mass is lower.

For the three largest grained preparations, charge-specific removal in low current density machining is shown to be significantly reduced compared with machining at higher current density (50 and 100 A/cm^2), and a more typical relationship between charge-specific removal and current density is observed. This is proposed to be a result of the reduction in the contribution of erosion to the material removal as grain size is reduced, and the phase ratio becomes increasingly skewed. The higher current densities tested show similar values of charge-specific removal generally independent of material precondition, thus the implication is that erosive contributions are either indeterminate or equivalent at these two current density levels, under these testing conditions. Discrete wash-out events are still likely to occur in these processing regimes, however at a lower frequency than at low current density, due to the increase in electropolishing phenomena, which equalise surface asperities, such as protruding α-phase grains.

5.8. Form observations

The microstructural contribution to the machined profile in EJP was assessed by appraising charge specific maximum depths for each material precondition, shown in Figure 5.11a. A positive trend in removal depth can be observed at all tested current densities for the three largest grained preconditions (550, 650, 700°C conditions), where depth increases are shown to be approximately consistent at the current densities tested here (20 A/cm^2,17%; 50 A/cm^2, 12%; 100 A/cm^2, 13%) across these material conditions. This is exemplified in the cross-sectional pit profiles showing the depth increase across the aforementioned preconditions in Figure 5.11b, at (20 A/cm^2). Deeper pits are of particular interest considering the lower removal efficiency of the 700°C condition at this current density level, and is suggestive of more precise material removal. Increasing grain size up to 11.3 μm (as-received, 450, and 550°C conditions, *see* Figure 5.2f) show no difference in removal depth, within the error range.

The deeper cuts in predominantly single-phase material are proposed to be a result of the ease of machinability of the β-phase. For such a material, removal occurs unperturbed at the centre of the impingement area, therefore appearing to localise dissolution. Pits therefore become deeper and narrower. A similar phenomenon has been previously reported in the EJP of Ti by Mitchell-Smith and Clare (2016) [25], considering electrochemically inert Ti-containing oxides. For a dual-phase material, the presence of slowly dissolving α-phase partially disrupts removal in the central region, broadening the form for controlled processing parameters, while the depth reduces, despite greater material removal rate for dual-phase materials at low current density. For the finest-

grained sample (800°C-tempered), removal depth is shown to increase with current density, a consequence of the large dispersion of α-phase. Removal of this inert and conjoined phase is largely dependent on the relative machinability, α<β, and thus is closely related to the current density parameter.

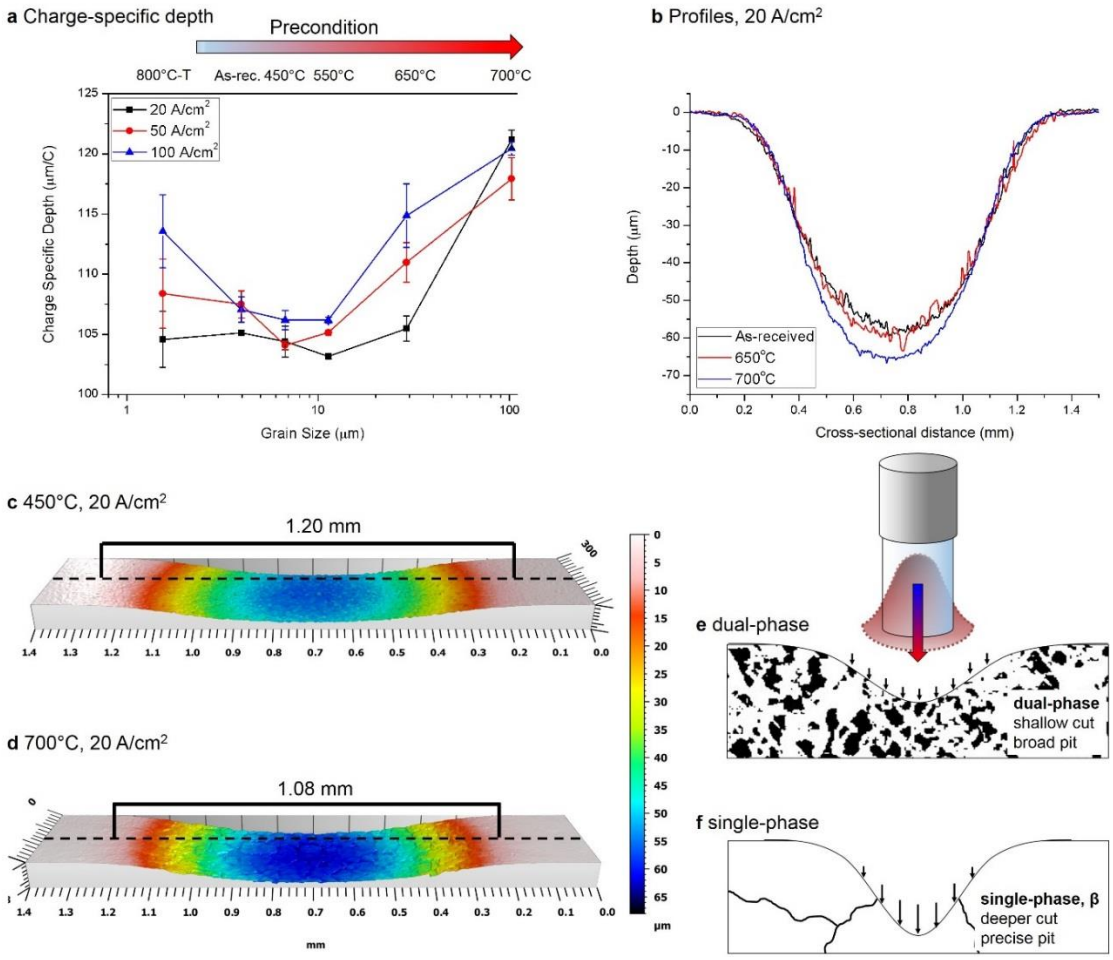


Figure 5.11: a) Maximum depth as a function of precondition at different current densities (20, 50 and 100 A/cm^2), showing increases between 550°C to 700°C preconditions. b) Cross-sectional profiles of pits machined at 20 A/cm^2, c) Reconstruction of a pit machined into the 450°C condition, showing a broad and shallower pit when compared with d), 700°C condition. e) Material removal disruption in the central region in a dual-phase material. f) In contrast, unperturbed removal occurs in the central area, thus broadening is reduced.

5.9. Summary

This chapter demonstrated that the topography, chemistry and form of the EJP generated feature is largely dictated by the microstructure even at high current densities (>300 A/cm^2). This is counterintuitive considering electropolishing mechanisms should dominate when processing $>J_{lim}$ for a given material. Partially, this is a result of high impingement velocities in EJP (≤30 m/s), which will suppress the diffusion layer thickness. This means that for dual-phase material systems of differential ECE, protrusions arising from differential MRRs may be greater than the polishing film thickness. Processing at low current densities is demonstrated to increase the leaching rate of the most reactive element, as increasing exposure time to the electrolyte increases selectivity. This is self-limiting in EJP, as upon depletion, the less reactive element is accrued at the surface. This is assistive as it prevents the sole removal of single phase types from dual-phase materials. The depth of this layer decreases with increasing current density.

For dual phase materials, the effect of the microstructure on the topography has been interrogated in EJP. The scale of topographic featuring for a given current density is determined not only by the grain size, but the overall phase ratio. Larger grains will result in greater surface roughness due to increasing the step height between dissimilar grains, however more polarised phase ratios (fewer grains of one type) results in fewer dissimilar boundaries. Therefore, polarised phase ratios result in smoother surfaces, regardless of grain size. It has been shown in EJP that grain size in dual phase systems affects not only the surface, but the removal rate through erosive-type removal, occurring by undercutting and wash-out, resulting from charge density focussing at boundaries.

6. Redefining the removal geometry in EJP

6.1. Introduction

The literature review highlighted areas in which EJP could be improved (*see* section 2.1.5). Specifically, identified areas relate to i) the poor dimensional accuracy and precision of EJP and ii) the poor electrochemical machinability of corrosion resistant materials. Modification of the applied electrolyte is proposed as a route through which these areas could be improved, while requiring no adaptions to either the tooling, or the apparatus.

Concerning electrolytes, the literature review indicated that passivating electrolytes, such as nitrates and sulfates, are generally employed in electrochemical processing technologies, where there is a desire to enhance the dimensional accuracy of the machined feature. This is largely the result of oxygen evolution in the low current density regions, which inhibits stray cutting. Despite widespread application of passivating electrolyte systems, contemporary EJP is limited by poor precision, taper and stray cutting. Therefore improvements in this regard will represent a valuable contribution to the field and increase the applicability in comparison to established micro-processing techniques, for example laser beam machining. Within the latter area concerning the micromachining of titanium, the literature review indicated that EJP studies concerning modification of the applied electrolyte have led to significant improvements in the micro-machinability, in terms of removal rates and precision, of tungsten containing materials. Titanium alloys also suffer from poor electrochemical processing. However, employing different electrolytes

beyond nitrate and chloride has been relatively unexplored in high-value manufacturing, an ideal target sector for EJP. Regarding titanium alloys, prior electrochemical research in these material systems has shown that halide-containing electrolytes, for example bromide and iodide can greatly reduce corrosion resistance, thus improving the electrochemical machinability. Such improvements could significantly increase the applicability of the technique towards aerospace manufacturing and are worthy of exploration. In addition, the Inconel 718 was investigated due to widespread application in aerospace and the poor conventional machinability, caused by rapid work-hardening.

6.2. Enhancing dimensional accuracy

6.2.1. Novel electrolyte systems

The experiments within this section were performed on Inconel 718 prepared as described in section 3.1.3. Prior literature indicates that nitrate-based electrolytes are most commonly applied in EJP instead of chloride (*see* section 2.3.2.3, page 53). This is due to the enhanced dimensional accuracy over cheaper chloride-based electrolyte solutions that makes nitrate more advantageous from a micromachining perspective. Dimensional accuracy enhancements over chloride result from i) lower electrolyte conductivity, which reduces the throwing power of the electrolyte and ii) from the formation of passive oxide films in the low current density area that consumes energy and represents a beneficial Faradaic loss. The latter mechanism effectively shields material removal, in comparison to chloride electrolytes, which readily de-passivate, regardless of applied current density. Since route i) (reducing electrolyte conductivity) will increase power consumption, or limit material

removal (depending on current or voltage limitation), it was decided to exploit a similar mechanism to ii).

To this end, iodide was identified as a suitable anion for doping of electrolyte solutions. In this regard, iodide is a strong reducing agent, such that the anodic oxidation of iodide to iodine, $E^{\ominus}\ 2I^- \rightarrow I_2 + 2e^- = -0.62\ V$ *vs.* standard hydrogen electrolyte (SHE), is extremely facile in comparison to commonly used anions, such as chloride, $E^{\ominus}\ 2Cl^- \rightarrow Cl_2 + 2e^- = -1.40\ V$ *vs*. SHE. The anodic generation of iodine is therefore proposed to represent a route through which energy that would otherwise be devoted to the anodic oxidation of nickel and other elements, is transferred. This competing anodic reaction would suppress material removal especially in the low energy regions of the current density distribution. To characterise electrolyte-material interactions, the efficiency of material removal across a range of energy levels in EJP was assessed, shown in Figure 6.1. In Figure 6.1a, electrolyte current efficiency is presented from J_{noz} = 20-200 A/cm^2, for conventional electrolytes: NaCl (2.3 M) and $NaNO_3$ (1.8 and 2.3 M). The jet velocity applied was 29.7 m/s.

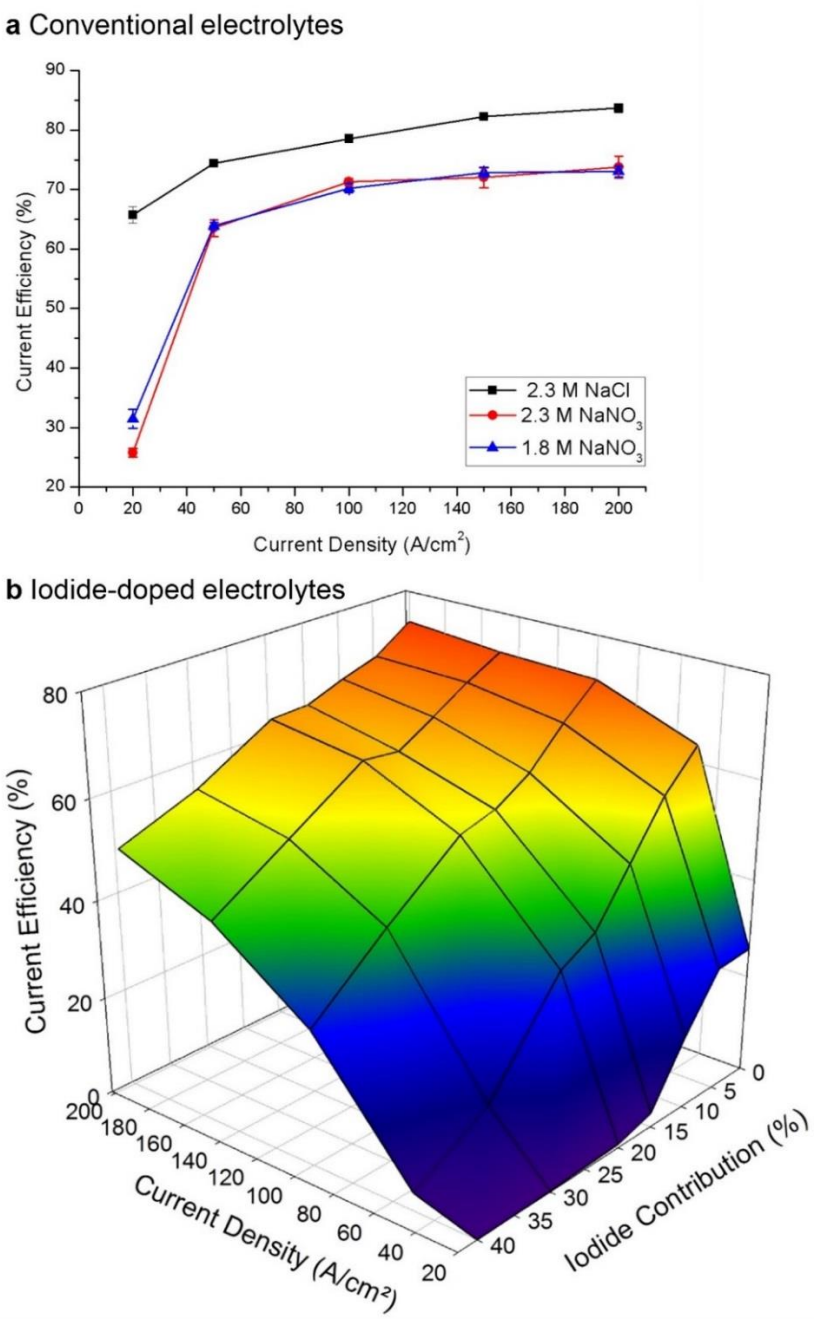


Figure 6.1: Effect of electrolyte on current efficiency in Inconel 718. a) Conventional electrolyte systems, b) increasing the contribution of iodide to ionic strength (2.3 M) suppresses material removal at all energy levels, although the effect is most marked at low current density, where removal is inhibited at concentrations >NaI 20%.

Consistent with prior observations, the current efficiency of NaCl demonstrates less dependence on current density than $NaNO_3$, due to the reduction of low current density passivation effects. In addition, decreasing the ionic strength of the electrolyte is shown to have negligible effect on the current efficiency within

these operating conditions. Whilst this may appear counterintuitive, it should be noted that current limitation was applied in this operation and the expected increase in electrical resistance was observed upon processing with the lower concentration electrolyte.

The effect of iodide doping of $NaNO_3$-based electrolyte at different concentrations, whilst maintaining the overall ionic strength (2.3 M) was assessed. Figure 6.1b shows that current efficiency is inversely proportional to iodide concentration for an Inconel 718 workpiece. Considering the increasing electrical conductivity of iodide-doped electrolytes over the un-doped $NaNO_3$, this phenomenon is likely due to mechanism ii): Faradaic losses within the process. This effect is especially marked at the lowest current density tested here (20 A/cm^2), and indicates the suitability of the dopant to suppression of low current density material removal.

To appraise this effect, pits processed in the same material at high current density (200 A/cm^2) were observed using focus-variation and scanning electron microscopies, shown in Figure 6.2. The strength of the dependence of current efficiency on current density, shown in Figure 6.1 can be correlated with the localisation of material removal and therefore the dimensional accuracy of EJP. For pits processed with NaCl, which demonstrates the weakest correlation between current density and current efficiency (*see* Figure 6.1a), large radius features can be observed (*see* Figure 6.2a, b), where significant removal can be detected in the low current density (edge) region of the machined profile. $NaNO_3$, as expected, shows significantly greater localisation of removal in comparison to NaCl, due to both the low current density passivation phenomena and the lower conductivity (*see* Figure 6.2c and d). Upon addition of iodide to

the electrolyte (in this case NaI 20%), further localisation of material is evident (*see* Figure 6.2e and f), caused by beneficial Faradaic losses. In addition, it can be seen that surface quality does not appear to be detrimentally affected by application of iodide doped electrolytes when processing this material system.

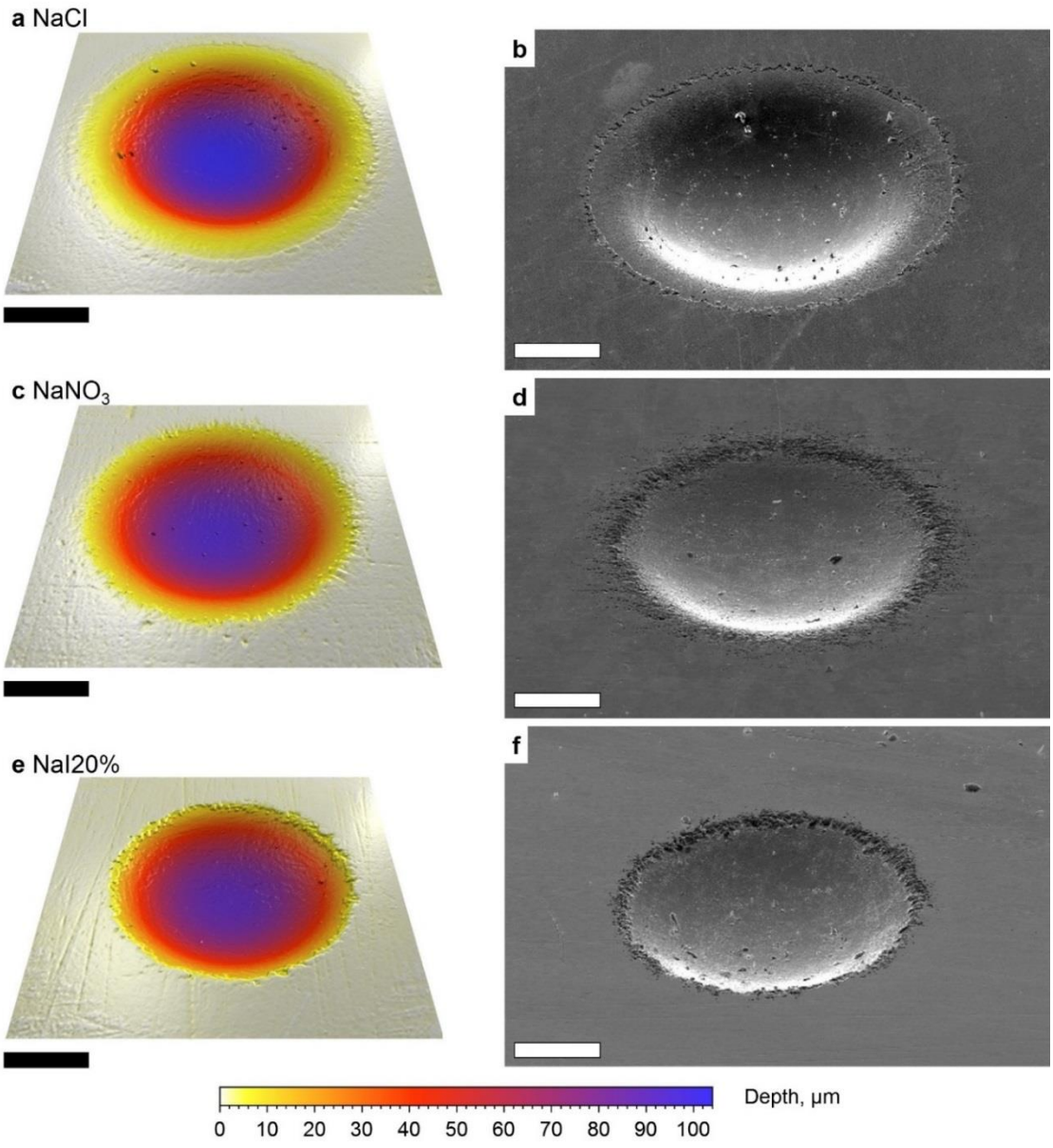


Figure 6.2: Effect of different electrolyte types on the removal feature. Pits machined at constant current density and dwell (200 A/cm^2, 4 s) using a 510 µm I.D. nozzle. a-b) NaCl, c-d) $NaNO_3$ and e-f) NaI 20%. All scale bars 250 µm.

The effect of changing the electrolyte on the key performance metrics of overcut $\left(\frac{kerf}{Nozzle\ I.D.}\right)$, and maximum pit depth were measured across current densities from 20-200 A/cm^2. The results are shown in Figure 6.3, in all cases overcut is shown to increase with current density, where greater material removal rates expand the feature and reduce removal localisation.

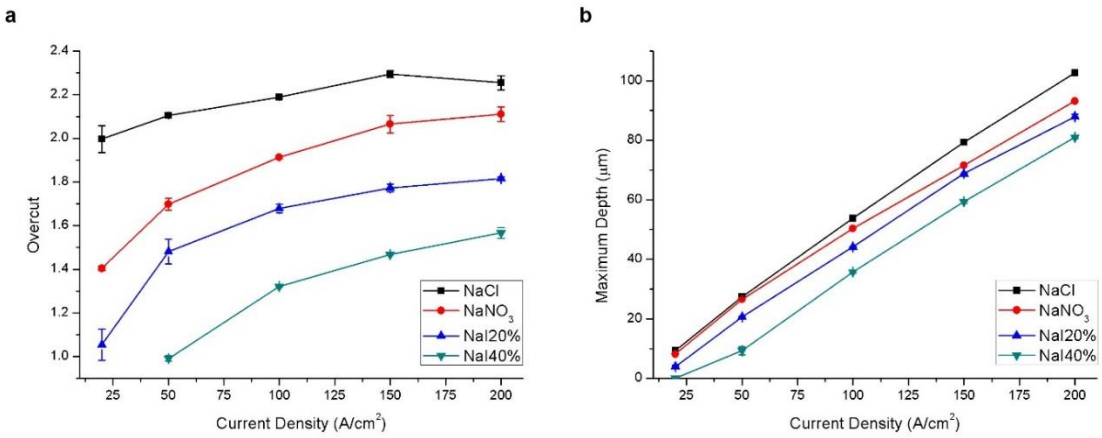


Figure 6.3: a) Overcut is significantly decreases upon iodide application as removal localises. b) While depth also decreases, the scale of this decrease is less than the overcut, indicating an increase in precision.

In Figure 6.3a, it is demonstrated that application of iodide to the electrolyte significantly reduces overcut, for example at high current density (200 A/cm^2), this metric is reduced by 31% compared with NaCl and 26% compared with $NaNO_3$ of the same ionic strength. Upon iodide addition, where features are processed at low current density, feature scale approaches the nozzle diameter (overcut = 1). Due to suppression of material removal upon addition of iodide, maximum depth is also decreased (*see* Figure 6.3b). However, the reduction in depth (negative performance characteristic) is shown to be less than overcut reductions at the same current density (200 A/cm^2), where maximum depth is reduced by 21% compared with NaCl and 13% compared with $NaNO_3$. This

indicates not only a localisation in machining, but an increase in the precision and aspect ratio of the deterministic feature.

6.2.2. Current filtering mechanism

Mechanistically, the localisation of material removal occurs through the development of an iodine film at the impingement region of the electrolyte. Evidence to support this is shown in the photographs in Figure 6.4, where a brown radial film is generated upon electrolysis in the presence of iodide (*see* Figure 6.4b). The brown film will occur where the concentration of iodine is greater than the saturation concentration of this molecule for a given solution. The termination point of the radial film expanding outwardly is likely to mark the saturation threshold, beyond which the effective iodine concentration is soluble. This occurs through dilution, and spontaneous reactions that are expected in such mixtures, for example the formation of triiodide: $I_2 + I^- \rightleftharpoons I_3^-$.

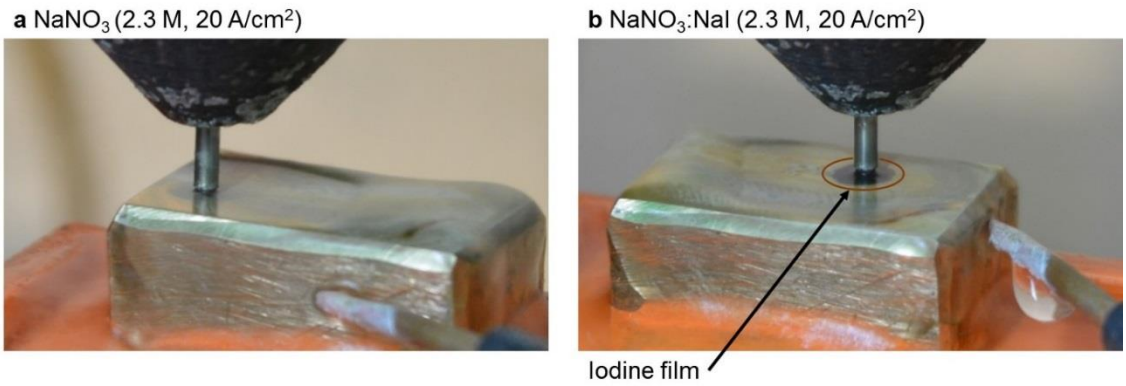


Figure 6.4: Photographs of EJP operations in a) sodium nitrate and b) iodide-doped (NaI20%) electrolytes. Anodic formation of iodine is evident as a brown radial film.

The effect of iodide dopants can therefore be elucidated, and is schematically shown (*see* Figure 6.5). For a case where conventional electrolytes, such as NaCl and to a lesser extent $NaNO_3$ are applied, material removal occurs as an approximate reflection of the current density distribution (*see* Figure 6.5a).

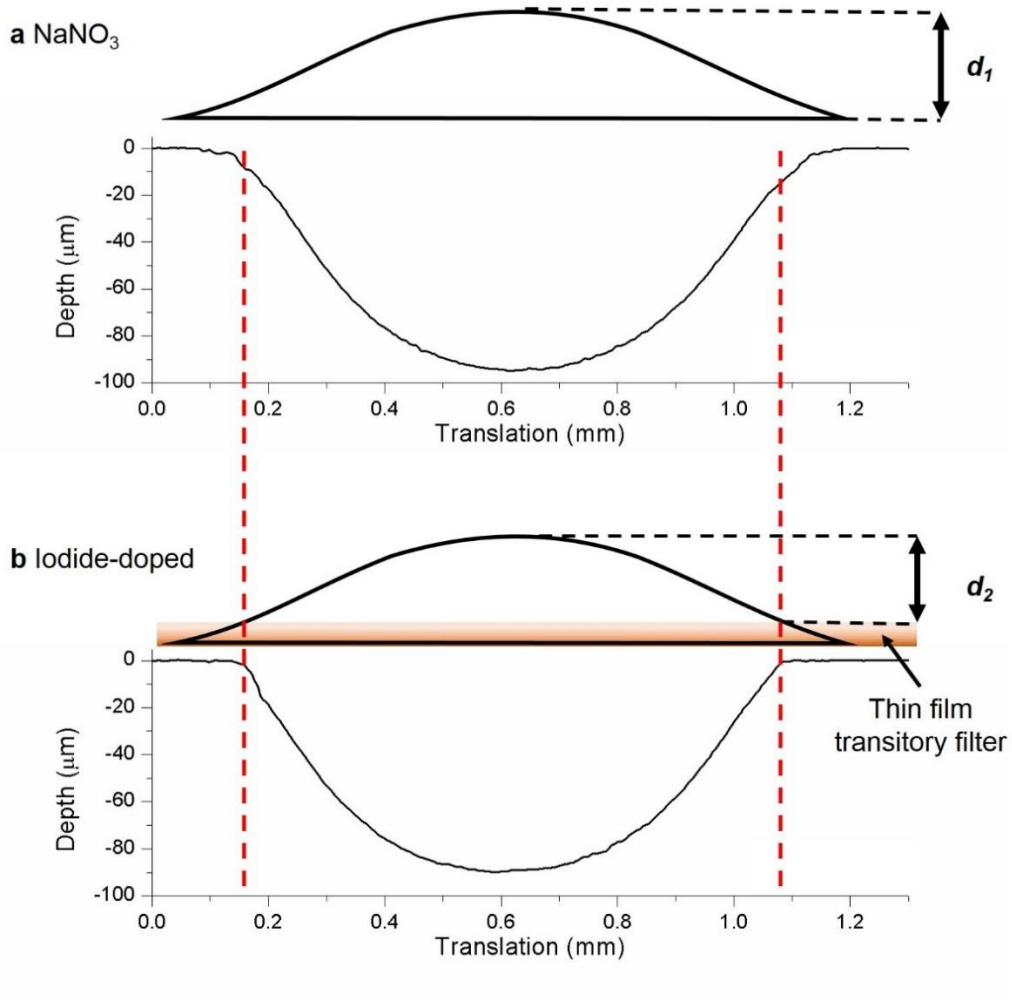


Figure 6.5: Overcut decreases are attributable to current filtering. a) Using conventional electrolytes, the majority of current removes material. b) Upon iodide addition, energy is transferred oxidising iodide, filtering the current density distribution edges, such that the effective machining current density follows the relationship $d_1>d_2$.

Here, a significant majority of the charge flux is successful in liberating material; current efficiency is high and the removal kerf is large. Upon iodide addition, energy is transferred to oxidise iodide to form an iodine film across the machining zone, creating a threshold such that the effective machining current density is reduced, considering the relationship $d_1>d_2$. While current efficiency is reduced, the removal kerf is effectively reduced by a threshold dictated by the surface concentration of iodide. The result is an effective transitory current filter

that leads to reductions in overcut and the suppression of material removal in low current density regions.

Considering the greater flexibility of striation-based processing regimes in planar feature generation, the NaI 40% electrolyte was compared with conventional $NaNO_3$ in terms of common performance characteristics at high current density (200 and 400 A/cm^2). Striations were processed using a 250 µm I.D. nozzle, at a translation velocity of 0.5 mm/s and 0.5 mm IEG. At both tested current densities, overcut is shown to be reduced by the same factor, approximately 20% and aspect improved, where the iodide-doped electrolyte is applied (*see* Figure 6.6). The improvement in aspect is shown to be dependent on the current density (5% at 200, 10% at 400 A/cm^2), which is indicative of a reduction in the depth difference between the two electrolytes upon increasing the current density. In this instance, at 200 A/cm^2, processing with NaI40% leads to a 16% depth reduction, whereas the higher current density leads to a 12% depth reduction against the $NaNO_3$ control electrolyte. The reconstructions acquired from surfaces processed with (*see* Figure 6.6c and d), show good edge definition and topographic consistency, although exposed precipitates are observed at the surface. These are also observed when processing using $NaNO_3$ at the same parameters.

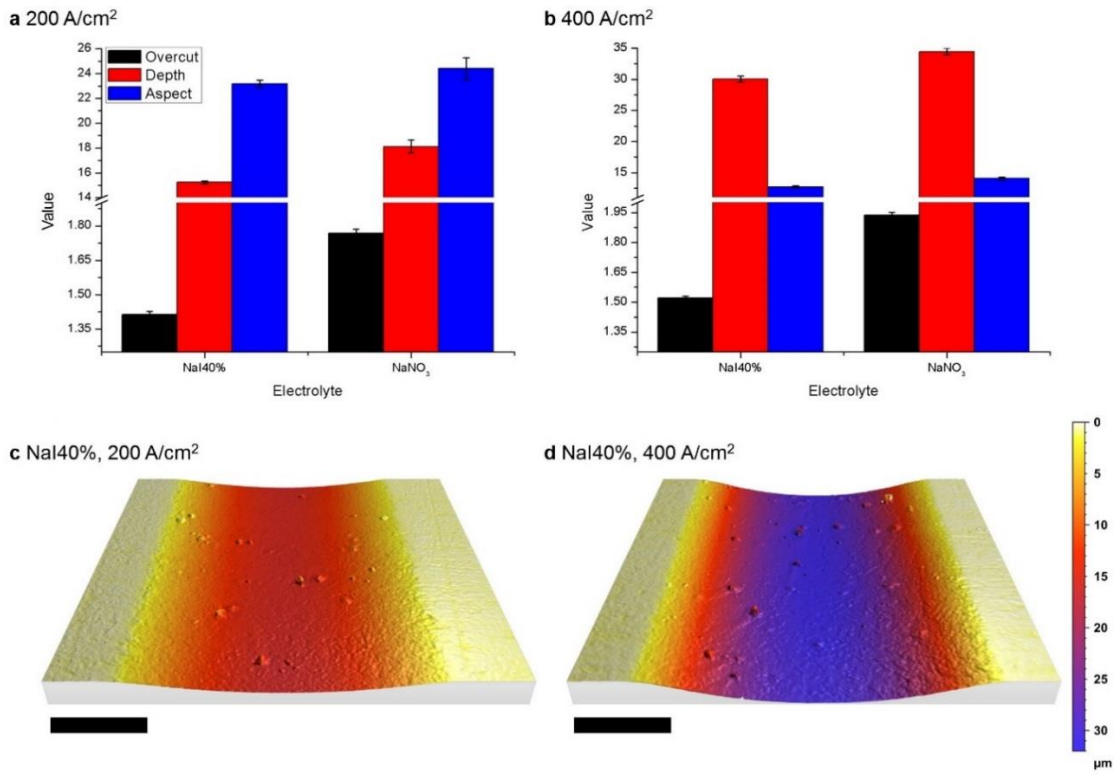


Figure 6.6: (Overleaf) High current density striation processing. EJP with NaI 40% is shown to improve overcut and aspect. The magnitude of aspect is dependent on the current density. Reconstruction scale bars are 100 µm. Error bars are the standard deviation from the mean.

The dependence of aspect improvement of NaI 40% over $NaNO_3$ with increasing current density further supports the idea of iodide generating an effective machining threshold. This is explored in the schematic in Figure 6.7. Increasing the current density increases the material removal rate, however the iodine formation reaction is largely dependent on the surface concentration of iodide within this operating range. Increasing current density therefore reduces the absolute difference in depth between NaI 40% and $NaNO_3$, and therefore improves the aspect and the gradient of the side wall. This is also supported by data shown in Figure 6.3b, where the difference in depth is relatively constant, regardless of applied energy In this case, increasing the linear charge density

would not affect the current filter, which is assumed to be a threshold. This mechanism also explains the slight overcut increase with current density.

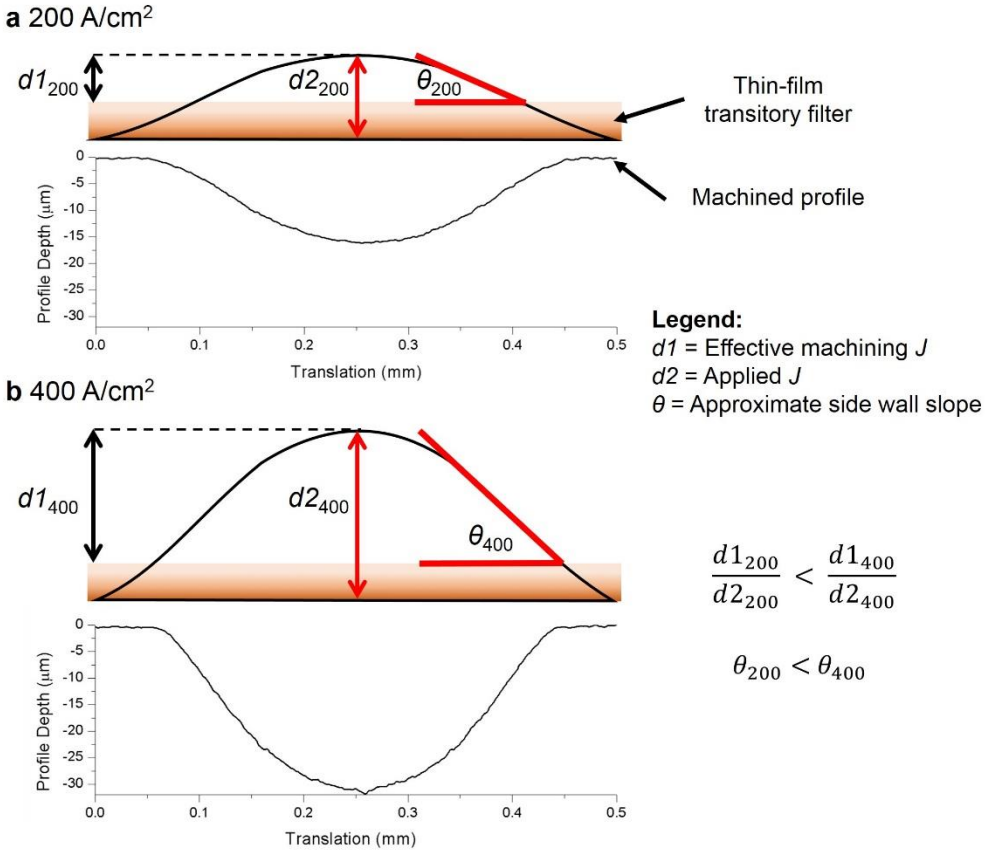


Figure 6.7: Absolute improvements in depth and aspect using iodide electrolytes can be made through increasing current density, a) 200 A/cm^2, b) 400 A/cm^2, as iodine formation reaction represents a threshold.

In addition to reducing the overcut of the processed feature, the iodide-based current filtering mechanism also reduces stray current machining in this material. This is shown in the secondary electron micrographs in Figure 6.8a, b, processed at high current density (400 A/cm^2). The clear decrease in the scale of stray cutting is visible due to the reduced effective current density in these edge regions.

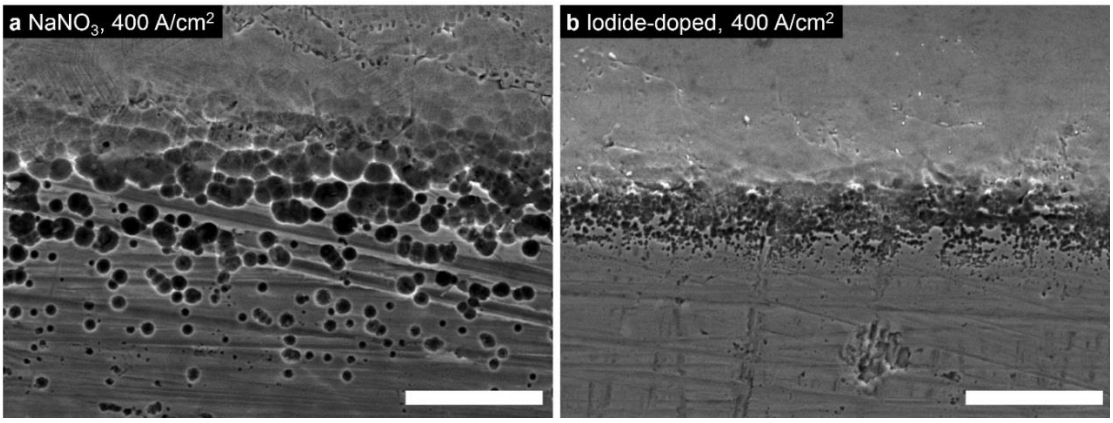


Figure 6.8: a) Sporadic material removal is limited by the application of iodide (b), reducing the effective machining current density at the edges. Scale bars 15 µm.

The bulk concentration of iodide within the electrolyte clearly affects the material removal rate (*see* Figure 6.1b). Considering a true current filtering mechanism, the iodide oxidation reaction will occur ahead of the anodic dissolution of nickel. This associates the effective threshold level with the incident supply of iodide to the surface. This has been explored in this chapter through increasing the bulk concentration of iodide, but logically, the incident supply level can be modulated with electrolyte velocity. These two influences were appraised with a metric; incident dopant concentration (IDC), expressed in M/s (*see* Equation 17).

$$IDC = C_B \cdot \dot{v}_j \qquad \textit{Equation 17}$$

Where C_B is the bulk concentration (*M/l*) of iodide (or any other similarly performing dopant) and $\dot{v}_j$ is the volumetric flow rate (*l/s*) of the electrolyte jet. Material removal as a function of IDC was appraised for NaI 40% across the total range of jet velocities permitted by the EJP apparatus and compared with conventional $NaNO_3$ electrolyte of identical ionic strength in a pit processing operation (100 A/cm^2, dwell 4 s). NaI 40% was applied as this enables the broadest range of IDC values for a given EJP system. When applying the nitrate

electrolyte (control), negligible correlation between jet velocity and material removal volume is observed (*see* Figure 6.9). Applying the NaI 40% electrolyte, a highly linear inverse correlation (R^2 = 0.9884) between jet velocity and removal volume is observed, which is related to the IDC. The role of the IDC in dictating the current threshold level is further supported by the similarity between the intercepts of the two electrolyte types ($NaNO_3$ = 0.0170, NaI40% = 0.0165). This demonstrates that as the IDC tends towards zero at very low jet velocities, the removal volume will tend towards that expected from the un-doped $NaNO_3$.

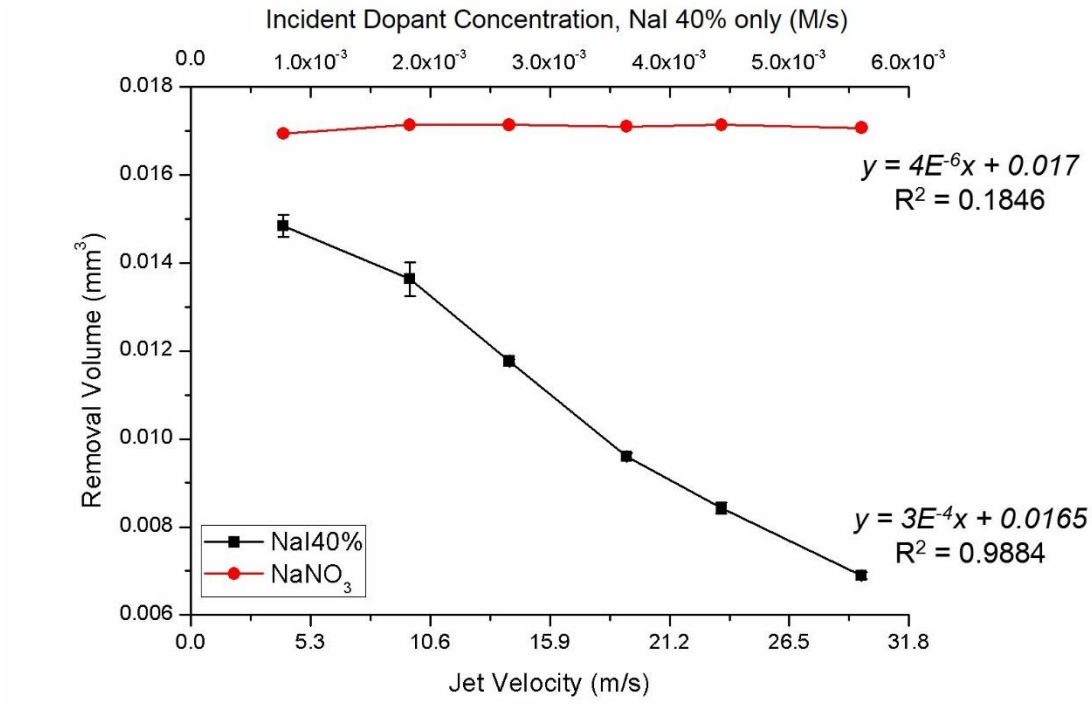


Figure 6.9: The incident concentration of iodide (IDC) dictates material removal for a given current density. Graph for NaI 40%, showing a strong inverse linear correlation between jet velocity (and IDC) and the material removal for pit machining, not observed in the control trial ($NaNO_3$, 2.3 M). Constant applied current density and dwell (100 A/cm^2, 4 s).

IDC values were calculated for all iodide-doped electrolyte systems tested in this section and are shown in the plot in Figure 6.10. Exemplar pits are shown across the IDC range for NaI 40%, whereby the increase in removal volume upon reducing jet velocity is clearly visible in the reconstructions (*see* Figure 6.10a-c). At the highest IDC (Figure 6.10a), overcut is 1.34 for this pit in line with Figure 6.3a, whereas at the lowest IDC tested in this electrolyte system (Figure 6.10c), overcut is 2.00 for the presented pit. Consideration of the IDC means that material removal can be effectively modulated across different electrolytes. This is shown for NaI 40% (v_j = 9.9 m/s, IDC = 1.82E^{-3} M/s) and NaI 20% % (v_j = 19.2 m/s, IDC = 1.83E^{-3} M/s). In both cases material removal volume is shown to be very similar (*see* Figure 6.10d and e), however enhanced localisation and dimensional accuracy is shown when applying the greater jet velocity in this case, due to the hydrodynamic effects that have been previously shown and simulated by Hackert-Oschätzchen et al. (2015) [77] to affect the geometric characteristics of the processed feature in EJP.

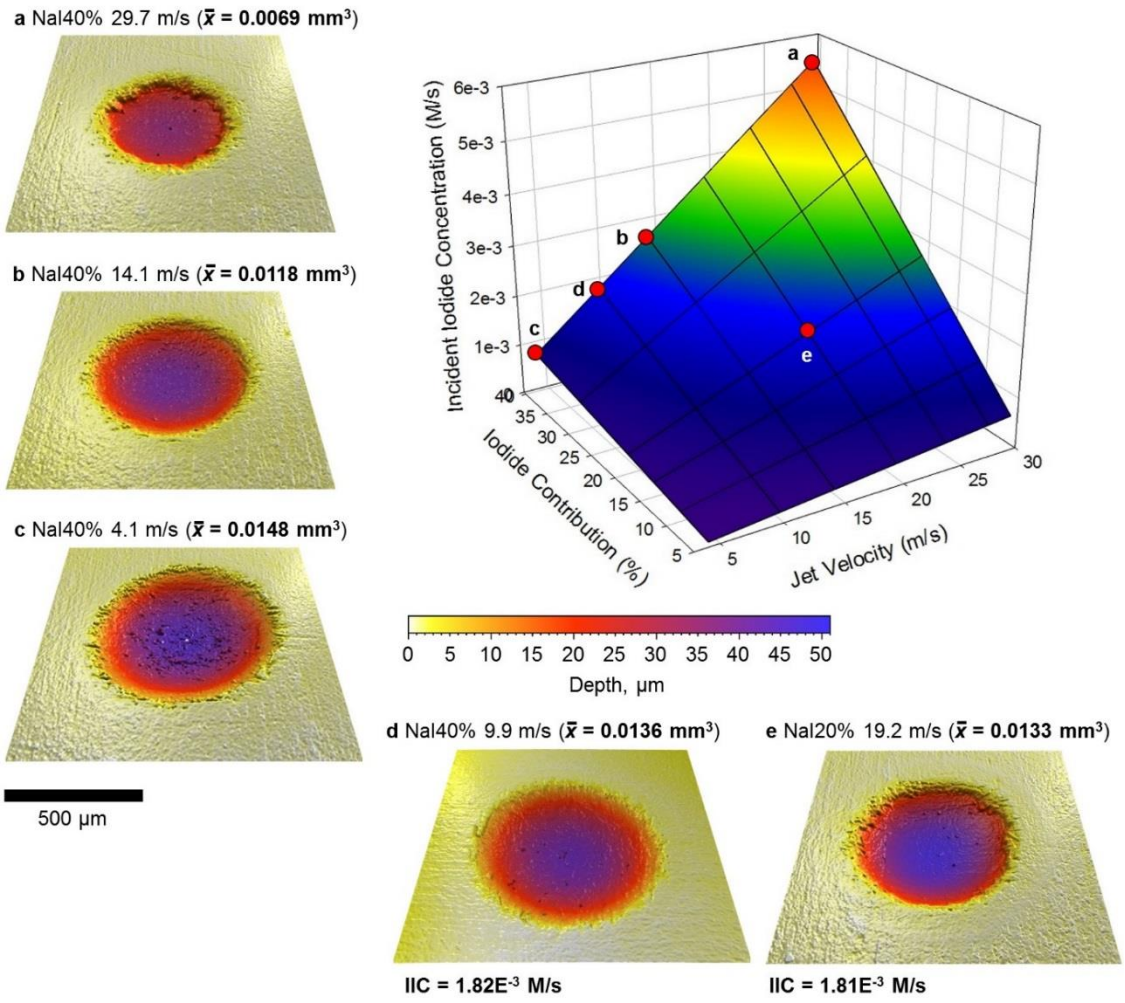


Figure 6.10: Incident dopant concentration and material removal (100 A/cm^2) for equimolar electrolyte systems (2.3 M). Increasing jet velocity increases IDC, which suppresses material removal. At equivalent IDC, removal is approximately equal at a given current density, regardless of iodide bulk concentration.

6.2.3. Scalability of micro-striations

Considering the dependence of the scale of the processed feature on the nozzle I.D., even when applying doped electrolytes, fine microchannels were processed using a 60 µm I.D. nozzle to generate filigree more consistent with that required from a micromachining process (0.5 mm/s, 400 A/cm^2). The feature resolution, shown in Figure 6.11, is comparable to that achievable through laser machining, at a small fraction of the capital cost and without thermally affecting the material.

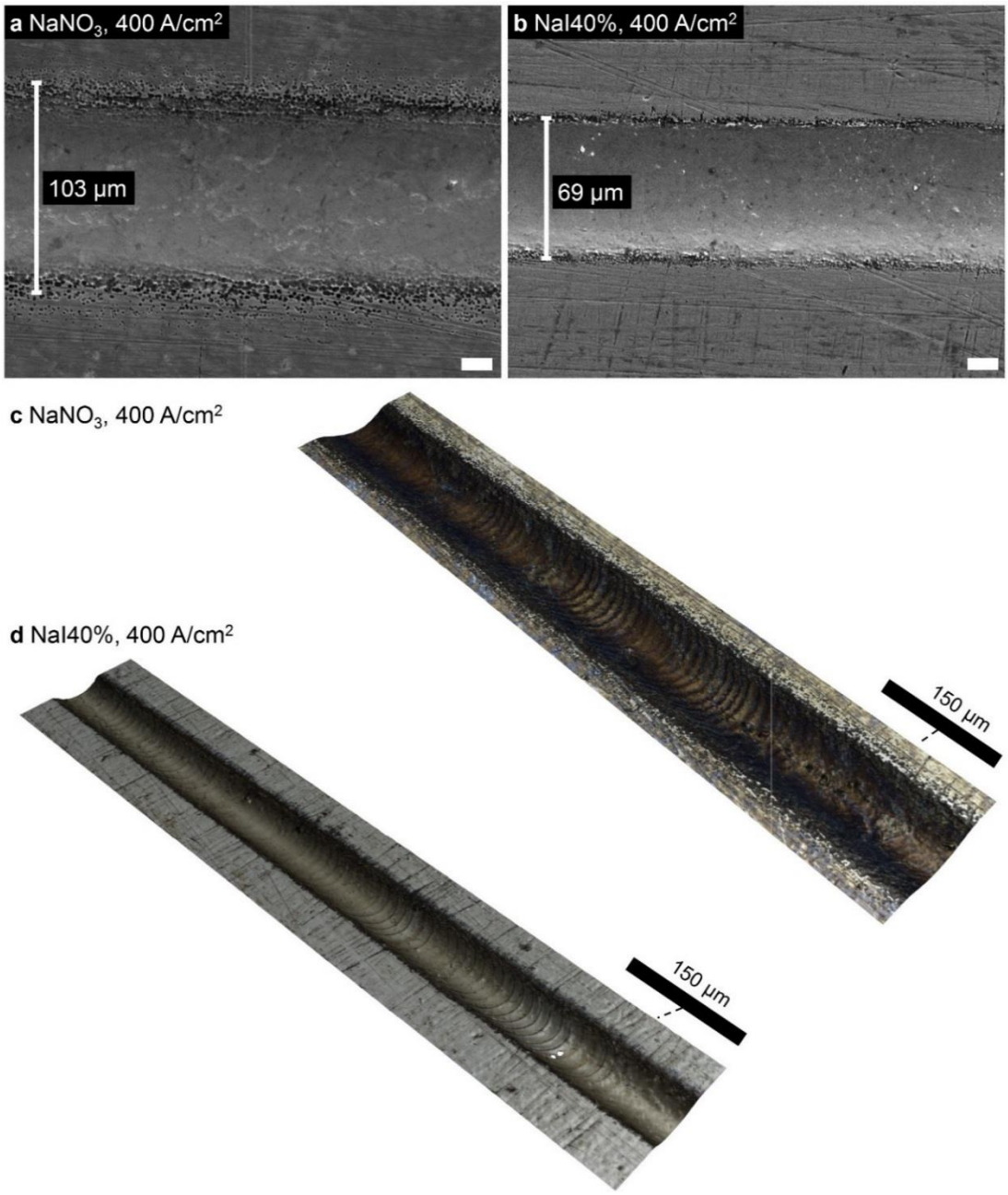


Figure 6.11: EJP using 60 µm I.D. nozzle. Kerf width approaches the nozzle I.D., even at high current density and surface quality doesn't appear to be detrimentally affected by the doped electrolyte system. SEM scale bars 15 µm.

The expected reduction in overall kerf width upon iodide addition is shown in Figure 6.11a, b (overcut for $NaNO_3$ = 1.72, for NaI 40% = 1.15), whereby the NaI40% kerf is shown to be approaching the nozzle I.D., even at elevated current density. In addition, the surface reconstructions (*see* Figure 6.11c and d) show that the topography is not adversely affected by iodide addition when

processing this material. Periodic striations are understood to relate to the pulsing nature of the pump power supply at this fine length scale, as they are visible with NaI 40% and in the un-doped $NaNO_3$ electrolyte. It is proposed that these could be overcome through a damping arrangement, correlating pump revolutions to traverse speed.

When processing at finer length scales, the reliability and repeatability of feature generation becomes increasingly dependent on the material. This is shown in Figure 6.12, processed using a 60 µm I.D. nozzle. The precipitates within this nickel superalloy are generally <10 µm in average size. For these precipitates, electrochemical dissolution rate is apparently significantly less than that of the bulk matrix and therefore deterministic processing strategies at length scales approaching the precipitate size will be affected by the distribution of these precipitates (generally localised at the grain boundaries) throughout the material. This leads to protruding phases, where the scale of the protrusion can represent a large proportion of the total kerf width (*see* Figure 6.12a). This would challenge the use of this material when generating fine-scale striations in certain applications, for example in flow channels, where the large scale of the protrusions as a proportion of the overall cut dimensions would affect fluid flow along the processed length.

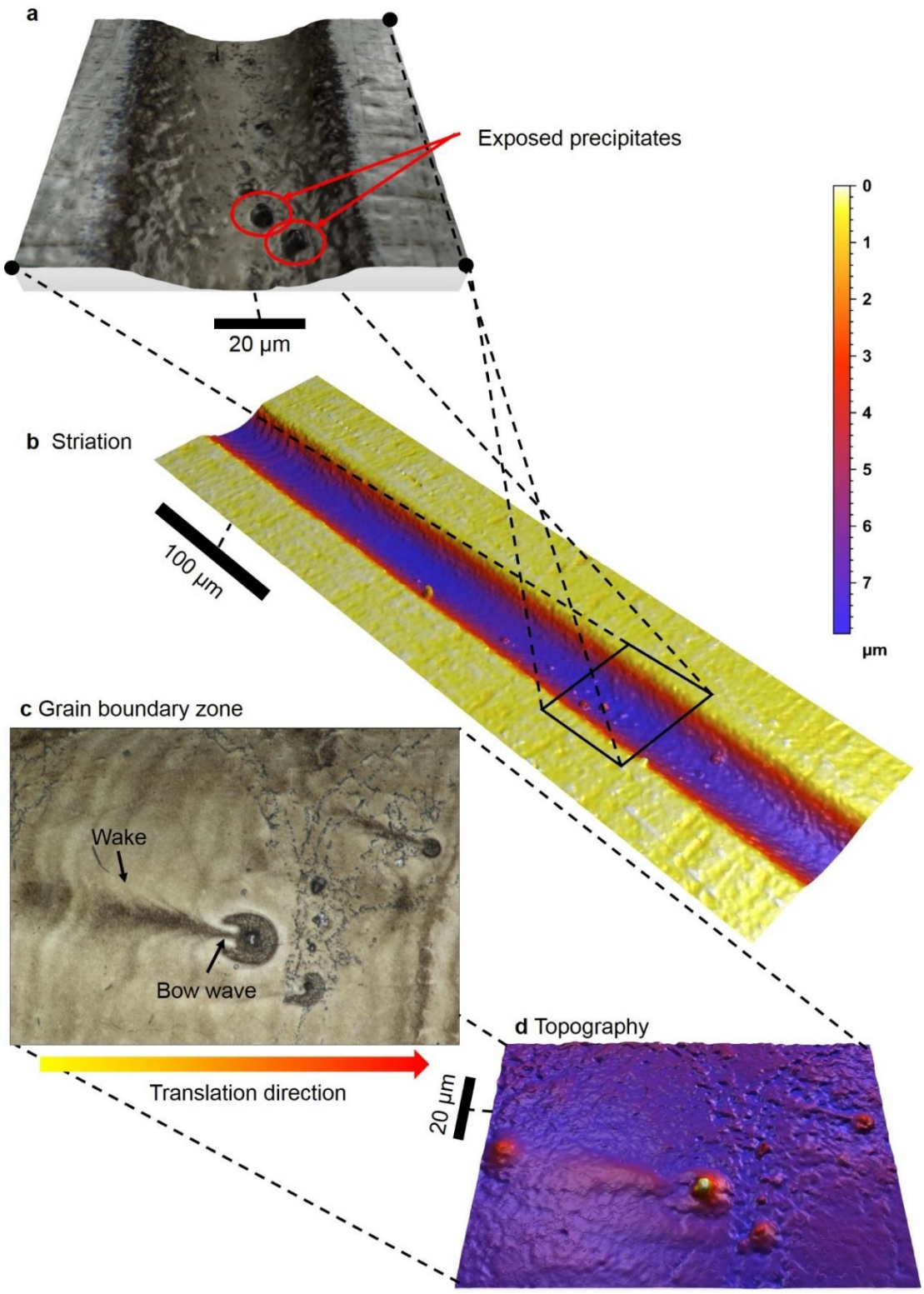


Figure 6.12: The repeatability of fine-scale featuring is limited by material precipitate size, even at high current density. Where geometric scale approaches precipitate size, aberrations in the cut profile occur. These protrusions alter the electrolyte flow dynamics over the surface, generating topographic undulations larger than the precipitate scale.

Therefore, the microstructure of the material must be considered to allow successful feature generation on this length scale, regardless of current density. To increase feature fidelity and repeatability at the small scale, more homogeneous materials, such as those without precipitates, are recommended. In addition, novel electrolytes or processing strategies could be developed to allow for more homogeneous material removal, regardless of the electrochemical dissolution characteristics of the discrete material phases.

6.3. EJP micromachining of titanium

The workpiece used in this section was Ti-6Al-4V, prepared as outlined in section 3.1.3. Ti-6Al-4V features widely in aerospace applications due to high specific strength and toughness, low density and high corrosion resistance. Therefore Ti-6Al-4V is an ideal target material for both selective machining and large-area processing operations, to which EJP could be applied. The literature review indicated that electrochemical processing of titanium alloys is limited by the large corrosion resistance of the material, where the high affinity towards oxygen results in the build-up of passivating layers during processing, leading to poor dimensional accuracy, edge definition, and poor removal rates.

Despite notable process adaptions, which have been identified in the literature review, for example: laser-assisted, abrasive-assisted, and ultrasonic-assisted strategies, use of EJP towards titanium materials remains industrially limited. These hybrid processes involve significant adaptions to the standard EJP apparatus and therefore hinder efficient application of the technique. To enhance industrial capability, it was decided to retain the simplicity of the

standard operating condition in EJP in this study. One way to address processing issues in titanium could be to alter the chemistry of the electrolyte feedstock, as this has been shown to reliably change workpiece response to electrochemical processing in a range of materials. Regarding titanium, classical investigations by Dugdale and Cotton (1964) [57], and Bannard (1976) [56] drew attention to the roles different halides could play in Ti ECM.

6.3.1. Surface generation in titanium

Ti-6Al-4V was processed (250 µm nozzle) with different electrolytes (2 M, 400 A/cm^2, 10 s dwell) and typical pit morphologies are shown in Figure 6.13. Processing with $NaNO_3$ leads to the formation of a relatively thick scale (≈150-300 µm) on the surface of the machined pits (*see* Figure 6.13a). This scale formed rapidly upon the start of the machining process, inhibiting further material removal and is largely responsible for the inferior performance of $NaNO_3$ in titanium processing. The optical micrograph in Figure 6.13b shows a yellowish hue in the surface which is likely to be a result of residual metal hydrates adsorbed or trapped within the oxide scale. This ‘trapping’ effect demonstrates that the poor performance is also linked to the inability of dissolved metal ions and transient complexes to be carried away from the machining surface by the electrolyte flow alone. Processing with NaCl (*see* Figure 6.13c-d) shows similar large-radius pits to Inconel 718 with the same electrolyte, related to the aggressiveness compared to $NaNO_3$, while NaBr generates smaller, but significantly rougher topographies at the same parameters (*see* Figure 6.13e-f). Processing with NaF generates undulating topographies (*see* Figure 6.13h), while the fluoride-doped mixture (*see* Figure 6.13i-j) is topographically similar to NaCl, with a reduction in kerf.

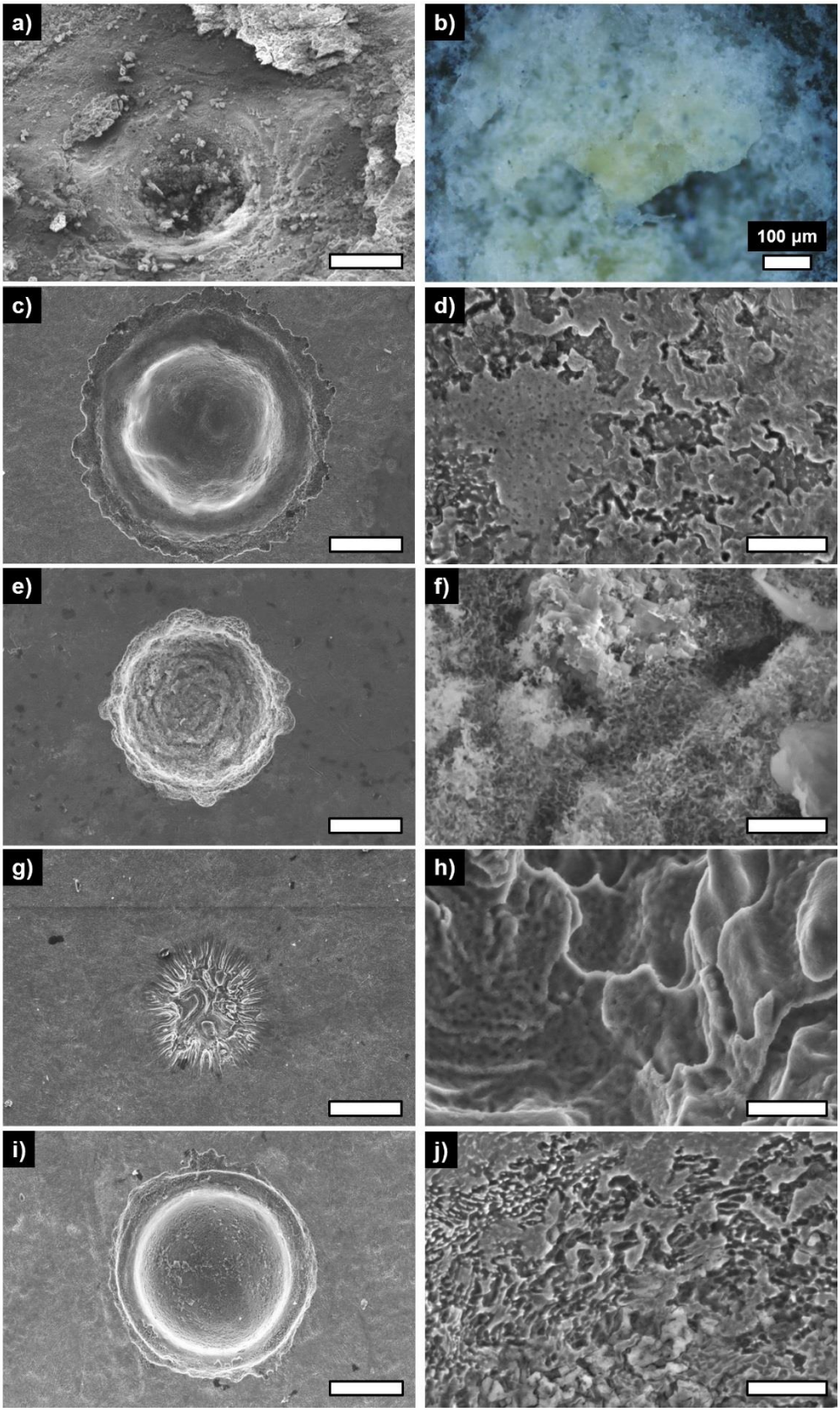


Figure 6.13: (Overleaf) Pit morphology and topography upon EJP in different electrolyte solutions. a-b) $NaNO_3$, c-d) NaCl, e-f) NaBr, g-h) NaF, i-j) NaF:NaCl. Left column scale bars 250 µm, right column scale bars 25 µm. Optical image scale bar 100 µm.

To quantify differences between the electrolytes, depth and overcut were appraised over a range of concentrations (2-4 M), shown in Figure 6.14. Removal depth is shown to be relatively constant across the concentration range for NaCl and NaBr electrolytes, indicating that these electrolytes are supplying the requested current at all tested concentrations. Conversely, $NaNO_3$ shows a positive linear correlation between concentration and material removal. This is likely to be related to increasing electrolytic conductivity across this range, which could enable machining to occur in spite of the presence of highly resistive scale, such as oxide films. In addition, overcut is reduced for $NaNO_3$ across the concentration range (*see* Figure 6.14b), which is also likely to result from higher conductivity electrolytes overcoming the highly resistive scale that has been previously shown to affect the cut width in this material.

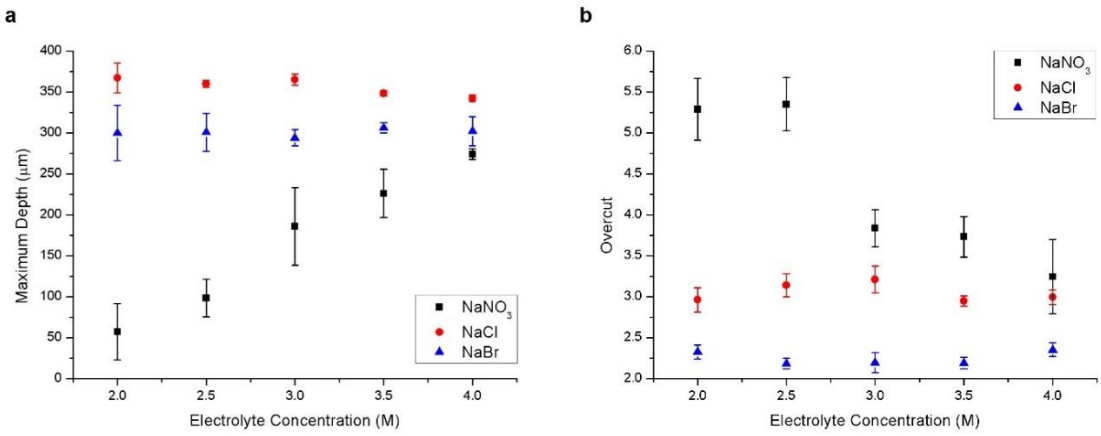


Figure 6.14: a) Maximum depth and b) overcut for different electrolytes across a range of concentrations. The inferiority of $NaNO_3$ in application to titanium EJP is likely to be related to the conductivity, whereby higher concentrations can overcome the high resistance associated with the oxide scale.

To elucidate the chemistry of the plate features formed in the presence of $NaNO_3$, samples were analysed with energy-dispersive X-ray spectroscopy (EDS), shown in Figure 6.15, where the scale is evidently anodically formed

oxygen-containing species. Raman vibrational analysis was performed on both the oxide scale and the exposed surface. Typical resulting spectra (*see* Figure 6.15d) indicate oxide response in both cases, for the exposed surface (pit base black) a relatively intense peak is located at approximately 150 cm^{-1}, which correlates with the known location of the peak associated with the E_g vibration of anatase TiO_2. In addition, weaker broad peaks are visible in this spectrum correlating with locations of the E_g (≈425 cm^{-1}), A_{1g} (610 cm^{-1}) and B_{2g} (≈790 cm^{-1}) vibrations in rutile (also TiO_2) [225]. In addition, a second order scattering mode is observed ≈245 cm^{-1}, which has been previously associated with the aforementioned rutile bands [225]. The oxide scale area displays the same vibrations, although those associated with rutile appear more intense and the anatase E_g vibration is broader and weaker. The relatively strong Raman vibrations indicate that the oxide scale is partially crystalline in nature, and is not entirely amorphous. However the purity is likely to be very poor considering the apparent adsorption of other metallic species thought to be responsible for the yellow hue, as well as formation within aqueous environment which is likely to result in high levels of hydration. The passivation scale appears to be composed of a mixture of at least two discrete oxide-containing structures.

Such anodic scale does not occur in the presence of more aggressive electrolyte systems, for example NaCl and NaBr. Although increasing the concentration of $NaNO_3$ is shown to largely overcome this scaling, highly concentrated electrolyte solutions are undesirable from a practical processing perspective and instead electrolytes based on halides demonstrate better response in terms of simple performance characteristics over lower concentration solutions.

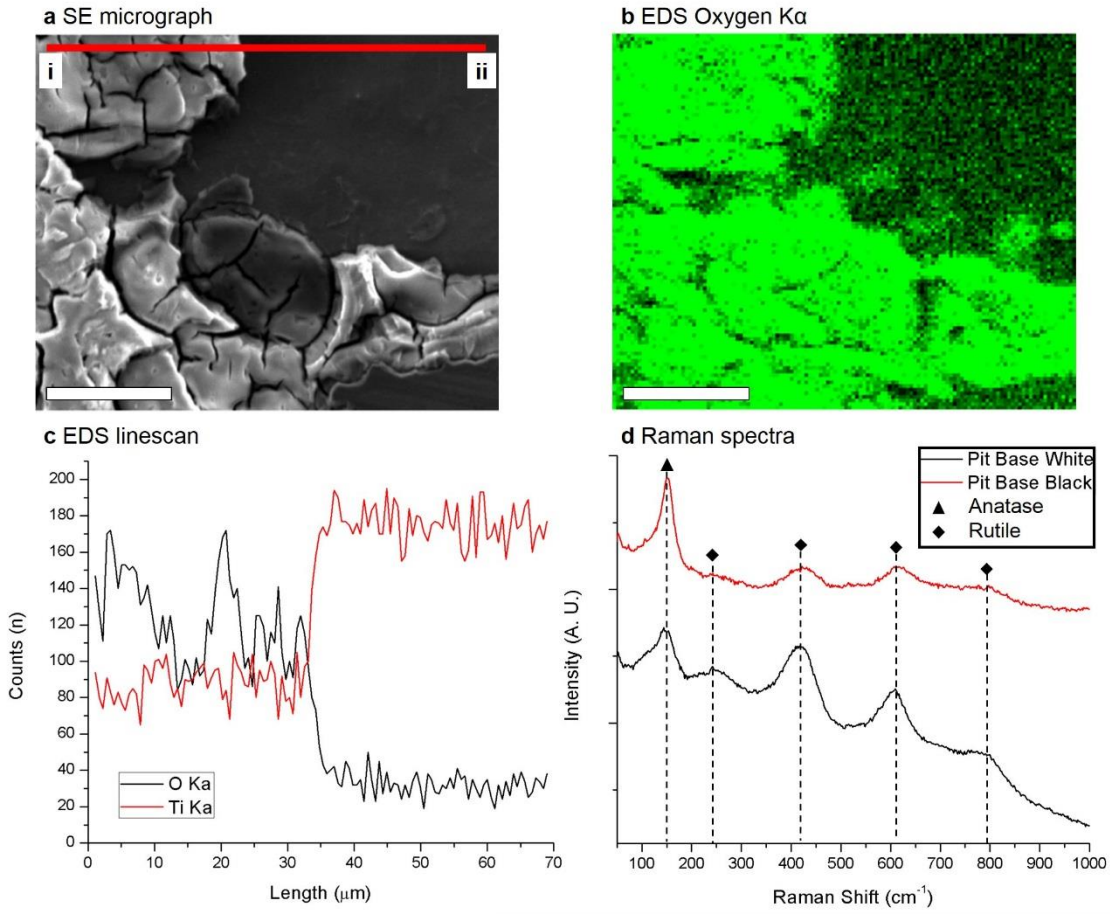


Figure 6.15: Chemical analysis of scale formation after EJP of titanium in $NaNO_3$. a) SE micrograph showing locations of EDS line and area acquisitions. b and c) Scale feature has a high concentration of oxygen, indicating the species to be an anodic oxide. d) Raman spectroscopy of the exposed surface (red) and the oxide scale (black), showing existence of both anatase and rutile phases. SEM scale bars 25 μm.

Although bromide-based electrolytes generated the pits with the lowest overcut, the resulting topography is very rough in comparison to processing at identical parameters using NaCl (*see* Figure 6.16a-b). Considering the more aggressive (de-passivating) nature of Br^- anions towards titanium in comparison to Cl^- (as indicated by Bannard [56]), this topography is likely the result of an etch-specific reaction. For a chloride-based electrolyte, the level of passivation, which effectively delocalises material removal away from localised microstructural properties, is greater. This results in a smoother and brighter surface

appearance, although the microstructure of the Ti-6Al-4V sheet can still be resolved in the electron micrograph.

To identify the roughening surface protrusions when processing this material with bromide-based electrolytes, a pit was sectioned and analysed with backscatter electron microscopy (*see* Figure 6.16c), indicating that the high mass contrast phase is largely responsible for the surface protrusions. This is likely to be the β-phase of this alloy, which is rich in vanadium. Further evidence to support this is given in Figure 6.16d, where a more intense EDS response is shown for this element in the surface protrusion, in comparison to the surrounding phase. Despite the general desire for smoother, defect-free surfaces in most engineering applications, the generation of such surface topographies in titanium alloys could lend itself to application in osseo-facing surfaces, where the high porosity surface, which is dictated by the dispersion of the β-phase within the material, appears to mimic bone structures in terms of length scale and frequency of porosity.

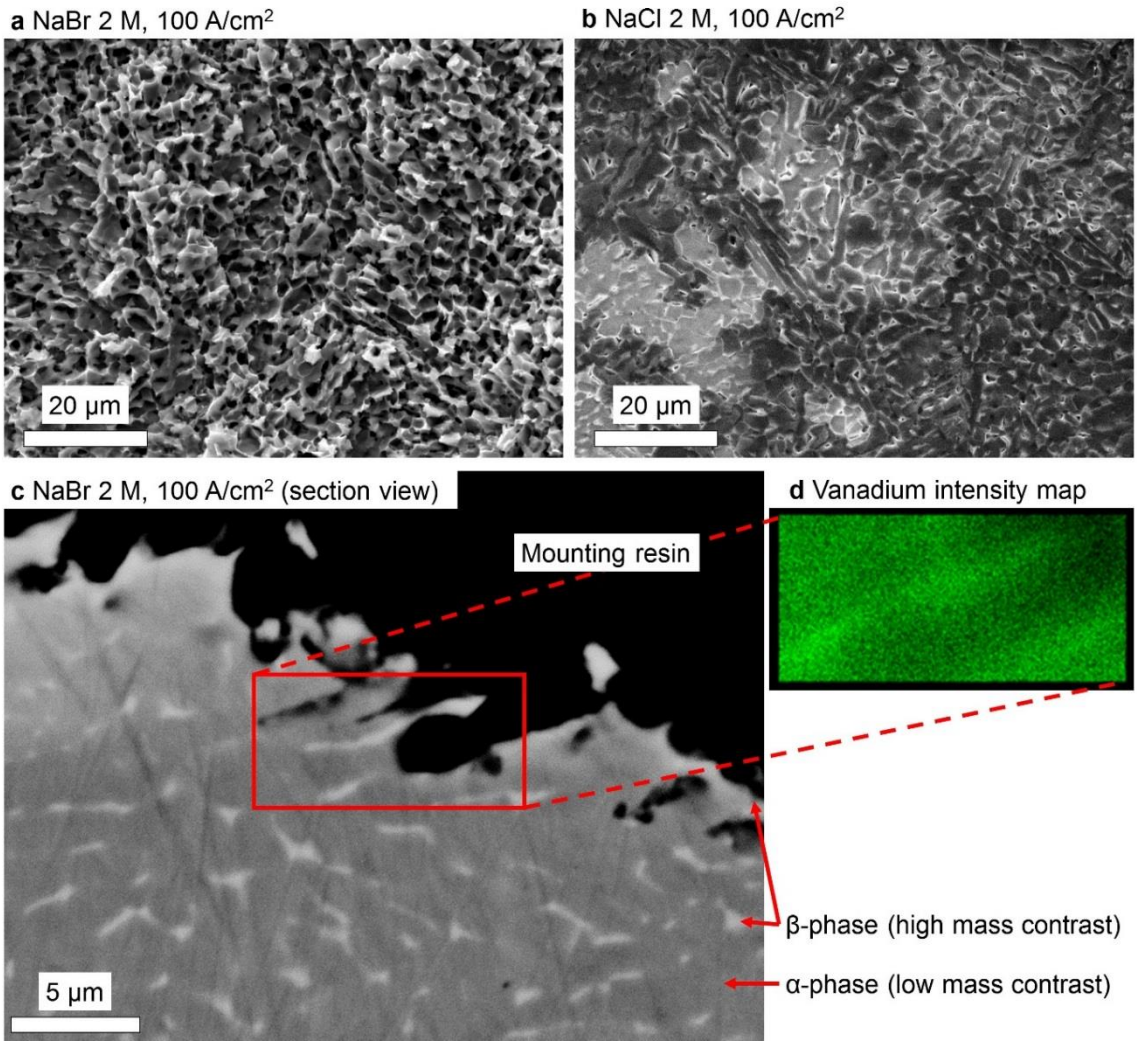


Figure 6.16: SE micrographs (ND) of topographies resulting from processing with NaBr and NaCl (2 M) at 100 A/cm^2, where NaBr processing results in etched surface. c) BSE micrograph of NaBr pit section showing high mass contrast phase protruding into the mounting resin (likely vanadium rich β-phase). d) This is supported by EDS analysis showing localised concentration of vanadium in the protruding vein.

6.3.2. Processing strategies in titanium

A planar processing strategy was employed to generate striations across a broad range of current densities (20-400 A/cm^2, 0.15 mm/s translation velocity). In striation machining, there is an energy domain below which stable machining is inhibited and material removal occurs as sporadic, stochastic pitting events along the length of the processed feature. This is shown in the reconstructions

processed with NaCl and NaI 30%, shown in Figure 6.17 (v_h = 0.15 mm/s). In NaCl, pitting occurs as shallow semi-regular pits, at the lowest current density tested (20 A/cm^2), however at the same current density, the addition of iodide inhibits continuous removal and a higher frequency of smaller pits are observed. Upon increasing the current density and thus the anodic potential, pits coalesce to generate striations with large-scale irregular overcut, shown in Figure 6.17b and c (50 and 75 A/cm^2 respectively), and an undulating basal surface. For the iodide-doped electrolyte, this effect leads to a serrated edge cut, characterised by periodic overcut fluctuations. Periodicity shown here at low current densities in NaI 30% is indicative of a dynamic electrochemical process, and is complemented by oscillatory electrode behaviour [226] (*see* section 6.4.1).

In addition, the onset of continuous material removal is shown to be electrolyte-dependent. In this case, continuous removal is inhibited by the addition of pit-promoting anions (where the oxide breakdown potential is suppressed), and prevented up to 150 A/cm^2 in NaI 30%. At high current density (see Figure 6.17d, 400 A/cm^2), material removal appears stable, overcut is more regular and the basal area appears to be more consistent with the input energy distribution. Conventionally, EJP is practised in the stable machining domain, the onset of which occurs at lower current densities in the case of materials with less passivating characteristics, such as steels, Ni-superalloys, and Cu alloys.

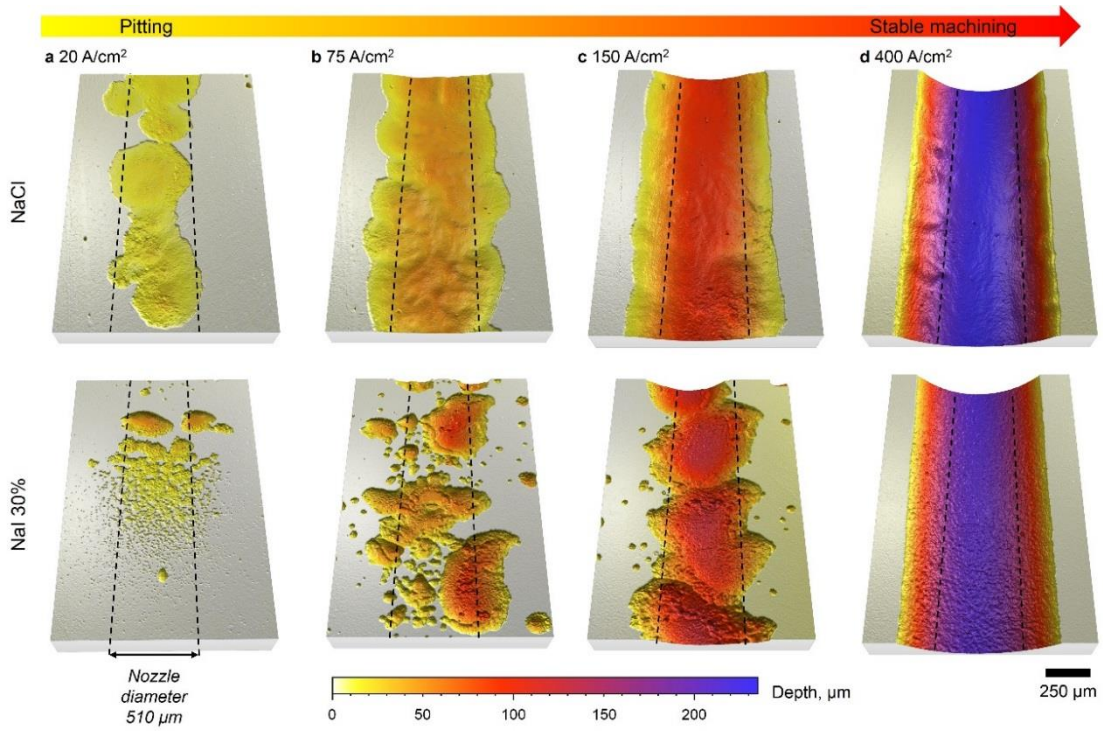


Figure 6.17: Pitting to stable processing regimes, with NaCl and NaI 30%. a) Low current density removal occurs as discrete pits. b and c) Pits coalesce and overcut increases with current density. d) At high current density, removal stabilises and overcut becomes more regular.

The transition from pitting to a stable machining regime, for all electrolytes, was characterised using total machined area, A_m, and overcut, O, shown in Figure 6.18. For the majority of cases, machined area is shown to increase sharply with current density for each electrolyte, up to a point, caused by the establishment of a stable striation feature. Further increases in current density beyond this point do not appear to significantly affect the total machined area. The exceptions to this are iodide containing electrolytes, whereby the machined area continues to increase, approximately linearly, across the current density range tested. A similar relationship can be observed regarding overcut (*see* Figure 6.18b), whereby the kerf of the machined features increases with current density, stabilising at approximately the same current density level (≥150 A/cm^2) for each electrolyte, again excluding those containing iodide.

Both machined area and overcut describe pit development, whereby pits form and coalesce at current densities <150 A/cm^2, leading to observed increases for all electrolytes tested. Interestingly, electrolytes doped with pit-promoting anions, lead to a lower machined area at low current density (<50 A/cm^2). For application as part of a conventional EJP cutting process, titanium should be processed at high current densities ≥200 A/cm^2, where the stability of feature generation is increased; this is defined as the 'stable machining threshold'.

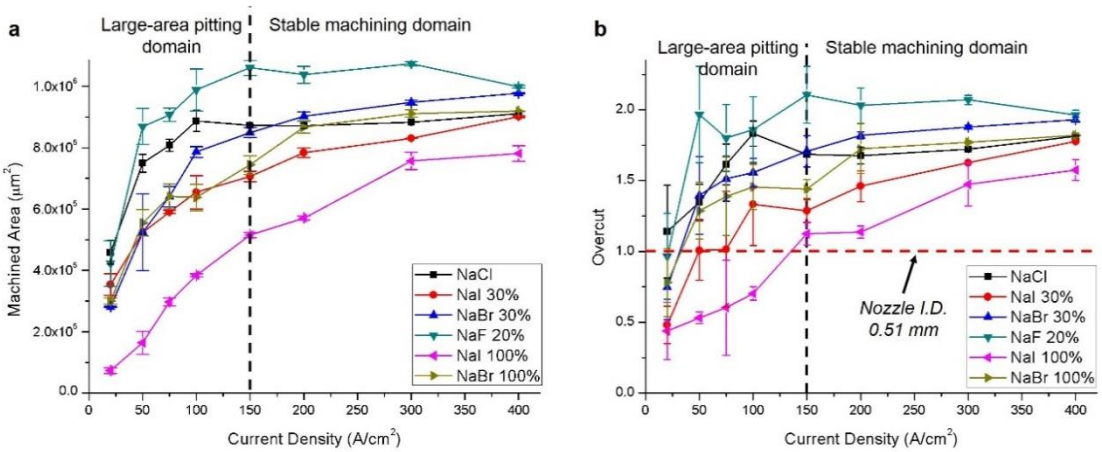


Figure 6.18: Total machined area and overcut as a function of applied current density and electrolyte type. For all cases, pitting can be determined at low current density, followed by a transition into a stable machining regime.

In addition to decreasing processed area upon addition of pit-promoting anions, pit depth increases (*see* Figure 6.19a). Pits formed in the absence of pit-promoting anions (which suppress the oxide breakdown potential) are significantly shallower and flatter than those formed in the presence of both bromide and iodide. This is largely a result of re-passivation, which is more favourable without pit-promoters. Pits instead grow laterally instead of vertically, increasing A_m, but decreasing the maximum cut depth, d_M, shown in Figure 6.19a.

Re-passivation of the workpiece surface is evidenced by the material removal per unit charge, which is also partially influenced by the electrolyte used (*see* Figure 6.18b). At low current density (<150 A/cm^2), charge-specific removal is greater for NaBr 30% and NaI 30% than NaCl. In addition, it is shown that this is the result of a combinatory effect between the base electrolyte (chloride) and the dopant, as NaI 100% demonstrates insignificant material removal at low current density. It is proposed that iodide readily de-passivates local surface region enabling chloride, which is more inert towards anodic oxidation, to enhance material removal.

In the stable machining domain (≥200 A/cm^2), material removal can be slightly enhanced through the addition of aggressive bromide anions to the electrolyte. In this regime, for most electrolytes, the charge-specific removal correlates with the weighted ECE of Ti-6Al-4V (1.198-1.206x10^{-5} g/C, *see* Appendix 3), considering dissolution to the Ti (IV) oxidation state. It is also apparent that iodide-doped electrolytes are unsuitable if the desired outcome is increased material removal. This is pertinent considering the lower oxide breakdown potential in comparison to chloride. This is due to transitory current filtering, where a portion of the charge passed is sacrificed to oxidise iodide to other iodine-containing compounds.

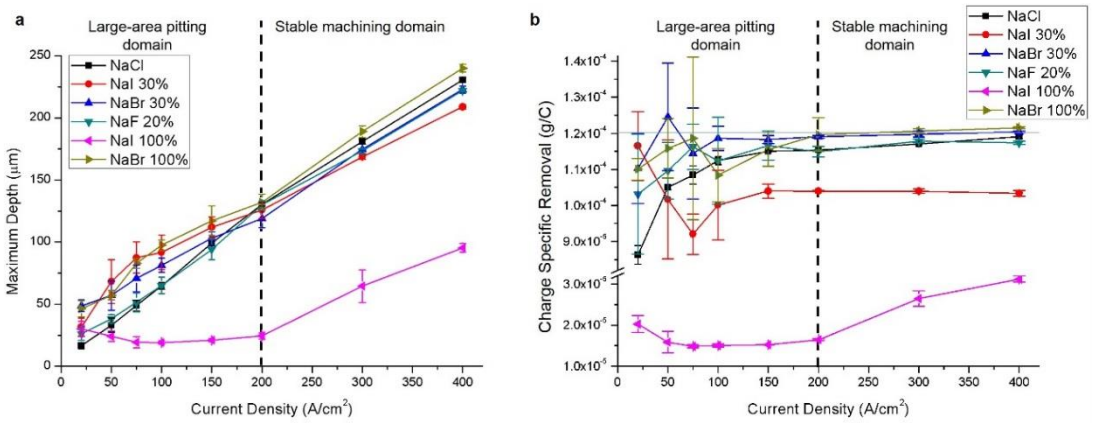


Figure 6.19: a) The relationship between cut depth and current density is linear >200 A/cm^2, but more complex in the pitting domain. Depth is increased <200 A/cm^2 for electrolytes doped with aggressive anions. In the stable machining domain, d_M is reduced for iodide containing electrolytes, due to transitory masking. This is shown for b) charge-specific removal, with lower material removal in the stable machining domain. Material removal can be enhanced by doping with bromide.

The proposed mechanism of re-passivation at the basal area of a pit is shown in the schematic in Figure 6.20. In the case of a passivating electrolyte system, more oxygen is evolved at the anode at low current densities (<150 A/cm^2) evidenced by the lower charge specific removal values in Figure 6.19b. This oxygen is therefore available to rapidly oxidise the TiX_4-type species (where X = F^-, Cl^-, I^-, Br^-) that are understood to compose the salt film [56] to reform a protective layer of TiO_2 (*see* Figure 6.20b). This layer increases the localised resistance at the basal area of the pit. Removal therefore lateralises, where the resulting pits are shallow and wide <150 A/cm^2, evidenced in the maximum depth data shown in Figure 6.19a. In contrast, in the presence of pit-promoters, such as bromide (*see* Figure 6.20c), oxygen evolution is suppressed, evidenced by the greater charge specific removal at low current density (*see* Figure 6.19b), therefore the TiX_4 salt film is retained, encouraging vertical removal and deep pits of higher aspect ratio.

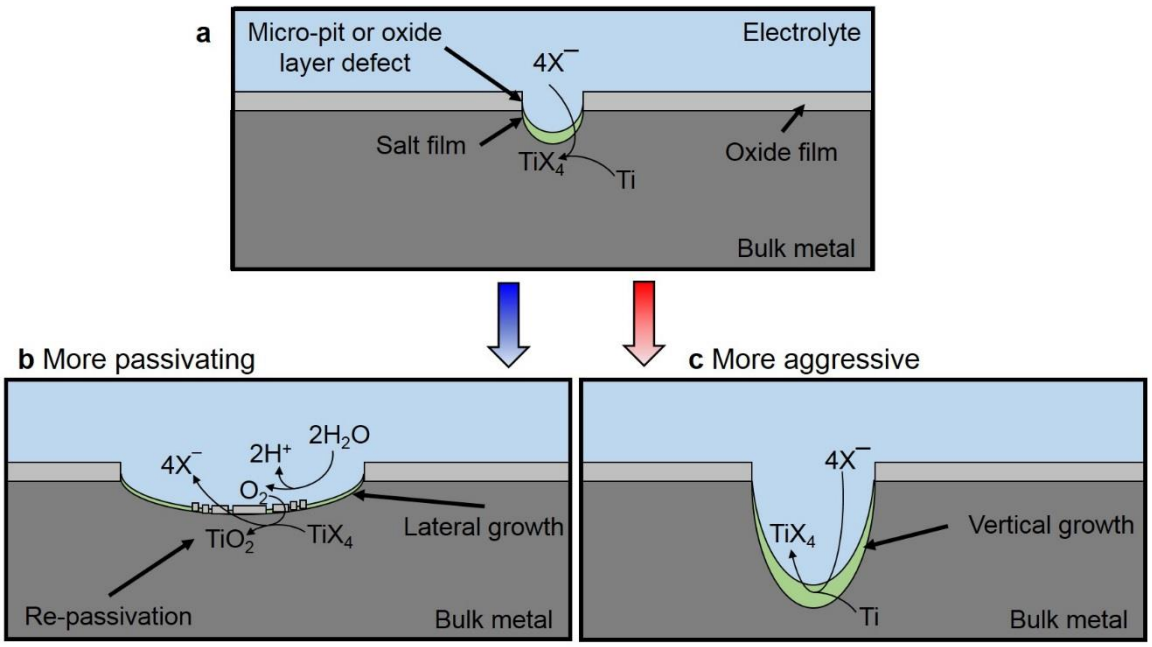


Figure 6.20: Schematic showing proposed re-passivation mechanism. a) From an initiated pit, with a TiX_4-type salt film, b) more passivating electrolytes evolve more oxygen, rapidly reforming a protective TiO_2 layer, lateralising removal. c) For an aggressive electrolyte, no such oxygen evolution occurs and the salt film is retained, promoting vertical growth.

6.3.3. Dimensional accuracy and fidelity

Where deterministic and well-defined microscale featuring is desired on a surface, processing within the stable processing domain (≥200 A/cm^2) is recommended as this gives greater repeatability and material removal characteristics compared with the large-area pitting domain. The dimensional accuracy of featuring generated in this domain, where material removal occurs predominantly within the transpassive dissolution regime, was appraised for all electrolytes. This is evidenced by Figure 6.18b, which shows the reduction in overcut achievable through application of iodide-containing electrolytes.

Dimensional accuracy was also appraised through striation edge definition, dev_c. This was measured from the deviation of the extracted edge contour from a best fit line (measured along 1 mm sample lengths, *see* methodology), shown

in Figure 6.21a. The results demonstrate that increasing current density within the stable cutting domain leads to straighter and more repeatable striation edges, in this material. In addition, doping with I^- reduces the spread of the total deviation from a straight line, where the un-doped NaCl leads to a total deviation of 1580 μm^2 (σ 45%), compared with 1560 μm^2 (σ 27%) for NaI 30% at 300 A/cm^2. Increasing current density (400 A/cm^2), NaI 30% further reduces deviation (910 μm^2, σ 13%), compared with NaCl (1150 μm^2, σ 18%). The striations processed with the Br^--doped electrolyte (NaBr 30%), show greater deviation at both 300 A/cm^2 (2430 μm^2, σ 36%) and 400 A/cm^2 (1460 μm^2, σ 33%) than either NaI 30% and NaCl, largely resulting from an increased ability to destabilise passivation in titanium. This is shown in the extracted exemplar profiles acquired from the edge of the striations in Figure 6.21b, where the localised anodic potential is assumed to be low. Profiles machined without bromide appear to have a steep section adjacent to the un-machined surface (5-10 µm in depth), in comparison to that machined in the presence of Br^-, which shows an edge profile in closer agreement to the applied Gaussian current density distribution.

Although the un-doped NaCl shows good edge definition in the stable machining domain compared with other electrolytes (except NaI 30%), the profile sections show a shouldering effect, more exaggerated in the fluoride electrolyte, which is proposed to result from re-passivation of the side wall as material is removed. In the presence of iodide or bromide, re-passivation is inhibited and material removal occurs in vertical manner (*see* Figure 6.21c, machined with NaI 30%). Conversely, for passivating electrolytes (*see* Figure 6.21d, NaF 20%), re-passivation occurs inhibiting vertical removal, leading to a

shouldering effect in the resulting profile, described in the mechanism in Figure 6.20. In this instance, current density would likely localise at the edges of the re-passivated area, leading to effective lateral machining and can result in pitting, which affects the deviation of the striation. Complementary tinted SE micrographs (taken from the 400 A/cm^2 striations) show the edge regions with the best dimensional accuracy, showing the straightest and most repeatable cut edges (NaI 30%, *see* Figure 6.21e) and the poorest dimensional accuracy, where re-passivation of the edge region leads to a deviating cut and lateral removal (NaF 20%, *see* Figure 6.21f).

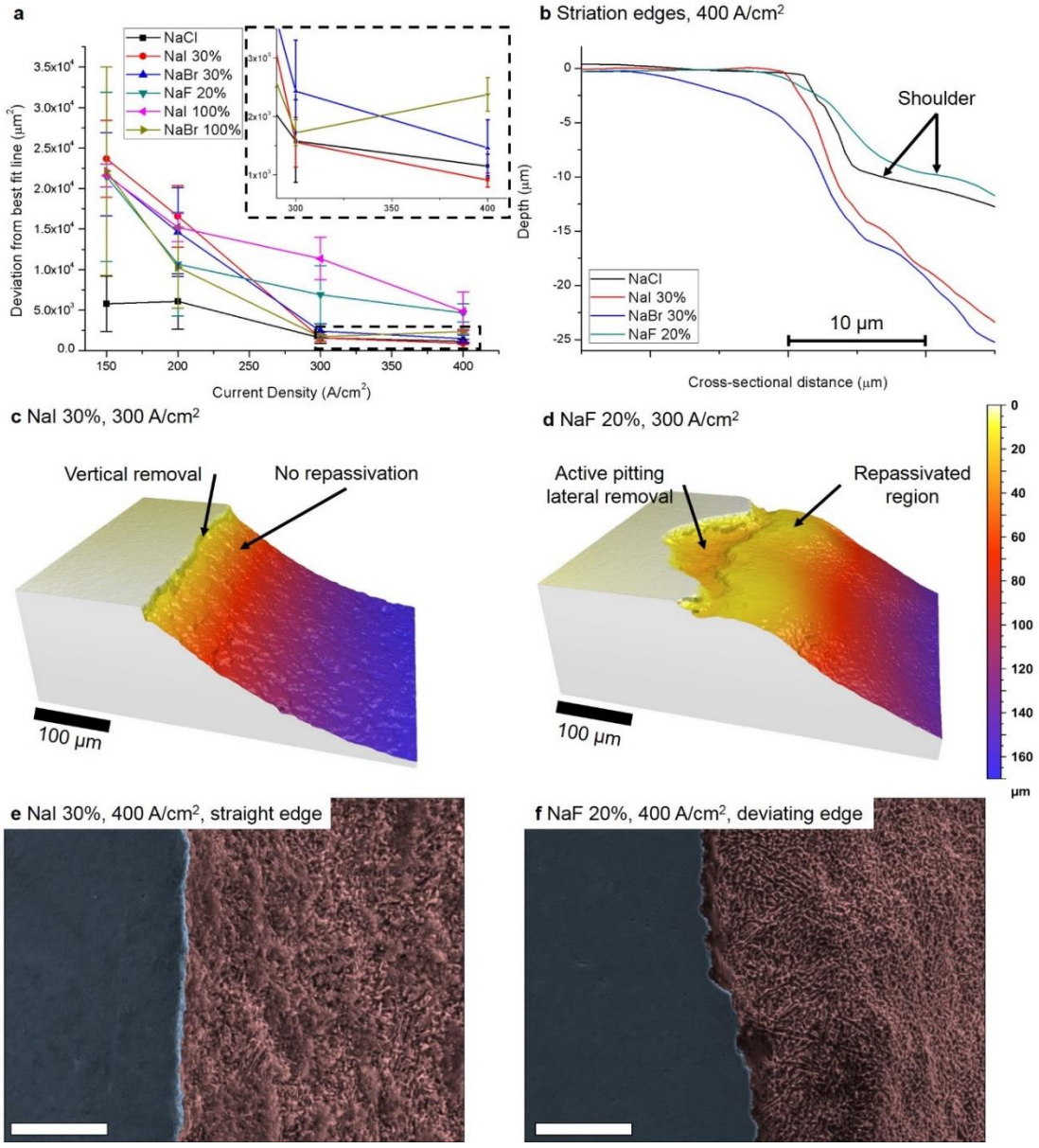


Figure 6.21: a) Edge deviation from best fit contour from 150-400 A/cm^2. Inset graph – NaCl and NaI 30% generate cuts with the straightest edges within the stable machining domain, however, b) extracted profiles of the track edges (400 A/cm^2) show shouldering of the NaCl and NaF 20%, not present in NaBr 30% or NaI 30%, caused by edge re-passivation, where charge flux is low. FVM reconstructions showing edge regions of striations (300 A/cm^2), c) with NaI 30% and d) NaF 20%. Reduced re-passivation leads to removal more consistent with the applied Gaussian distribution, where re-passivation, leads to localised inconsistencies in the applied current. Subsequently material removal may lateralise, leading to undulations. Tinted SE micrographs show the microscale edge definition when using e) NaI 30% and f) NaF 20% at 400 A/cm^2. SEM scale bars 50 μm.

The shouldering effect is shown by the most passivating electrolytes tested here was appraised through analysis of the profile in comparison to an arc of best fit, considering the total profile area, A_p (*see* methodology). The data, shown in Figure 6.22a, demonstrate that deviation is reduced and repeatability increased at high current densities (>200 A/cm^2), when processing with NaBr 30% (0.9%, σ = 0.1%) and NaI 30% (0.7%, σ = 0.1%) electrolytes, compared with un-doped NaCl (1.2%, σ = 0.2%) (values quoted for 400 A/cm^2). In addition, evidence for a combinatory effect is shown, whereby the correlation between the machined profile and the best-fit arc resulting from the addition of Br^- and I^-, is not observed in un-doped electrolytes, where these anions compose 100% of total anion concentration: NaI 100% (13%, σ = 1.8%), NaBr 100% (1.5%, σ = 0.3%).

Figure 6.22b considers FWHM in terms of the total kerf for each electrolyte within the stable cutting region, whereby a greater result is indicative of a steeper side wall slope. Excluding NaI 100%, all electrolytes show an upward trend in this metric in the stable cutting domain. This supports overcut data, which doesn't change significantly in this processing region (*see* Figure 6.18). The depth, however, is shown to increase linearly as the charge passed is increased (*see* Figure 6.19a), such that processing at greater current density leads to steeper side wall slopes. This indicates that the dimensional accuracy of the machined feature is largely independent of charge passed, within this parameter set and suggests that even greater side wall slopes are achievable through multi-pass processing. Increasing the applied current density beyond 400 A/cm^2 is not recommended as arcing and sparking is often observed beyond this region, possibly resulting from the breakdown of gas evolved at

both electrodes. This decreases the surface integrity and quality and thermally affects the workpiece material.

The ability to effect consistent machining is shown in the SE micrographs of track sections, showing stochastic and uncontrolled flaring across the length of the processed feature upon machining with passivating NaF 20% (see Figure 6.22c), which is decreased in the absence of F^- anions processing with un-doped NaCl (see Figure 6.22d). Upon addition of aggressive anions, decreasing instability is observed, and striations appear repeatable and without lateral flaring (see Figure 6.22e and f), processed with NaBr 30% and NaI 30%, respectively).

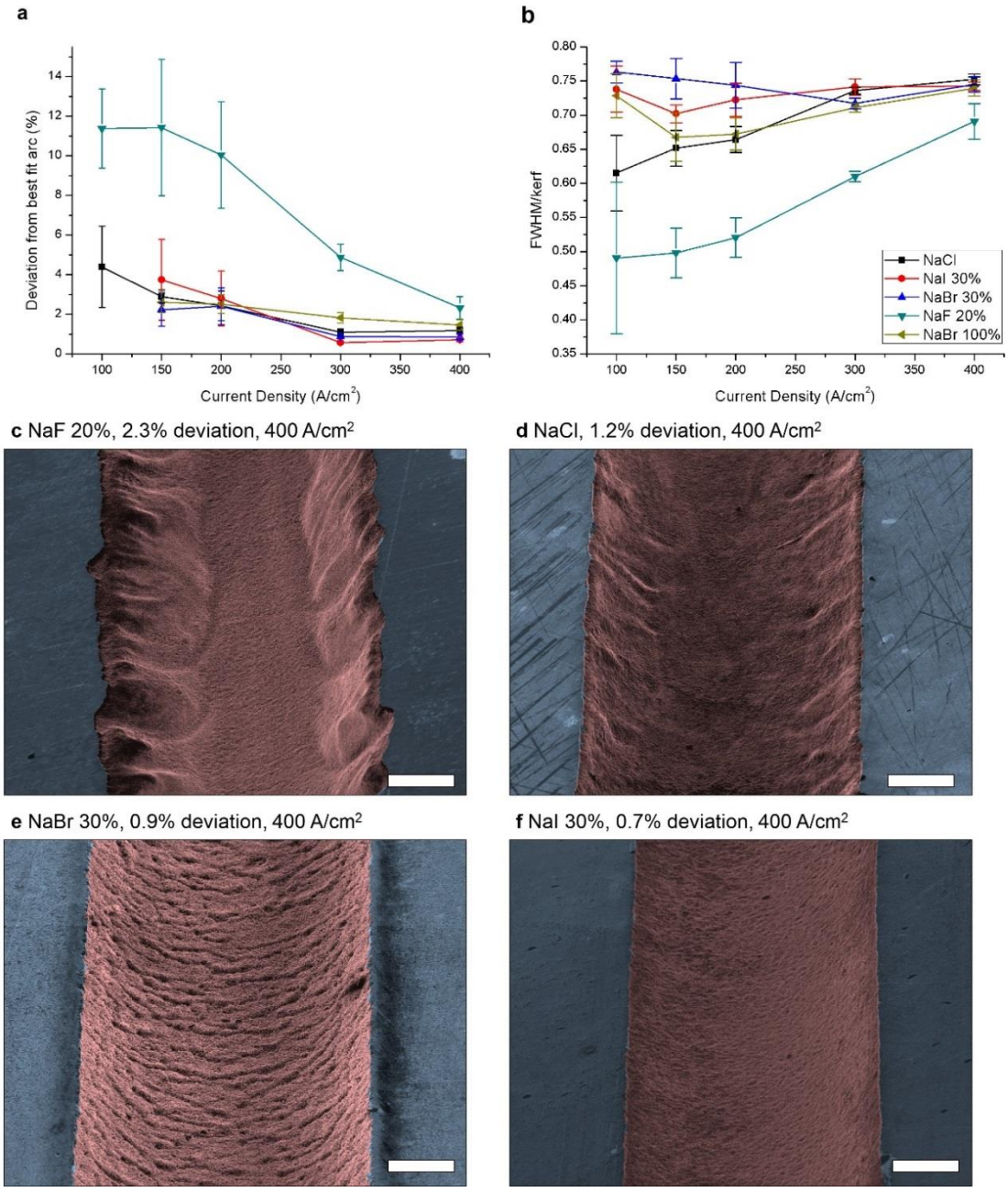


Figure 6.22: a) Graph showing the profile deviation from the best-fit arc, considering the total profile area, A_p. Here, it is shown that additions of both Br^- and I^- can reduce the profile deviation from that achieved using un-doped NaCl. b) Graph showing the profile width at half of the maximum depth, considering the total kerf. All electrolytes show a positive trend in this domain, indicative of kerf-width independent of charge passed in this region. SE micrographs showing machined features (red) processed with electrolytes at 400 A/cm², c) NaF 20%, showing significant flaring, inferior to the control sample, d) NaCl. Through additions of aggressive anions, flaring is shown to reduce further, e) NaBr 30% and f) NaI 30% and features agree more with the applied Gaussian current density distribution. SE scale bars are 200 µm.

Combinatory effects are demonstrated, whereby small additions of both Br^- and I^- can significantly enhance dimensional accuracy, as well as other cutting characteristics, such as material removal. Here, it has been shown that small additions of aggressive dopants to the electrolyte aid processing in the stable cutting domain (≥200 A/cm^2). Enhanced cut edge definition and profile definition are achievable through the reduced probability of side wall re-passivation, which result in profile shouldering and flaring, as the jet translates.

Microchannel generation is one area to which EJP has been applied through exploitation of planar processing strategies. In order to realise such featuring in titanium-based materials, the NaI 30% electrolyte was applied at high current density (>300 A/cm^2), where the resulting surface is shown in Figure 6.23. Both 510 and 250 μm diameter nozzles were applied in workpiece processing. Good dimensional accuracy, repeatability and large material removal are demonstrated in Ti-6Al-4V where the sample was created in <5 minutes processing time.

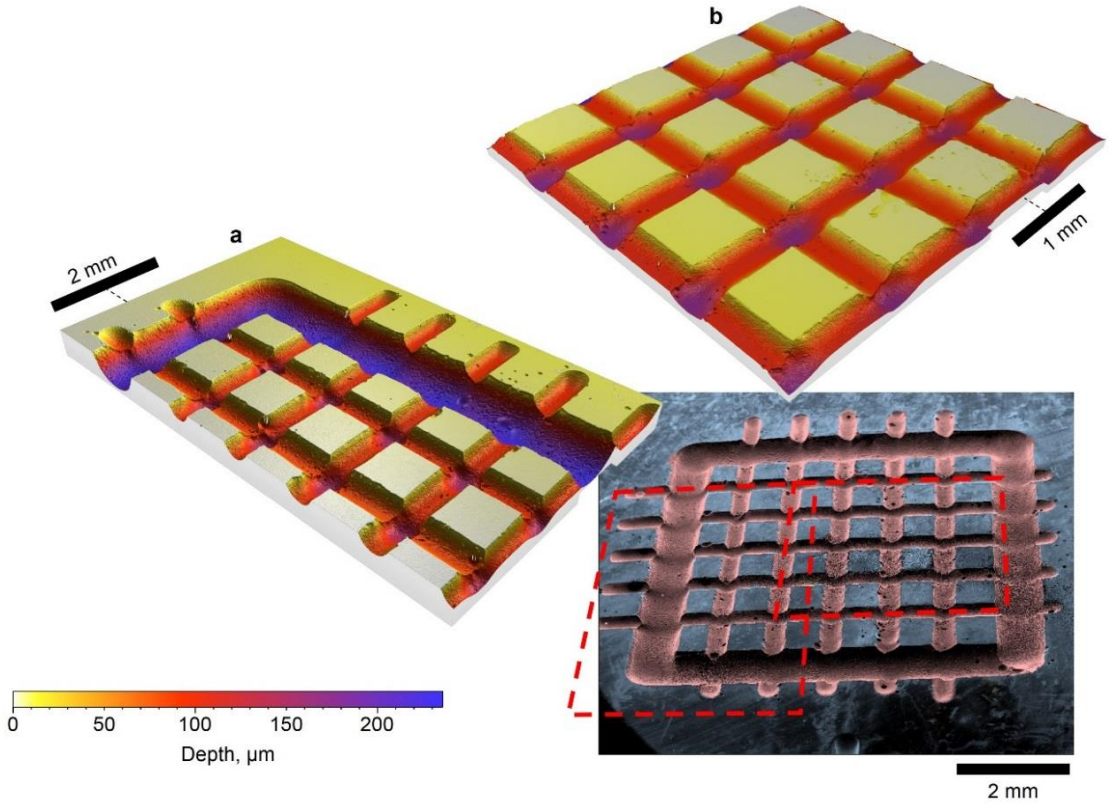


Figure 6.23: Processing titanium sheet at high current density (≥300 A/cm^2) using NaI30% to reliably machine microchannel features. This compares favourably with the striations processed by Liu et al. (2017) [84] in TB6, considering stray cutting and much reduced processing time (processing at 10 µm/s with NaCl).

6.4. Novel material removal mechanisms

In this section, hitherto unexplored jet-specific electrochemical phenomena are reported and the mechanisms have been proposed, which could expedite the generation of both large-area surface textures for mechanical applications, and fractal surface structures for increasing transport efficiency in microchannel arrays. This section was performed in Ti-6Al-4V, where novel processing mechanisms exploit the highly passivating nature of the material.

6.4.1. Periodic electrochemical oscillations

Processing at low current density (J_{noz} = <200 A/cm^2) leads to discrete periodic pitting events within the jet affected zone, evidenced by the surface reconstructions in Figure 6.17. The morphology of the pitting appears to be largely determined by electrolyte type (*see* Figure 6.18d-f), where dopants such as iodide and bromide, which suppress the oxide breakdown potential, are observed to generate multiple deep and narrow pits. Interestingly, processing in this regime with such electrolytes leads to cyclic ‘staccato’ removal, whereby pits form semi-regular packets, shown in Figure 6.24a (processed with NaI 30% at 50 A/cm^2). Each discrete removal event appears to occur through the coalescence of micro-pitting events. This leads to an increase in depth in the direction of translation as the feature propagates, before the stability of the pit breaks down and removal abruptly halts (*see* Figure 6.24b). The non-machined part of the staccato cycle can be correlated with a spike in the electrode potential and increasing resistance (considering a constant current processing operation), where quasi-periodic oscillations can be observed in the inter-potential peak (*see* Figure 6.24c). SE micrographs show similar surface textures at the basal areas of the coalescing micro-pits and the mature macro-pit prior to propagation breakdown (*see* Figure 6.24d and e), which is indicative of a similar chemical and energetic environment.

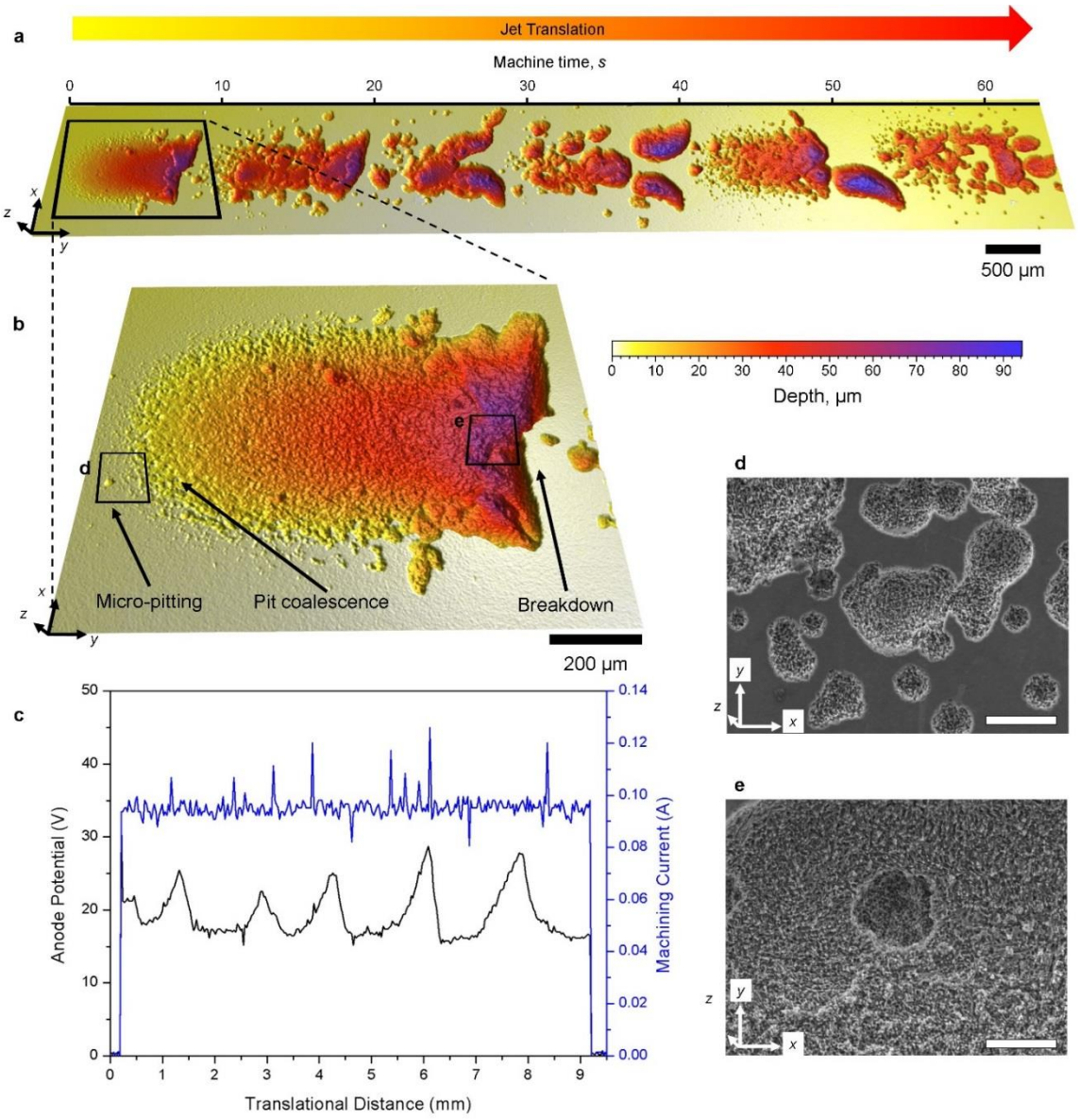


Figure 6.24: Quasi-periodic pitting with aggressive electrolytes. a) Striation processed at low current density (50 A/cm^2, v_h = 0.15 mm/s) showing staccato-type material removal. b) Formation occurs through the coalescence of micro-pitting events and terminates in abrupt pit break down. c) The potential trace measured across the same surface presented in a). d, e) SE micrographs showing the coalescing micro-pits and mature pit surface, similar textures are observed at each point, scale bars are 50 µm.

The mechanism of the quasi-periodic pitting is likely to result from a differential in the lateral propagation velocity of a discrete pitting event and the nozzle translation velocity, shown in Figure 6.25. At the start of a discrete pitting event, upon micro-pit coalescence, material is removed as an approximate reflection

of the Gaussian current density distribution (*see* Figure 6.25a). For a case where nozzle translation velocity is greater than lateral propagation velocity, the nozzle will start to overlap the un-machined material, which is insulated by strongly passivating oxide films. This causes the current density distribution to focus towards the trailing end of the electrolyte jet, still exposed to the basal areas of the pit, and is thought to be responsible for the depth increases observed along a given pitting event (*see* Figure 6.25b). The current focussing effect is considered to be responsible for the gradual increase in resistance prior to a discrete electrode potential spike, whereby the charge flux is transferred through a decreasing portion of the electrolyte jet (*see* Figure 6.24c).

Propagation of a discrete event will continue until the resistance associated with material removal at the basal region of a propagating pit, Ω_p, becomes greater than the breakdown resistance of the native oxide film, Ω_o, at which point micro-pits will form in the leading edge of the electrolyte jet (*see* Figure 6.25c). At this instant, the current density distribution defocusses from the trailing edge and resistance rapidly decreases, leading to a sharp decrease in measured electrode potential. This leads to discrete phenomena governing the periodicity: i) micro-pitting and coalescence into a coherent feature, ii) deepening removal profile caused by current density focussing and eventually iii) breakdown, where it is energetically unfavourable to continue the propagation of a discrete pitting event (*see* Figure 6.25d). For a material processed at a given current density, regime i) will be determined mainly by the electrolyte (governing the stability of the oxide film), whereas regimes ii-iii) are likely to also be dependent on the nozzle diameter and other conventional processing factors.

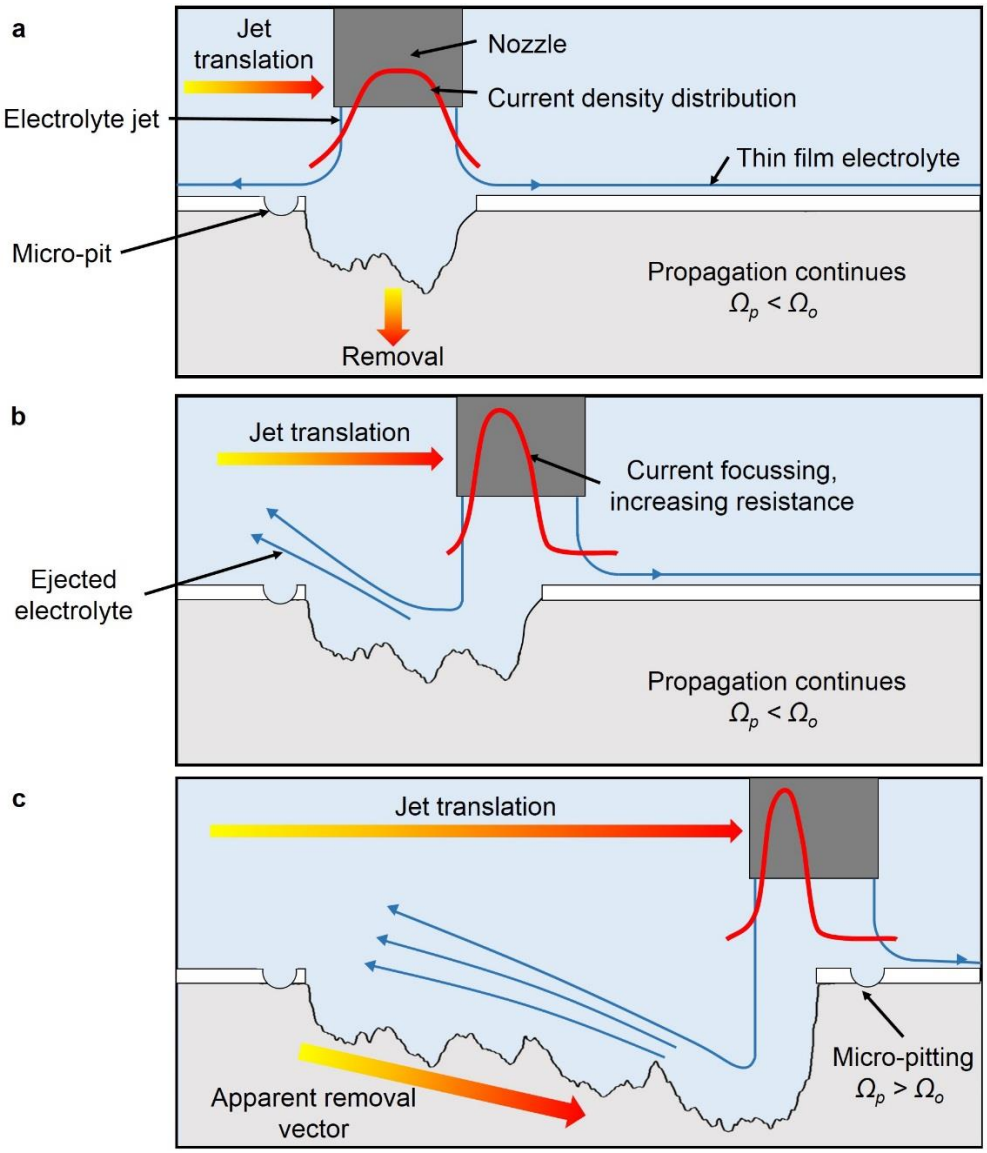


Figure 6.25: The mechanism of periodic staccato machining cycles. a) Upon coalescence, current density distribution is Gaussian in nature. b) When v_h>lateral propagation velocity, current density focusses to the trailing edge, increasing global resistance. c) Where resistance of the pit base is greater than the resistance of the oxide film, micro-pits form, propagation abruptly stops and resistance rapidly drops. d) This leads to an effective deepening of the pit feature along the translation vector.

It is stressed that in most iterations of EJP, processing at low current density does not result in the same quasi-periodicity in electrode response. This effect is likely to be limited to strongly passivating materials processed with aggressive

electrolytes, such that the velocity of pit propagation is slower than the translation velocity.

The precise location of micro-pit nucleation is heavily influenced by the integrity of the passivating oxide layer in the material. For a material such as titanium, with high corrosion resistance, the probability of micro-pit nucleation is significantly increased at defects in the oxide layer, compared with a non-passivating material. This is shown in Figure 6.26, on which micro-pit nucleation clearly aligns with the residual grinding marks, where the integrity of the native oxide layer is reduced. Finer polishing steps lead to more stochastic micro-pit distribution in the coalescence region of the staccato cycle, however the sensitivity of pit nucleation to surface defects provides a potential route through which a pre-set feature morphology could be applied to a surface prior to EJP.

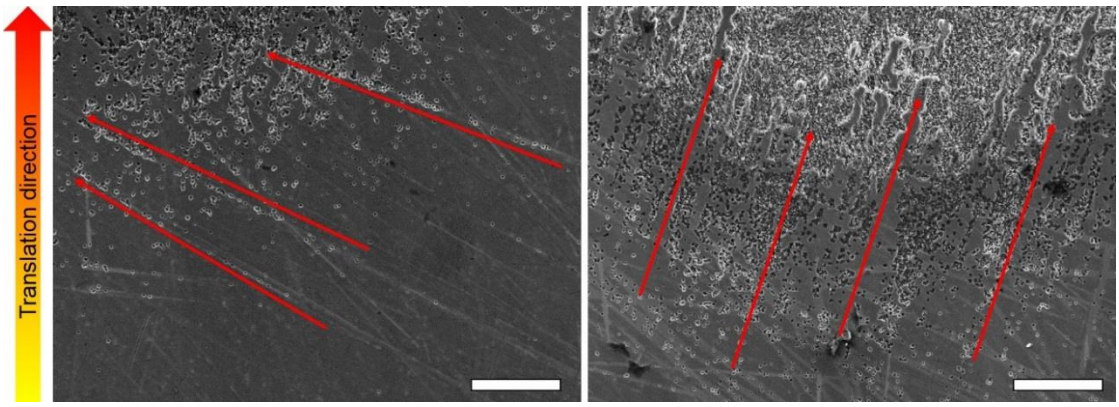


Figure 6.26: Nucleation of micro-pits is influenced by prior surface features. Pits are shown to align with the direction of the grind marks. Scale bars are 100 µm.

The effect of conventional EJP parameters on the quasi-periodicity was elucidated through analysis of potential difference traces. In this instance, a decrease in the frequency of the inter-potential peaks is assumed to be an indicator of increased stability of pit propagation. Considering the geometric constraints of the proposed overlap mechanism (*see* Figure 6.25), increasing

nozzle diameter is observed to decrease frequency and increase the regularity of the oscillations. This indicates increased propagation stability (*see* Figure 6.27). Of all the factors aside from current density, nozzle diameter appears to be the major determiner of the oscillation frequency. Increasing nozzle diameter increases the linear charge density required to achieve equivalent J_{noz}, thus the MRR is increased, which may be the cause of the increased stability.

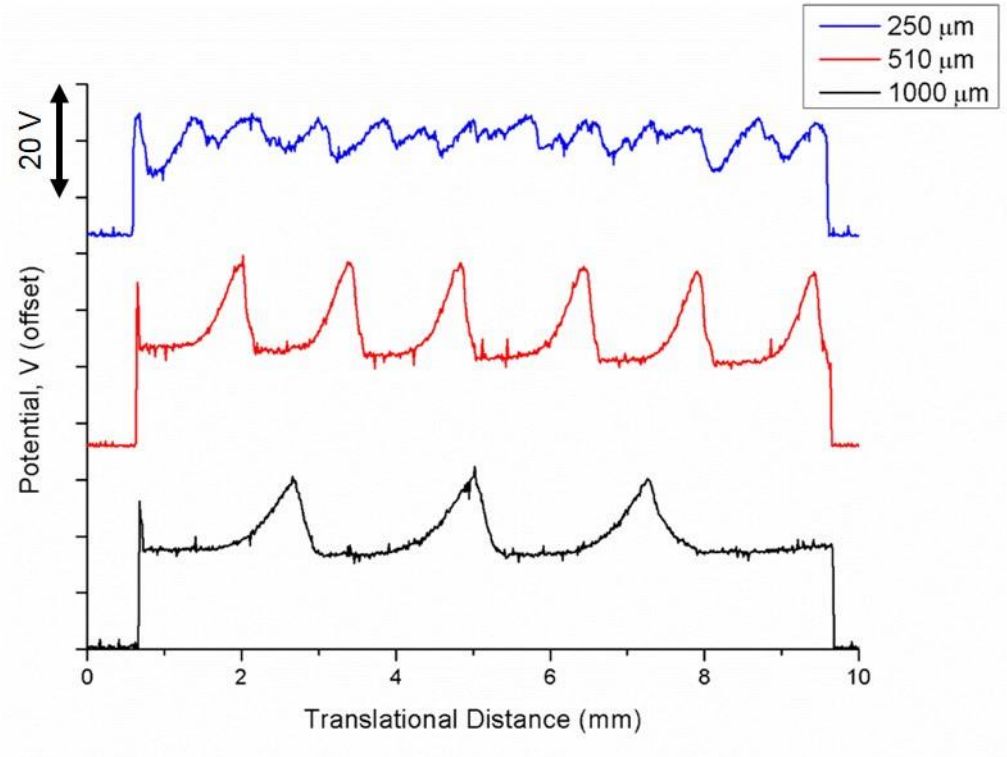


Figure 6.27: Oscillation frequency is inversely proportional to nozzle size. J_{noz} = 50 A/cm^2, v_h = 0.3 mm/s, v_j = 16.3 m/s.

Further evidence is shown in Figure 6.28, whereby decreasing the linear charge density through increasing translation velocity is observed to decrease the inter-potential peak spacing, $(\frac{d}{d_N})$, for a given nozzle diameter in the operating range presented (v_h = 0.1-0.3 mm/s). In addition, processing below this range (v_h = 0.05 mm/s) results in no observed periodicity and continuous striations are

machined; proposed to result from a case where the propagation velocity of the pitting event is greater than or equal to the nozzle translation velocity.

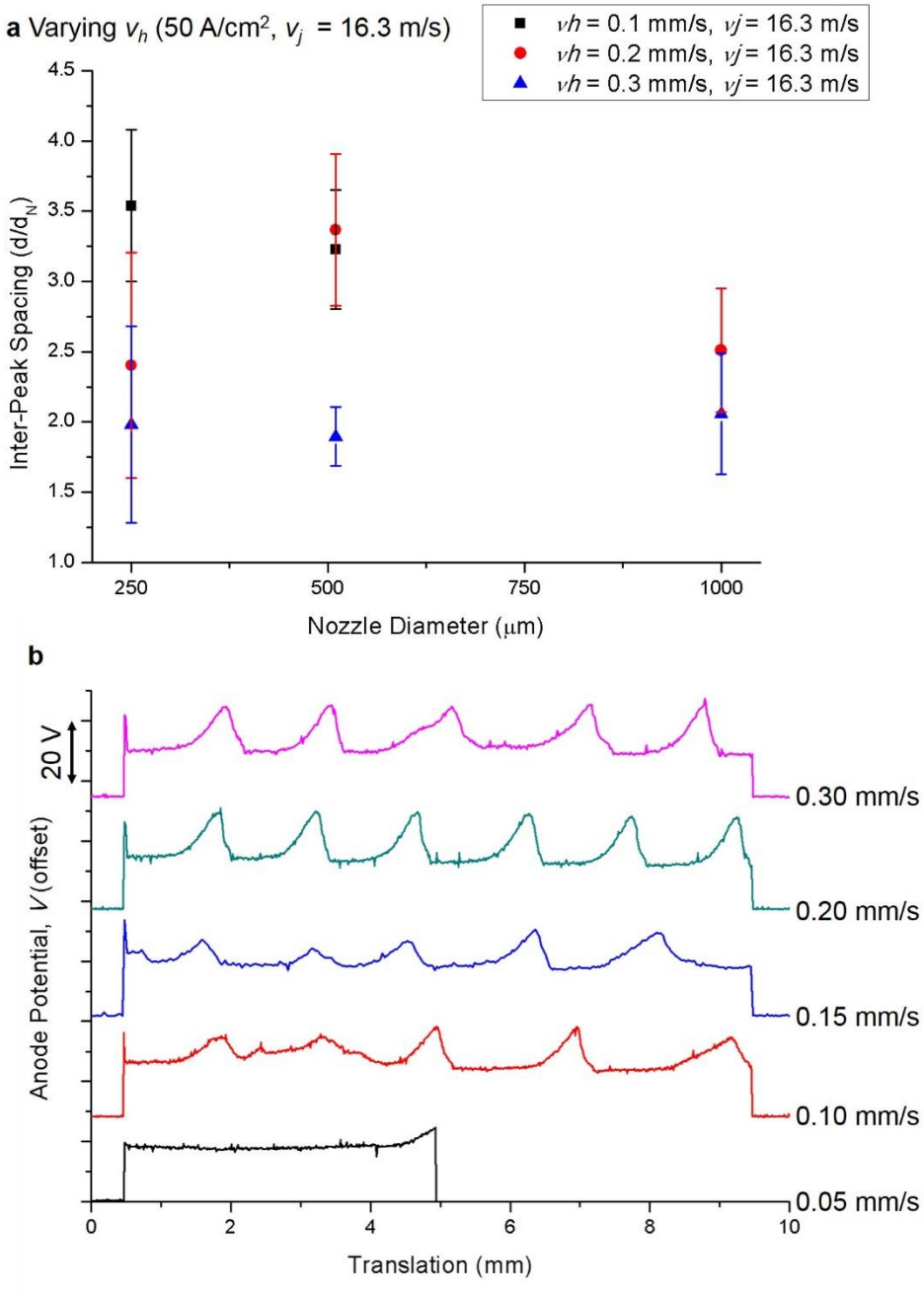


Figure 6.28: Varying the feed rate is shown to slightly affect the inter-peak spacing for a given nozzle diameter. Faster feed rates appear to decrease propagation stability. When processing at the lowest feed rate (0.05 mm/s), oscillations are all but inhibited.

Considering the inverse relationship between the incident dopant concentration (IDC) at the anode and the MRR (*see* section 6.2.2, page 188) it is recognised

that the discrete electrolyte chemistry at the anode will change with electrolyte jet velocity, v_j. This is especially pertinent regarding both the application of anions that are readily anodically oxidised, such as iodide, and the large electrode potentials employed (for example, a minimum of ≈15 V during processing, Figure 6.24c). In light of the strong dependence of pit morphology on the electrolyte chemistry, it is necessary to appraise the impact of differing v_j on the inter-potential peak spacing. The results are shown in Figure 6.29a, b, acquired at constant J_{noz} (50 A/cm^2), v_h (0.2 mm/s) and nozzle I.D. (510 µm). With greater v_j, (*see* Figure 6.29b) the inter-potential peak spacing increases, and the peaks become increasingly defined. The morphology of the coalescing micro-pits, prior to discrete large-area pit formation, was appraised using SE microscopy and shows significantly narrower pits at high v_j (*see* Figure 6.29c) than low v_j (*see* Figure 6.29d). The broadening of the pitting is indicative of a transition towards a less aggressive electrolyte solution, which is reflected in the lower IDC at low v_j. The oxidation of iodide is assumed to be rapid, therefore lowering the jet velocity and the supply of this anion to the anode will limit the aggressive contribution to the removal characteristics, in addition to increasing bulk material removal. The pitting morphology becomes more consistent with that expected from chloride electrolytes without aggressive dopants, material removal rate increases, and the periodicity of the potential traces destabilises.

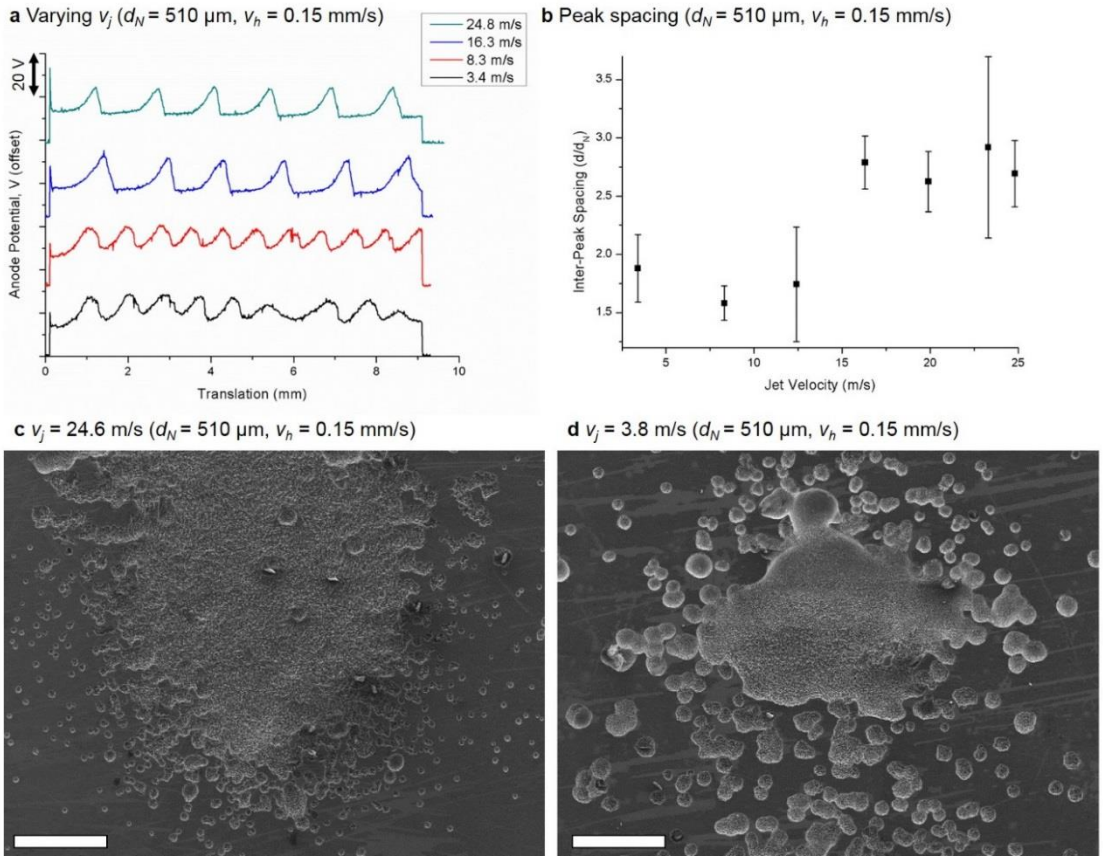


Figure 6.29: Influencing the quasi-periodicity of pit propagation with electrolyte jet velocity. Increasing jet velocity increases the stability of the propagating pit and therefore b) the peak spacing, likely resulting from the change in incident electrolyte chemistry. This is evidenced in the SE micrographs which show different micro-pit morphologies at c) high and d) low jet velocity. Scale bars are 200 µm.

The mechanism of periodic pitting is therefore complex, however it is evident that certain conditions must to be adhered to before periodic electrochemical oscillations are permitted in EJP: i) the material must be largely corrosion resistant, ii) aggressive electrolytes, such as iodide or bromide for titanium, should be applied, iii) current density must be low (≤150 A/cm^2 for this material), iv) translation velocity must be greater than the lateral growth rate of the corrosion pits (>0.05 mm/s for this material-electrolyte combination). Condition i) increases the restriction of material removal to pre-existing active areas, such as corrosion pits. Condition ii) prevents re-passivation of basal area of the pre-

existing pit, which promotes downward growth ahead of a lateral expansion. Condition iii) limits the localised charge flux at a given point on the surface, enabling processing outside of the stable operating regime, and condition iv) leads to current density focussing at the trailing edge of the electrolyte jet due to overlap.

One such route through which the quasi-periodic oscillatory removal could be employed as a processing strategy is through the generation of enhanced mechanical lock-loading surfaces, where the depth increases across each pit as a function of pit length. Considering the prolific application of titanium alloys towards skeletal implants, such surface processing could be employed to enhance the mechanical bonding of tissue and bone towards the implant material. Furthermore, these characteristic anisotropic removal regions could lead to enhanced interfacial adhesion in a number of applications, such as carbon fibre reinforced polymer-titanium materials. A typical surface is shown in Figure 6.30, where the surface would be loaded in line with the EJP toolpath.

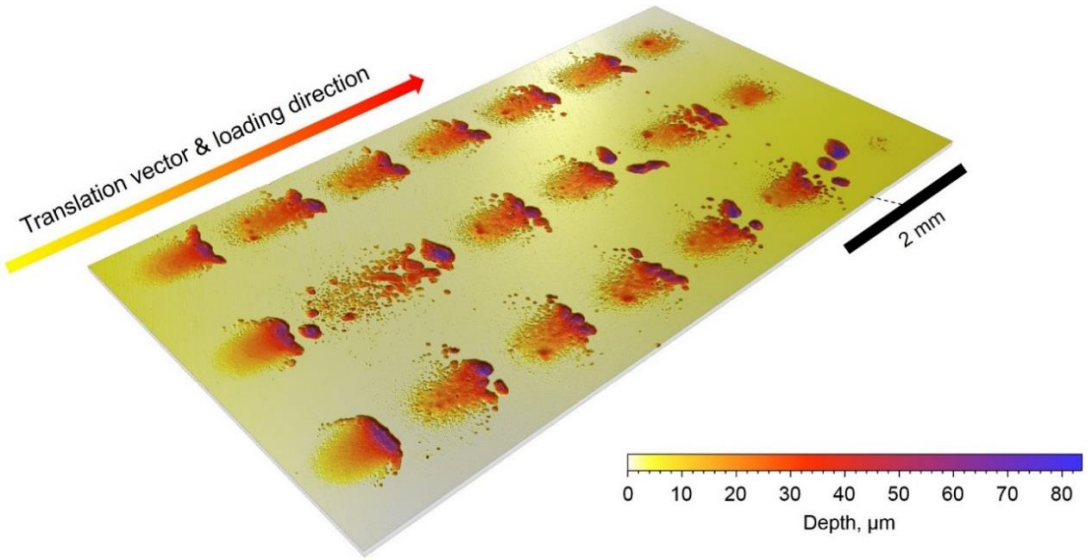


Figure 6.30: Employing periodic electrochemical oscillations to surface texture large areas of material.

6.4.2. Propagating individual pits

In EJP, the scale of microchannel featuring is limited by the size of the nozzle, where feature resolution approaching the nozzle diameter has been presented in section 6.2.3 (in this case 60 µm). However, further refinement of nozzle size as a route through which to generate features <50 µm in EJP is challenging, due to the susceptibility of small nozzles to block when the necessary high-concentration and viscosity electrolyte solutions required for processing are employed. Therefore the generation of feature sizes at these length scales are currently unachievable without masking techniques, which complicate processing and increase the time and cost penalty. In order to generate features such as microchannels at length scales finer than the nozzle diameter, a different removal mechanism must be exploited. Operation within low current density regimes (<150 A/cm^2) has been shown to generate discrete pits at length scales <0.5 nozzle diameter in iodide and bromide-doped electrolytes (*see* Figure 6.18b), albeit as part of a stochastic process. Considering the demonstrated ability of EJP to propagate discrete removal events through exploitation of nozzle translation (*see* section 6.4.1, page 222), controlled propagation of individual corrosion pits presents one such route through which sub-micron features could be generated.

The proposed mechanism of controlling discrete corrosion pit propagation is shown in Figure 6.31a for Ti-6Al-4V sheet. In Figure 6.31a, the surface reconstruction acquired after static EJP in NaI 100% (2.3 M) electrolyte (100 A/cm^2, 4 s dwell), shows outwardly radiating pits from the central impingement point, where feature growth is evidently influenced by the electrolyte flow in addition to the surface potential. Pits are initiated in the high current density

region of the electrolyte jet where material removal is more favoured. Here, stochastically distributed (or controlled, *see* Figure 6.26) defects in the oxide layer are significantly easier to break down (de-passivate). Upon localised de-passivation, material removal is initiated as a discrete pitting event, which subsequently propagates, where the direction is influenced by the radial flow regime of the impinging jet, resulting in outward fractal-type growth. When the jet is translated (*see* Figure 6.31c), the movement contributes a directional bias to the propagation of the pits, resulting in feathered surfaces with branching features divergent from the translation direction. In this case, pits propagate with the jet translation, whilst still being influenced by the radial flow, which sweeps the growing pit features perpendicular to the translation direction (*see* Figure 6.31d).

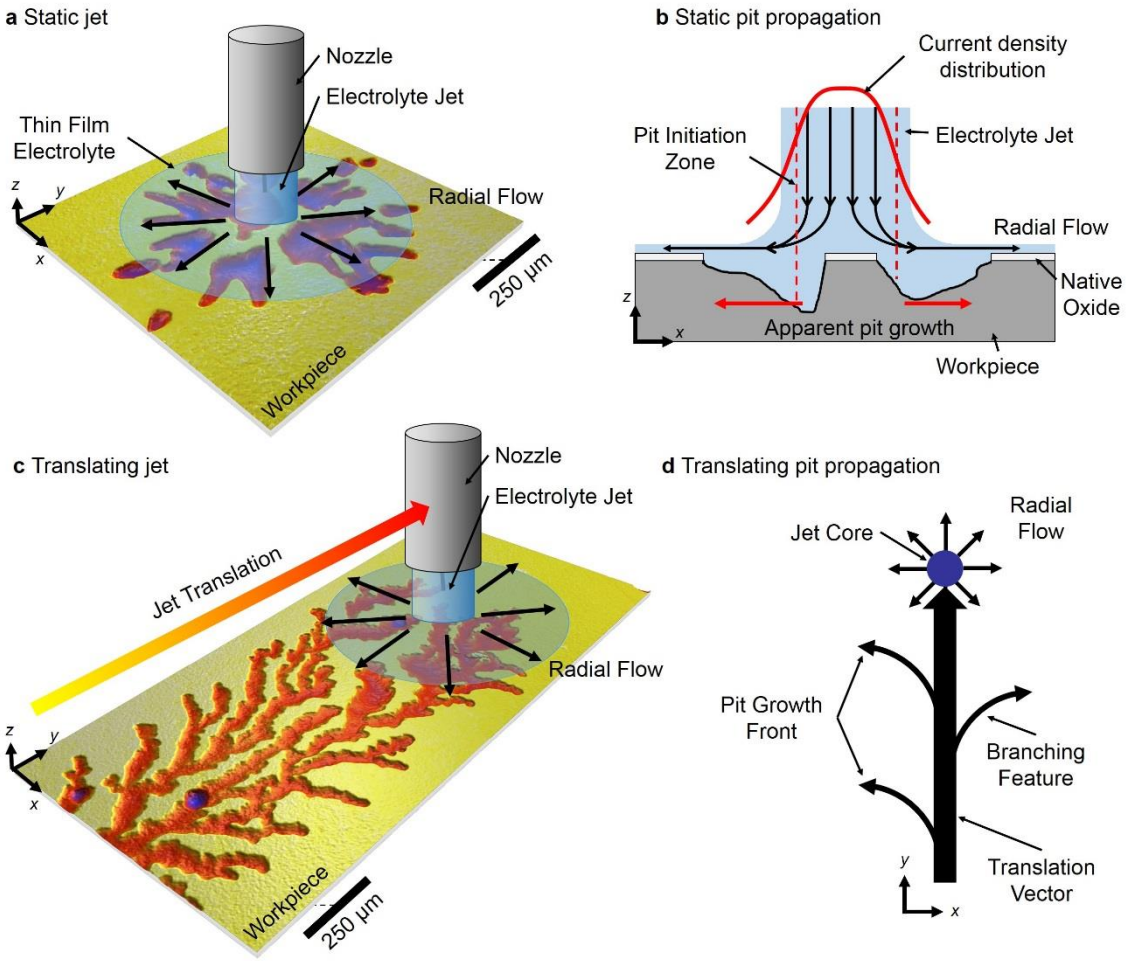


Figure 6.31: The mechanism of controlling pit propagation. a) Outwardly radiating pits from the central impingement point in static processing. b) Pits are initiated in the central region of the electrolyte jet and the growth direction is influenced by the radial flow regime of the electrolyte jet. c) Jet translation contributes a directional bias pit growth, resulting in feathered surfaces with branching features divergent from the translation direction. d) Pit growth is influenced by both translation and flow velocity.

Considering the radial pitting field visible in Figure 6.31a, it is likely that electrolyte impingement velocity will influence the morphology of the fractal structures. However, prior investigations detailed in section 6.2.2 demonstrated that increasing jet velocity decreases MRR when using iodide-doped electrolytes in EJP, due to the sacrificial anodic reaction converting iodide into molecular iodine. This obfuscates the characterisation of this process parameter on the morphology, as material removal is not only influenced by the

linear charge density, but IDC. Therefore, it is necessary to appraise charge specific removal with this electrolyte (NaI100%) in titanium across a range of jet velocities (2.9-23.6 m/s) at 100 A/cm^2, where a more complex relationship is observed in Figure 6.32.

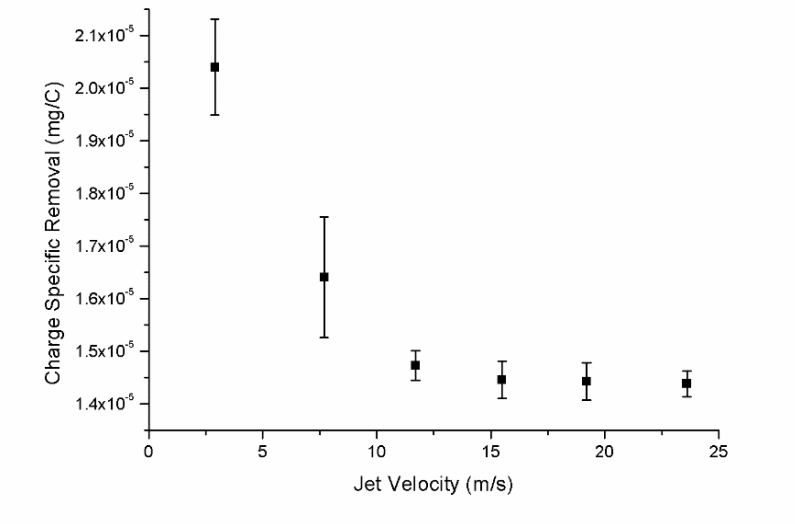


Figure 6.32: Charge specific removal of Ti-6Al-4V in NaI100% considering the jet velocity. The relationship is discrete from that observed in the doped electrolyte case.

Section 6.2.2 studied a hybrid electrolyte system of two discrete anions, (base NO_3^-, dopant I^-), whereby the graph in Figure 6.9 indicates common intercepts for the un-doped $NaNO_3$ and NaI 40% electrolytes when processing Inconel 718. Common intercepts indicate that in the doped case, the nitrate anion is responsible for the majority of the material removal, where MRR reduces linearly with jet velocity. In the case of NaI 100% applied in this section, there is no competing anion in the bulk electrolyte, therefore the MRR is largely dependent on the availability of iodide or other anodically generated anions to effect material liberation. Figure 6.32 shows a region where the MRR is dependent on the electrolyte flow velocity (<10 m/s), beyond which material removal demonstrates negligible dependence on v_j; appearing to be limited.

This relationship can be understood considering the limited solubility of molecular iodine in aqueous solutions (0.0133 M in deionised water at 25 °C) [227]. Increasing electrolyte flow velocity (incident concentration of iodide), will increase the rate of the primary filtering reaction: $2I^- \rightleftharpoons I_2 + 2e^-$, however as the low solubility limit of iodine is approached, this rate will fall. This reaction is associated with the inverse relationship between MRR and v_j, observed <10 m/s in Figure 6.32. Beyond the solubility limit, further increases in iodide supply do not increase the concentration of iodine, further current filtering is inhibited and therefore the MRR stabilises.

Sole dependence on this solubility-limited mechanism is challenged by the chemistry of the electrolyte, where the presence of iodide will spontaneously generate triiodide upon reaction with iodine: $I^- + I_2 \rightleftharpoons I_3^-$. Triiodide generation occurs with a 99% conversion efficiency (Ramette and Sandford, 1965) [227], and would therefore decrease the effective surface concentration of iodine, driving the primary filtering reaction. The effective masking level in this case would depend on the rate of this secondary reaction within the flow, chemical and energetic conditions of the process. In addition, the anionic nature of triiodide could complicate dissolution phenomena, as such species would be electrostatically drawn to the workpiece anode and could affect material removal under certain conditions. This demonstrates that the opportunity for certain chemistries to occur is driven by the dynamics of the process.

Subsequently, the effect of changing the jet velocity on the morphology of the pitting phenomena was explored in this electrolyte at the same energy level (100 A/cm^2). The surface reconstructions in Figure 6.33a-d show that increasing the jet velocity changes the morphology of the pitted surface; at low flow rate,

the feature appears as a striation, which is indicative of a more continuous removal mechanism. This can be correlated with the greater MRR at this jet velocity. Upon increasing the jet velocity beyond 10 m/s, branching inflections (and a fractal-type machined feature) can be observed, which appear to refine in width with increasing velocity, shown in the graph in Figure 6.33e, where the mean microchannel kerf width at 23.6 m/s is 31% of the nozzle I.D. (159 μm, σ = 17%). The difference in upper and lower widths is however not shown to vary as significantly, although an increase (18%) can be determined in the region where branching inflections are generated between 11.7 m/s (mean = 548 μm, σ = 2.3%) and 23.6 m/s (mean = 649 μm, σ = 4.9%). This is increase is due to the increasing radial bias to the growth direction from the greater jet velocity, which expands the feature.

In light of the independence of MRR on jet velocity ≥11.7 m/s outlined in Figure 6.32, it is notable that the processed area of the features are shown to decrease, approximately linearly in this range (*see* Figure 6.33f). This is indicative of deeper microchannels, which is reflected in the complementary surface reconstructions, considering the colour scale, which could result from enhanced evacuation of machining debris at greater jet velocity. The number of branching inflections in the machined feature is shown to increase significantly between 7.7 and 11.7 m/s, indicating that these inflections are generated mainly in the region where the material removal is independent of jet velocity. This effect is therefore likely to be dependent on the saturation of iodine at the anode surface (*see* Figure 6.32).

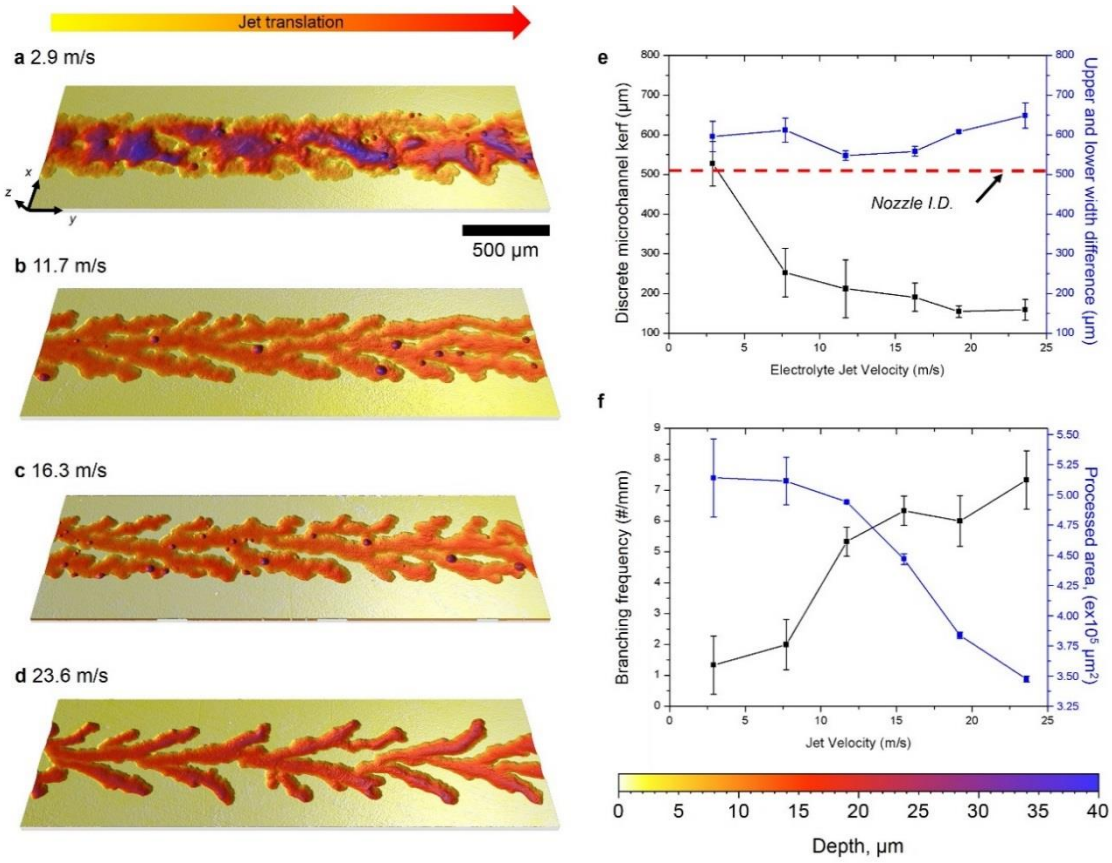


Figure 6.33: Effect of electrolyte jet velocity on the morphology of fractal features. a-d) Surface reconstructions showing a refinement of the microchannel kerf (100 A/cm^2, 0.15 mm/s), reflected in the graph in e). f) The processed area decreases across the jet velocity range, where the branching frequency increases beyond 10 m/s.

Considering the presence of a stable operating region of the jet velocity >10 m/s, identified as a region where the surface concentration of iodine is saturated, further experimentation was undertaken within this range, unless otherwise stated, where all studies used a 510 µm diameter nozzle.

The effect of applied current density on the morphology of the propagated pitting phenomena in NaI 100% under controlled translation (0.15 mm/s) and flow (19.2 m/s) conditions was appraised through observations of features processed 20-400 A/cm^2. Figure 6.34a-d show reconstructed surfaces that clearly demonstrate an increase in the frequency of branching inflections with

current density, as well as an insignificant change in depth of cut (<30 µm) in the presented reconstructions (≤200 A/cm^2). The mean kerf widths shown in Figure 6.34e, of the discrete microchannel structures are shown to be significantly narrower than the nozzle diameter at low current densities (75 A/cm^2 = 26%, 100 A/cm^2 = 24% of nozzle I.D.), effectively demonstrating the principle of propagating single pitting events along a toolpath. The extreme sectional difference (in horizontal *x*) between opposing branch tips should also be considered (*see* blue series), as this more accurately reflects the effective processing width under this parameter set.

No data was returned for the lowest current density tested (20 A/cm^2) as continuous removal of this nature was not observed over the controlled sample length (1 mm). The correlation between applied current density and the frequency of branching inflections can be seen in Figure 6.34f (black series), where an approximately linear correlation is observed ≤200 A/cm^2, beyond which the branching frequency is significantly reduced as the pits coalesce into the track morphology observed in the conventional striation EJP domain. This is supported by data showing an approximately linear increase in processed area <300 A/cm^2, beyond which no further increases are observed. The correlation between branching frequency and applied energy, is likely to result from increasing probability of the initiation of discrete pitting events.

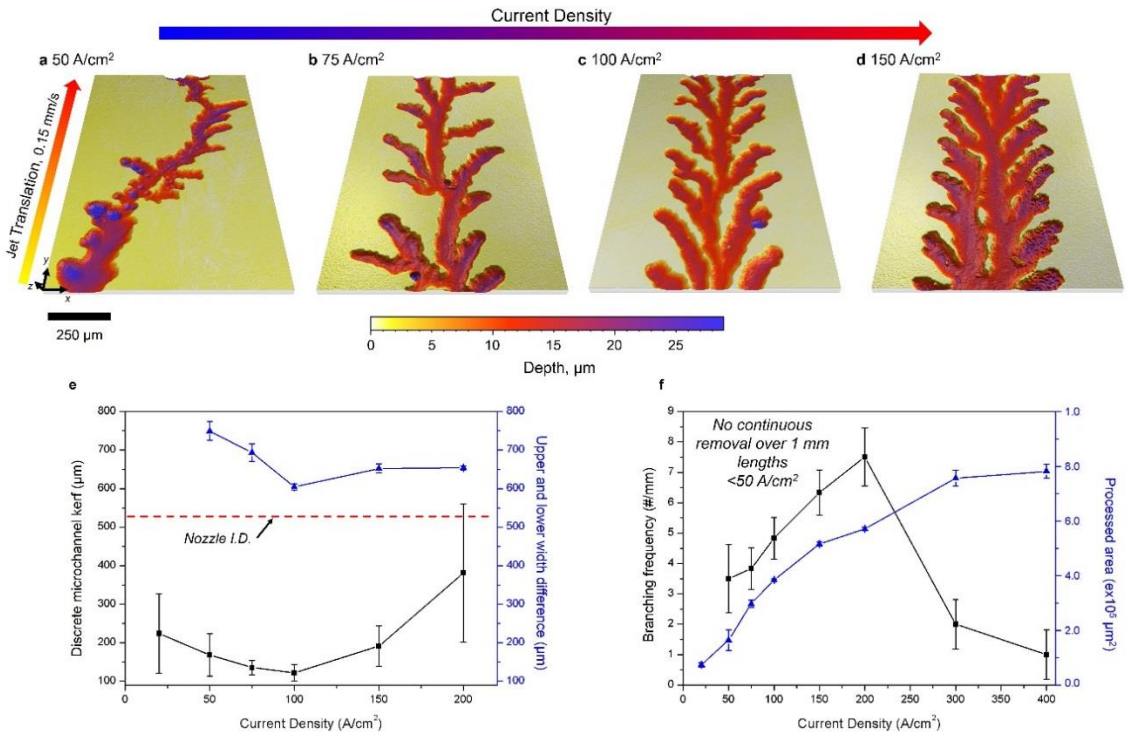


Figure 6.34: Current density and pit propagation. a-d) Reconstructions (0.15 mm/s, 19.2 m/s), demonstrating control over frequency of branching events, where branching probability increases with linear charge density. Cut depth does not appear to significantly change over these parameters, remaining <30 µm in all cases. e) Microchannel kerf widths are <nozzle diameter and increase with current density >100 A/cm^2 as a more stable cutting domain is established. However, it should be noted that the greatest horizontal difference (over 1 mm sampling length) between extreme branches is greater than the nozzle diameter for each current density tested here. Lowest current density tested (20 A/cm^2) did not result in continuous removal over 1 mm sample lengths using the control parameters (v_h, v_j). f) Branching frequency is increases with current density across this range, after which branches coalesce into continuous striation features observed in conventional EJP.

Considering the proposed mechanism of fractal structuring to be caused by the propagation of discrete corrosion pits through translating the electrolyte jet, the translation velocity, v_h, is likely to alter the morphology. To this end, the effect of varying v_h on the morphology was appraised, whereby current density (100 A/cm^2) and flow velocity (19.2 m/s) were controlled and translation velocity was varied from 0.1-0.5 mm/s.

Figure 6.35a-e show sections of processed workpiece (l = 4 mm), whereby branching frequency increases, and microchannel kerf width appears to reduce with increasing translation speed. In addition, reducing $\overline{\lambda_q}$ in this case appears to reduce the depth of each discrete microchannel. Microchannel kerf width is observed to reduce from 190 μm (σ = 12%) at v_h = 0.1 mm/s, to 56 μm (σ = 31%) at v_h = 0.5 mm/s (*see* Figure 6.35f), the latter of which represents a microchannel kerf <11% of the nozzle I.D. The horizontal difference between opposing extreme points appears not to vary significantly within this range of parameters. Branching frequency is shown to increase in a linear manner with increasing translation velocity (*see* Figure 6.35g), although the stability of the propagating pits reduces with this variable, such that when processing at 0.5 mm/s, pit propagation is inhibited over satisfactory sample lengths (*see* Figure 6.35e). In this case, increasing the translation velocity clearly increases the branching frequency. This effect is likely to be caused by the destabilisation of discrete pitting events as the jet is translated away at higher velocities, which is likely to increase the pitting probability in order to satisfy material removal. A greater pitting frequency will increase the probability of discrete branch inflections. At low translation velocity, pits are able to propagate more readily with the jet translation and remain stable for longer time periods.

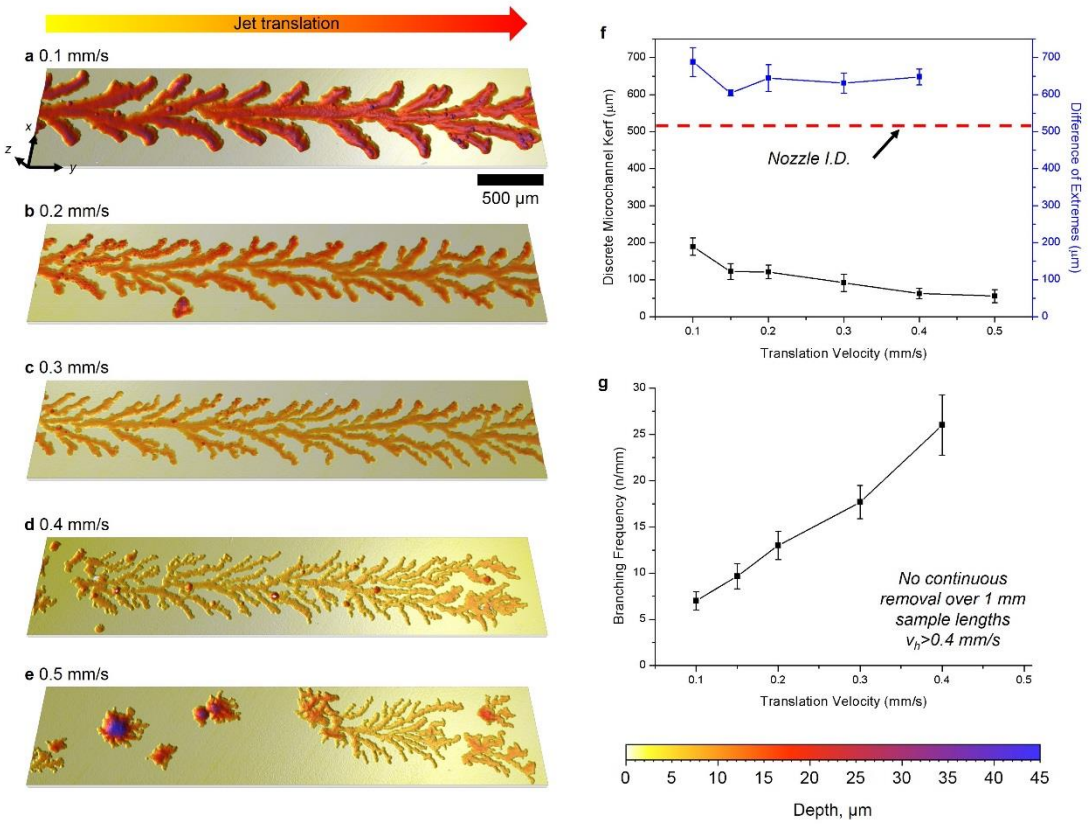


Figure 6.35: Influence of jet translation speed on pitting morphologies, at controlled current density (100 A/cm^2) and flow velocity (19.2 m/s). a-e) Increasing translation velocity from 0.1-0.5 mm/s increases branching frequency and reduces discrete microchannel kerf width. f) Although kerf width is reduced with increasing translation velocity, the difference between obverse branches is approximately static within this parameter set. f) Branching frequency increases linearly with translation speed, although instability of propagation over measurement length (1 mm) results from processing v_h>0.4 mm/s.

From these sets of experiments, branching frequency appears to have a complex dependence on multiple factors. Branches are predominantly generated where the surface concentration of iodine is saturated. Branching frequency appears to have little direct dependence on linear charge density, $\overline{\lambda_q}$. Increasing current density (and therefore $\overline{\lambda_q}$), increases branching frequency <200 A/cm^2 at constant v_h. However, increasing jet translation velocity at constant current density (therefore reducing $\overline{\lambda_q}$), branching frequency

is also increased. Instead, the probability of branching can be increased by either destabilising the propagation of existing pitting events (through increasing translation velocity), or by increasing the probability of new pit initiation (through increasing the process energy – current density) and *vice versa*.

6.5. Summary

This chapter demonstrated how consideration of the electrolyte-material interactions in EJP can be controlled to reduce the scale of the processed feature towards those achievable using other, significantly more expensive methods, such as laser beam micromachining. In this regard, the scale of the EJP feature has been reduced below that previously reported in the literature (<1.5-2.5 d_N) and thus the capability of the technique as an appropriate micromachining strategy has been further established.

Firstly, a transient current threshold, achieved through doping conventional electrolyte solutions with reducing agents such as iodide, has been reported and mechanistically interrogated in terms of both anode surface concentration and applied energy. The mechanism has been shown to allow feature processing to approach the nozzle diameter at high current density and dopant concentrations. The current threshold has been developed for EJP, however the mechanism could potentially be applied to other electrochemical processing strategies whereby a localised energy density distribution is exploited. One such example is electrochemical micromachining (EMM), however the response of the transient current filter to the ms and ns-order pulse times needs to be established to determine the viability of successful mechanism translation.

Secondly, it has been shown that processing of titanium with EJP is significantly more repeatable in high current density regimes (>300 A/cm^2), beyond which has been conventionally applied in EJP. In addition, it has been demonstrated that doped electrolyte mixtures of different halide containing electrolytes can improve the micromachining characteristics of titanium alloys beyond that achievable using conventional EJP electrolytes ($NaNO_3$ and NaCl), and beyond that achieved when employing pure solutions of the same dopant chemistries. The latter point indicates a synergistic response, whereby both dopant and base anions contribute towards key performance indicators, such as dimensional accuracy and material removal. This has been explored for both iodide and bromide dopants, which lower the breakdown potential of the passivating oxide films. The enhanced de-passivation characteristics allow for significantly improved edge definition and profile deviation.

Thirdly, two novel jet-specific material removal phenomena are reported, and discrete mechanisms have been identified, which have been shown to reliably generate discrete microchannel features at a small percentage (<30%) of the nozzle diameter, hitherto unreported in EJP. Both phenomena exploit low current density regimes, whereby material removal response becomes significantly more stochastic. The first mechanism involves ‘staccato’-type cyclical removal and accompanying electrical response, which appear to be quasi-periodic in nature. This is largely a result of the interaction between highly passivating materials and aggressive electrolytes at low current densities. At the very least, exploration of this phenomenon is valuable to the wider community as it indicates the existence of an operating domain outside of which the EJP practitioner would wish to process, where reliable deterministic

featuring is desired. However, the application of quasi-periodic pitting phenomena is suggested as route through which large surface areas can be rapidly processed. The second mechanism involves the propagation of discrete corrosion pits to generate fractal surface textures along the length of the toolpath. A high degree of control over the morphologies of these features are shown through considering the applied energy, flow regime and the translation velocity. Such surface processing is suggested as a route through which high surface area microchannel arrays could be applied to materials to enhance fluid-transport characteristics.

7. EJP coating and surface modification

7.1. Introduction

Plating processes are commonly used for the deposition of metallic coatings to modify the surface properties from those of the bulk. Increasingly, surface engineers seek manufacturing technologies which can selectively produce complex surfaces, for example through nanoparticle incorporation. Considering the selective, automatable and low cost nature of the technique, EJP coating has the potential to rapidly execute processing strategies consistent with contemporary and future surface requirements. The literature review (*see* section 2.4) indicated several notable studies on the subject of EJP coating; these have demonstrated the capability of the technique as a route through which material can be selectively deposited. Such investigations have begun to establish the technique as a viable method of maskless plating, co-deposition and anodization.

However, these studies demonstrated that optimum plating conditions, in terms of final roughness and deposit integrity, are largely incompatible with high-throughput processing strategies required by industry. Currently, satisfactory EJP coatings are only achievable when processing within low energy regimes (<10 A/cm^2), where the local deposition rate is low. In addition, the integrity of a given deposit is strongly dependent on the homogeneity of the total deposition process, such that small perturbations in a preceding layer will significantly affect the topography of all succeeding depositions [228]. Adaptations to the technique, such as lapping, have been presented as methods successful in overcoming this deleterious effect, however they represent additional

processing steps. This is a concern considering the already significant processing times in comparison to other selective manufacturing techniques. Therefore, for EJP coating to be applied as a viable technique beyond that of a purely academic nature, challenges to process efficiency must be overcome, and investigations to this effect represent valuable research contributions. One such method is the use of chemical additives to the electrolyte. Such chemistries are commonly applied in conventional electroplating baths, however their application towards EJP has not been appraised.

In addition, the literature review indicated that EJP has been adapted to execute selective anodic oxidation aluminium. Plasma electrolytic oxidation (PEO) has been shown to be suitable for the creation of mechanically robust hard-facing surfaces of high corrosion resistance, however this has not been reported in EJP. To this end, this chapter will investigate the application of chemical additives to enhance the efficiency of jet electrodeposition, and to appraise the application of EJP towards the generation of PEO-type coatings.

7.2. Jet electrodeposition

7.2.1. Considerations for jet electrodeposition

Prior investigations have shown that deposit integrity has strong dependence on the input current density in electrodeposition (*see* section 2.4.2) [9, 228]. The Gaussian nature of this distribution in the standard operating condition of EJP therefore challenges efficient homogenous deposition. The effect of current density distribution on the morphology of the deposit can be observed in the stitched SE micrographs in Figure 7.1, deposited with a $CuSO_4$ (1 M) electrolyte

at relatively high current density (50 A/cm^2). In this case, both the size and the frequency of nodule formation reduces radially away from the jet core as the current density and the effective Cu^{2+} concentration decreases.

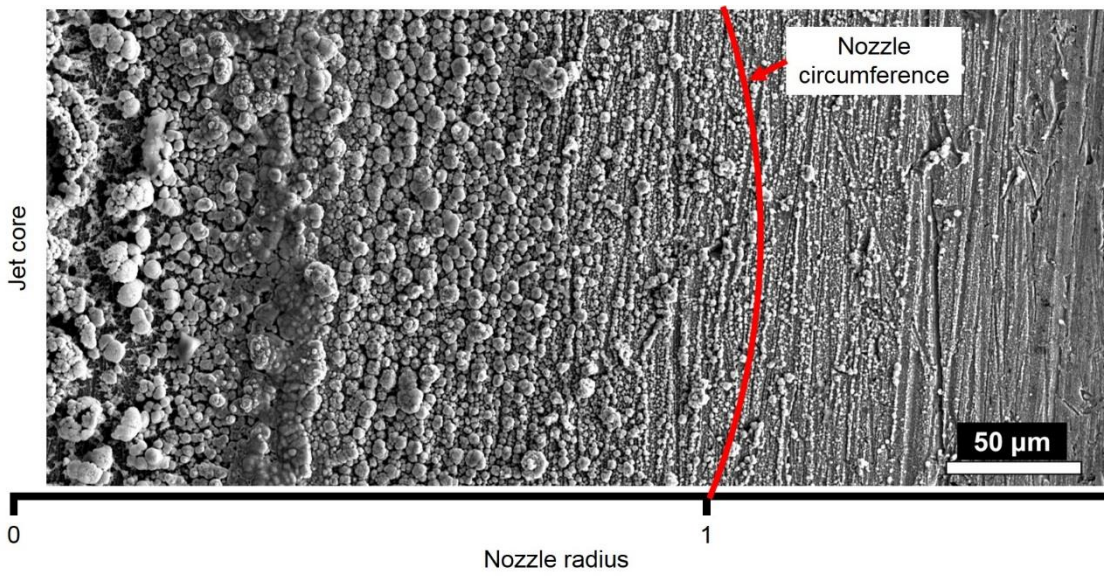


Figure 7.1: Stitched SE micrographs showing a decrease in nodule size radially away from the jet core. This is related to the current density distribution (50 A/cm^2).

The frequency of nodular deposition is related to the local current density, which dictates the speed of deposition. Generally, continuous surfaces are sought by engineers for most applications, however nodular surfaces such as those readily achievable through EJP, demonstrate high surface areas. Conventionally electrodeposited surfaces with morphologies at similar length scales have been shown to be applicable towards modulating wettability [229]. The adhesion of the deposited copper is also demonstrated to be strongly dependent on the cleanliness of the substrate surface. In some cases, deposition on a poorly prepared substrate can lead to coating delamination, revealing the underlying workpiece, indicative of weak bonding. This highlights the necessity of clean substrates and removal of surface contamination.

The effect of bulk copper concentration on the nodule size at the central area (0.25 nozzle radii from centre point) of depositions generated at high current density (50 A/cm^2) was determined using particle size analysis tool in ImageJ software (*see* section 3.6.2). In the range tested (0.15-1 M) at this current density, the concentration of copper (and therefore electrolyte conductivity) appears to make little difference to the size distributions of the nodules and all distributions appear broad (*see* Figure 7.2). At all tested concentrations, 96-98% of the nodules were sized between 0.8-6 µm. The mean nodule size across all concentrations was 2.68 µm with a large deviation (σ = 50%), resulting from the broad size distribution.

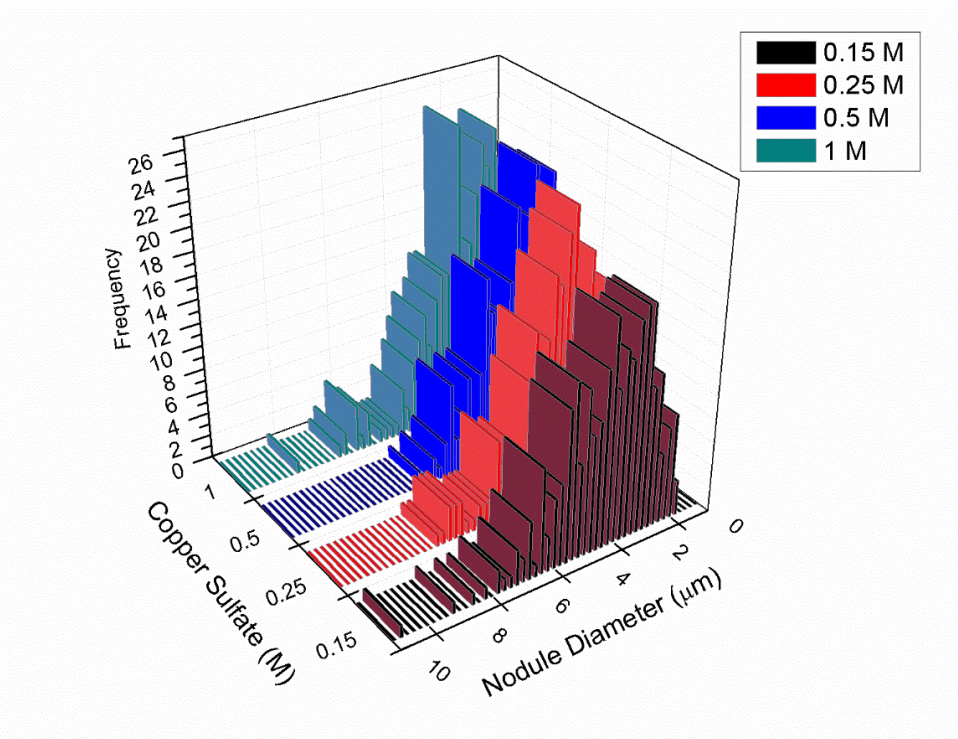


Figure 7.2: Nodule size histogram of the deposit jet core, electrodeposited at high current density (50 A/cm^2) above the limiting current density. Nodule size is largely independent of copper sulfate concentration for the range tested (0.15-1 M).

In this case, the rate of deposition is great at high current density, which rapidly depletes the concentration of Cu^{2+} at the cathode faster than the rate of

diffusion, governing cation migration towards the cathode within the diffusion layer. The inverse relationship between diffusion rate and diffusion layer thickness, δ_N, leads to the observed nodule formation as small asperities reduce local δ_N and thus, positive feedback is established whereby material is deposited on pre-existing protrusions. Within this region, the localisation of deposition is independent of the cation concentration in the bulk electrolyte.

The effect of lowering input current density on the nodule size was investigated for two of the tested electrolytes (0.5 and 1 M) and is shown in the SE micrographs in Figure 7.3. Considering deposition at 5 A/cm^2 (<10 V), processing with 1 M solution (*see* Figure 7.3b) leads to more continuous deposition. In addition, nodule size at this current density is shown to be significantly larger using the higher concentration electrolyte, which is indicative of increasing growth stability (0.5 M: 5.63 μm, σ = 66%; 1 M: 15.68 μm, σ = 48%). This is caused by a greater proportion of mass transfer occurring through reduction of Cu^{2+} rather than water and is in agreement with electroplating theory considering the $\frac{J}{C_B}$ relationship (*see* section 2.4.2). When observing the surfaces coated using 0.5 M electrolyte, no difference can be determined in the nodule size between the two current densities and the mean nodule size is shown to be similar to the overall mean acquired over multiple solution concentrations at 50 A/cm^2 (30 A/cm^2, 0.5 M: 5.40 μm, σ = 51%). In addition, alignment of nodular growths in Figure 7.3 is consistent with the underlying surface texture of the substrate. This also demonstrates the capability EJP to generate structured surfaces upon a template or seeding surface.

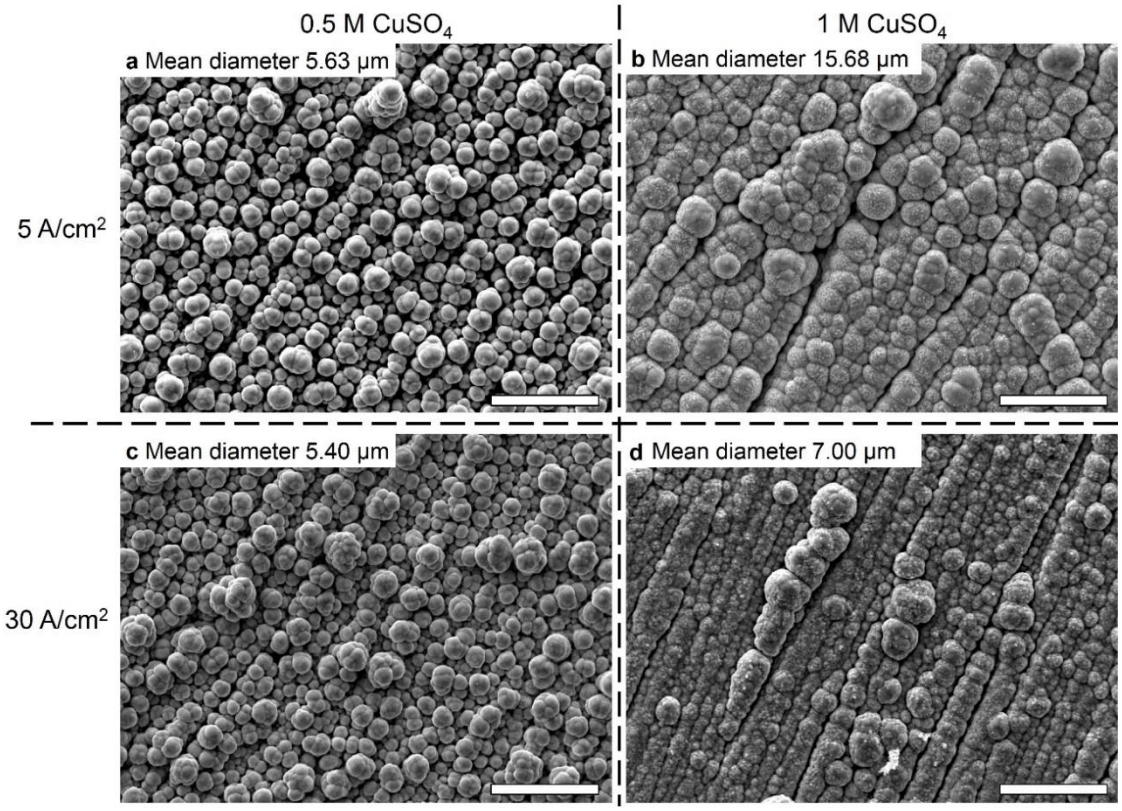


Figure 7.3: SE micrographs of the surface of deposits processed at 5 A/cm^2 in: a) 0.5 M $CuSO_4$ and b) 1 M $CuSO_4$, and at 30 A/cm^2 in: c) 0.5 M $CuSO_4$ and d) 1 M $CuSO_4$. Scale bars are 20 µm.

At lower current density, the surface concentration of Cu^{2+} at the cathode is depleted at a slower rate, thus the diffusion layer is thinner. The relationship between current density and nodulation is schematised in Figure 7.4. At high current density, where the diffusion layer is greater than the scale of the surface asperities, there is a difference in local thickness over the asperity (δ_N1) and over valley areas (δ_N2), where $\delta_N1 < \delta_N2$. The diffusion rate is significantly faster over the asperity and the nodule propagates. In electrodeposition, this effect is termed *negative micro-throw* [164]. Where the diffusion layer is smaller than the asperity, such as at low current density (*see* Figure 7.4b), the difference between δ_N1 and δ_N2 becomes negligible such that the asperity propagation does not accelerate, called *neutral micro-throw*.

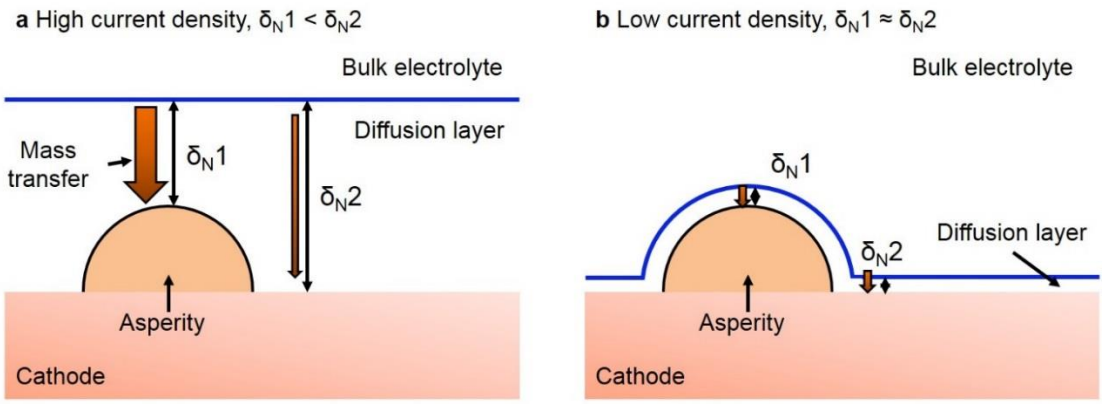


Figure 7.4: Schema: a) processing above limiting current density leads to propagation of pre-existing defects and results in nodulation, b) processing below limiting current density does not lead to nodule growth.

For processing below the limiting current density, bulk electrolyte concentration will have greater effect on the stability of nodular features, thus nodule size and continuity increases with concentration at low current density. These effects are responsible for the apparent alignment of nodular features parallel to the pre-existing grind marks as shown in Figure 7.3d. In addition, alternate reactions such as cathodic proton and water reduction (depending on pH level) are likely to occur at the higher potentials required to generate large current densities, which could disrupt nodule growth stability. Cross sections of spot depositions carried out at relatively high (20 A/cm^2) and low (5 A/cm^2) current densities are shown in Figure 7.5, where the samples were mounted in resin prior to characterisation. At high current density, nodular growths are observed, where the size of the nodule appears to increase away from the workpiece. This results from the negative micro-throw at these processing conditions. Upon processing at lower current density, this effect is still observed (comparing the profile of the substrate and the top surface of the coating), although the effect is markedly reduced.

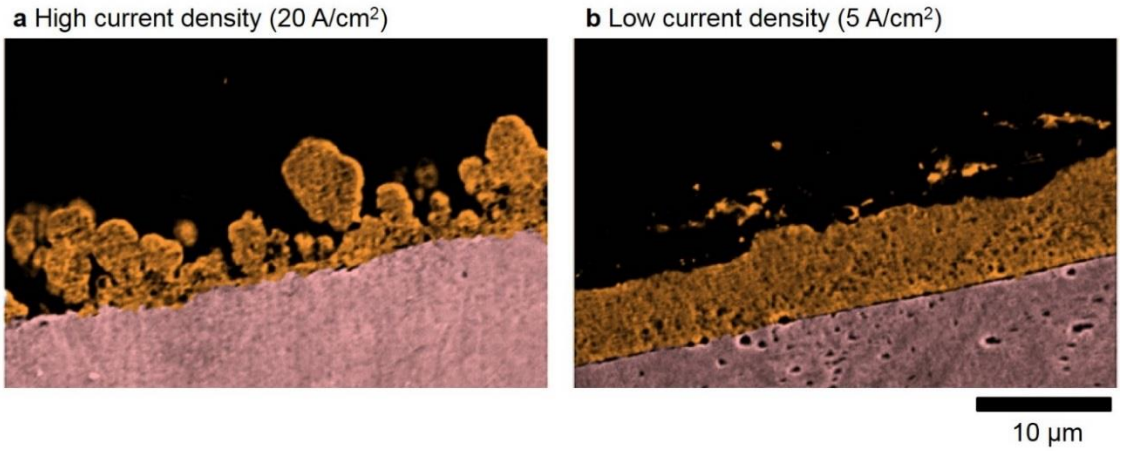


Figure 7.5: Tinted cross-section SE micrographs of EJP-coatings (orange) on substrates (red) mounted in resin and viewed in cross section. a) High current density, showing nodules, and b) low current density, showing more continuous deposition.

When processing at lower supplied current densities (<20 A/cm^2) using pure solutions of $CuSO_4$, deposited material is generally embedded with crystals of high symmetry (*see* Figure 7.6). EDS point analysis (red dot denoting spectral acquisition point) indicates that these are an oxide species of copper, compared with the matrix (green dot). For the embedded crystal, the stoichiometry (≈2:1) is highly suggestive of the cuprous form (Cu_2O) rather than CuO. This is also evidenced by the apparent cubic morphology of the crystals (where Cu_2O is cubic and CuO monoclinic), and the apparent readiness of co-nucleation between the cubic copper matrix and the oxide crystal. Electrodeposition of Cu_2O has previously been demonstrated through the reduction of Cu^{2+} [230], albeit at greater pH (13), which is indicative of a localised chemical environment close to the cathode (diffusion layer) in comparison to the bulk electrolyte.

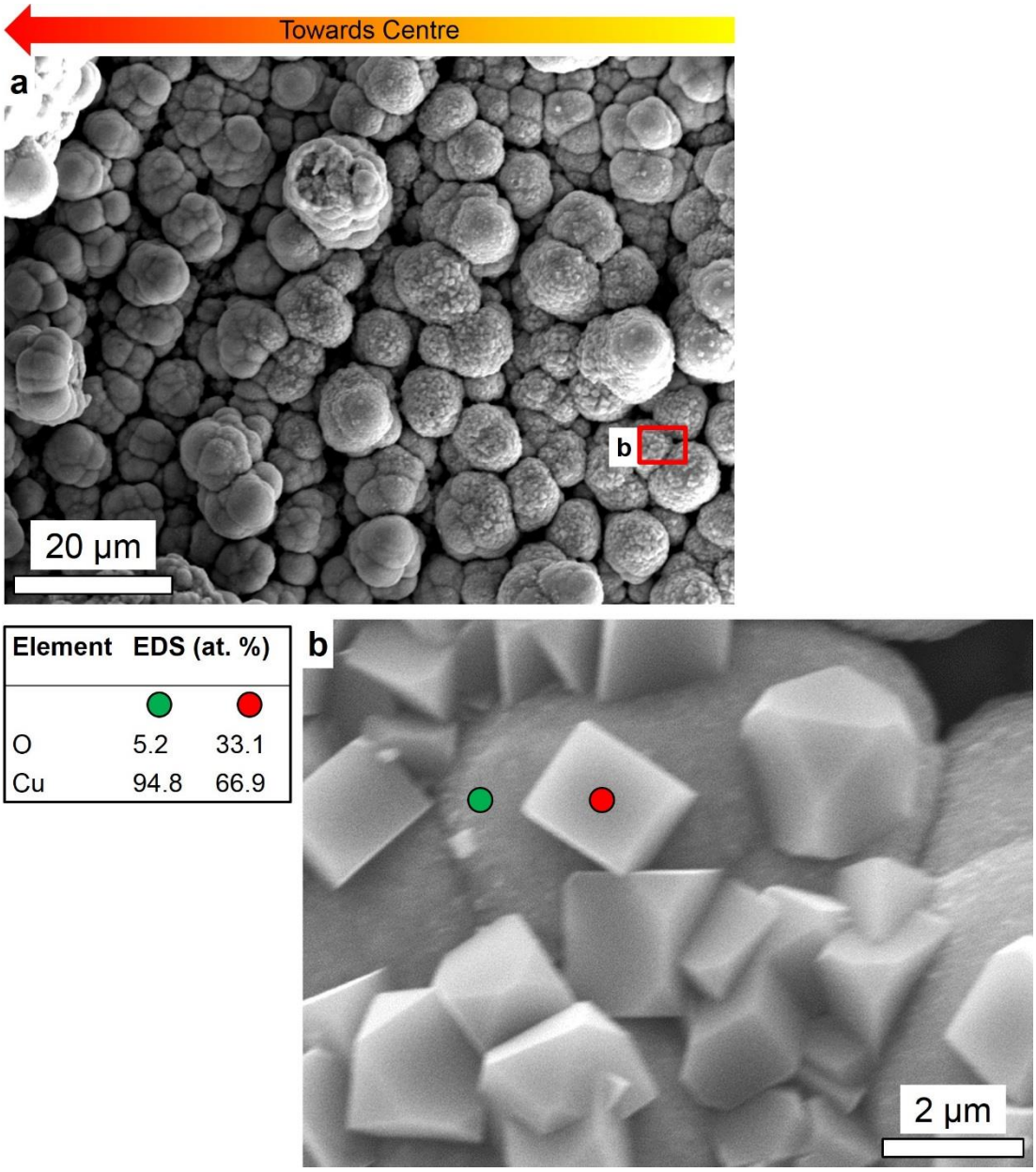


Figure 7.6: a) When the current density supplied at the nozzle is low (20 A/cm^2), deposits away from the jet core are embedded with cubic crystals (b), likely to be Cu_2O.

7.2.2. Nodule size modulation

EJP coating copper at high current density can generate dendritic-type features, where the dendritic length scales are consistent with those shown to impact functional properties such as wettability [229]. Although a small degree of control over nodule size has been demonstrated through reductions in current density and increasing copper concentration (*see* Figure 7.3), such adaptions

serve to increase processing time and cost. This would largely inhibit any application of EJP coating in industrial usage. Therefore a method of attenuating nodule growth and demonstrable control over nodule size at greater current densities using reduced concentrations of expensive copper salts, could prove valuable. While the nodule size deposited was shown to be largely independent of copper concentration (*see* Figure 7.2) in pure $CuSO_4$ electrolytes at high current density, the addition of other chemistries to the electrolyte is presented as a route through which nodule size can be modulated. In this investigation, Na_2SO_4 was selected due to both the common sulfate anion to the base electrolyte ($CuSO_4$), and the inability of metallic sodium to be electrodeposited in aqueous environments. The SE micrographs in Figure 7.7 (deposited at 50 A/cm^2) show a decrease in apparent nodule size in the central area as the sodium sulfate concentration is increased. This is indicative of lower surface purity, likely to be caused by the occurrence of interfering cathodic reactions discrete from the electro-reduction of copper.

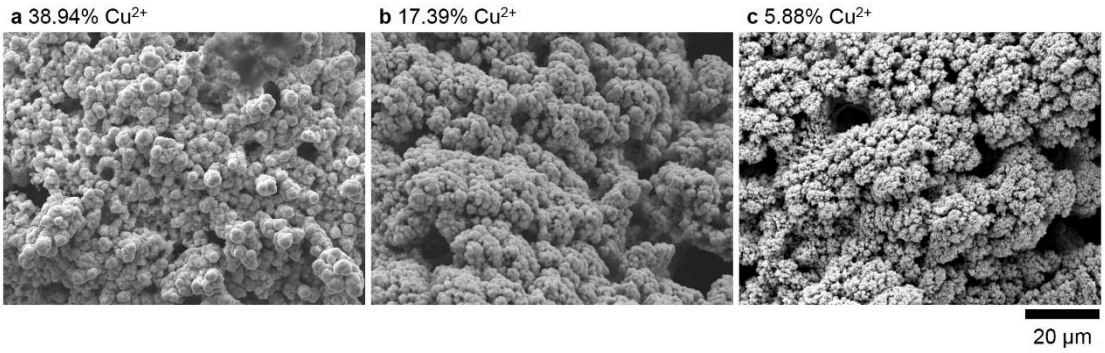


Figure 7.7: SE micrographs acquired whereby the copper concentration contributes a decreasing proportion to the overall ionic strength: a) 38.94%, b) 17.39% and c) 5.88%. Nodule sizes are shown to reduce.

The effect of sodium sulfate addition on nodule size is shown in Figure 7.8, where this factor is shown to be independent of overall solution concentration.

In this set of experiments, the total ionic strength of each solution was changed (1.15-3.4 M), where both $CuSO_4$ (*see* Figure 7.8a) and Na_2SO_4 (*see* Figure 7.8b) were modulated, while the other component was fixed. For a fixed concentration of sodium sulfate (*see* Figure 7.8a), increasing the ionic strength is shown to increase the overall size distribution of nodules. Conversely, for a fixed concentration of $CuSO_4$ (*see* Figure 7.8b), increasing the ionic strength through additions of Na_2SO_4, is shown to reduce and narrow the nodule size distribution.

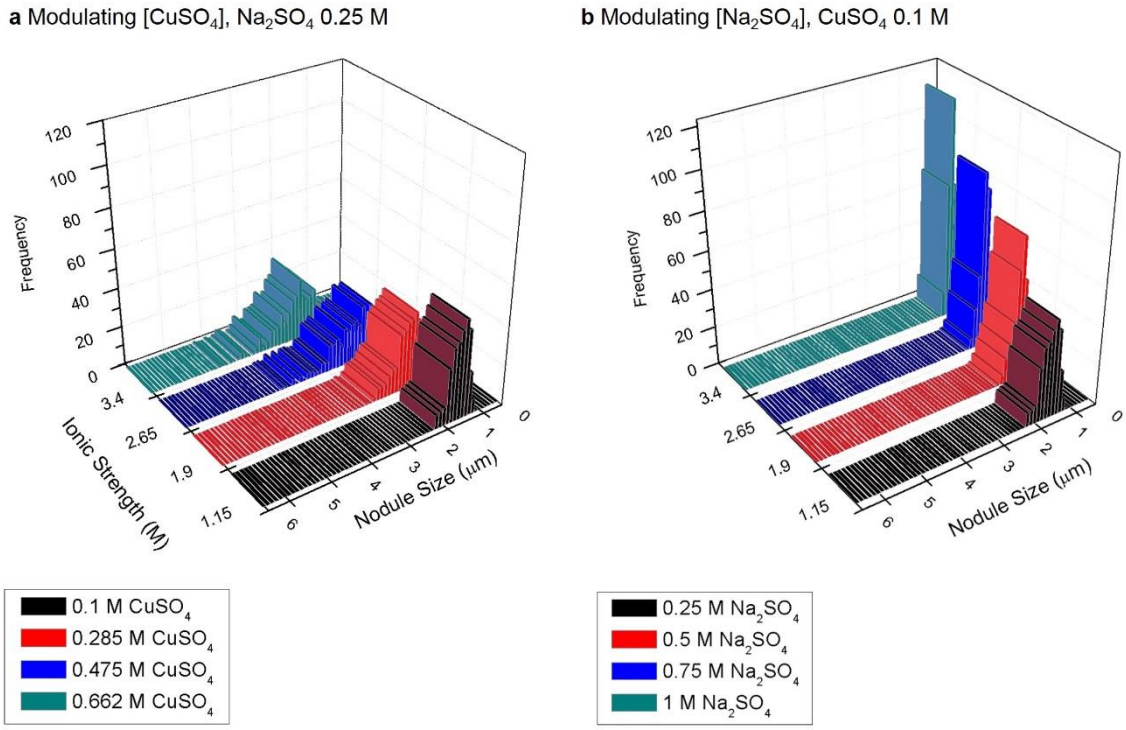


Figure 7.8: For deposits processed at high current density (50 A/cm^2), nodule size is shown to be largely independent of ionic strength, evidenced by fixing the concentration of a) Cu^{2+} and b) Na^+.

It can be determined that the contribution of Cu^{2+} towards the total ionic strength influences the nodule size, with a strong positive correlation (*see* Figure 7.9). As this contribution increases (6-39% for the electrolytes tested here), the size

distribution broadens and average nodule size increases, even though the overall ionic strength appears not to influence the nodule size.

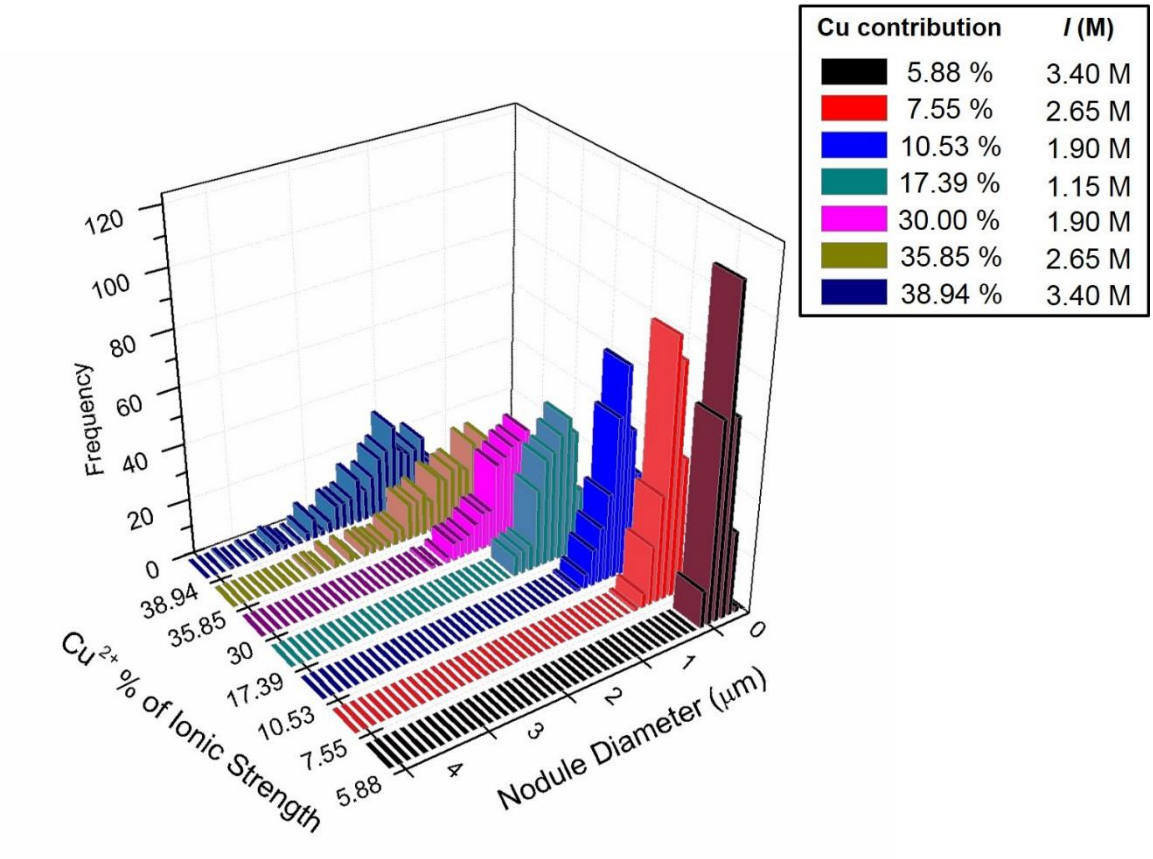


Figure 7.9: Nodule size is shown to be related to the percentage contribution of Cu^{2+} to the ionic strength.

Increasing the contribution to ionic strength from the copper cation increases the mean nodule diameter and also creates a broader distribution. At higher contributions to the ionic strength from copper as opposed to sodium, a greater nodule size is observed due to a higher purity in the deposit, which promotes sustained nodule growth. Greater contributions to the ionic strength from the sodium content in the electrolyte allow some modulation of nodule size by arresting nodule growth, thus smaller nodules are observed. These observations create a means by which the nodule size within a deposit can be modulated. While practitioners may seek to deposit continuous surfaces,

emerging applications may make use of dendritic surface structures. In the set of experiments shown in Figure 7.9, the acidity of the solutions was not regulated. However, there exists an inverse relationship copper sulfate concentration and pH. This is pertinent considering that altering the electrolyte acidity has been shown to affect deposit morphology in prior electrodeposition studies of copper, to the extent that it is generally only recommended to carry out conventional electroplating in acidic baths (*see* section 2.4.2) [164]. This also means that the average nodule size appears to have an inverse correlation with the bulk pH level of each tested electrolyte (*see* Figure 7.10).

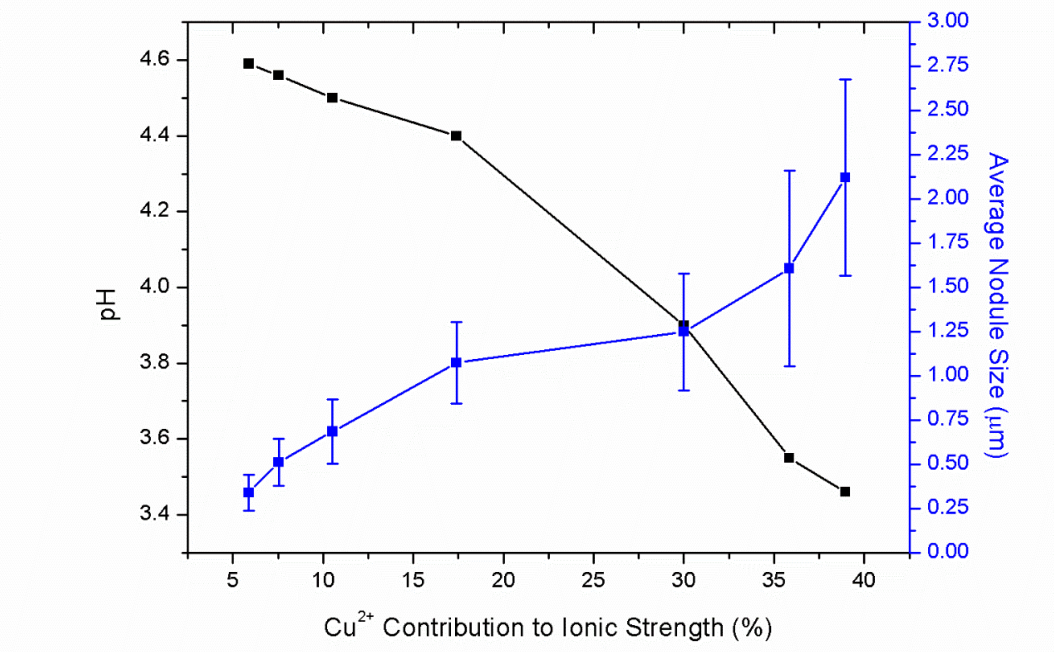


Figure 7.10: Increasing nodule size appears to be inversely related to the acidity of the bulk electrolyte.

Considering the propensity of higher pH to lead to oxide formation in electrodeposition, this effect was tested with equivalent bulk electrolyte acidities (pH 2), more representative of those applied in conventional electrodeposition. Electrolytes were prepared with graduated concentrations of copper sulfate and sodium sulfate, where the ionic strength of the copper sulfate and sodium

sulfate components was fixed at 1.15 M. In Figure 7.11, the effect of increasing the concentration of sodium sulfate has upon the deposit morphology is clearly evident, even at equivalent bulk electrolyte acidity (pH 2). Nodule morphology appears to follow the same trend to that observed in Figure 7.9, where size is reduced with increasing sodium sulfate concentration. This indicates that the mechanism of nodule size suppression is independent of bulk electrolyte acidity at this current density (50 A/cm^2). In addition, it can be observed that bulkier and more porous deposits are generated upon increasing sodium sulfate addition alongside an evolution in nodule morphology, where the high porosity challenges effective comparison of deposition efficiency.

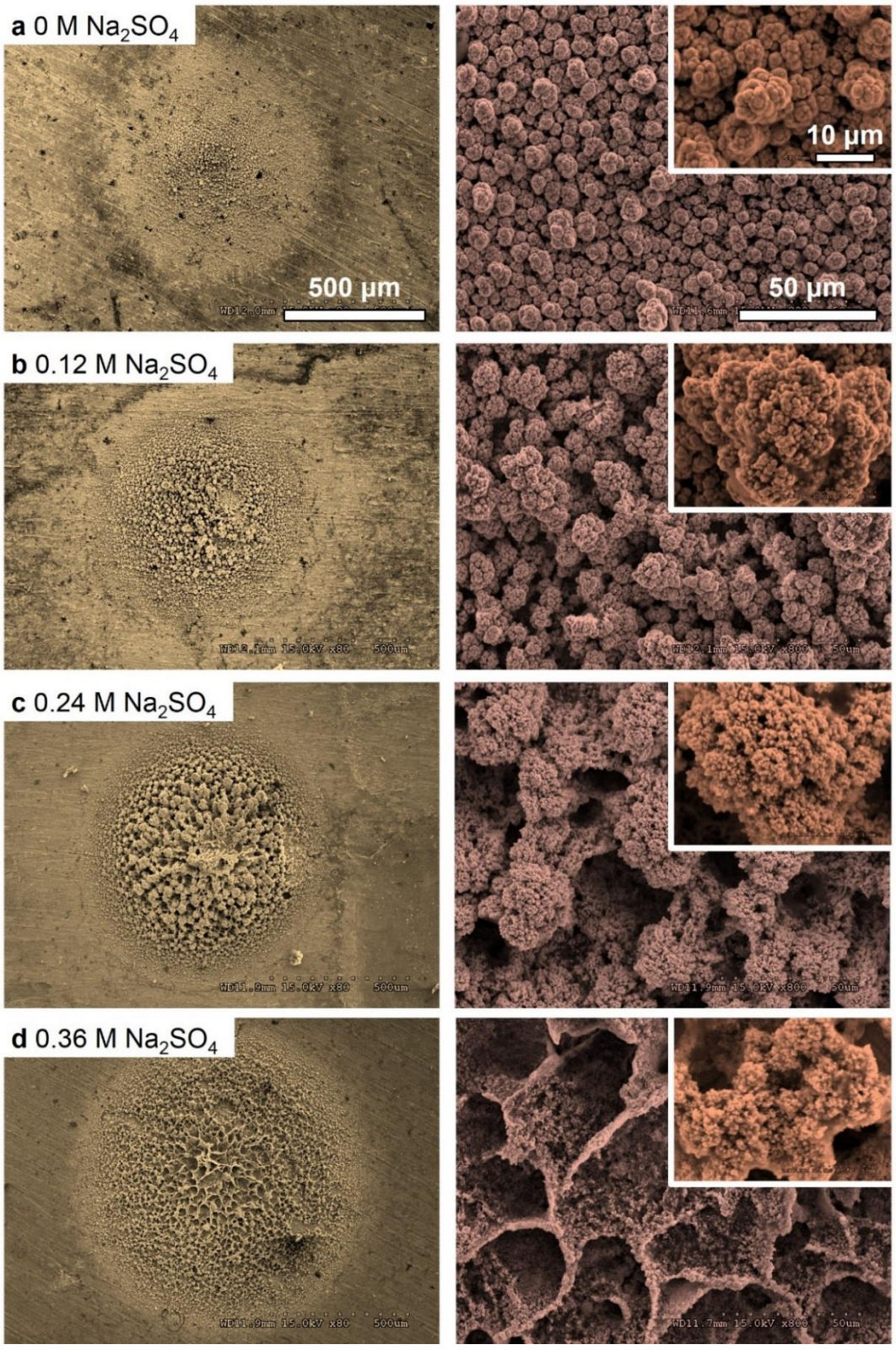


Figure 7.11: Nodule size modulation with sodium sulfate is independent of acidity (50 A/cm^2, 3 s dwell). Electrolytes buffered to pH 2 with H_2SO_4, increasing the concentration of sodium sulfate: a) 0 M, b) 0.12 M, c) 0.24 M and d) 0.36 M, reduces nodule size.

Regarding Figure 7.11, the attenuation of nodule size through sodium sulfate doping appears to have limited dependence on the overall bulk electrolyte pH, however within the diffusion layer at the cathode, which is relatively large at high current density, the chemical environment is discrete from the bulk. As the contribution of copper towards the total ionic strength is reduced, charge transfer at the cathode is likely to shift towards reactions discrete from the electro-reduction of copper (*see* Equation 18). Such reactions will include cathodic proton reduction (*see* Equation 19) and possibly the reduction of water (*see* Equation 20) at the high current densities and electrode potentials applied in this investigation. The latter reactions would serve to increase the pH in the vicinity of the cathode.

$$Cu^{2+}_{(aq)} + 2e^- \rightleftharpoons Cu_{(s)} \qquad \textit{Equation 18}$$

$$H^{+}_{(aq)} + 2e^- \rightarrow H_{2(g)} \qquad \textit{Equation 19}$$

$$2H_2O_{(l)} + 2e^- \rightarrow H_{2(g)} + 2OH^-_{(aq)} \qquad \textit{Equation 20}$$

In the bulk electrolyte, the strong convective mixing of the impinging electrolyte jet of high acidity would serve to rapidly dilute and buffer any hydroxyl anions generated through mechanisms such as Equation 20, however within the diffusion layer in the vicinity of the cathode, the reduction of protons and water is likely to increase the local pH as shown in the schematic in Figure 7.12. The Pourbaix diagram of copper in aqueous solutions indicates that the electrodeposited metal in more basic environments tends towards surface oxidation [231]. This would disrupt crystallisation and lead to a greater nucleation frequency of smaller nodular features. In addition, the proposed reduction of water is further supported by the regular porosity evident in Figure

7.11c and d. The scale of these pores processed at high concentrations of Na_2SO_4 are approximately an order of magnitude greater than the nodule diameter, and are likely to be a result of gas evolution (H_2) at the cathode. Competing cathode reactions are proposed to be the mechanism governing the attenuation of nodule size, considering the effects of bulk ionic strength, overall copper concentration and bulk acidity have been largely disregarded.

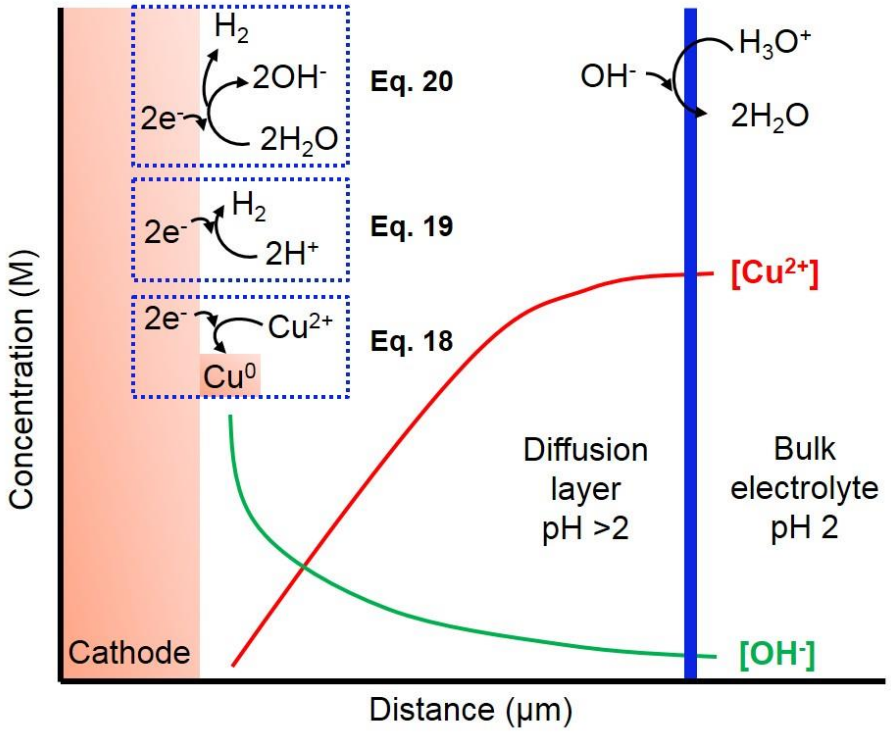


Figure 7.12: Within the diffusion layer, $[Cu^{2+}]$ will decrease towards the cathode (red line). At low $[Cu^{2+}]$, water reduction could occur generating hydrogen gas and possibly hydroxyl species. For acidic bulk concentrations, $[OH^-]$ will be buffered, but within the diffusion layer, the pH will increase, attenuating nodule growth.

7.2.3. Thiourea doping

In order to suppress deposit nodulation in conventional electrodeposition, chemical additives are often employed (*see* section 2.4.2), which affect the micro-throwing power of the electrolyte system. To demonstrate a level of control over nodulation, thiourea was added to a sodium sulfate containing

electrolyte ($CuSO_4$ 0.5 M, Na_2SO_4 0.25 M), expected to generate nodular deposits, even at lower current densities. The suppression of nodulation and the effect on the surface morphology is observed in the concentration range of thiourea tested (0.14-6.57 mM), shown in Figure 7.13. Critically, deposits are observed to go from discontinuous nodule type structures toward a more continuous deposit with increasing concentrations of thiourea, where each nodule is associated with the initiation event and growth of an individual crystal.

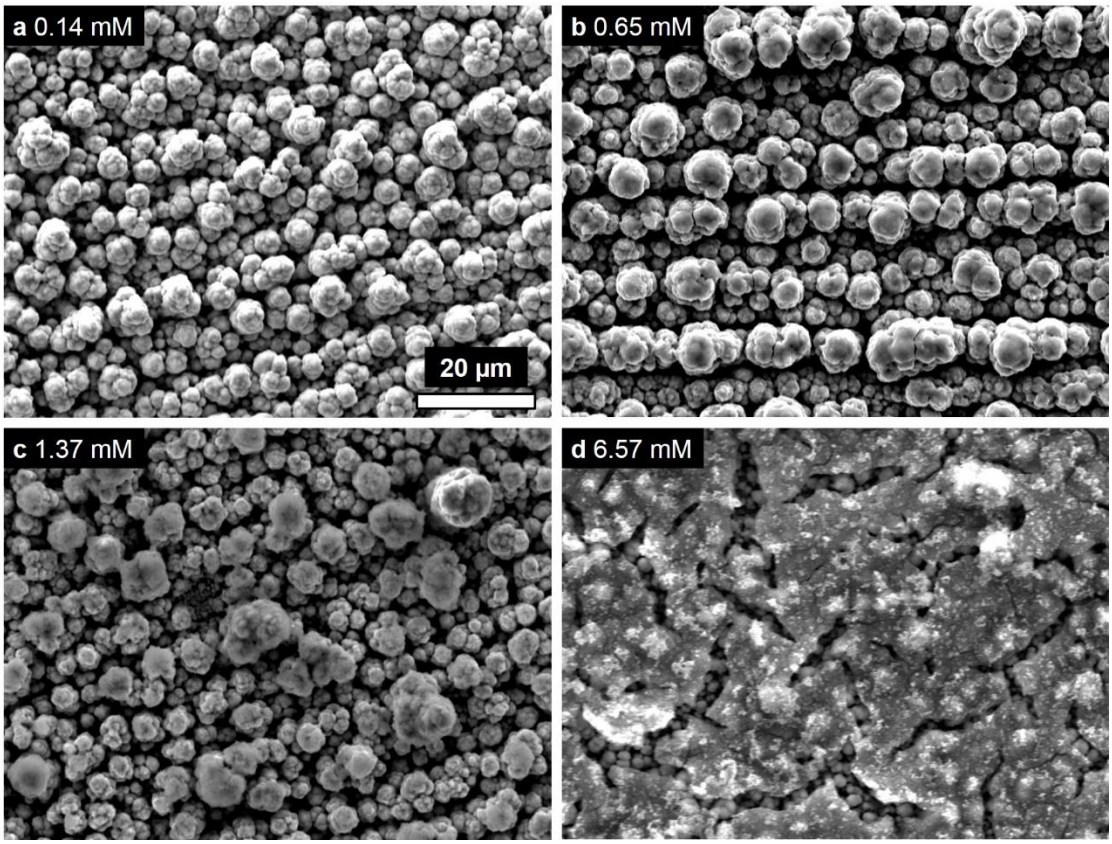


Figure 7.13: The morphology of EJP deposits can be modified with increasing thiourea concentration (5 A/cm^2). a) 0.14 M, b) 0.65 M, c) 1.37 M and d) 6.57 M. Note the transition of discontinuous nodule growth through to a near continuous surface.

This effect is termed *positive micro-throw* and is associated with a levelling of the surface topography. The mechanism by which transition migrates from primarily nodular morphology to a near-continuous surface relates to the adsorption of thiourea at crystallisation sites. This results in higher localised

resistance and preferential crystal growth in other sites, such as valley areas, therefore improving the plating distribution.

Thiourea therefore leads to the densification of electrodeposited Cu in EJP, which enables processing at significantly greater current density. An example of this is shown in Figure 7.14, processed at current densities an order of magnitude greater than those typically employed in conventional electrodeposition (100 A/cm^2 compared with <10 A/cm^2). These spot depositions were generated in relatively short timescales (3 s), where the deposit geometry becomes less stochastic and more consistent with the applied current density distribution as the concentration of thiourea within the electrolyte is increased. The ability to generate stable deposits at greater current density is vital for the proliferation of EJP as a coating technique, as processing in conventional EJP coating regimes is incompatible with high-throughput manufacturing.

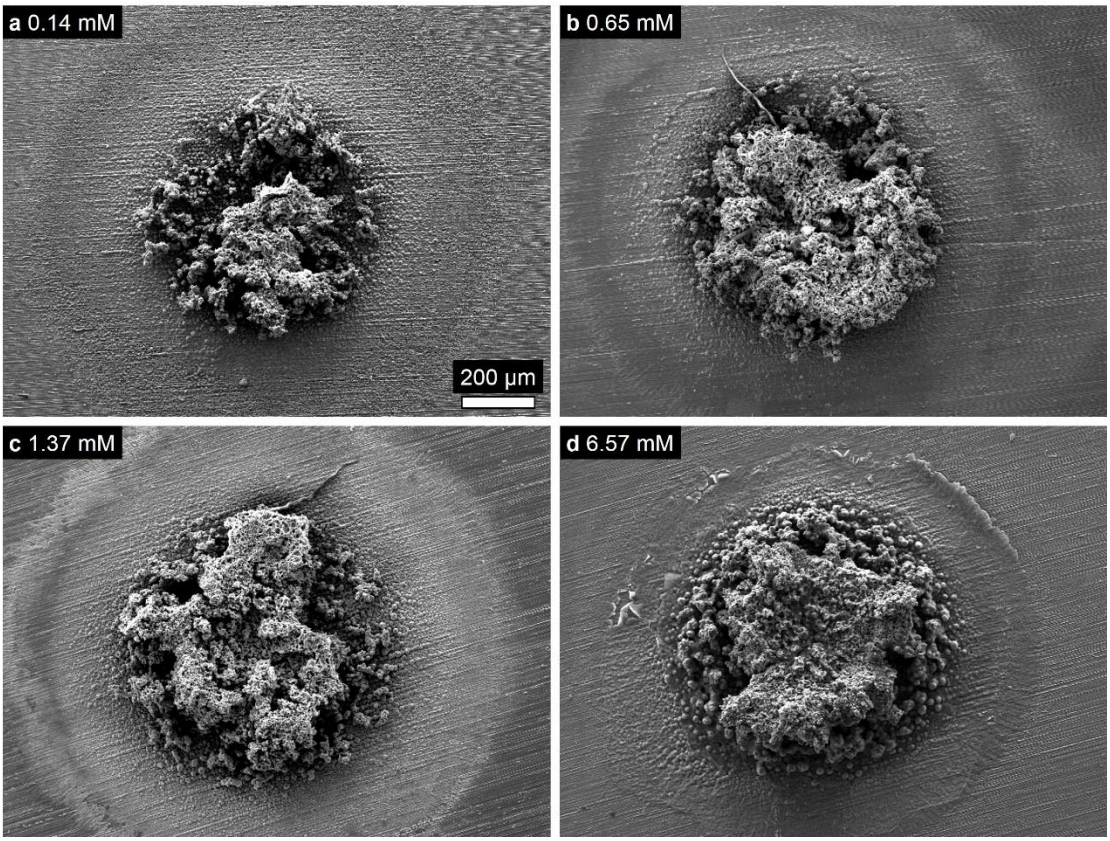


Figure 7.14: Copper densifies with increasing thiourea concentration even at high current density (100 A/cm^2). a) 0.14 M, b) 0.65 M, c) 1.37 M and d) 6.57 M.

Further increases in thiourea concentration (>10 mM) within the electrolyte is limited however, by the formation of crystalline precipitates on and within the deposit, (*see* Figure 7.15). These species will affect the surface chemistry and properties of the deposit, therefore identification and an understanding of their formation is required. Needle-like crystals have been observed in conventional electrodeposition studies in the presence of similar thiourea concentrations (1 mM) by Donepudi et al. (2001) [232], who reported the occurrence of sulfur within the crystalline phase (using EDS). The formation of such phases also resulted in an increase in electrical resistance during deposition. The apparent discrepancy between the concentrations at which these precipitous crystalline phases are observed (1 mM in comparison to >10 mM), is likely to be a result

of the faster electrolyte jet velocities employed in EJP in this investigation (16.3 m/s), in comparison to the agitation of the conventional plating bath employed by Donepudi et al. Such velocities will suppress surface adhesion of non-matrix phases and are therefore likely to inhibit observation until much greater concentrations are employed. EDS performed on the needle-like crystals confirmed the presence of sulfur (12-13 at.%), nitrogen (30-35 at.%), carbon (20-30 at.%) and oxygen (15-20 at.%), with the remainder Cu. Elemental quantification of carbon is challenging in EDS due to the ubiquity of adventitious carbon, however considering the stoichiometry of thiourea, $SC(NH_2)_2$, the ratio of S:N (≈1:2) in the EDS spectra appears to correlate with the dopant. No nitrogen signal was observed in any EDS spectrum acquired on deposits generated without thiourea.

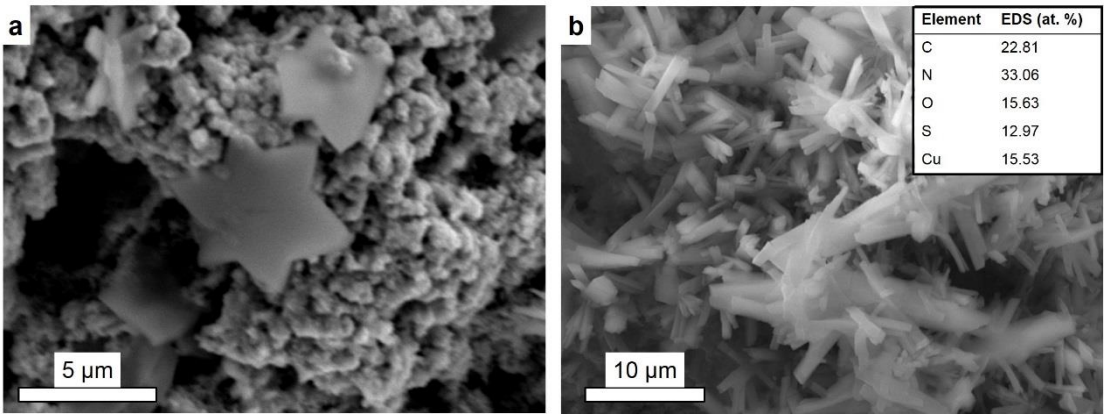


Figure 7.15: EJP with high thiourea concentrations (>10 mM) leads to formation of crystalline phases at the deposit surface. a) Hexagram crystals, and b) needle-like crystals, where the EDS derived S:N ratio correlates with that of thiourea (spectrum acquired over total field of view).

Planar hexagram crystal phases with apparent six-fold rotational symmetry, such as those observed in Figure 7.15a, formed in addition to the needle-like crystals. These display a discrete chemical composition, with no evidence of nitrogen signal in EDS spectra. Hexagrams are shown to be embedded in the

copper matrix during deposition, and also contain sulfur (*see* Figure 7.16), where oxygen is shown to localise with the sulfur at a S:O ratio of ≈1:6-7. This ratio is relatively close to SO_4^-, considering a proportion of the oxygen signal will be associated with the underlying copper deposit in the form of a surface oxide phase, which is confirmed in the EDS map for oxygen in Figure 7.16 (white). Identification of the counter-ion presents a challenge however, as such crystallography is unlikely to be consistent with $CuSO_4$, given that the pentahydrate form, the most likely to crystallise in aqueous conditions, is triclinic in structure. Furthermore, no sodium was detected in EDS, which would appear to eliminate the possibility of Na_2SO_4 crystallisation, although it should be noted that there is spectral overlap between Cu L_α and L_β (0.928 and 0.947 keV) and Na K_α (1.040 keV). In addition, only anhydrous Na_2SO_4 is understood to be hexagonal, the formation of which is considered unlikely in the aqueous environment of EJP. The existence of either of these highly soluble compounds is also challenged by the washing routine in deionised water after processing, prior to characterisation.

These crystalline phases have only been observed at high thiourea concentrations (>10 mM). Should high thiourea concentrations be required, for example as a means of further extending the current density operating range, it is likely that increasing the electrolyte jet velocity will act to reduce the effective surface concentration of crystalline impurity phases. The formation of these crystalline phases appears to be aided by the large surface area deposits, upon which the phases nucleate and the precipitation could be related to a saturation as other species are depleted at the evolving cathode surface.

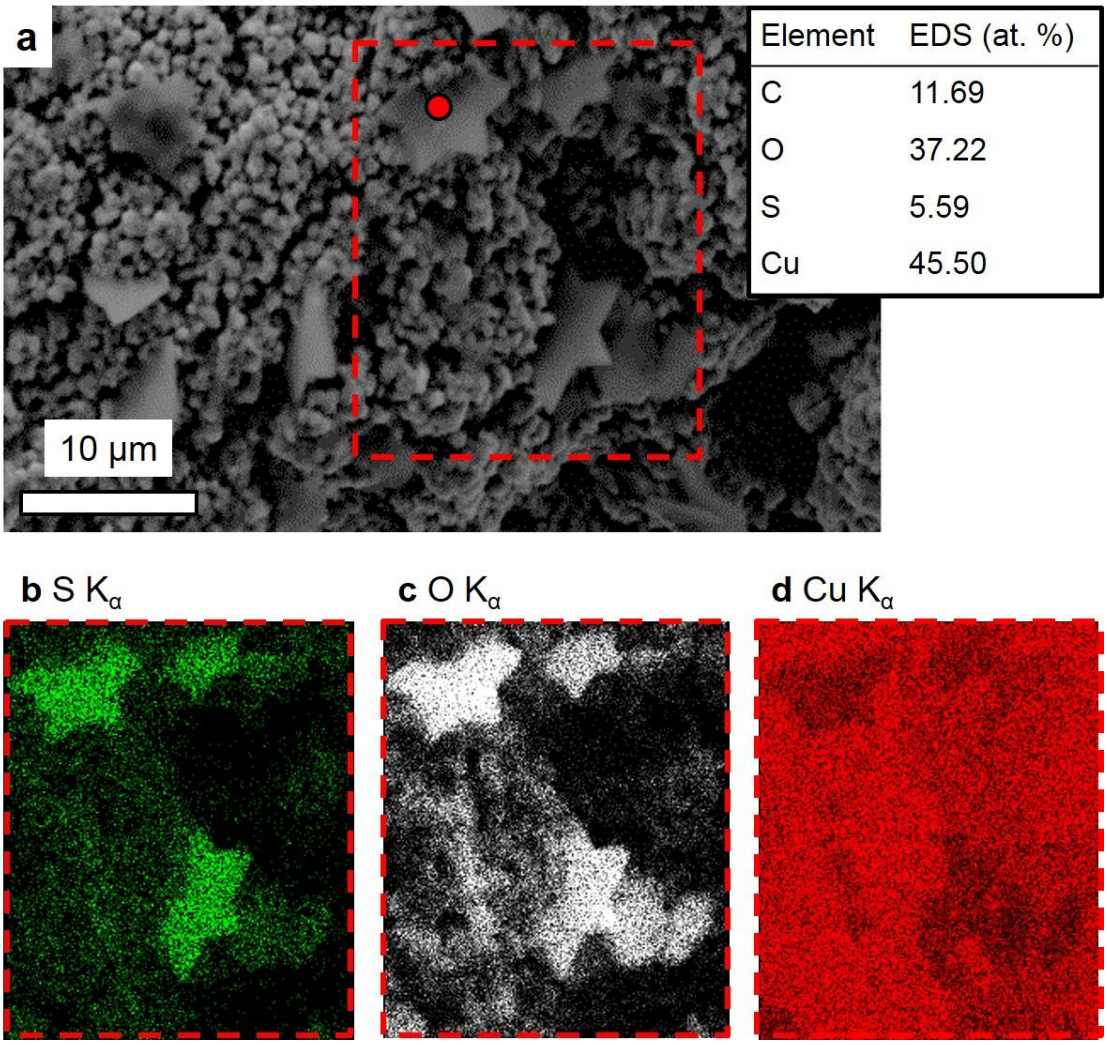


Figure 7.16: a) SE micrograph of hexagrams embedded in electrodeposited surface, shown by EDS as composed of: b) sulfur and c) oxygen, with limited Cu in the crystals (d). Red dot marks point of spectral acquisition for results shown in the table inset.

7.2.4. Silica codeposition

The use of the electrolyte plating media to act as a carrier for fine particles represents a useful augmentation to EJP coating and is referred to as jet co-deposition (*see* section 2.4.3). Silica was selected in this study as the material has been demonstrated to have tuneable water-facing properties, when appropriate chemistries are applied to the surface [233]. This is pertinent considering the scale of nodulation reproducible with EJP coating is consistent with featuring shown to affect surface wettability [65]. The design of the carrier

electrolyte used in EJP has been shown to have a significant effect on the morphology of the deposit, and will also affect the distribution of the reinforcement. Agglomeration within micro and nano-particulate suspensions is widely reported [234]. The formation of nanoparticle agglomerates within the electrolyte will have the undesired effect of producing an uneven distribution of reinforcements in the final deposit.

In order to create superior distributions for the reinforcement media within the composite the zeta potential, ζ, across a range of concentrations and pH levels was evaluated using laser Doppler electrophoresis (*see* section 3.7.4). Consistent with the theory for colloidal silica suspensions, a higher pH is shown to dramatically reduce zeta potential magnitude and hence the repulsive force between particles [235]. This is due to the protonation of surface silanol groups (*see* Figure 7.17). This challenges efficient suspension and co-deposition as agglomerations will form due to Van der Waals forces, which overcome the reduced electrostatic repulsion. In order to evaluate this effect, zeta potential was measured over a range of pH values (2-4.5) obtained through the addition of sulfuric acid and varying concentrations of copper sulfate (10-50 mM). Figure 7.17a shows a clear trend dominated by the pH as opposed to the copper sulfate concentration although a clear shielding effect is evident, which neutralises the surface charge on the silica.

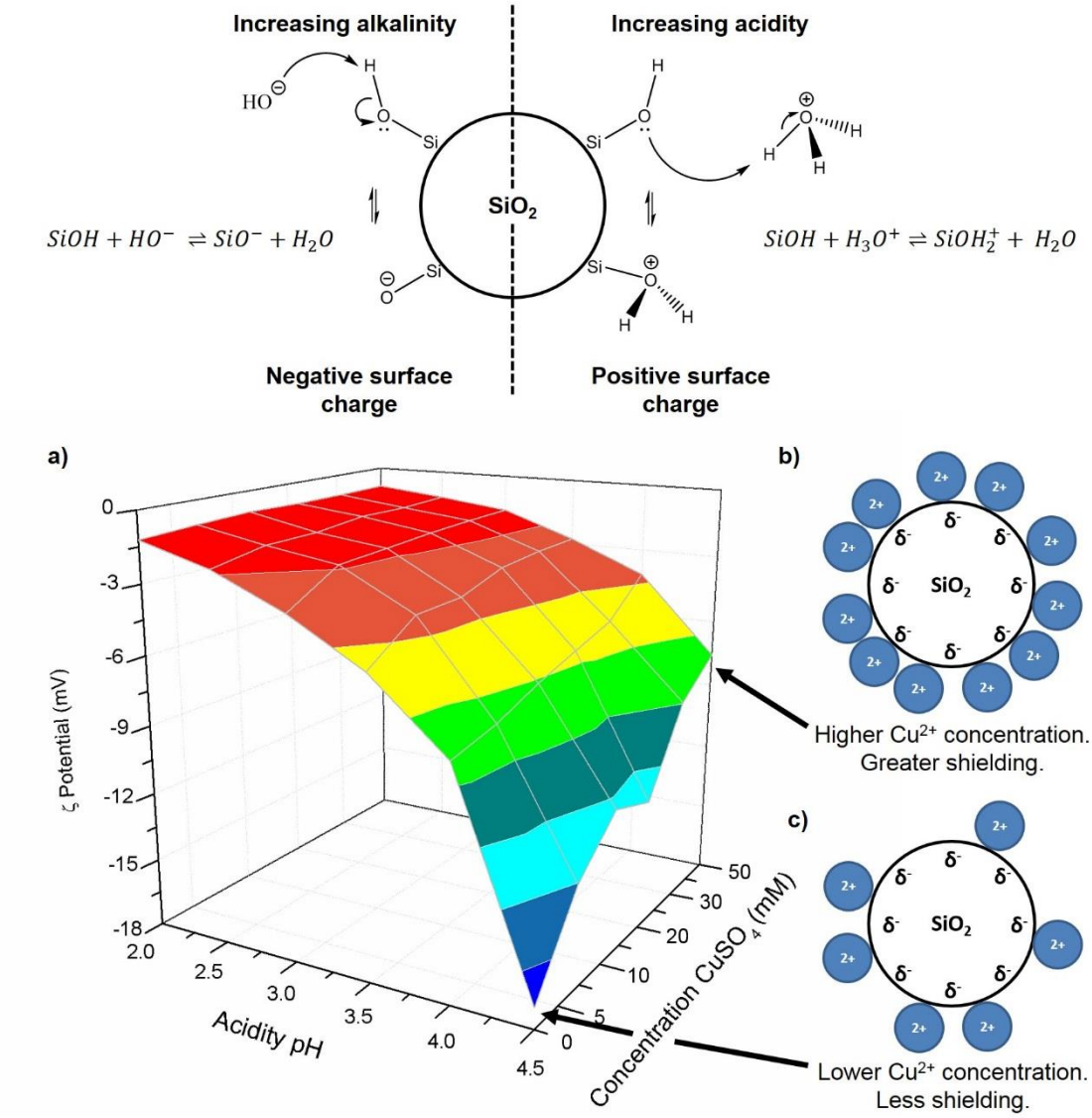


Figure 7.17: In alkaline environments, silanol groups are deprotonated, increasing ζ potential and suspension stability. Conversely, acidifying electrolytes protonates these groups and the negative ζ potential decreases such that Van der Waals forces are more able to overcome electrostatic repulsion. a) Combinatory relationship of acidity and concentration upon the zeta potential of the electrolyte b) and c) the mechanism of ζ potential neutralisation through electrostatic shielding in a high and low concentration Cu^{2+} electrolyte respectively.

This presents challenges to efficient silica-copper co-deposition strategies in EJP. Conventionally, acidic and relatively highly concentrated copper electrolytes are employed in electrodeposition, however such approaches would create an unstable environment towards suspended silica. Strategies to

functionalise the surface of silica to make it hydrophobic have been adopted, for example by Terzieva et al. (2000) [236], which have enabled the successful co-deposition within acidic plating baths. This approach could be adopted in EJP, however the objective of this investigation concerned the deposition of silica, whilst retaining its wettability characteristics. As increasing the concentration of Cu^{2+} destabilises the silica suspension, concentrations evaluated in this section are lower than those used previously for bulk EJP coating strategies (*see* sections 7.2.1, page 247 and 7.2.2, page 254). Surface charge considerations allow the design of electrolytes with better particle dispersions and should reduce the agglomeration phenomena within deposits. Regarding the measured zeta potential, even at the low $CuSO_4$ concentrations tested here, the surface charge magnitude is shown to be less polarised than -25 mV for all electrolytes tested. This means that suspended silica within all electrolytes is unstable, thus the reservoirs were agitated with magnetic stirring throughout subsequent co-deposition work.

The effect of co-deposition in a poorly dispersed solution is shown in Figure 7.18, using the electrolyte: $CuSO_4$ (0.1 M) Na_2SO_4 (0.7 M) buffered to pH 2 with H_2SO_4 (50 A/cm^2). The mass of nanoparticle silica within the electrolyte was maintained (0.3 g/l). A low Cu^{2+} concentration was selected to reduce the shielding effect. Considering the average supplied silica particle size (quoted as 200-300 nm), the large particle, which EDS inspection confirms to be silica, is most likely to be an agglomerate of many particles. The scale of the agglomerated particle is an order of magnitude greater than the average nodule size for this electrolyte condition (<1 μm). True co-deposition and integration within the matrix is not possible when the matrix crystal size is significantly

smaller than the particle reinforcement size and in this case the particle has been rejected from the deposit.

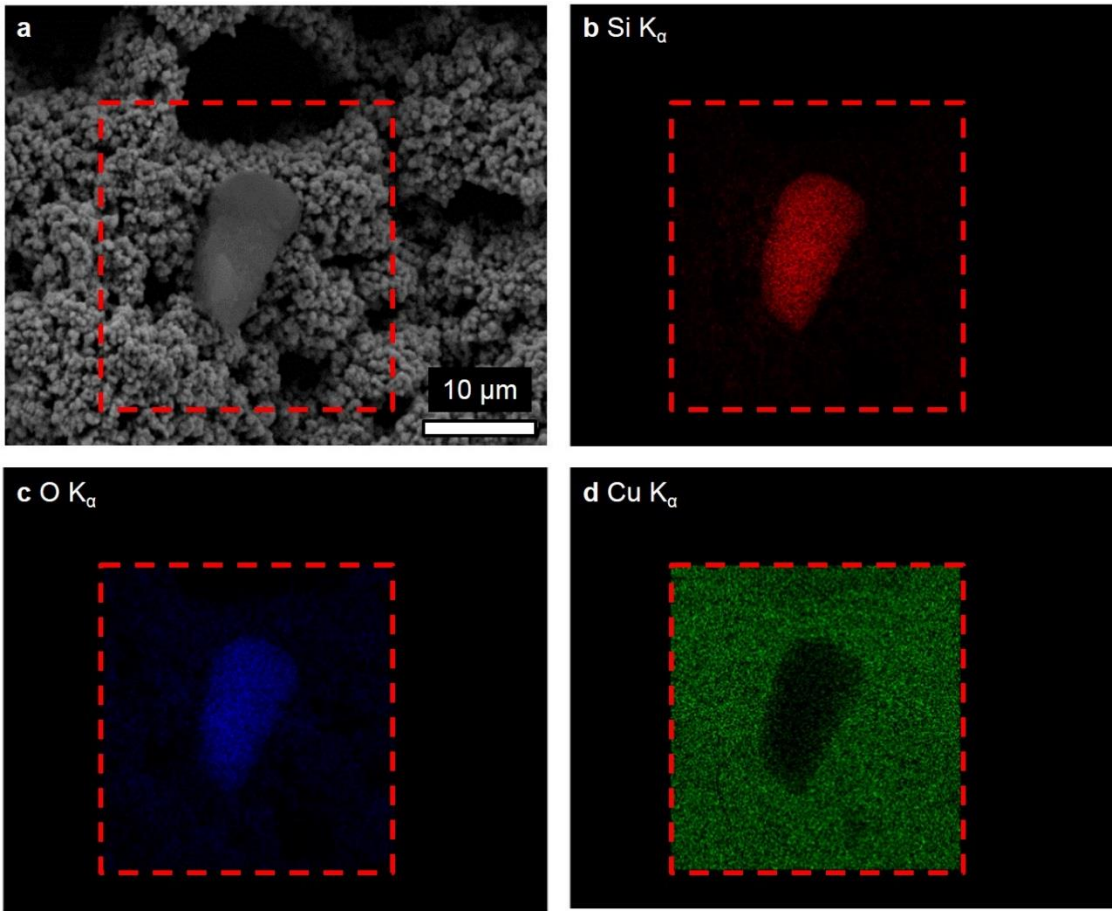


Figure 7.18: a) SE micrograph showing silica agglomeration at the surface caused by the acidic electrolyte (pH 2), considering the mean diameter of the supplied nanoparticle feedstocks (200-300 nm). EDS intensity maps for b) Si, c) O, and d) Cu.

Through decreasing the acidity of the same electrolyte to pH 4.5, it is possible to generate more homogenous distributions of silica, which appear to be integrated within the deposit (*see* Figure 7.19). In this case, a better dispersion of silica in the less acidic solution, results in no observable surface agglomerations. Silica appears to be more dispersed within the deposit. Single nodules display some localisation, which is to be expected where the crystal size approaches the nanoparticle size. More homogeneous silica distributions within the deposit are possible using this electrolyte, even though the effective

ζ potential is more neutral than -25 mV. This is likely a result of the high impingement velocities employed in this investigation, where the large kinetic energy of the electrolyte destabilises silica agglomerates. Acidity regulation is still required considering the visible surface agglomerations shown at the same parameters undertaken at pH 2 (*see* Figure 7.18)

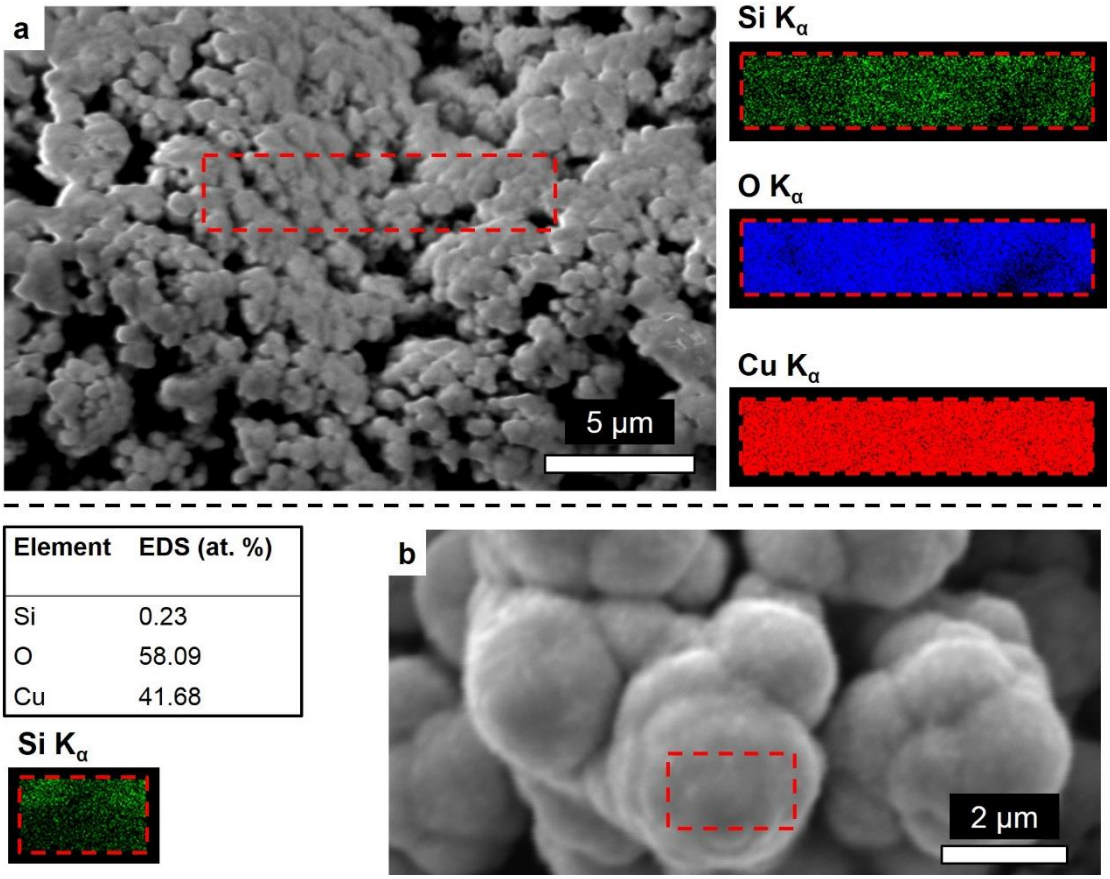


Figure 7.19: a) At pH 4.5, stable dispersions are created within the electrolyte, resulting in apparent homogeneous codeposition (compared with poor dispersions in Figure 7.18). b) Discrete nodules contain localised silicon signal corresponding to the supplied particle size. Table inset: elemental quantification of field of view shown in b).

An additional approach making use of both the morphology enhancing agent (thiourea) alongside sodium sulfate addition to control nodule size, and a fine dispersion of silica (0.3 g/l), was then attempted, shown in Figure 7.20.

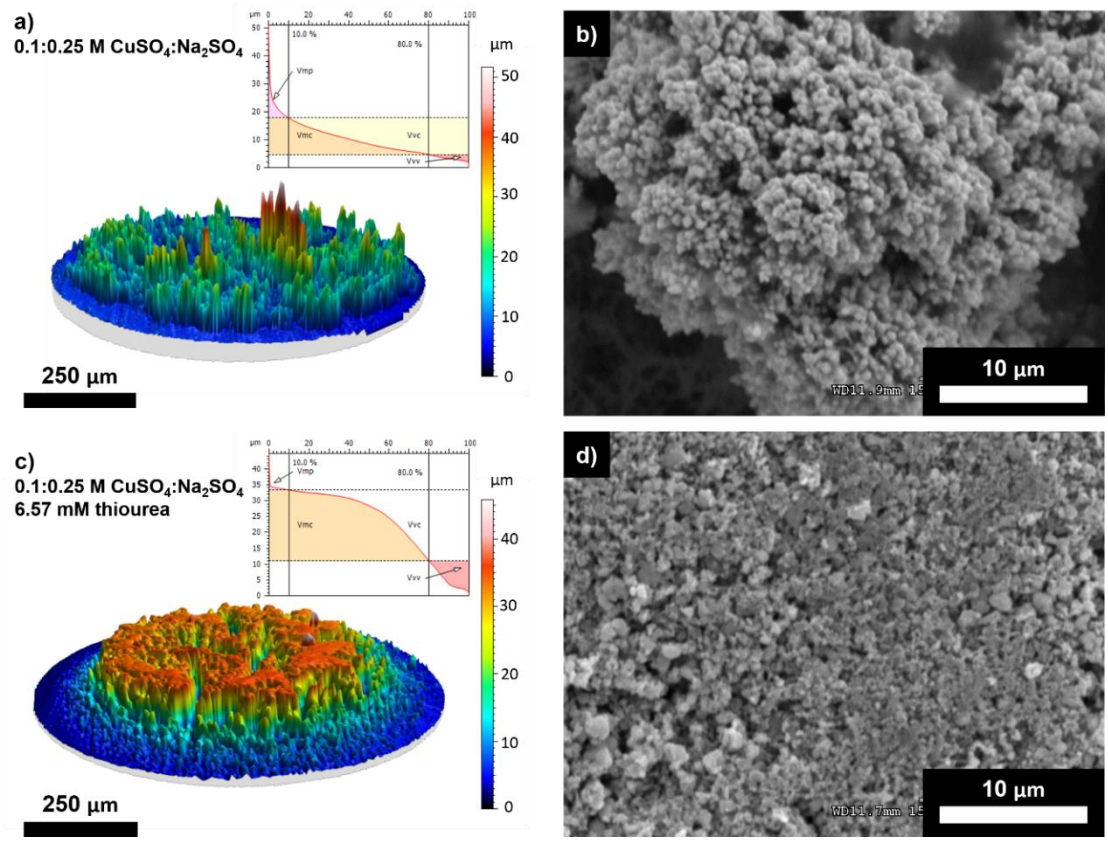


Figure 7.20: Reconstructions of deposits (FVM 20x objective) processed with a) $CuSO_4$:Na_2SO_4 feedstock solution at a ratio of 0.1:0.25 M (pH 4.5), b) Corresponding SE micrograph. c) The same electrolyte with 6.57 mM thiourea, leading to a denser and more compact deposit, d) confirmed in SE micrograph. Inset are the Abbot curves from each deposit, demonstrating greater core volume upon thiourea addition.

When comparing SE micrographs (*see* Figure 7.20b, d), of deposit surfaces for the same electrolyte, buffered to pH 4.5, with and without thiourea addition (6.57 mM), a marked difference in surface finish and distribution of silica within the surface (compared with Figure 7.18 and Figure 7.19) is visible. It is demonstrated that further control of morphology has been obtained allowing for the deposition of denser and more even copper and superior silica dispersion. The inset Abbot curves in Figure 7.20 show greater bulk volume as a result of using the hybrid electrolyte. Using the volume parameter ratio of *Vmc*/*Vvc*, core material volume and void space (*see* section 3.6.1), a 2.5-fold increase in

density is recorded. In addition, the peak material volume, *Vmp*, is also shown to be reduced upon thiourea addition, supported by flatter surfaces visible in the reconstruction.

The addition of nanoparticles to conventional electrodeposition electrolytes results in inhomogeneous distributions of the nanoparticle reinforcement and poor deposition uniformity in EJP. Through surface charge considerations it is possible to adapt the carrier electrolyte in order to enhance the distribution of these and also improve deposit appearance through the use of chemical additives. Similar to common plating methodologies the more acidic the carrier, the better deposition surfaces due to less oxidation, giving rise to larger nodule sizes. However, at lower pH, silica is less negatively charged, therefore less electrostatic repulsion is experienced between particles. In order to improve this lower acidity is preferred. It is therefore evident for suspended particulate EJP, the electrolyte should be optimised for both matrix material deposition efficiency and deposit quality, but also to maintain a good distribution of the suspended media.

7.3. Jet plasma electrolytic oxidation

7.3.1. Control of jet plasma electrolytic oxidation

Considering the high current density that is a characteristic of EJP techniques, it was proposed that the existing apparatus could be readily adapted towards plasma electrolytic oxidation (PEO) as a method to selectively generate hard-facing and corrosion-resistant surfaces. The literature review (*see* section 2.4.4) indicated the workpiece, generally a valve metal such as titanium or aluminium,

is required to be held at large anodic potentials >100 V and passivating electrolytes employed [189].

The onset of jet-PEO was characterised for Ti-6Al-4V in a neutral pH Na_2SO_4 electrolyte by gradually increasing the current density from 20-100 A/cm^2 for point processing (4 s dwell time). At low current densities (<30 A/cm^2) the workpiece was anodically coloured, corresponding to titanium oxides of reported layer thickness <300 nm (*see* Figure 7.21a-c). The thickness therefore appears to be related to the applied current density distribution, which is proportional to the electrical field gradient [108]. EJP >30 A/cm^2 resulted in orange-coloured plasma discharge across the local jet impingement region during processing, and the development of optically dull greyish-white films under ambient lighting conditions (*see* Figure 7.21d-i). This is likely to represent the transition between two discrete oxidation mechanisms, separated by the formation of a high-temperature plasma, which has not been reported in EJP.

Beyond 30 A/cm^2, the development of the discharge plasma is likely to correlate with the dielectric breakdown of the passivating films generated in the process as detailed in section 2.4.4. In all cases, both electrode potential and current appeared stable during processing. In this case, the onset of dull point coatings is likely to represent the transition from athermal anodic oxidation to a plasma-based process such as PEO. As current density is further increased >40 A/cm^2, dark speckles appear within the central region of the coating. Processing at the highest current densities here (75 and 100 A/cm^2), some bulk material removal is observed, as a flat-bottomed pit ≈200 μm in diameter.

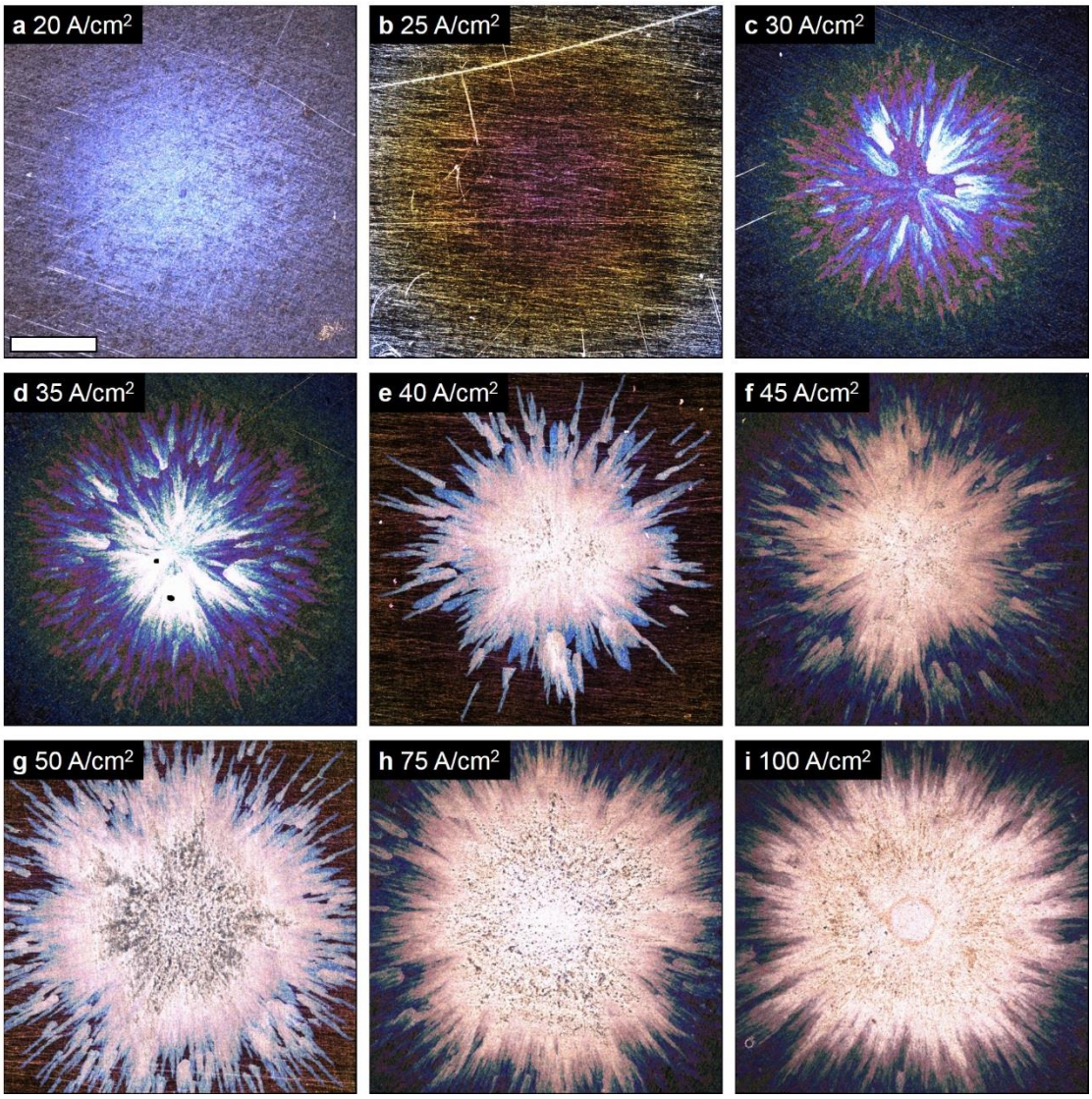


Figure 7.21: In Na_2SO_4, the transition from athermal anodic oxidation to PEO coating is associated with a change in visual appearance >30 A/cm^2 (a-c). Optical micrographs showing vibrant coloured titanium oxides correlate with thicknesses ≈10-300 nm, depending on hue. d-i) Grey-white regions are significantly thicker. All fields of view identical (2.06x2.06 mm). Scale bar 500 µm.

The transition from vivid colouration (indicative of oxides <300 nm thickness) towards optically dull (and rougher) coatings occurs between 30-35 A/cm^2 in this electrolyte-material system at this dwell time. The comparative optical and BSE micrographs shown in Figure 7.22 demonstrate the mass contrast expected from surface oxidation. In addition, mass contrast is enhanced at 35 A/cm^2, which is indicative of significantly increased oxide layer thickness.

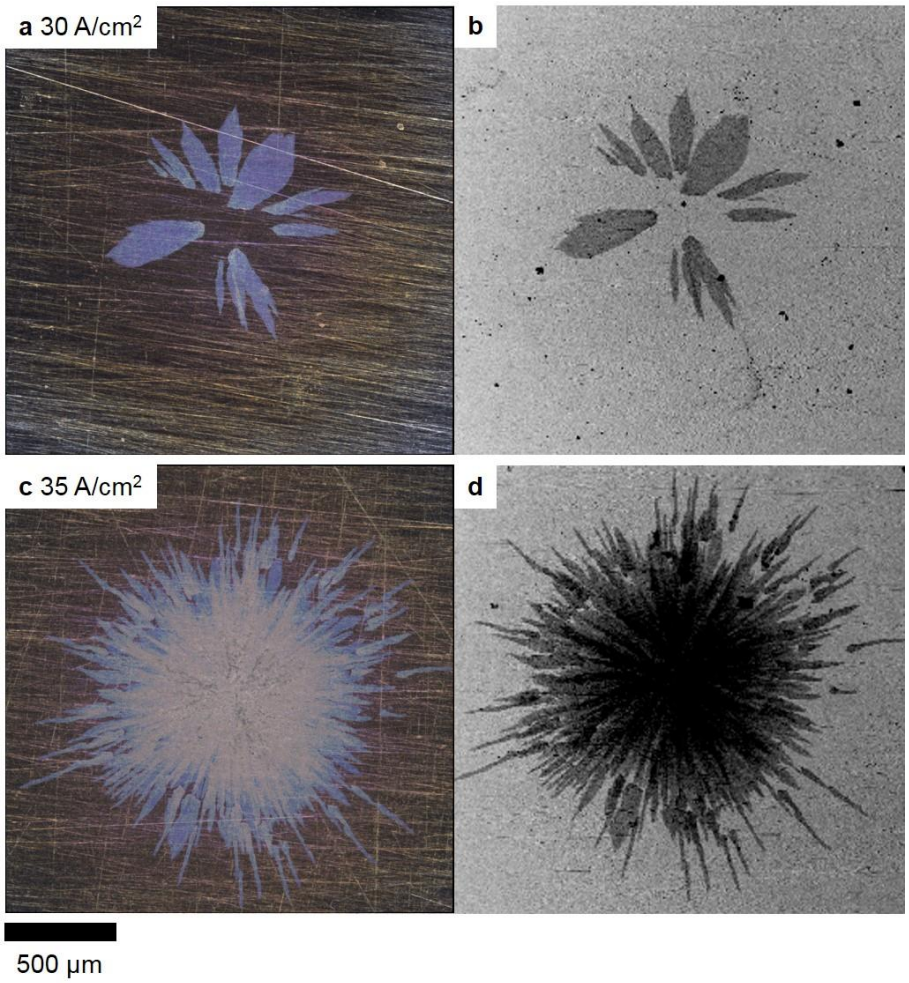


Figure 7.22: Comparative optical (a, c) and BSE (b, d) micrographs showing major film development between 30-35 A/cm^2. Mass contrast is enhanced in this range.

Further evidence for the existence of a plasma electrolytic oxidation is shown in the SE micrographs in Figure 7.23. Surface topography is consistent with ceramic coatings achieved in conventional bath-based PEO investigations (*see* section 2.4.4). In this case, the sub-micron pores visible in Figure 7.23b correspond with micro electrical discharge channels through the oxide coating, while the nodular featuring likely correlates with the location of plasma bubble implosion. Considering similar chemical and electrical environments to conventional PEO studies and the similar topographies, PEO is considered to be the major surface modifying mechanism during EJP under these parameters.

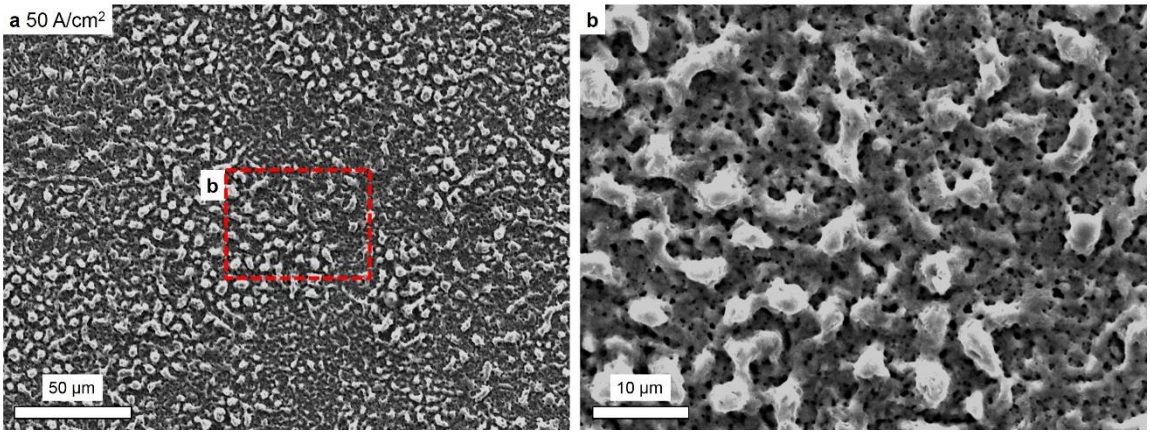


Figure 7.23: SE micrographs: a) low magnfication, b) high magnification, showing the surface after processing at 50 A/cm^2 in Na_2SO_4. A nodular texture is observed with sub-micron pores on the spot coating.

The depth of material removal after processing >75 A/cm^2 is relatively small (≈10 µm) and is accompanied by a surface textural difference (*see* Figure 7.24). This material removal phenomenon is likely to be distinct from anodic dissolution, discussed in Chapters 4, 5 and 6. Instead, removal here is likely due to a plasma driven process, given the effective removal diameter is <90% of the nozzle internal diameter, the mechanism of which is discussed below. In any case, material removal is largely undesirable in a coating process, thus an operational regime can be defined for this electrolyte material system, whereby spot PEO coatings at this dwell time (4 s) can be reliably generated >30 A/cm^2 and <75 A/cm^2 if bulk removal is to be avoided. It is likely that removed material could be redeposited during the processing, although further investigation is required.

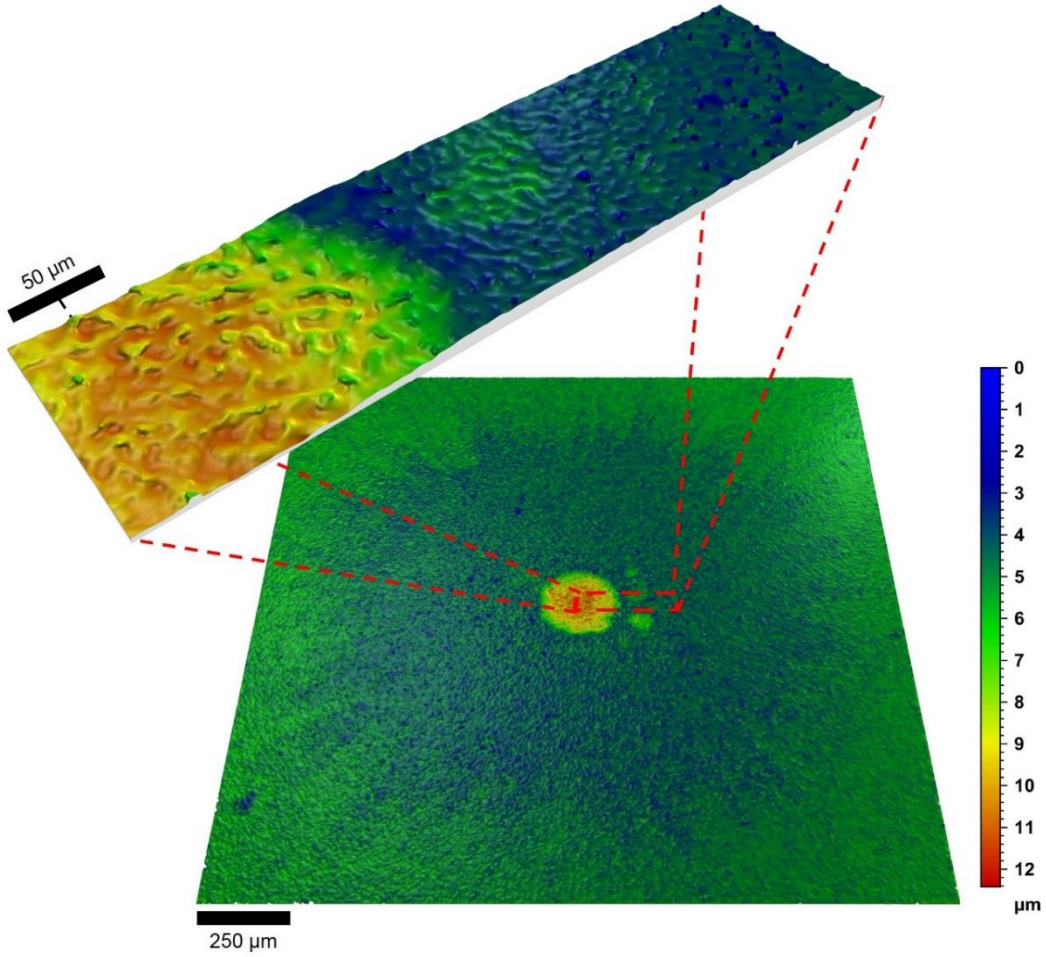


Figure 7.24: Processing at 100 A/cm^2. Oxide is shown to grow ≤7 µm from the unprocessed surface. Central removal region is shown to be texturally discrete from the grown oxide.

The topographic difference between the central removal region and the rest of the PEO coating at 100 A/cm^2 is shown in the SE micrograph Figure 7.25. Nodule formation is observed to be lower than the exterior zone, although the scale of undulations in the central removal zone is larger (*see* Figure 7.24). In addition, the frequency of micro-pores appears to be greater in the central region. An increasing number of micro-pores is indicative of a greater number of discrete electrical discharges through the coating, which is likely to be responsible for the observed material removal. The localisation of discharges

below the nozzle is unsurprising, given this is where current density, potential gradient and plasma generation are the greatest.

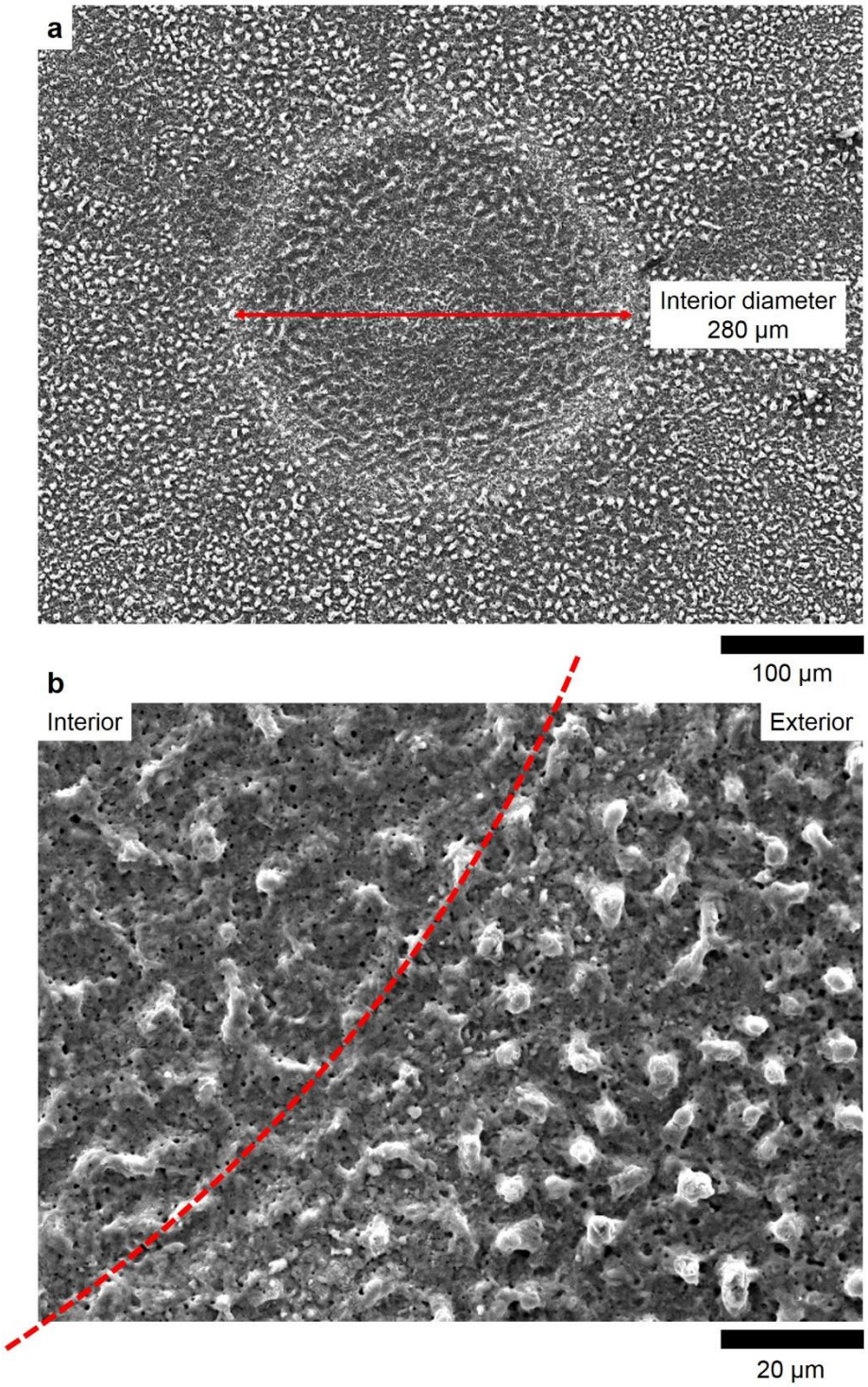


Figure 7.25: a) SE micrograph of spot coating processed at 100 A/cm^2. b) Topography in central removal region is discrete from the exterior, where nodulation is increased. Red arc corresponds to nozzle circumference.

A schematic of this mechanism is shown in Figure 7.26, adapted from Hussein et al. (2013) [237]. In this instance, small plasma discharges occur over the oxide film leading to nodular growths consistent with conventionally generated PEO films. Upon increasing the total charge passed (either temporally or energetically), the PEO coating grows through oxygen diffusion into the metal and titanium diffusion into the film [191]. Plasma discharges subsequently lead to molten oxide eruptions, which solidify, leaving characteristic micro-pores.

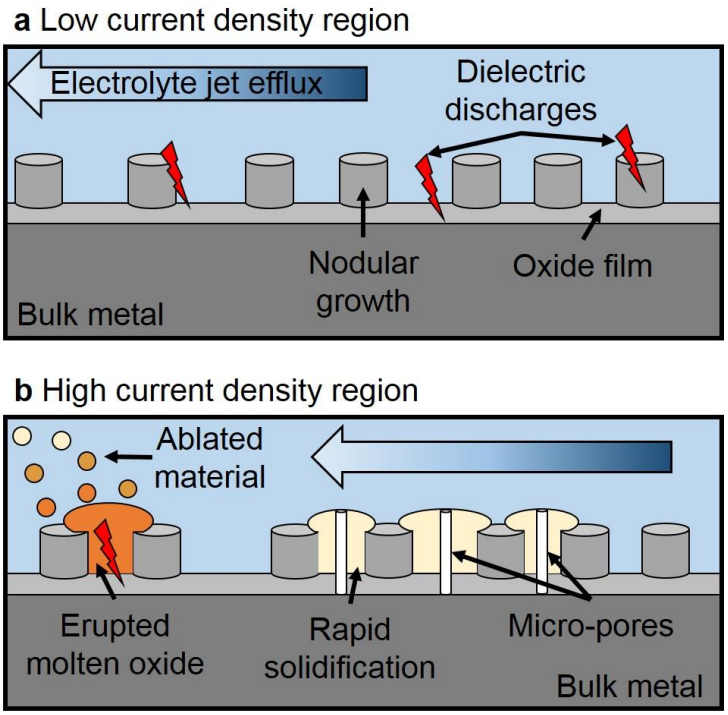


Figure 7.26: a) Nodular growths outside of the central removal region are consistent with conventional PEO film morphologies. b) Within the central removal region, discrete molten oxide eruptions occur at greater frequency, leading to ablation and evacuation in the jet. Schematic adapted from Hussien et al. (2013) [237].

The number of discrete molten oxide eruptions is likely to be greater in the central region of the jet, where the current density is the greatest. In the case of a jet electrochemical technique, where there is a rapid flow of electrolyte across the anode surface, some of the ablated material resulting from these eruptions

will be evacuated before re-deposition. In a conventional bath PEO process without rapid electrolyte efflux, a greater proportion of the ablated material will be re-deposited onto the surface, followed by reincorporation into the oxide film upon subsequent discharges. No evidence of electrolyte contamination was observed experimentally through EDS of the PEO coatings.

The large radius of the PEO films is indicative of poor processing selectivity, where the surface has been chemically modified over an area significantly greater than the nozzle diameter (*see* Figure 7.27). In this case, concentric circles are superimposed over the optical micrograph representing the nozzle diameter (blue), approximate PEO coating diameter (red) and limit of perceivable anodic colouring (green). For this spot coating, the PEO coating diameter is >4 times the nozzle diameter, while the anodic colouring limit is >10 times the nozzle diameter.

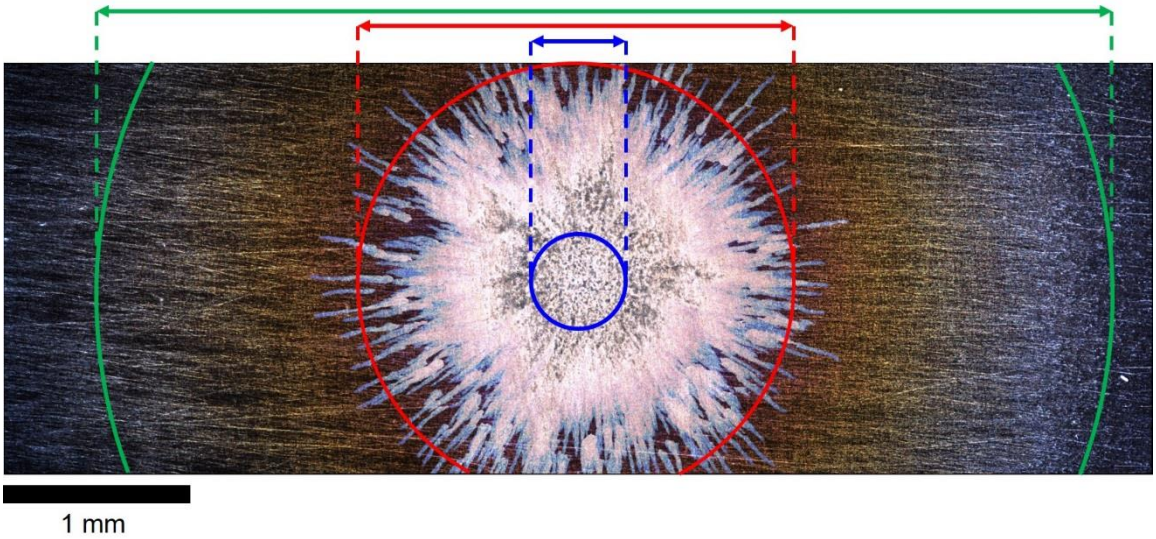


Figure 7.27: Selectivity of jet-PEO is generally poor in Na_2SO_4. Blue circle marks nozzle diameter, red circle marks approximate PEO coating diameter (4.6 d_N) and green arcs mark approximate limit of anodic colouring (10.7 d_N).

Increasing selectivity presents a challenge that has not been reported in conventional PEO studies, which generally aim to evenly coat a given part. Selectivity in conventional PEO is largely limited to control over the dipping of the part into the electrolyte bath. Considering phase stability within an electrochemical system (*see* section 2.1.5), an increase in acidity will generally suppress the development of oxide films. While this is also likely to inhibit vertical growth of the PEO films, the objective was to restrict radial expansion. To appraise this effect, Jet-PEO was undertaken at current densities from 30-100 A/cm^2 using the same base electrolyte (Na_2SO_4 1 M), but buffered to both high acidity (pH 2) and alkalinity (pH 13). Constriction of the oxide growth was observed upon increasing acidity (*see* Figure 7.28), manifesting as a decrease in both the diameter of the anodically coloured and PEO regions (mean of 3.09 at pH 2, 3.82 at pH 7 and 4.66 at pH 13 for 100 A/cm^2). In addition, radial coating expansion is reduced when processing >75 A/cm^2 for this dwell time (mean of 1.10 for 35 A/cm^2 to 3.71 at 75 A/cm^2 for pH 7 electrolyte). Furthermore, buffering electrolyte to high alkalinity (pH 13) significantly increases PEO film coverage, enabling a route through which electrolyte composition can be influenced by design intent, considering the desire to either selectively process (lower pH) or large-area processing (higher pH).

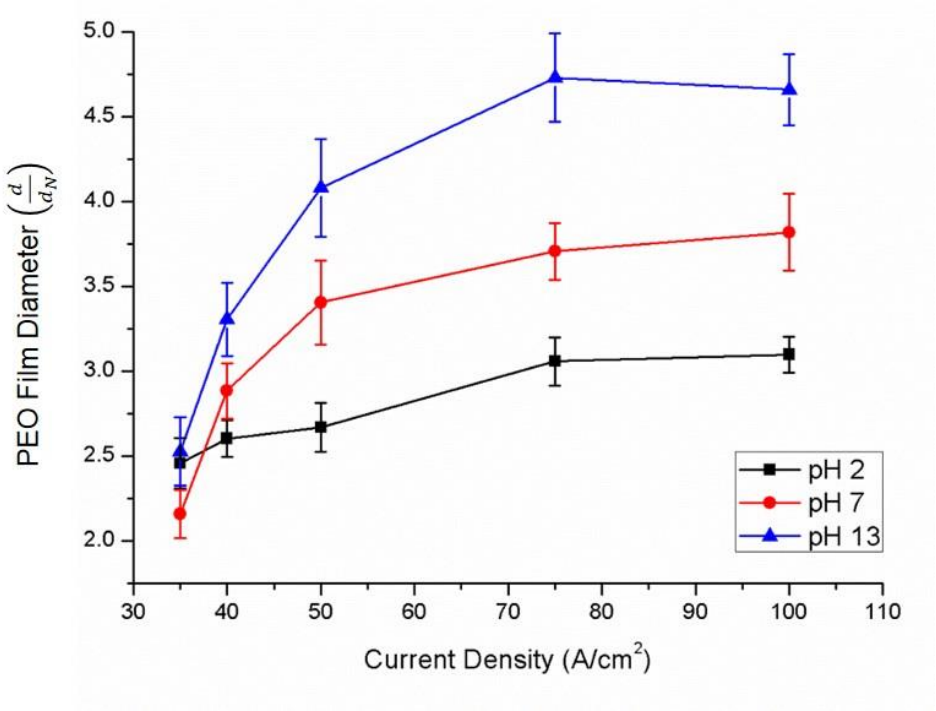


Figure 7.28: PEO film diameter with acidity and current density. Error bars are the standard deviation from the mean returned from three spots (four orientations per spot).

In addition to restricting the radial expansion of the PEO film, increasing the acidity also enhances removal in the central region when processing at high current density, shown in Figure 7.29. In this case, the maximum removal depth increases from approximately 4-5 μm at pH 13 to 11-12 μm at pH 2. This is likely due to destabilisation of the passivating oxide films in the highly acidic environment, which would enable greater energy transfer through material removal. Discrete central material removal for this acidic electrolyte can be avoided through processing <75 A/cm^2 at this dwell time, where selectivity enhancements can still be observed over the high pH electrolytes.

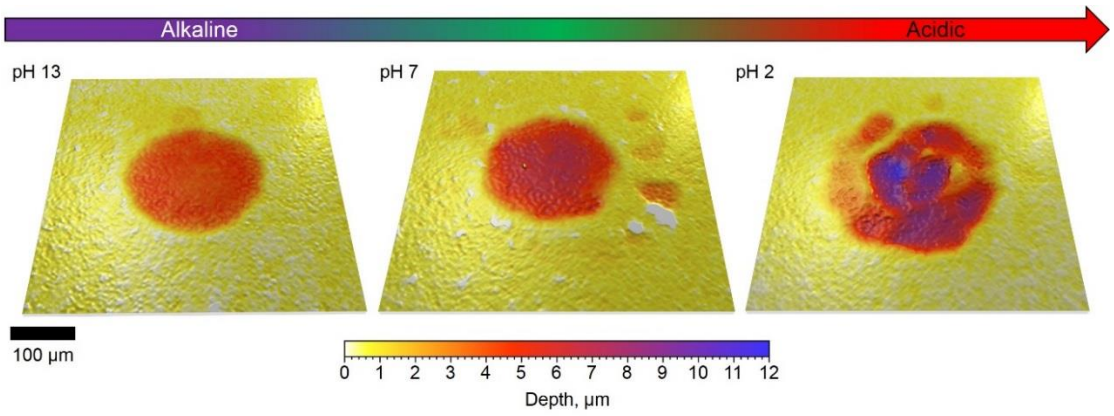


Figure 7.29: Surface reconstructions after processing at 100 A/cm^2, showing the relationship between electrolyte pH and material removal.

Considering the improvement in both achievable feature geometry and processing speed when applying planar processing strategies in comparison to spot coatings, the mechanism was applied while translating the jet. Feasibility of PEO mechanism translation is important in the context of direct-write surface processing, in which electrochemical jet techniques excel. To this end, striation features were processed using neutral Na_2SO_4 (1 M), at current densities between 50-100 A/cm^2, and v_h = 0.1, 0.05 mm/s. A typical example of a translated selective PEO film is shown in the optical micrograph in Figure 7.30, processed at 50 A/cm^2, v_h = 0.1 mm/s. In this micrograph, the central removal region (darker area) is visible, where the total charge passed, Q, is greater under this operating condition than the 50 A/cm^2 spot coating (4 s dwell). The directions of the radial oxide growth streaks appear to be field-oriented, consistent with spot processing oxide morphologies (*see* Figure 2.23).

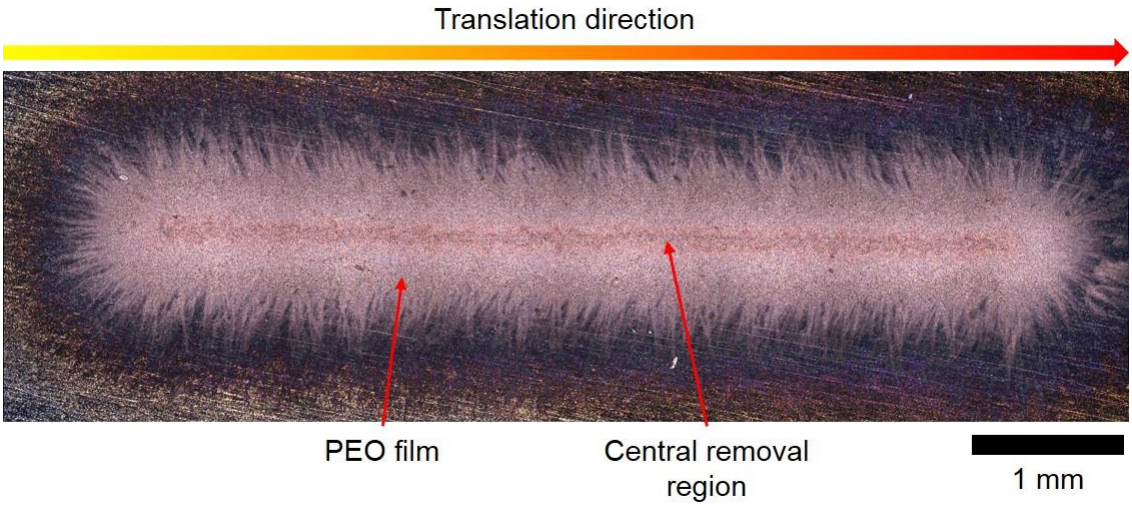


Figure 7.30: Optical micrograph showing translated PEO film. Processed at 50 A/cm^2, 0.1 mm/s with Na_2SO_4, pH 7.

The material removal in the central region was correlated with linear charge density, $\overline{\lambda_q}$, for the striation features, shown in the reconstructions in Figure 7.31a-c. These reconstructions show an increase in removal volume with current density, however this trend relating to charge specific removal, M_σ, appears to plateau where $\overline{\lambda_q}$>2 C/mm (*see* Figure 7.31d). The charge specific removal is significantly smaller than the ECE of the material (1.19-1.20x10^{-5} g/C, *see* Appendix 3), which is expected from a process mechanism reliant on anodically generated oxygen. The positive trend between $\overline{\lambda_q}$ and M_σ however, is indicative of a smaller proportion of total charge transferred through oxygen evolution as material removal rates increase. Such removal regions are largely undesirable in a coating or surface modification process, although this can be modulated with appropriate energy and dwell considerations. In addition, the translated central removal region processed at these parameter sets leads to a consistent cut where the kerf is <0.5 d_N. For example at 50 A/cm^2, 0.1 mm/s (*as* Figure 7.31a), the average kerf is 104 µm (σ = 21%), which is 0.2 d_N.

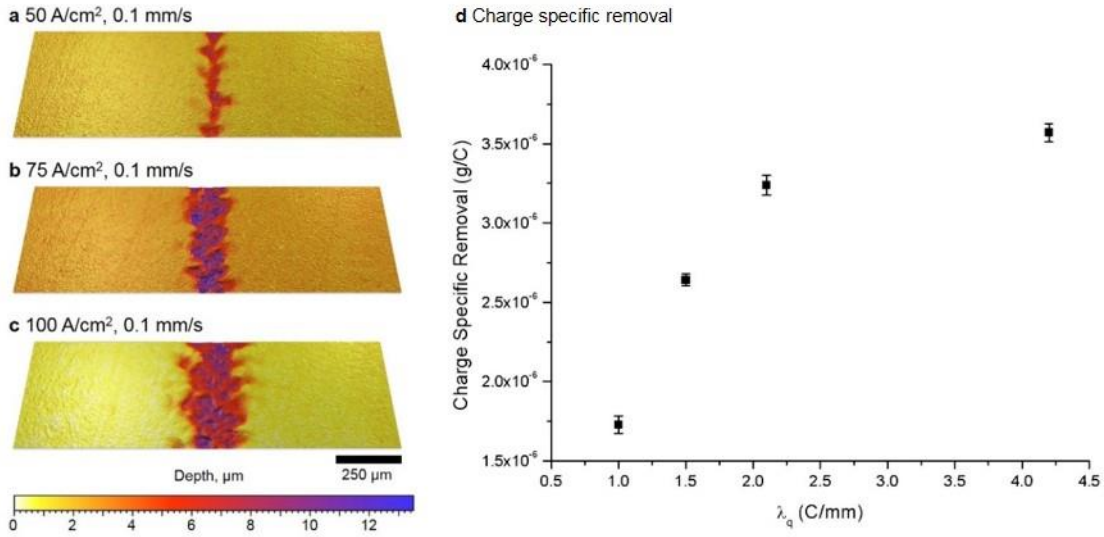


Figure 7.31: a-c) Reconstructions showing the central removal region of the translated PEO coatings between 50-100 A/cm^2. d) Charge specific removal increases with linear charge density, $\overline{\lambda_q}$, indicative of reducing oxygen evolution.

7.3.2. Interrogation of jet-PEO coatings

The PEO-type coating mechanism would be expected to form titanium dioxide phases on Ti-6Al-4V, the existence of which was confirmed using EDS. Analysis of the central removal and outer oxidation region (typical examples are shown in Figure 7.32a-b), returned equivalent chemical compositions. Each sample region tested displayed an approximate 1:2 atomic ratio of Ti:O, indicative of the stoichiometry of TiO_2. Raman vibrational spectroscopy was employed to determine structure of the TiO_2 phases present on the jet-PEO surface. Figure 7.32c shows evidence for rutile through intense peaks corresponding to the E_g (425 cm^{-1}), A_{1g} (610 cm^{-1}) and B_{2g} (790 cm^{-1}) vibrations, a small peak corresponding to the B_{1g} vibration (170 cm^{-1}) and a second order scattering mode (≈245 cm^{-1}) [225]. The intensity of these rutile bands is greater than those formed in the same material using $NaNO_3$ electrolyte (*see* Chapter 6, Figure 6.15). This is indicative of a higher order of crystallinity within the material, which

is expected considering rutile is the stable TiO_2 phase >600 °C [238]. Given the existence of plasma discharge at all but the lowest current densities tested in this study, this transition temperature would have been exceeded, although there remains a broad peak associated with the E_g vibration (≈150 cm^{-1}) of anatase [225]. The intensity of the Raman vibrational bands is shown to be greater in the nodular features than the porous films, which is likely to be a concentration effect, where the sampling volume is significantly greater through the nodule. The two spectra are however shown to be chemically identical.

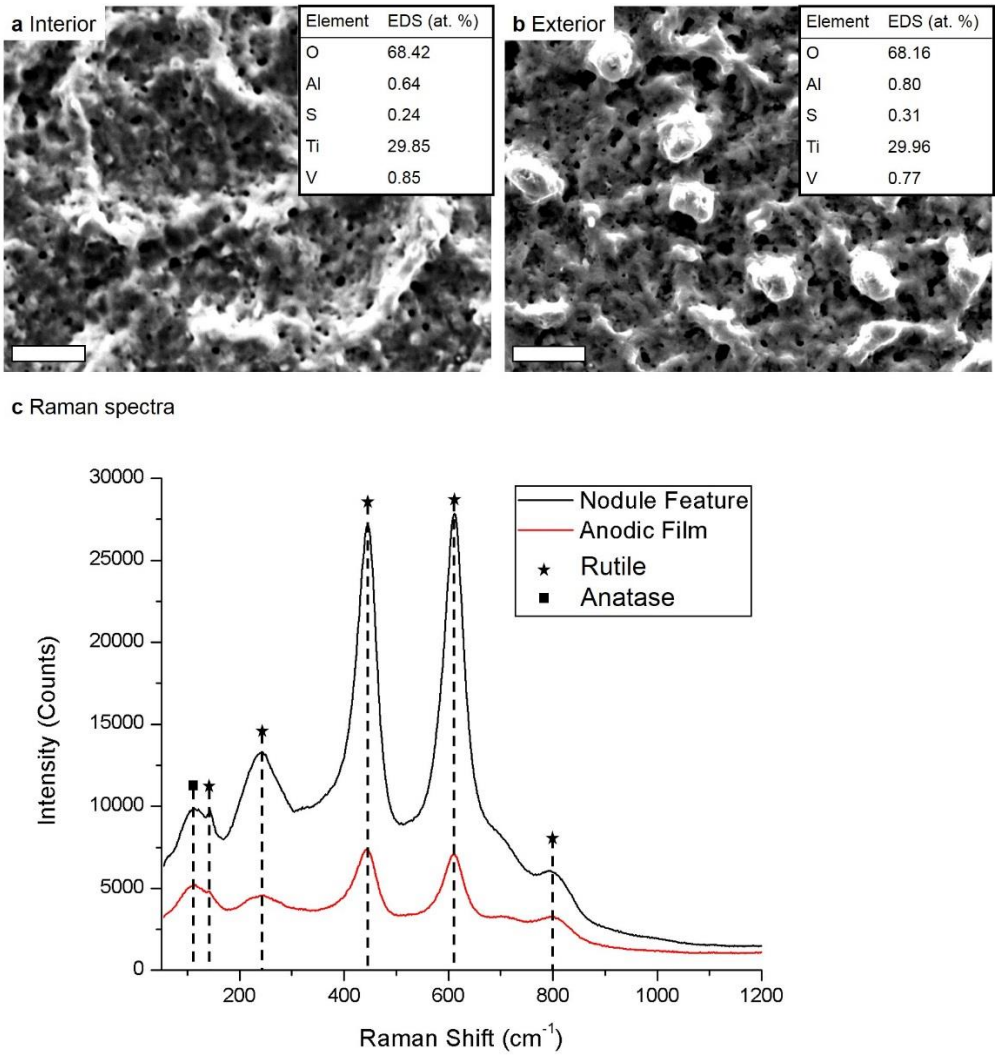


Figure 7.32: a-b) SE micrographs of nodules and film with EDS spectra acquired over field of view. c) Raman spectra showing equivalent chemistry at both nodule and film, although greater intensity is indicative of a concentration effect. Scale bars are 5 µm.

The thickness of the PEO surface films were appraised through cross-sectional observation and analysis with SEM and EDS. The split field of view image of a sectioned, resin-mounted sample processed at high current density (100 A/cm^2) and translated at a velocity of 0.1 mm/s (*see* Figure 7.33), shows the existence of a modified surface band of lower apparent mass in BSE mode. This can be correlated with an interfacial layer when viewed in SE mode. In Figure 7.33, the micrographs were taken from the region adjacent to the central removal region.

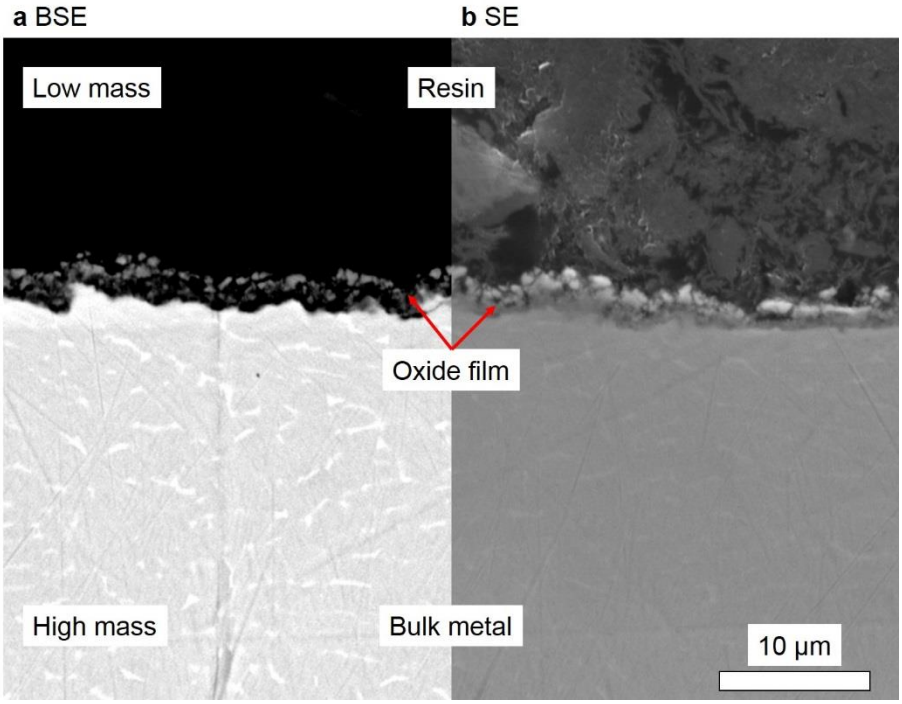


Figure 7.33: Split field of view image of cross-sectioned sample processed at 100 A/cm^2, v_h = 0.1 mm/s, a) BSE micrograph showing low mass resin and high mass Ti-6Al-4V, with poor mass contrast interface. b) SE micrograph of porous oxide film.

Interfacial regions were subsequently appraised using EDS for the striation feature processed at 100 A/cm^2 at 0.1 mm/s. In Figure 7.34, the porous interfacial region shows localisation of oxygen signal (*see* Figure 7.34c – green) consistent with the existence of a rutile-type surface film indicated in the Raman spectroscopy and normal direction EDS (*see* Figure 7.32). This oxygen signal

is unlikely to solely be an artefact of the resin composition, as it does not correlate exactly with the carbon signal localisation (*see* Figure 7.34c – blue). This demonstrates that for this particular process parameter set, the PEO film thickness is <5 µm thick, considering the scale bars. Furthermore, the intensity of the titanium signal reduces towards the interface compared with bulk metal.

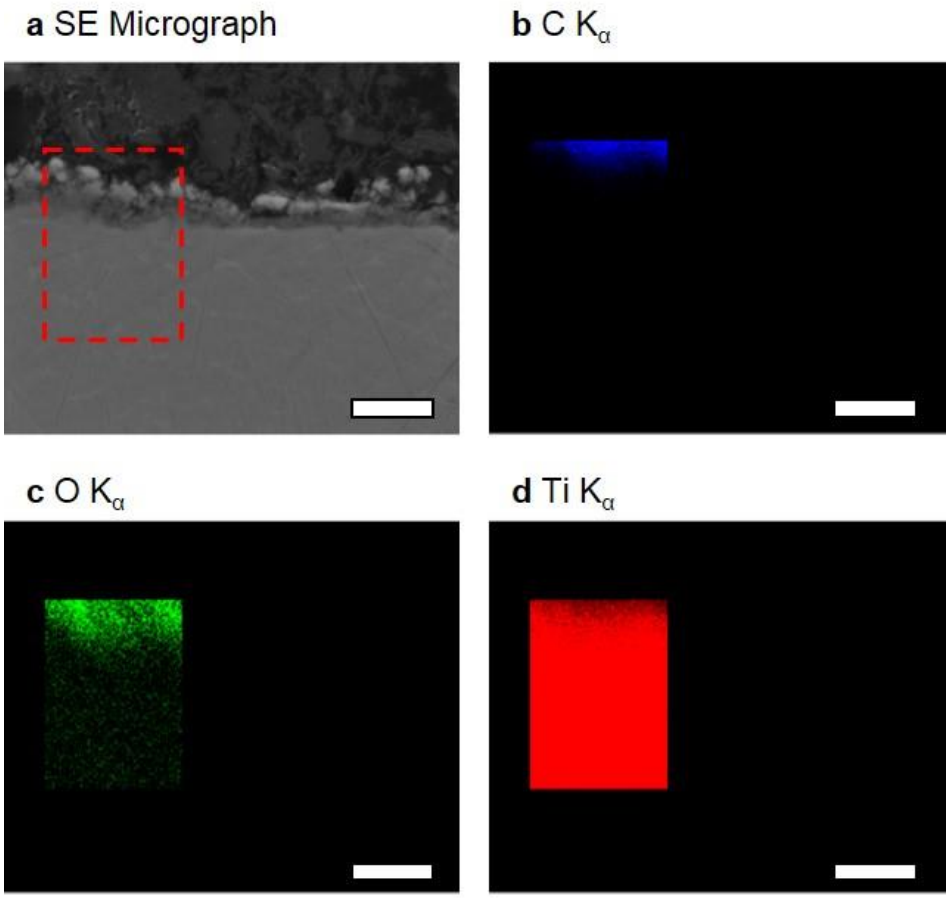


Figure 7.34: a) SE micrograph of sectioned PEO oxide. EDS confirmation of oxide layer thickness of <5 µm, b) carbon, c) oxygen and d) titanium. Scale bars 5 µm.

The relationship between PEO film thickness and linear charge density was appraised through sectioning striations processed at different parameter sets and shown in Figure 7.35, where oxide thickness is shown to increase from ≈1.8 µm ($\overline{\lambda_q}$ = 1.0 C/mm) to ≈4.0 µm ($\overline{\lambda_q}$ = 4.2 C/mm).

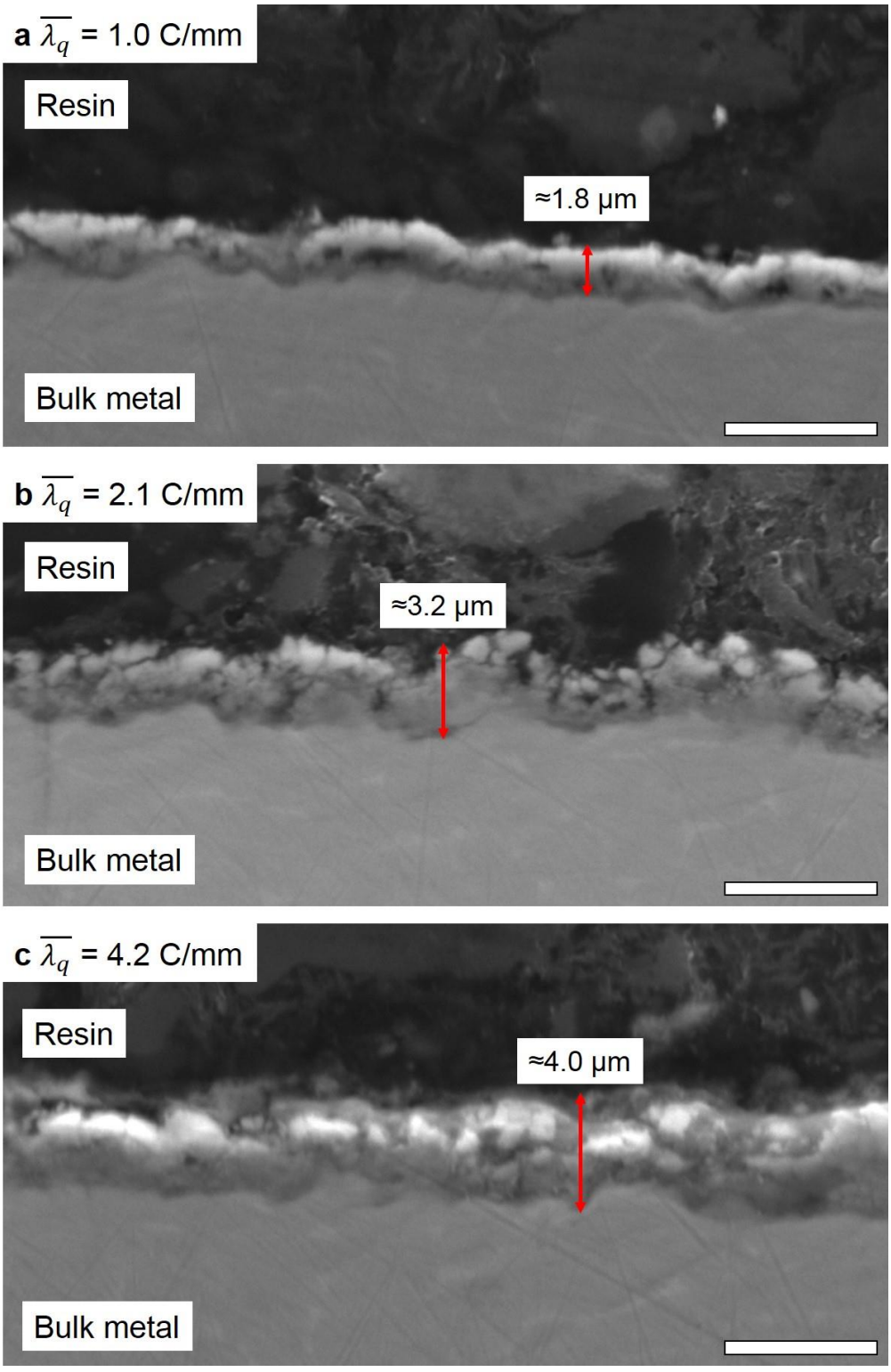


Figure 7.35: PEO film thickness is shown to be influenced by the linear charge density, $\overline{\lambda_q}$, a) 50 A/cm^2, 0.1 mm/s, b) 100 A/cm^2, 0.1 mm/s, c) 100 A/cm^2, 0.05 mm/s. Scale bars are 5 µm.

The relationship between thickness and $\overline{\lambda_q}$ is not precisely linear, although current density and translation velocity represent convenient and easily adaptable process parameters that can be manipulated to modulate PEO film thickness. In addition it should be noted that all of the conditions applied to generate striations in this investigation resulted in a small amount of material removal within the toolpath (*see* Figure 7.31).

Ceramic rutile phases, such as those generated during jet-PEO have mechanical properties which could make them desirable for mechanically robust surfaces, especially considering the poor tribological properties of metallic titanium. This was partially appraised through micro-hardness testing of spot coatings, using an indenter (*see* section 3.5.4). While it is acknowledged that this measurement strategy is not ideal considering the indenter size in comparison to the general PEO film thickness (<5 μm), Figure 7.36 shows that spot PEO films have a greater returned hardness value than unprocessed Ti-6Al-4V sheet control sample (295 HV). This is pertinent considering the plastic deformation recorded by the indenter is a hybrid of the PEO film and the underlying titanium alloy. Decreasing indent size in comparison to the control sample was observed even at current densities where only anodization was understood to have occurred ≤30 A/cm^2, whereby anodized coating thickness will be 5-100 nm [239]. The indent size is likely to correlate with the thickness of the PEO film, which is evidenced through the effect of increasing electrolyte acidity, considering oxide growth suppression at low pH.

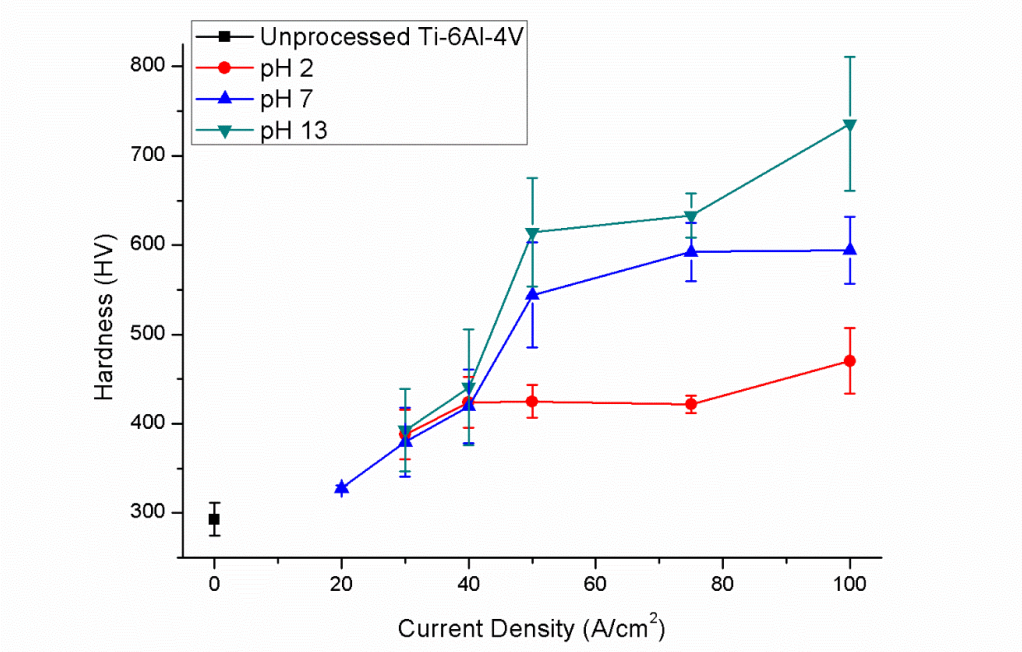


Figure 7.36: Vickers hardness of spot coatings (300 gf). Every treatment was shown to generate harder surfaces than the as-received material. Error bars represent the standard deviation from the mean returned over a minimum of five discrete indents.

7.4. Summary

This chapter demonstrated how, through simple adaptions to the carrier electrolyte and polarity, EJP can be employed as a selective coating and surface modification process. This has been undertaken through two discrete mechanisms based on electrodeposition and plasma electrolytic oxidation (PEO). The former involving a cathodic polarisation of the workpiece and the latter an anodic polarisation. The objective of this chapter was to significantly increase the versatility of EJP and explore discrete selective coating strategies that can be executed without hardware alterations.

Jet electrodeposition is limited by low deposition rates. Increasing this rate results in deposit nodulation with poor size control. It has been shown that in jet electrodeposition, adaptions to the electrolyte using non-toxic salts can enable

nodule size modulation at greater current densities. Deposit stability was also increased through addition of thiourea, commonly applied in conventional electroplating. This enabled deposit morphology to appear more consistent with the applied current density distribution at high current densities, typically an order of magnitude greater than those conventionally applied in EJP. Such processing conditions greatly increase the deposition rate and therefore the technique applicability.

In addition, considerations for co-deposition of nanoparticles from suspensions within carrier electrolytes have been proposed, specifically for copper and silica codeposition. The effective co-deposition of this material system is challenging due to the instability of SiO_2 suspensions in acidic media, and the instability of Cu electrodeposition in non-acidic media. Unstable nanoparticle suspensions will lead to agglomeration, poor codeposition and rejection from the deposited matrix. However, it has been shown that sufficient consideration of electrolyte chemistry can enable fine dispersions within the matrix, even at moderately acidic pH, where such nanoparticle suspensions are unstable. The codeposition mechanism is assisted by the large kinetic energies of the impinging jet in comparison to conventional bath methods; these overcome weak attractive molecular forces between nanoparticles, breaking up agglomerates.

In this thesis, it has been shown that PEO can be undertaken in EJP, whereby the aerospace alloy Ti-6Al-4V has been selectively oxidised using benign Na_2SO_4 electrolytes to create a more robust ceramic film than the unprocessed sheet, discrete from the mechanism of anodization. The selectivity of such jet-PEO coatings is fairly poor, however a route through which this can be enhanced for a given current density has been explored through reducing the

pH of the bulk electrolyte solution. The jet-PEO coatings formed on this substrate are demonstrated to be predominantly TiO_2, of the thermodynamically stable phase rutile. This opens up a new research field in EJP, where PEO film compositions and functional properties can be adapted to generate interfacial layers specific to jet-based electrochemical techniques.

8. Conclusions

This thesis aimed towards enhancing the industrial applicability of electrochemical jet processed features on metals, considering both the microscale surface and the broader geometric form. Progress towards this overall aim was broken down through consideration of the targeted objectives detailed in section 1.1. To conclude this thesis, the progress made towards achieving the predetermined objectives is outlined in this chapter.

Considering the first objective: to understand the role of material precondition in defining the topography and form, the microstructural precondition has been shown to affect the resulting topography of both pure materials and multiple phase alloys. This includes operation under parameters where microstructure was not thought to make a difference, such as high current density electropolishing regimes. This is proposed to be influenced by the high jet impingement velocities in EJP (≤30 m/s), which suppress the development of mass transport limited conditions within the diffusion layer. Changing the thermal and stress history is shown to influence topography, whereby cold-rolling reductions have been correlated with roughness after EJP <300 A/cm^2. In this case, undulations are caused by characteristic slip bands revealed at the surface and pores are understood to initiate at lattice defects. High energy processing strategies (>300 A/cm^2) can overcome microstructurally affected regions and reduce pore sizes, which is important considering an overall drive towards more homogenous surfaces.

Additional surface defining mechanisms are demonstrated for multiple phase materials. In this case, the ultimate surface roughness is a function of the grain

size and the phase ratio, in addition to the current density. For the brass material system investigated, roughness increases with grain size up to ≈10 μm (average grain size 1.5 μm, areal amplitude, *Sa* = 0.365 μm; average grain size 11.3 μm, areal amplitude *Sa* = 0.658 μm), after which dominant phase ratios appear to determine the surface roughness. In this regard, the smoothest surfaces at J_{noz} = 300 A/cm^2 (*Sa* = 0.065 μm), were achieved with the predominantly single-phase sample (700 °C), which has an average grain size of ≈105 μm. This is correlated with the increase in achievable step height when the size of the more inert phase is increased, whereby decreasing inert phase concentration decreases the number of discrete steps.

Furthermore, in multiple-phase alloys it has been shown that surface chemistry is influenced by the current density, whereby low energy processing strategies deplete the concentration of the more oxidisable species >2 μm in depth from the surface, which is analogous to dezincification in corrosion science. Surface compositions more representative of the bulk composition are achievable through processing at higher current densities (>100 A/cm^2). It has been shown that erosive removal effects are reported for metallic phases that would otherwise dissolve electrochemically. This elevates removal rates at low current densities for small grained materials (as received removal = 0.3556 mg/C, 700 °C removal = 0.3334 mg/C). In addition, the form is partially dependent on the microstructural precondition, where pit depths are increased by up to 17% when processing materials with polarised phase ratios, independent of current density. This is likely caused by the perturbation of inert phases, which appear to planarize material removal. Such affects are important when considering the desire to apply EJP towards high-value alloys, in addition to complicated

manufacturing strategies that lead to complex and inhomogeneous microstructures.

Considering the second stated objective to: enhance the applicability of EJP towards materials characterisation, investigations concerned primarily with the achievement of the first objective reinforced understanding of the capability of EJP to generate topography dictated by the internal microstructure of the workpiece. In this thesis, EJP exploited to perform microstructural etching of different materials, such as Ni, Al, and Ti. This enabled rapid microstructural qualification without preliminary polishing steps or hazardous chemical etchants.

The thesis subsequently explored how the topographical interrogation of similar surfaces could be executed to gain an understanding of localised crystallographic texture in polycrystalline pure material workpieces. This could ultimately enable intimate microstructural information to be acquired for a given part in line with a high-throughput processing strategy. Topography analysis was applied to generate three colour orientation texture maps, where the correlation with down-sampled EBSD data was determined to be approximately 68% for a Ni workpiece. Sources of error have been identified, the quantification of which is the subject of forthcoming work.

The third stated objective specifically targeted a reduction in the dependence of feature geometry on the input current density distribution. Considering the overall aim of enhancing the applicability of the technique, this was undertaken without altering the standard operating condition, where only electrolyte chemistries and applied current densities were modulated. Work towards this

objective was carried out by applying novel electrolyte chemistries which were developed to exploit facile side reactions across the anode surface. The result of this has been shown to be a current filtering effect, representing a threshold to enhance precision, dimensional accuracy and edge definition of processed features (where pit overcut is reduced by up to 31% compared with conventional electrolytes). Such chemistries were applied to the processing of titanium alloys, whereby enhanced dimensional accuracy (representing a reduction in edge deviation of 21%), is demonstrated without further apparatus adaptations, through doping electrolytes with small amounts of bromide and iodide.

Furthermore, different jet-specific dissolution phenomena have been reported, demonstrating a further reduction in the dependence of material removal from the applied current density distribution. The first involves a staccato-type removal mechanism, where the propagation of removal features can become unstable, displaying periodicity. Information pertaining to the avoidance of this regime is supplied to aid the wider community, however it is suggested that this mechanism could be exploited to surface texture mechanical parts. The second novel jet-specific dissolution phenomenon relates to the controlled propagation of singular pitting events along the length of the toolpath at a small fraction of the nozzle diameter (less than 0.05 d_N with 510 µm nozzle). This significantly reduces the scale of the geometric feature, leading to complex surface patterns, which could be applied to surfaces to enhance factors such as fluid transport and electrochemical response.

The forth thesis objective specifically targeted increases in the efficiency of EJP coating. To this end, the viability of the process towards selective coating more compatible with industry has been advanced, where modulation of deposition

morphology, stability, apparent density and deposition rate is demonstrated through energetic and chemical considerations. In addition, the co-deposition of Cu-SiO_2 metal matrix composites, highly challenging and therefore not previously reported in EJP has been undertaken, where control over nanoparticle dispersion within deposits can be exercised through adaptions to the input electrolyte chemistry.

Furthermore, the plasma electrolytic oxidation mechanism has been demonstrated in EJP. This will lead to significant new research avenues, whereby robust surface phases, with interesting surface properties can be selectively and cheaply applied. Although processing selectivity is currently relatively poor for jet-deposited electrolytic oxides, this can be enhanced through modulating electrolyte acidity, whereby film diameters can be reduced by 19% through buffering the electrolyte to pH 2 instead of the neutral Na_2SO_4 electrolyte.

This thesis has demonstrated the versatility of EJP towards a number of different processing strategies, beyond a planar machining technique. This is a direct result of the very broad range of operating energies and chemical environments achievable in the processing. This enables the execution of multiple discrete electrochemical mechanisms, depending on electrolyte choice, process parameter and material selection.

9. Future work

Considering the broad spectrum of the work undertaken, there are a number of interesting research avenues that require further investigation and must be tackled by a multi-disciplinary team. These are summarised in this section.

Within Chapter 4, the conceptual proof behind an entirely novel crystallographic characterisation technique has been demonstrated, which can characterise and map the orientation textures of materials in measurement and processing times unparalleled by existing methods. The potential for industrial impact is therefore great, and it can be envisaged that with refinement, the limited analysis time and cost penalty could enable rapid characterisation of not only high-value components, but higher throughput parts of lower value. Application of crystallographic characterisation to mass production strategies could inform design engineers and materials scientists for the avoidance of over-engineering, leading to savings in material or processing cost.

Besides rapidity, a key strength of the characterisation technique is versatility, whereby orientation dependent topographies can be applied to areas constrained solely by the nozzle geometry. There is no fundamental upper limit to analysis area. Considering ambient condition characterisation, and general technological miniaturisation trends, it is therefore not impossible to imagine a portable tool that will enable this process to characterise structural materials in-situ to directly observe environmental effects. In this regard, the benign electrolyte chemistries make the technique amenable to close operator contact.

Such applications require process improvement in terms of resolution, topography generation and compatible materials. The latter point will require an

acute knowledge of the orientation-dissolution reaction for a given material. In light of this, only cubic materials have been characterised by the technique. This is an important area of progress considering the widespread application of hexagonal materials such as titanium, which have more complex microstructures and will result in complicated orientation topographies.

In addition, the controllable etching process allows for topographies to be generated at different volumetric depths. This will enable the development of a 3D tomographic materials characterisation method, and could be applied to additively manufactured parts to appraise functional grading.

Within Chapter 5, the results demonstrated a strong topographic dependence on microstructure for dual-phase materials in regions where electropolishing mechanisms should dominate. This was proposed to result from the suppression of the diffusion layer at high jet velocity. Implicit in this suggestion is the impression that decreasing the jet velocity will enhance the development of polishing films, thus will likely decrease the roughness. Changing the flow velocity will also (detrimentally) affect processed feature form, therefore consideration of the design intent is important when selecting the operational parameters. In addition, it is proposed that for certain materials, where quenching from high temperatures freezes metastable single-phase compositions, EJP can be applied to generate low roughness features of high dimensional accuracy. Considering single-phase materials can be inferior in terms of conventional mechanical properties, a post-EJP tempering stage could be applied to acquire the desired bulk microstructure, whilst retaining the excellent processing characteristic of the single phase. Furthermore, the application of EJP to create robust abrasive surfaces can be envisaged, such

as through processing conventional machining tooling like cutters and bits. For example, hard WC phases can be revealed from a cobalt matrix in a conventional WC-Co material, leading to a WC-rich cutting surface, while retaining the same overall toughness of the cutting bit. In the same manner, EJP could readily be applied to selectively dress conventional tooling.

Chapter 6 demonstrated novel jet-specific removal phenomena. The ability to generate fractal-type surface structuring at length scales not previously reported in EJP is worthy of further investigation. Such fractal microchannel morphologies appear to mimic natural fluid transport systems, for example efficient vascular networks that have been refined by billions of years of natural selection. The ability to rapidly create these fractal architectures could revolutionise microfluidic transport efficiency and therefore could be applied to an array of different processes, for example the generation of proton exchange membrane fuel cells (PEMFCs). PEMFC usage is largely limited by the material type (generally graphite), which is difficult to conventionally process due to low toughness. This brittle nature also inhibits widespread automotive application. Lightweight materials, such as titanium alloys could provide the stiffness and strength desirable, but application is currently limited by manufacturing speed. Through appropriate electrolyte selection, EJP could be applied to rapidly impart microchannels of stochastic fractal geometries associated with more effective fluid transport. The toughness of metals will enable PEMFC architectures to be applied to thinner bipolar plates, which will enhance the achievable power density of these fuel cells, where transport and heat transfer efficiency is vastly improved through fractal vascular networks.

Plasma electrolytic oxides (PEOs), such as those generated in-jet in Chapter 7, have been demonstrated to affect the mechanical and fluid-facing properties of titanium surfaces. In this thesis, a route through which valve metals can be selectively hard-faced has been demonstrated. Metals such as titanium, aluminium and magnesium are characterised by poor tribological properties. Considering the drive towards light-weighting of mechanical parts in automotive and aerospace sectors, the ability to selectively enhance the wear properties and hardness of such materials is a research area of sustained interest. Such surfaces also have been applied to enhance the biocompatibility of implant materials, such as titanium and magnesium. The latter is of particular interest towards in-vivo biodegradable implants, whereby control over the corrosion properties (through selective oxidation) will enable modulation of the in-vivo lifetime of a given biodegradable implant.

Future work in this area will involve the adapting the electrolyte system to incorporate into the PEO coating, discrete species that will change the functional or mechanical properties of the surface. Conventionally within PEO processing strategies, this is achieved through soluble additions to the electrolyte, for example sodium silicate Na_2SiO_3, which can result in very hard quartz-type species within the coating. Given the capability of EJP to project nanoparticle chemistries onto the processed surface, insoluble SiO_2 or graphene nanoparticles could easily be applied into the PEO processing strategy. This will undoubtedly influence the crystallisation of other expected oxide phases such as rutile, and should be explored further.

References

[1] B. Bhattacharyya, Chapter 2 - Electrochemical Machining: Macro to Micro, Electrochemical Micromachining for Nanofabrication, MEMS and Nanotechnology, William Andrew Publishing2015, pp. 25-52.
[2] J. Mitchell-Smith, J.W. Murray, M. Kunieda, A.T. Clare, Electrolyte Jet Machining for Surface Texturing of Inconel 718, in: D. Bahre, A. Rebschlager (Eds.) INSECT, Saarbrucken, 2014, pp. 111-118.
[3] F. Klocke, A. Klink, D. Veselovac, D.K. Aspinwall, S.L. Soo, M. Schmidt, J. Schilp, G. Levy, J.-P. Kruth, Turbomachinery component manufacture by application of electrochemical, electro-physical and photonic processes, CIRP Annals - Manufacturing Technology 63(2) (2014) 703-726.
[4] A. de Silva, J.A. McGeough, Surface Effects on Alloys Drilled by Electrochemical Arc Machining, Proceedings of the Institution of Mechanical Engineers, Part B: Management and engineering manufacture 200(4) (1986) 237-246.
[5] G. Bussu, P.E. Irving, The role of residual stress and heat affected zone properties on fatigue crack propagation in friction stir welded 2024-T351 aluminium joints, International Journal of Fatigue 25(1) (2003) 77-88.
[6] J. Joffe, Boiling-point elevation, Journal of Chemical Education 22(6) (1945) 270-272.
[7] A.K.M. De Silva, P.T. Pajak, J.A. McGeough, D.K. Harrison, Thermal effects in laser assisted jet electrochemical machining, CIRP Annals - Manufacturing Technology 60(1) (2011) 243-246.
[8] D. Graham, Electro-Chemical Deburring, in: S.A. Tobias (Ed.), Proceedings of the Twentieth International Machine Tool Design and Research Conference: Sub-Conference on Electrical Processes, Palgrave Macmillan UK, London, 1980, pp. 613-616.
[9] M. Kunieda, R. Katoh, Y. Mori, Rapid Prototyping by Selective Electrodeposition Using Electrolyte Jet, CIRP Annals - Manufacturing Technology 47(1) (1998) 161-164.
[10] H. Goel, P.M. Pandey, Performance evaluation of different variants of jet electrochemical micro-drilling process, Proceedings of the Institution of Mechanical Engineers, Part B: Journal of Engineering Manufacture (2016) 1-14.
[11] M. H.-Oschätzchen, A. Martin, G. Meichsner, M. Kowalick, H. Zeidler, A. Schubert, Inverse Jet Electrochemical Machining for Functional Edge Shaping of Micro Bores, Procedia CIRP 6 (2013) 378-383.
[12] N. Guglielmi, Kinetics of the Deposition of Inert Particles from Electrolytic Baths, Journal of The Electrochemical Society 119(8) (1972) 1009-1012.
[13] M. Faraday, Experimental Researches in Electricity. Fourth Series, Philosophical Transactions of the Royal Society of London 123 (1833) 507-522.
[14] B. Kabanov, R. Burstein, A. Frumkin, Kinetics of electrode processes on the iron electrode, Discussions of the Faraday Society 1(0) (1947) 259-269.
[15] H. Helmholtz, Studien über electrische Grenzschichten, Annalen der Physik 243(7) (1879) 337-382.
[16] R.J. Leese, A. Ivanov, Electrochemical micromachining: An introduction, Advances in Mechanical Engineering 8(1) (2016) 1687814015626860.
[17] J.P. Hunt, Metal Ions in Aqueous Solution, W. A. Benjamin, Inc., New York, 1963.
[18] P.A. Jacquet, On the Anodic Behavior of Copper in Aqueous Solutions of Orthophosphoric Acid, Transactions of The Electrochemical Society 69(1) (1936) 629-655.
[19] J. Edwards, The Mechanism of Electropolishing of Copper in Phosphoric Acid Solutions: I . Processes Preceding the Establisment of Polishing Conditions, Journal of The Electrochemical Society 100(7) (1953) 189C-194C.
[20] C. Wagner, Contribution to the Theory of Electropolishing, Journal of The Electrochemical Society 101(5) (1954) 225-228.
[21] C. Karakus, D.T. Chin, Metal Distribution in Jet Plating, Journal of The Electrochemical Society 141(3) (1994) 691-697.
[22] D. Landolt, Fundamental aspects of electropolishing, Electrochimica Acta 32(1) (1987) 1-11.
[23] K.W. Mao, M.A. LaBoda, J.P. Hoare, Anodic Film Studies on Steel in Nitrate-Based Electrolytes for Electrochemical Machining, Journal of The Electrochemical Society 119(4) (1972) 419-427.

[24] W. Natsu, T. Ikeda, M. Kunieda, Generating complicated surface with electrolyte jet machining, Precision Engineering 31(1) (2007) 33-39.
[25] J. Mitchell-Smith, A.T. Clare, ElectroChemical Jet Machining of Titanium: Overcoming Passivation Layers with Ultrasonic Assistance, Procedia CIRP 42 (2016) 379-383.
[26] R. Ippolito, S. Tornincasa, G. Capello, G.F. Micheletti, Electron-Jet Drilling — Basic Involved Phenomena, CIRP Annals - Manufacturing Technology 30(1) (1981) 87-90.
[27] M.S. Rajput, P.M. Pandey, S. Jha, Modelling of high speed selective jet electrodeposition process, Journal of Manufacturing Processes 17 (2015) 98-107.
[28] W. Wang, S.Q. Qian, X.Y. Zhou, Microstructure and oxidation-resistant of ZrO2/Ni coatings applied by high-speed jet electroplating, Journal of Materials Science 45(6) (2010) 1617-1621.
[29] R.G. Ehl, A.J. Ihde, Faraday's electrochemical laws and the determination of equivalent weights, Journal of Chemical Education 31(5) (1954) 226-232.
[30] J.W.M. Bush, J.M. Aristoff, A.E. Hosoi, An experimental investigation of the stability of the circular hydraulic jump, Journal of Fluid Mechanics 558 (2006) 33-52.
[31] M. Hackert, G. Meichsner, A. Schubert, Fast Micro Structuring with Electrolyte Jet Machining, 4th International Symposium on Electrochemical Machining Technology, Chemnitz, 2007.
[32] F.M. White, Fluid Mechanics, 7th ed., The McGraw-Hill Companies, Inc., New York, 2010.
[33] M. Hackert, G. Meichsner, A. Schubert, Generating Micro Geometries with Air Assisted Jet Electrochemical Machining, EUSPEN 8th International Conference, Zurich, 2008.
[34] R.C. Alkire, T.J. Chen, High-Speed Selective Electroplating with Single Circular Jets, Journal of The Electrochemical Society 129(11) (1982) 2424-2432.
[35] L.A. Romero, F.M. Dickey, Lossless laser beam shaping, J. Opt. Soc. Am. A 13(4) (1996) 751-760.
[36] L. Quan, W.J.D. A., Prediction of electrodeposition rates from an impinging jet, AIChE Journal 42(2) (1996) 391-404.
[37] M. Datta, L.T. Romankiw, D.R. Vigliotti, R.J. von Gutfeld, Jet and Laser-Jet Electrochemical Micromachining of Nickel and Steel, Journal of The Electrochemical Society 136(8) (1989) 2251-2256.
[38] K. Yoneda, M. Kunieda, Numerical Analysis of Cross Sectional Shape of Micro-Indents Formed by the Electrochemical Jet Machining (ECJM), Journal of The Japan Society of Electrical Machining Engineers 29(62) (1995) 1-8.
[39] J. Kozak, K.P. Rajurkar, R. Balkrishna, Study of Electrochemical Jet Machining Process, Journal of Manufacturing Science and Engineering 118(4) (1996) 490-498.
[40] M. Hackert, G. Meichsner, A. Schubert, Simulation of the Shape of Micro Geometries generated with Jet Electrochemical Machining, COMSOL Conference Hannover, 2008.
[41] J.F. Wilson, Practice and Theory of Electrochemical Machining, Wiley-Interscience, New York, 1971.
[42] M.G. Fouad, G.H. Sedahmed, Effect of gas evolution on the rate of mass transfer at vertical electrodes, Electrochimica Acta 17(4) (1972) 665-672.
[43] K.P. Rajurkar, D. Zhu, J.A. McGeough, J. Kozak, A. De Silva, New Developments in Electro-Chemical Machining, CIRP Annals - Manufacturing Technology 48(2) (1999) 567-579.
[44] J.A. McGeough, Advanced Methods of Machining, Chapman and Hall Ltd., UK, 1988.
[45] P. Delahay, M. Pourbaix, P.V. Rysselberghe, Potential-pH Diagram of Lead and its Applications to the Study of Lead Corrosion and to the Lead Storage Battery, Journal of The Electrochemical Society 98(2) (1951) 57-64.
[46] M. Pourbaix, Thermodynamics and corrosion, Corrosion Science 30(10) (1990) 963-988.
[47] M. Pourbaix, Significance of Protection Potential in Pitting and Intergranular Corrosion, CORROSION 26(10) (1970) 431-438.
[48] A. Nannichi, 1st Report : Experimental Study on the Electrolytic Nozzling Micro-holes in Copper Study on the Electrolytic Process of Nozzling Micro-holes in Metals, Journal of the Japan Society of Precision Engineering 27(323) (1961) 781-787.
[49] G.R. Booker, R. Stickler, Large-Area “Jet” Electrolytic Polishing of Ge and Si, Journal of The Electrochemical Society 109(12) (1962) 1167-1171.
[50] M. Sen, H.S. Shan, A review of electrochemical macro- to micro-hole drilling processes, International Journal of Machine Tools and Manufacture 45(2) (2005) 137-152.
[51] A. Spieser, A. Ivanov, Recent developments and research challenges in electrochemical micromachining (μECM), The International Journal of Advanced Manufacturing Technology 69(1) (2013) 563-581.

[52] B. Bhattacharyya, M. Malapati, J. Munda, Experimental study on electrochemical micromachining, Journal of Materials Processing Technology 169(3) (2005) 485-492.
[53] J.D. Whitaker, J.B. Nelson, D.T. Schwartz, Electrochemical printing: software reconfigurable electrochemical microfabrication, Journal of Micromechanics and Microengineering 15(8) (2005) 1498-1503.
[54] B. Bhattacharyya, Chapter 7 - Influencing Factors of EMM, Electrochemical Micromachining for Nanofabrication, MEMS and Nanotechnology, William Andrew Publishing2015, pp. 123-143.
[55] D. Landolt, Throwing Power Measurements during High Rate Nickel Dissolution under Active and Transpassive Conditions, Journal of The Electrochemical Society 119(6) (1972) 708-712.
[56] J. Bannard, On the electrochemical machining of some titanium alloys in bromide electrolytes, Journal of Applied Electrochemistry 6(6) (1976) 477-483.
[57] I. Dugdale, J.B. Cotton, The anodic polarization of titanium in halide solutions, Corrosion Science 4(1) (1964) 397-411.
[58] M. Hackert-Oschätzchen, A. Martin, G. Meichsner, M. Zinecker, A. Schubert, Microstructuring of carbide metals applying Jet Electrochemical Machining, Precision Engineering 37(3) (2013) 621-634.
[59] G.S. Kelsey, The Anodic Oxidation of Tungsten in Aqueous Base, Journal of The Electrochemical Society 124(6) (1977) 814-819.
[60] M. Datta, D. Harris, Electrochemical micromachining: An environmentally friendly, high speed processing technology, Electrochimica Acta 42(20) (1997) 3007-3013.
[61] Y. Yang, W. Natsu, W. Zhao, Realization of eco-friendly electrochemical micromachining using mineral water as an electrolyte, Precision Engineering 35(2) (2011) 204-213.
[62] S.H. Ryu, Micro fabrication by electrochemical process in citric acid electrolyte, Journal of Materials Processing Technology 209(6) (2009) 2831-2837.
[63] Y. Zhao, M. Kunieda, N. Obi, S. Watanabe, Development of electrolyte filtration system for ECM taking into account removal of chromium (VI) ions, Precision Engineering 49 (2017) 211-219.
[64] L.H. Shu, K. Ueda, I. Chiu, H. Cheong, Biologically inspired design, CIRP Annals - Manufacturing Technology 60(2) (2011) 673-693.
[65] K. Liu, L. Jiang, Bio-inspired design of multiscale structures for function integration, Nano Today 6(2) (2011) 155-175.
[66] X. Liu, P.K. Chu, C. Ding, Surface nano-functionalization of biomaterials, Materials Science and Engineering: R: Reports 70(3-6) (2010) 275-302.
[67] B. Mete, G.-R. Tatiana, S. Peter, Influence of Surface Topography on Heat Transfer in Shear-Driven Liquid Films, Journal of Physics: Conference Series 395(1) (2012) 12164-12173.
[68] T. Kawanaka, S. Kato, M. Kunieda, J.W. Murray, A.T. Clare, Selective Surface Texturing Using Electrolyte Jet Machining, Procedia CIRP 13 (2014) 345-349.
[69] M. Hackert-Oschätzchen, G. Meichsner, M. Zinecker, A. Martin, A. Schubert, Micro machining with continuous electrolytic free jet, Precision Engineering 36(4) (2012) 612-619.
[70] M. Sen, H.S. Shan, Analysis of hole quality characteristics in the electro jet drilling process, International Journal of Machine Tools and Manufacture 45(15) (2005) 1706-1716.
[71] T. Ikeda, W. Natsu, M. Kunieda, Electrolyte Jet Machining Using Multiple Nozzles, Journal of The Japan Society of Electrical Machining Engineers 40(94) (2006) 82-89.
[72] D.T. Ardi, Y.G. Li, K.H.K. Chan, L. Blunt, M.R. Bache, Surface topography and the impact on fatigue performance, Surface Topography: Metrology and Properties 3(1) (2015) 15007-15023.
[73] E.S. Gadelmawla, M.M. Koura, T.M.A. Maksoud, I.M. Elewa, H.H. Soliman, Roughness parameters, Journal of Materials Processing Technology 123(1) (2002) 133-145.
[74] T. Kawanaka, S. Kato, M. Kunieda, J.W. Murray, A.T. Clare, Micro Textured Surface Created by Electrolyte Jet Machining, ASPEN Taiwan, 2013.
[75] M. Sen, H.S. Shan, Electro jet drilling using hybrid NNGA approach, Robotics and Computer-Integrated Manufacturing 23(1) (2007) 17-24.
[76] T. Kawanaka, M. Kunieda, Mirror-like finishing by electrolyte jet machining, CIRP Annals - Manufacturing Technology 64(1) (2015) 237-240.
[77] M. Hackert-Oschätzchen, R. Paul, M. Kowalick, A. Martin, G. Meichsner, A. Schubert, Multiphysics Simulation of the Material Removal in Jet Electrochemical Machining, in: V. Schulze (Ed.) 15th CIRP Conference on Modelling of Machining Operations (15th CMMO), Karlsruhe, 2015, pp. 197-202.

[78] B. Bhattacharyya, Chapter 3 - Principle of Material Removal in Electrochemical Micromachining, Electrochemical Micromachining for Nanofabrication, MEMS and Nanotechnology, William Andrew Publishing2015, pp. 53-67.
[79] J. Kozak, M. Zybura-Skrabalak, Some Problems of Surface Roughness in Electrochemical Machining (ECM), Procedia CIRP 42 (2016) 101-106.
[80] J.V. Macpherson, M.A. Beeston, P.R. Unwin, Imaging local mass-transfer rates within an impinging jet and studies of fast heterogeneous electron-transfer kinetics using the microjet electrode, Journal of the Chemical Society, Faraday Transactions 91(5) (1995) 899-904.
[81] K.P. Rajurkar, D. Zhu, B. Wei, Minimization of Machining Allowance in Electrochemical Machining, CIRP Annals 47(1) (1998) 165-168.
[82] M. Hackert-Oschätzchen, G. Meichsner, H. Zeidler, M. Zinecker, A. Schubert, Micro Machining of Different Steels with Closed Electrolytic Free Jet, AIP Conference Proceedings 1353(1) (2011) 1337-1343.
[83] K. Miyoshi, M. Kunieda, Fabrication of Micro Rods of Cemented Carbide by Electrolyte Jet Turning, 18th CIRP Conference on Electro Physical and Chemical Machining (ISEM XVIII), Tokyo, 2016, pp. 373-378.
[84] W. Liu, S. Ao, Y. Li, Z. Liu, H. Zhang, S.M. Manladan, Z. Luo, Z. Wang, Effect of Anodic Behavior on Electrochemical Machining of TB6 Titanium Alloy, Electrochimica Acta 233 (2017) 190-200.
[85] K.P. Rajurkar, B. Wei, J. Kozak, J.A. McGeough, Modelling and Monitoring Interelectrode Gap in Pulse Electrochemical Machining, CIRP Annals 44(1) (1995) 177-180.
[86] D. Landolt, P.F. Chauvy, O. Zinger, Electrochemical micromachining, polishing and surface structuring of metals: fundamental aspects and new developments, Electrochimica Acta 48(20) (2003) 3185-3201.
[87] R. Schuster, V. Kirchner, P. Allongue, G. Ertl, Electrochemical Micromachining, Science 289(5476) (2000) 98-101.
[88] T. Haisch, E. Mittemeijer, J.W. Schultze, Electrochemical machining of the steel 100Cr6 in aqueous NaCl and NaNO3 solutions: microstructure of surface films formed by carbides, Electrochimica Acta 47(1–2) (2001) 235-241.
[89] F. Klocke, S. Harst, M. Zeis, A. Klink, Energetic Analysis of the Anodic Double Layer During Electrochemical Machining of 42CrMo4 Steel, Procedia CIRP 42 (2016) 396-401.
[90] M. Datta, D. Landolt, Surface Brightening during High Rate Nickel Dissolution in Nitrate Electrolytes, Journal of The Electrochemical Society 122(11) (1975) 1466-1472.
[91] Z. Liu, H. Nouraei, M. Papini, J.K. Spelt, Abrasive enhanced electrochemical slurry jet micro-machining: Comparative experiments and synergistic effects, Journal of Materials Processing Technology 214(9) (2014) 1886-1894.
[92] B. Lauwers, J.P. Kruth, K.P. Rajurkar, M.M. Sundaram, A.P. Malshe, Review of Electrochemical and Electrodischarge Machining, Proceedings of the Seventeenth CIRP Conference on Electro Physical and Chemical Machining (ISEM), Leuven, 2013, pp. 13-26.
[93] M.M. Lohrengel, K.P. Rataj, T. Münninghoff, Electrochemical Machining—mechanisms of anodic dissolution, Electrochimica Acta 201 (2016) 348-353.
[94] H. Zhang, J. Xu, J. Wang, Investigation of a novel hybrid process of laser drilling assisted with jet electrochemical machining, Optics and Lasers in Engineering 47(11) (2009) 1242-1249.
[95] E.-S. Lee, Machining Characteristics of the Electropolishing of Stainless Steel (STS316L), The International Journal of Advanced Manufacturing Technology 16(8) (2000) 591-599.
[96] D. Landolt, R.H. Müller, C.W. Tobias, High Rate Anodic Dissolution of Copper, Journal of The Electrochemical Society 116(10) (1969) 1384-1390.
[97] M. Weinmann, M. Stolpe, O. Weber, R. Busch, H. Natter, Electrochemical dissolution behaviour of Ti90Al6V4 and Ti60Al40 used for ECM applications, Journal of Solid State Electrochemistry 19(2) (2015) 485-495.
[98] P.T. Pajak, A.K.M. Desilva, D.K. Harrison, J.A. McGeough, Precision and efficiency of laser assisted jet electrochemical machining, Precision Engineering 30(3) (2006) 288-298.
[99] A.K.M. DeSilva, P.T. Pajak, D.K. Harrison, J.A. McGeough, Modelling and Experimental Investigation of Laser Assisted Jet Electrochemical Machining, CIRP Annals - Manufacturing Technology 53(1) (2004) 179-182.
[100] P.T. Pajak, A.K.M. De Silva, J.A. McGeough, D.K. Harrison, Modelling the aspects of precision and efficiency in laser-assisted jet electrochemical machining (LAJECM), Journal of Materials Processing Technology 149(1–3) (2004) 512-518.

[101] R.J. von Gutfeld, M.H. Gelchinski, L.T. Romankiw, D.R. Vigliotti, Laser-enhanced jet plating: A method of high-speed maskless patterning, Applied Physics Letters 43(9) (1983) 876-878.
[102] Z. Zhang, M. Cai, Q. Feng, Y. Zeng, Comparison of different laser-assisted electrochemical methods based on surface morphology characteristics, The International Journal of Advanced Manufacturing Technology 71(1-4) (2013) 565-571.
[103] D. Nicoara, A. Hedes, I. Sora, Ultrasonic Enhancement of an Electrochemical Machining Process 5th WSEAS International Conference on Applications of Electrical Engineering, Prague, 2006, pp. 213-218.
[104] S. Skoczypiec, Research on ultrasonically assisted electrochemical machining process, The International Journal of Advanced Manufacturing Technology 52(5) (2011) 565-574.
[105] C. Madore, D. Landolt, Electrochemical micromachining of controlled topographies on titanium for biological applications, Journal of Micromechanics and Microengineering 7(4) (1997) 270-275.
[106] D. Baehre, A. Ernst, K. Weißhaar, H. Natter, M. Stolpe, R. Busch, Electrochemical Dissolution Behavior of Titanium and Titanium-based Alloys in Different Electrolytes, Procedia CIRP 42 (2016) 137-142.
[107] X. Lu, Y. Leng, Electrochemical micromachining of titanium surfaces for biomedical applications, Journal of Materials Processing Technology 169(2) (2005) 173-178.
[108] W. Liu, S. Ao, Y. Li, Z. Liu, Z. Wang, Z. Luo, Z. Wang, R. Song, Jet electrochemical machining of TB6 titanium alloy, The International Journal of Advanced Manufacturing Technology 90(5) (2017) 2397-2409.
[109] F. Wang, J. Zhao, Y. Lv, Z. Yang, J. Yao, Y. He, Z. Tian, Electrochemical machining of deep narrow slits on TB6 titanium alloys, The International Journal of Advanced Manufacturing Technology 92(5) (2017) 3063-3071.
[110] C.J. Park, M.M. Lohrengel, T. Hamelmann, M. Pilaski, H.S. Kwon, Grain-dependent passivation of surfaces of polycrystalline zinc, Electrochimica Acta 47(21) (2002) 3395-3399.
[111] J.H. Seo, J.-H. Ryu, D.N. Lee, Formation of Crystallographic Etch Pits during AC Etching of Aluminum, Journal of The Electrochemical Society 150(9) (2003) B433-B438.
[112] M. Schneider, S. Schroth, S. Richter, S. Höhn, N. Schubert, A. Michaelis, In-situ investigation of the interplay between microstructure and anodic copper dissolution under near-ECM conditions – Part 1: The active state, Electrochimica Acta 56(22) (2011) 7628-7636.
[113] A. Schreiber, C. Rosenkranz, M.M. Lohrengel, Grain-dependent anodic dissolution of iron, Electrochimica Acta 52(27) (2007) 7738-7745.
[114] S. Ye, C. Ishibashi, K. Uosaki, Anisotropic Dissolution of an Au(111) Electrode in Perchloric Acid Solution Containing Chloride Anion Investigated by in Situ STMThe Important Role of Adsorbed Chloride Anion, Langmuir 15(3) (1999) 807-812.
[115] M. Zamin, M.B. Ives, Effect of Chloride Ion Concentration on the Anodic Dissolution Behavior of Nickel, CORROSION 29(8) (1973) 319-324.
[116] T.R. Beck, Pitting of Titanium: II . One-Dimensional Pit Experiments, Journal of The Electrochemical Society 120(10) (1973) 1317-1324.
[117] E. Martinez-Lombardia, V. Maurice, L. Lapeire, I. De Graeve, K. Verbeken, L. Kestens, P. Marcus, H. Terryn, In Situ Scanning Tunneling Microscopy Study of Grain-Dependent Corrosion on Microcrystalline Copper, The Journal of Physical Chemistry C 118(44) (2014) 25421-25428.
[118] M. Schneider, S. Schroth, S. Richter, S. Höhn, N. Schubert, A. Michaelis, In-situ investigation of the interplay between microstructure and anodic copper dissolution under near-ECM conditions—Part 2: The transpassive state, Electrochimica Acta 70 (2012) 76-83.
[119] M. Schneider, S. Schroth, N. Schubert, A. Michaelis, In-situ investigation of the surface-topography during anodic dissolution of copper under near-ECM conditions, Materials and Corrosion 63(2) (2012) 96-104.
[120] K. Kinoshita, D. Landolt, R.H. Muller, C.W. Tobias, Stoichiometry of Anodic Copper Dissolution at High Current Densities, Journal of The Electrochemical Society 117(10) (1970) 1246-1251.
[121] H. Kaesche, Microtunnelling during selective alloy dissolution and during pitting, Materials and Corrosion 39(4) (1988) 153-161.
[122] J.P. Hoare, Oxide Film Studies on Iron in Electrochemical Machining Electrolytes, Journal of The Electrochemical Society 117(1) (1970) 142-145.
[123] D.V.V. Moll, R.C. Salvarezza, H.A. Videla, A.J. Arvia, The Pitting Corrosion of Nickel in Different Electrolyte Solutions Containing Chloride Ions, Journal of The Electrochemical Society 132(4) (1985) 754-760.

[124] Z. Szklarska-Smialowska, Review of Literature on Pitting Corrosion Published Since 1960, CORROSION 27(6) (1971) 223-233.
[125] J.M. Kolotyrkin, Pitting Corrosion of Metals, CORROSION 19(8) (1963) 261t-268t.
[126] C.A. Coughanowr, B.A. Dissaux, R.H. Muller, C.W. Tobias, Electrochemical machining of refractory materials, Journal of Applied Electrochemistry 16(3) (1986) 345-356.
[127] H. T., M.E. J., S.J. W., On the influence of microstructure and carbide content of steels on the electrochemical dissolution process in aqueous NaCl-electrolytes, Materials and Corrosion 53(10) (2002) 740-755.
[128] F. Klocke, S. Harst, F. Karges, M. Zeis, A. Klink, Modeling of the Electrochemical Dissolution Process for a Two-phase Material in a Passivating Electrolyte System, Procedia CIRP 58 (2017) 169-174.
[129] B. Walther, J. Schilm, A. Michaelis, M.M. Lohrengel, Electrochemical dissolution of hard metal alloys, Electrochimica Acta 52(27) (2007) 7732-7737.
[130] K. Mizugai, N. Shibuya, M. Kunieda, Study on Electrolyte Jet Machining of Cemented Carbide, International Journal of Electrical Machining 18 (2013) 23-28.
[131] Z. Liu, H. Nouraei, J.K. Spelt, M. Papini, Electrochemical slurry jet micro-machining of tungsten carbide with a sodium chloride solution, Precision Engineering 40 (2015) 189-198.
[132] J.C. Walker, T.J. Kamps, J.W. Lam, J. Mitchell-Smith, A.T. Clare, Tribological behaviour of an electrochemical jet machined textured Al-Si automotive cylinder liner material, Wear 376–377, Part B (2017) 1611-1621.
[133] C. Rotty, A. Mandroyan, M.L. Doche, J.Y. Hihn, Electropolishing of CuZn brasses and 316L stainless steels: Influence of alloy composition or preparation process (ALM vs. standard method), Surface and Coatings Technology 307 (2016) 125-135.
[134] M. Burger, L. Koll, E.A. Werner, A. Platz, Electrochemical machining characteristics and resulting surface quality of the nickel-base single-crystalline material LEK94, Journal of Manufacturing Processes 14(1) (2012) 62-70.
[135] X. Wang, N. Qu, P. Guo, X. Fang, X. Lin, Electrochemical Machining Properties of the Laser Rapid Formed Inconel 718 Alloy in NaNO3 Solution, Journal of The Electrochemical Society 164(14) (2017) E548-E559.
[136] F. Klocke, S. Harst, L. Ehle, M. Zeis, A. Klink, Surface integrity in electrochemical machining processes: An analysis on material modifications occurring during electrochemical machining, Proceedings of the Institution of Mechanical Engineers, Part B: Journal of Engineering Manufacture 232(4) (2018) 578-585.
[137] O.V. Krishnaiah Chetty, V. Radhakrishnan, A study on the influence of grain size in electrochemical machining, International Journal of Machine Tool Design and Research 21(1) (1981) 57-69.
[138] M. H.-Oschätzchen, N. Lehnert, M. Kowalick, C. Scherf, A. Martin, A. Schubert, Analysis of an Electrochemical Machining Process for Particle Reinforced Aluminium Matrix Composites 2016 COMSOL Conference, Munich, 2016, pp. 1-5.
[139] D. Melisova, B. Weiss, R. Stickler, Nucleation of persistent slip bands in Cu single crystals under stress controlled cycling, Scripta Materialia 36(9) (1997) 1061-1066.
[140] A. Martin, M. Hackert-Oschätzchen, N. Lehnert, A. Schubert, Analysis of the fundamental removal geometry in electrochemical profile turning with continuous electrolytic free jet, Procedia CIRP 68 (2018) 466-470.
[141] A. Schubert, M. Hackert, G. Meichsner, M. Zinecker, A. Martin, Evaluation of the Influence of the Electric Potential in Jet Electrochemical Machining 7th International Conference on Electrochemical Machining Technology, Vienna, 2011, pp. 47-54.
[142] W. Natsu, S. Ooshiro, M. Kunieda, Research on generation of three-dimensional surface with micro-electrolyte jet machining, CIRP Journal of Manufacturing Science and Technology 1(1) (2008) 27-34.
[143] D.T. Chin, C.H. Tsang, Mass Transfer to an Impinging Jet Electrode, Journal of The Electrochemical Society 125(9) (1978) 1461-1470.
[144] M. H.-Oschätzchen, A. Martin, G. Meichsner, A. Schubert, Analysis of strategies for gap control in jet electrochemical machining, in: R. Leach (Ed.) 14th International Conference & Exhibition of the European Society of Precision Engineering and Nanotechnology 2014, Dubrovnik, 2014, pp. 439-442.
[145] M.Y. Zanjani, H. Zeidler, A. Martin, A. Schubert, Application of laser scanning as a Pre-machining metrology technique in Jet-ECM, Proceedings of the 17th International Conference of the European Society for Precision Engineering and Nanotechnology, EUSPEN 2017, 2017, pp. 185-186.

[146] Z. Liu, C. Gao, K. Zhao, K. Wang, Machining of microchannel at SS316 surface using abrasive-assisted electrochemical jet machining, The International Journal of Advanced Manufacturing Technology 95(1) (2018) 1143-1152.
[147] A. Malik, A. Manna, Investigation on the laser-assisted jet electrochemical machining process for improvement in machining performance, The International Journal of Advanced Manufacturing Technology 96(9) (2018) 3917-3932.
[148] M. Kunieda, K. Mizugai, S. Watanabe, N. Shibuya, N. Iwamoto, Electrochemical micromachining using flat electrolyte jet, CIRP Annals - Manufacturing Technology 60(1) (2011) 251-254.
[149] G. Mayank, C. Fuchen, K. Masanori, Analysis of Reactions Determining Current Efficiency in Electrochemical Machining, Procedia CIRP 68 (2018) 511-516.
[150] S.M. Zhu, C. Larsson, J. Bannard, On the Use of Dilute Solutions as ECM Electrolytes, 7th International Symposium on Electrochemical Machining, Birmingham, 1983, pp. 405-415.
[151] A.K.M. De Silva, H.S.J. Altena, J.A. McGeough, Influence of Electrolyte Concentration on Copying Accuracy of Precision-ECM, CIRP Annals - Manufacturing Technology 52(1) (2003) 165-168.
[152] S.D. Dhobe, B. Doloi, B. Bhattacharyya, Surface characteristics of ECMed titanium work samples for biomedical applications, The International Journal of Advanced Manufacturing Technology 55(1) (2011) 177-188.
[153] M. Hackert, G. Meichsner, S. Jahn, A. Schubert, Investigating the Influence of Dynamic Jet Shapes on the Jet Electrochemical Machining Process, COMSOL Conference, Paris, 2010.
[154] M. Hackert-Oschätzchen, R. Paul, A. Martin, G. Meichsner, N. Lehnert, A. Schubert, Study on the dynamic generation of the jet shape in Jet Electrochemical Machining, Journal of Materials Processing Technology 223 (2015) 240-251.
[155] B. Lauwers, F. Klocke, A. Klink, A.E. Tekkaya, R. Neugebauer, D. McIntosh, Hybrid processes in manufacturing, CIRP Annals - Manufacturing Technology 63(2) (2014) 561-583.
[156] M.H. Gelchinski, L.T. Romankiw, D.R. Vigliotti, R.J. von Gutfeld, Electrochemical and Metallurgical Aspects of Laser-Enhanced Jet Plating of Gold, Journal of The Electrochemical Society 132(11) (1985) 2575-2581.
[157] A. Malik, A. Manna, Study on Precision Microholes Using Pulsed Laser with Jet Electrochemical Machining, Arabian Journal for Science and Engineering (2017) 4593-4608.
[158] H. Zhang, J.W. Xu, J.M. Wang, Green Laser Drilling Assisted with Jet Electrochemical Machining of Nickel-Based Superalloy, Key Engineering Materials 426-427 (2010) 75-80.
[159] M. Hackert-Oschätzchen, N. Lehnert, A. Martin, A. Schubert, Jet Electrochemical Machining of Particle Reinforced Aluminum Matrix Composites with Different Neutral Electrolytes, IOP Conference Series: Materials Science and Engineering 118(1) (2016) 12036-12042.
[160] N. Lehnert, M. Hackert-Oschätzchen, A. Martin, A. Schubert, Derivation of Guidelines for Reliable Finishing of Aluminium Matrix Composites by Jet Electrochemical Machining, Procedia CIRP 68 (2018) 471-476.
[161] A.A.G. Bruzzone, H.L. Costa, P.M. Lonardo, D.A. Lucca, Advances in engineered surfaces for functional performance, CIRP Annals - Manufacturing Technology 57(2) (2008) 750-769.
[162] W.F. Cui, L. Jin, L. Zhou, Surface characteristics and electrochemical corrosion behavior of a pre-anodized microarc oxidation coating on titanium alloy, Materials science & engineering. C, Materials for biological applications 33(7) (2013) 3775-3779.
[163] N.P. Padture, M. Gell, E.H. Jordan, Thermal Barrier Coatings for Gas-Turbine Engine Applications, Science 296(5566) (2002) 280-284.
[164] F.A. Lowenheim, Electroplating, McGraw-Hill, USA, 1978.
[165] J.C. Fletcher, Scanning Nozzle Plating System, in: NASA (Ed.) USA, 1974.
[166] P.J. N., Apparatus for Electroplating Selected Areas, in: USPTO (Ed.) USA, 1969.
[167] R. Alkire, J.B. Ju, High Speed Selective Electroplating with Impinging Two-Dimensional Slot Jet Flow, Journal of The Electrochemical Society 134(2) (1987) 294-299.
[168] D.P. Barkey, R.H. Muller, C.W. Tobias, Roughness Development in Metal Electrodeposition: I . Experimental Results, Journal of The Electrochemical Society 136(8) (1989) 2199-2207.
[169] R. Winand, Electrocrystallization - theory and applications, Hydrometallurgy 29(1) (1992) 567-598.
[170] S.J. Dover, A.E.W. Rennie, G.R. Bennet, Rapid Prototyping using Electrodeposition of Copper, SFFF Symposium, University of Texas at Austin, 1996, pp. 191-198.

[171] C.E. Bocking, B. Cameron, The Use of High Speed Selective Jet Electrodeposition of Gold for the Plating of Connectors, Transactions of the IMF 72(1) (1994) 33-40.
[172] C.E. Bocking, High Speed Selective Jet Electroplating of Gold and Gold Alloys Using Single Circular Jets, Institute of Polymer and Materials Engineering, Loughborough Universtiy of Technology, Loughborough, 1994.
[173] M. De Vogelaere, V. Sommer, H. Springborn, U. Michelsen-Mohammadein, High-speed plating for electronic applications, Electrochimica Acta 47(1) (2001) 109-116.
[174] G. Qiao, T. Jing, N. Wang, Y. Gao, X. Zhao, J. Zhou, W. Wang, High-speed jet electrodeposition and microstructure of nanocrystalline Ni–Co alloys, Electrochimica Acta 51(1) (2005) 85-92.
[175] J.P. Celis, J.R. Roos, C. Buelens, A Mathematical Model for the Electrolytic Codeposition of Particles with a Metallic Matrix, Journal of The Electrochemical Society 134(6) (1987) 1402-1408.
[176] I. Corni, R.J. Chater, A.R. Boccaccini, M.P. Ryan, Electro co-deposition of Ni–Al2O3 composite coatings, Journal of Materials Science 47(14) (2012) 5361-5373.
[177] A. John Rethinam, G.N.K. Ramesh Bapu, R.M. Krishnan, Deposition of nickel–mica electrocomposites and characterisation, Materials Chemistry and Physics 85(2–3) (2004) 251-256.
[178] F.K. Sautter, Electrodeposition of Dispersion-Hardened Nickel - Al2 O 3 Alloys, Journal of The Electrochemical Society 110(6) (1963) 557-560.
[179] H. Takeuchi, Y. Tsunekawa, M. Okumiya, Formation of Compositionally Graded Ni-P Deposits Containing SiC Particles by Jet Electroplating, Materials Transactions, JIM 38(1) (1997) 43-48.
[180] S.J. Osborne, W.S. Sweet, K.S. Vecchio, J.B. Talbot, Electroplating of Copper–Alumina Nanocomposite Films with an Impinging Jet Electrode, Journal of The Electrochemical Society 154(8) (2007) D394-D399.
[181] S.J. Osborne, Electrocodeposition of nanoparticle composite films using an impinging jet electrode, Materials Science and Engineering, University of Californa, San Diego, San Diego, 2006.
[182] D. Thiemig, A. Bund, J.B. Talbot, Electrocodeposition of Nickel Nanocomposites Using an Impinging Jet Electrode, Journal of The Electrochemical Society 154(10) (2007) D510-D515.
[183] D. Thiemig, Investigation on the Mechanism of Electrocodeposition and the Structure-Properties Correlation of Nickel Nanocomposites Fakultät Mathematik und Naturwissenschaften, Technischen Universität Dresden, Dresden, 2008.
[184] D. Thiemig, A. Bund, J.B. Talbot, Model of Electrocodeposition Using an Unsubmerged Impinging Jet Electrode, Journal of The Electrochemical Society 155(12) (2008) D798-D804.
[185] A. Bund, D. Thiemig, Influence of bath composition and pH on the electrocodeposition of alumina nanoparticles and nickel, Surface and Coatings Technology 201(16) (2007) 7092-7099.
[186] J. Man, S. Zhang, J. Li, B. Zhao, Y. Chen, Effects of electrolyte pH on morphologies and mechanical properties of α-Al2O3/Ni composite coatings and role of zeta potentials in co-deposition process, Surface and Coatings Technology 249 (2014) 118-124.
[187] Y. Mori, M. Kunieda, Maskless Coloring of Titanium Alloy using Electrolyte Jet, JSEME Annual Meeting, 1997, pp. 13-16.
[188] D. Kuhn, A. Martin, C. Eckart, M. Sieber, R. Morgenstern, M. Hackert-Oschätzchen, T. Lampke, A. Schubert, Localised anodic oxidation of aluminium material using a continuous electrolyte jet, IOP Conference Series: Materials Science and Engineering 181(1) (2017) 12042-12051.
[189] A.L. Yerokhin, X. Nie, A. Leyland, A. Matthews, Characterisation of oxide films produced by plasma electrolytic oxidation of a Ti–6Al–4V alloy, Surface and Coatings Technology 130(2) (2000) 195-206.
[190] M. Sieber, F. Simchen, R. Morgenstern, I. Scharf, T. Lampke, Plasma Electrolytic Oxidation of High-Strength Aluminium Alloys—Substrate Effect on Wear and Corrosion Performance, Metals 8(5) (2018) 356-370.
[191] G. Barati Darband, M. Aliofkhazraei, P. Hamghalam, N. Valizade, Plasma electrolytic oxidation of magnesium and its alloys: Mechanism, properties and applications, Journal of Magnesium and Alloys 5(1) (2017) 74-132.
[192] A.L. Yerokhin, X. Nie, A. Leyland, A. Matthews, S.J. Dowey, Plasma electrolysis for surface engineering, Surface and Coatings Technology 122(2) (1999) 73-93.

[193] T. Mi, B. Jiang, Z. Liu, L. Fan, Plasma formation mechanism of microarc oxidation, Electrochimica Acta 123 (2014) 369-377.
[194] F. Jin, P.K. Chu, K. Wang, J. Zhao, A. Huang, H. Tong, Thermal stability of titania films prepared on titanium by micro-arc oxidation, Materials Science and Engineering: A 476(1) (2008) 78-82.
[195] Y.-K. Shin, W.-S. Chae, Y.-W. Song, Y.-M. Sung, Formation of titania photocatalyst films by microarc oxidation of Ti and Ti–6Al–4V alloys, Electrochemistry Communications 8(3) (2006) 465-470.
[196] Y.-T. Sul, The significance of the surface properties of oxidized titanium to the bone response: special emphasis on potential biochemical bonding of oxidized titanium implant, Biomaterials 24(22) (2003) 3893-3907.
[197] O.a.P.R. Group, How to clean a sample prior to lithography. http://optics.eee.nottingham.ac.uk/wiki/How_to_clean_a_sample_prior_to_lithography, 2011 (accessed 10/9/2018).
[198] N.A. Lange, Lange's Handbook of Chemistry, 15th ed., McGraw-Hill, New York, 1999.
[199] J. Mitchell-Smith, A. Speidel, I. Bisterov, A.T. Clare, Electrolyte Multiplexing in Electrochemical Jet Processing, Procedia CIRP 68 (2018) 483-487.
[200] P. Walker, W. Tarn, CRC Handbook of Metal Etchants, CRC Press, USA, 1991.
[201] T.B. Britton, J. Jiang, Y. Guo, A. Vilalta-Clemente, D. Wallis, L.N. Hansen, A. Winkelmann, A.J. Wilkinson, Tutorial: Crystal orientations and EBSD — Or which way is up?, Materials Characterization 117 (2016) 113-126.
[202] D. Brandon, K. W.D., Microstructural Characterization of Materials, John Wiley and Sons Ltd., England, 2008.
[203] R. Smith, S. Sharples, W. Li, M. Clark, M. Somekh, Orientation imaging using spatially resolved acoustic spectroscopy, Journal of Physics: Conference Series 353(1) (2012) 12003-12010.
[204] L. Wenqi, C. Jethro, W.A. John, J.S. Richard, C. Matt, G.S. Michael, D.S. Steve, Orientation Characterisation of Aerospace Materials by Spatially Resolved Acoustic Spectroscopy, Journal of Physics: Conference Series 520(1) (2014) 12017-12021.
[205] G. Moroni, W.P. Syam, S. Petrò, A simulation method to estimate task-specific uncertainty in 3D microscopy, Measurement 122 (2018) 402-416.
[206] G.S. Bumbrah, R.M. Sharma, Raman spectroscopy – Basic principle, instrumentation and selected applications for the characterization of drugs of abuse, Egyptian Journal of Forensic Sciences 6(3) (2016) 209-215.
[207] N.R. Pal, S.K. Pal, A review on image segmentation techniques, Pattern Recognition 26(9) (1993) 1277-1294.
[208] E.O. Hall, The Deformation and Ageing of Mild Steel: III Discussion of Results, Proceedings of the Physical Society. Section B 64(9) (1951) 747-753.
[209] T. Ikehara, T. Tsuchiya, Crystal orientation-dependent fatigue characteristics in micrometer-sized single-crystal silicon, Microsystems &Amp; Nanoengineering 2 (2016) 16027-16036.
[210] K. Sato, T. Yoshioka, T. Ando, M. Shikida, T. Kawabata, Tensile testing of silicon film having different crystallographic orientations carried out on a silicon chip, Sensors and Actuators A: Physical 70(1) (1998) 148-152.
[211] Z.F. Yue, Z.Z. Lu, C.Q. Zheng, Evaluation of creep damage behavior of nickel-base directionally solidified superalloys with different crystallographic orientations, Theoretical and Applied Fracture Mechanics 25(2) (1996) 127-138.
[212] T.M. Pollock, Alloy design for aircraft engines, Nature Materials 15 (2016) 809-815.
[213] B.L. Adams, S.I. Wright, K. Kunze, Orientation imaging: The emergence of a new microscopy, Metallurgical Transactions A 24(4) (1993) 819-831.
[214] R. Borrajo-Pelaez, P. Hedström, Recent Developments of Crystallographic Analysis Methods in the Scanning Electron Microscope for Applications in Metallurgy, Critical Reviews in Solid State and Materials Sciences (2017) 1-20.
[215] J.R. Helliwell, S. Harrop, J. Habash, B.G. Magorrian, N.M. Allinson, D. Gomez, M. Helliwell, Z. Derewenda, D.W.J. Cruickshank, Instrumentation for Laue diffraction (invited), Review of Scientific Instruments 60(7) (1989) 1531-1536.
[216] R.R. Keller, R.H. Geiss, Transmission EBSD from 10 nm domains in a scanning electron microscope, Journal of Microscopy 245(3) (2012) 245-251.

[217] S.K. Mukherjee, S. Kumar, P.K. Srivastava, A. Kumar, Effect of valency on material removal rate in electrochemical machining of aluminium, Journal of Materials Processing Technology 202(1) (2008) 398-401.
[218] X. Yang, X. Liu, Y. Lu, S. Zhou, M. Gao, J. Song, W. Xu, Controlling the Adhesion of Superhydrophobic Surfaces Using Electrolyte Jet Machining Techniques, Scientific Reports 6 (2016) 23985-23994.
[219] J.F.B. J. A. Lillard, D. G. Kolman, Morphology of Pits in Nickel: Anisotropic Growth Due to Crystallographic Orientation, in: M. Seo, H. Takahashi (Eds.) Proceedings / [Electrochemical Society], Electrochemical Society, 1999, pp. 453-462.
[220] M. Yasuda, F. Weinberg, D. Tromans, Pitting Corrosion of Al and Al-Cu Single Crystals, Journal of The Electrochemical Society 137(12) (1990) 3708-3715.
[221] R.K. Leach, Optical Measurement of Surface Topography, Springer-Verlag, Berlin, 2011.
[222] P. Ekberg, R. Su, R. Leach, High-precision lateral distortion measurement and correction in coherence scanning interferometry using an arbitrary surface, Opt. Express 25(16) (2017) 18703-18712.
[223] F. J. Humphreys, M. Hatherly, Recrystallization and Related Annealing Phenomena, 2nd ed., Elsevier Ltd, Oxford, 2004.
[224] P. García, S. Rivera, M. Palacios, J. Belzunce, Comparative study of the parameters influencing the machinability of leaded brasses, Engineering Failure Analysis 17(4) (2010) 771-776.
[225] O. Frank, M. Zukalova, B. Laskova, J. Kürti, J. Koltai, L. Kavan, Raman spectra of titanium dioxide (anatase, rutile) with identified oxygen isotopes (16, 17, 18), Physical Chemistry Chemical Physics 14(42) (2012) 14567-14572.
[226] J.L. Hudson, T.T. Tsotsis, Electrochemical reaction dynamics: a review, Chemical Engineering Science 49(10) (1994) 1493-1572.
[227] R.W. Ramette, R.W. Sandford, Thermodynamics of Iodine Solubility and Triiodide Ion Formation in Water and in Deuterium Oxide, Journal of the American Chemical Society 87(22) (1965) 5001-5005.
[228] C.E. Bocking, High-Speed Selective Jet Electrodeposition of Gold and Copper GEC J. Res. 9 (1992) 130-142.
[229] A. Augustin, K. Rajendra Udupa, K. Udaya Bhat, Effect of coating current density on the wettability of electrodeposited copper thin film on aluminum substrate, Perspectives in Science 8 (2016) 472-474.
[230] W. Septina, S. Ikeda, M.A. Khan, T. Hirai, T. Harada, M. Matsumura, L.M. Peter, Potentiostatic electrodeposition of cuprous oxide thin films for photovoltaic applications, Electrochimica Acta 56(13) (2011) 4882-4888.
[231] B. Beverskog, I. Puigdomenech, Revised Pourbaix Diagrams for Copper at 25 to 300°C, Journal of The Electrochemical Society 144(10) (1997) 3476-3483.
[232] V.S. Donepudi, R. Venkatachalapathy, P.O. Ozemoyah, C.S. Johnson, J. Prakash, Electrodeposition of Copper from Sulfate Electrolytes: Effects of Thiourea on Resistivity and Electrodeposition Mechanism of Copper, Electrochemical and Solid-State Letters 4(2) (2001) C13-C16.
[233] J. Laskowski, J.A. Kitchener, The hydrophilic—hydrophobic transition on silica, Journal of colloid and interface science 29(4) (1969) 670-679.
[234] J. Jiang, G. Oberdörster, P. Biswas, Characterization of size, surface charge, and agglomeration state of nanoparticle dispersions for toxicological studies, Journal of Nanoparticle Research 11(1) (2009) 77-89.
[235] P. Atkins, J.d. Paula, Physical Chemistry, 9th ed., Oxford University Press, W. H. Freeman and Company, 2010.
[236] V. Terzieva, J. Fransaer, J.P. Celis, Codeposition of Hydrophilic and Hydrophobic Silica with Copper from Acid Copper Sulfate Baths, Journal of The Electrochemical Society 147(1) (2000) 198-202.
[237] R.O. Hussein, X. Nie, D.O. Northwood, An investigation of ceramic coating growth mechanisms in plasma electrolytic oxidation (PEO) processing, Electrochimica Acta 112 (2013) 111-119.
[238] D.A.H. Hanaor, C.C. Sorrell, Review of the anatase to rutile phase transformation, Journal of Materials Science 46(4) (2011) 855-874.
[239] M.V. Diamanti, B. Del Curto, V. Masconale, C. Passaro, M.P. Pedeferri, Anodic coloring of titanium and its alloy for jewels production, Color Research & Application 37(5) (2012) 384-390.

Appendices

Appendix 1: As-received composition for brass Cu39Zn2Pb and the calculated weighted alloy ECE at minimum and maximum compositions.

	Cu (wt. %)	Cu (at. %)	Zn	Pb (wt. %)	Pb (at. %)	ECE (mg/C)
Min.	58.0	59.3	Balance	1.5	0.5	0.337
Max.	60.0	61.7		2.5	0.8	0.339

Appendix 2: Nominal composition of Inconel 718 and ECE to calculate removal.

	Ni	Cr	Nb	Mo	Ti	Al	Co	Si	Mn	Cu	C	P	Fe
Wt. %	53.4	18.8	5.27	2.99	1.02	0.50	0.17	0.12	0.07	0.07	0.03	0.01	Bal.
ECE (mg/C)	0.304	0.18	0.019	0.025	0.124	0.093	0.031	0.073	0.285	0.659	0.018	0.006	0.019

Appendix 3: Nominal composition of Ti-6Al-4V sheet used in this thesis.

	N	C	H	O	Fe	Al	V	Ti	Other Elements
wt. % min.	-	-	-	-	-	5.50	3.50	-	-
wt. % max.	0.05	0.10	0.0125	0.20	0.30	6.75	4.50	Bal.	0.4 (total)
									ECE (g/C)
Min.						5.50	3.50	91.00	1.2056×10^{-5}
Max.						6.75	4.50	88.75	1.1977×10^{-5}

Appendix 4: EJP parameters used in the microstructural investigations: Cu, Ni, Al.

Process parameter	
Applied current density (A/cm^2)	20, 50, 100, 150, 200, 250, 300, 350, 400, 450
Dwell time (s)	4
Nozzle internal diameter (mm)	0.51
Inter-electrode gap (mm)	0.5
Electrolyte jet velocity (m/s)	29.0
Concentration (M)	2.3
Electrolyte conductivity (mS/cm)	136.56 (± 0.05) *at 22.7 – 23.2 °C ($NaNO_3$)*
	165.24 (± 0.06) *at 22.8 – 23.3 °C (NaCl)*

Appendix 5: EJP parameters used in the brass (Cu39Zn2Pb) investigation.

Universal parameters	**Value**		
Nozzle internal diameter (mm)	0.51		
Inter-electrode gap (mm)	0.5		
Electrolyte jet velocity (m/s)	25.0		
$NaNO_3$ concentration (M)	2.3		
Pit machining	Mean current density (A/cm^2)	Charge per pit (C)	Dwell time (ms)
	20	0.546	14000
	50	0.566	5600
	100	0.534	2667
	150	0.558	1806
	200	0.560	1366
	250	0.560	1098
	300	0.563	918
	350	0.554	778
	400	0.559	682
	450	0.532	589
Striation machining	**Value**		
Traverse velocity (µm/s)	500		
Mean current density (A/cm^2)	20, 100, 300		

Appendix 6: Electrolytes used for enhancing precision and dimensional accuracy in Inconel 718. All conductivities measured at 23 °C (±0.2 °C)

Electrolyte	Composition Ratio	Ionic Strength (M)	Electrolyte Conductivity (mS/cm^{-1})
NaCl	2.3 : 0	2.3	165.4 (σ = 0.1%)
$NaNO_3$	2.3 : 0	2.3	136.6 (σ = 0.03%)
$NaNO_3$	1.8 : 0	1.8	116.0 (σ = 0.1%)
$NaNO_3$ + 5% NaI (**NaI5%**)	2.185 : 0.115	2.3	137.7 (σ = 0.1%)
$NaNO_3$ + 10% NaI (**NaI10%**)	2.07 : 0.23	2.3	139.7 (σ = 0.1%)
$NaNO_3$ + 15% NaI (**NaI15%**)	1.955 : 0.345	2.3	141.8 (σ = 0.1%)
$NaNO_3$ + 20% NaI (**NaI20%**)	1.84 : 0.46	2.3	143.3 (σ = 0.2%)
$NaNO_3$ + 30% NaI (**NaI30%**)	1.61 : 0.69	2.3	145.6 (σ = 0.1%)
$NaNO_3$ + 40% NaI (**NaI40%**)	1.38 : 0.92	2.3	149.4(σ = 0.1%)

Appendix 7: Electrolytes used in preliminary titanium EJP study.

Electrolyte	Concentration tested (M)
NaCl	2, 2.5, 3, 3.5, 4
$NaNO_3$	2, 2.5, 3, 3.5, 4
NaBr	2, 2.5, 3, 3.5, 4
NaF	0.5
NaCl : NaF	2 (3 : 1 composition ratio)

Appendix 8: Electrolytes to enhance processing of titanium

Electrolyte	Composition Ratio
NaCl	2.3 : 0
NaI 30%	1.61 : 0.69
NaBr 30%	1.61 : 0.69
NaF 20%	1.84 : 0.46
NaI 100%	0 : 2.3
NaBr 100%	0 : 2.3

Appendix 9: EJP parameters for processing Inconel 718.

Pit machining parameters	Value
Nozzle internal diameter (mm)	0.51
Inter-electrode gap (mm)	0.5
Dwell time (s)	4
Approximate mean current density (A/cm^2)	20, 50, 100, 150, 200
Electrolyte jet velocity (m/s)	4.1, 9.7, 14.1, 19.3, 23.5, 29.7
Striation machining parameters	**Value**
Nozzle internal diameter (mm)	0.25, 0.06
Inter-electrode gap (mm)	0.5
Traverse velocity (µm/s)	500
Approximate current density (A/cm^2)	200, 400
Electrolyte jet velocity (m/s)	23.5

Appendix 10: EJP parameters for processing Ti-6Al-4V.

Pit machining parameters	**Value**
Nozzle internal diameter (mm)	0.25
Inter-electrode gap (mm)	0.5
Dwell time (s)	10
Approximate mean current density (A/cm^2)	408
Electrolyte jet velocity (m/s)	23.5
Striation machining parameters	**Value**
Nozzle internal diameter (mm)	1, 0.51, 0.25
Inter-electrode gap (mm)	0.5, 0.3
Traverse velocity (µm/s)	100, 150, 200, 300, 400, 500
Approximate current density (A/cm^2)	20, 50, 75, 100, 150, 200, 300, 400
Electrolyte jet velocity (m/s)	3.4, 8.3, 12.4, 16.3, 19.9, 24.8

Appendix 11: Electrolytes used in electrodeposition. Deionised water used as solvent.

Trial set	**Chemicals**	**Composition ranges**
Nodule sizing	$CuSO_4.5H_2O$	0.1-0.662 M
	Na_2SO_4	0-1 M
	H_2SO_4	pH 2-4.5
Trial set	**Chemicals**	**Composition ranges**
Meso-behaviour (thiourea addition)	$CuSO_4.5H_2O$	0.5 M
	Na_2SO_4	0.25 M
	Thiourea	0.14-6.57 mM
	Silica powder	0.3 g/L
Trial set	**Chemicals**	**Composition ranges**
Surface charge (zeta potential)	$CuSO_4.5H_2O$	0-50 mM
	H_2SO_4	pH 2-4.5
	Silica powder	0.1 g/L
Trial set	**Chemicals**	**Composition ranges**
Hybrid electrolyte	$CuSO_4.5H_2O$	0.02-0.5 M
	Na_2SO_4	0-1 M
	H_2SO_4	pH 2-4.5
	Thiourea	0-15 mM
	Silica powder	0.3 g/L